UNIVERSIDADE DE SÃO PAULO
Instituto de Física

Investigação da estrutura nuclear de altos spins por meio de espectroscopia gama e reações com íons pesados

José Roberto Brandão de Oliveira

Monografia apresentada ao Instituto de Física da Universidade de São Paulo para obtenção de título de livre-docência

SÃO PAULO
2001

À prole, presente e futura.

Agradecimentos:

Agradeço aos inúmeros colegas e amigos, nacionais ou estrangeiros, e à familia, que contribuíram para a realização dos vários trabalhos aqui sistematizados, e às instituições, idem, FAPESP, CNPq, USP, LBL e INFN. A omissão de nomes evita (comodamente) hierarquizar com inevitável injustiça. Tá?

Resumo

Este trabalho sistematiza a investigação da estrutura nuclear através de espectroscopia gama de reações com íons pesados em diversas regiões de massa da tabela de nuclídeos. A relação entre modelos teóricos e resultados experimentais, assim como os equipamentos e técnicas que possibilitam a realização das experiências são discutidos. Dezoito artigos publicados são apresentados.

Abstract

This work systematizes the investigation of the nuclear structure by means of gamma spectrocopy of heavy-ion reactions in various mass regions of the nuclide chart. The relation between theoretical models and experimental results, as well as the equipment and techniques which allow the performance of experiments are discussed. Eighteen published articles are presented.

Sumário

Capítulo 1

Introdução

Reações com íons pesados possibilitam a investigação do núcleo atômico em sua terceira dimensão principal - momento angular. Nas últimas 2 ou 3 décadas enorme quantidade de informação foi obtida através de técnicas de espectroscopia gama em linha deste tipo de reações, consistindo de esquemas de níveis detalhados, medidas de vidas médias, fatores giromagnéticos etc. Modelos cada vez mais sofisticados foram desenvolvidos objetivando a explicação dos mecanismos que geram alto momento angular no núcleo. O sucesso dos modelos em determinados momentos, aliado ao seu fracasso em outros são a principal justificativa para investimentos em equipamentos cada vez mais sensíveis e capazes de isolar e estudar os eventos mais raros e exóticos. A próxima geração destes equipamentos consistirá de sistemas virtualmente capazes de detectar e identificar todas as partículas emitidas em uma reação o que será fundamental para a investigação de uma nova dimensão - a temperatura nuclear. Além disso novos sistemas aceleradores permitirão a utilização de feixes radioativos, possibilitando a investigação da estrutura nuclear em limites extremos de suas dimensões.

Núcleos são sistemas bem isolados, por isso há tão poucas dimensões relevantes. Mas são difíceis de examinar, ao contrário de por exemplo uma árvore, cujo funcionamento não seria razoável tentar compreender sem referência a praticamente um ecossistema. Alguém poderia pensar que esta última é mais difícil de estudar. Talvez seja. Mas pelo menos para a árvore podemos olhar, e para o gramado ao seu redor. Do núcleo só temos os "gramados" espectrais para analisar. Dele só imaginamos o que podemos auxiliados (às vezes dificultados...) pelos modelos.

Os modelos são uma forma simplificada de descrever a estrutura nuclear. Eles evidenciam certos aspectos que são "os mais relevantes" num certo contexto, simetrias por exemplo. Pode-se afirmar o mesmo de qualquer outro campo da ciência, mas é particularmente evidente neste. O núcleo não tem um ponto central, como o átomo, ao qual dirige-se a força principal de interação sobre as suas partículas. Mas apresenta características semelhantes às do modelo de camadas atômico, como se suas partículas "orbitassem" um campo central. O núcleo não é um corpo rígido, aliás nem é um sistema clássico. Mas comporta-se

aproximadamente como tal sob certas (outras) condições. Os núcleos deformados apresentam *bandas rotacionais* em que a energia cresce com o quadrado do momento angular. Isto indica que apesar de tratar-se de um sistema com número elevado de partículas, interagindo de forma complicada e pouco conhecida, ele comporta-se de forma análoga à de um rotor rígido clássico, cuja estrutura interna permanece aproximadamente a mesma, independentemente da velocidade angular de rotação. Aliás "muito análoga" no caso de núcleos superdeformados, descobertos décadas após a elaboração do modelo rotacional.

As medidas experimentais não se fazem porém de forma linear, sempre com objetivos claros e definidos. Somos limitados às possibilidades e recursos, mesmo em países em que estes não são tão escassos.

Este trabalho procura sistematizar mais de 10 anos de pesquisas. É uma tarefa difícil pela razão que acabamos de mencionar. Para proporcionar um panorama geral foi omitido relativamente pouco. São incuídos 18 artigos de um total de 29, em princípio cabíveis. Alguma ênfase será dada a resultados mais recentes, e a mais antigos que revelaram maior interêsse em sua sequência. Todas as medidas foram realizadas com utilização de técnicas de espectroscopia gama em linha de reações com íons pesados, descritas em linhas gerais no capítulo 3. Os estados de alto spin são populados através de reações de fusão-evaporação. Os raios gama são detectados em espectrômetros de alta resolução com utilização de detectores de Germânio hiperpuro (GeHP). Técnicas de coincidência $\gamma-\gamma$ permitem a reconstrução do esquema de níveis nuclear. Medidas de vidas médias dos estados são obtidas com técnicas baseadas em efeito Doppler. De modo geral prova-se a interrelação entre graus de liberdade de partícula independente e coletivos. Esta expressão enfraqueceu-se por estar em quase todos os livros. Mas está no âmago do modo como vemos a estrutura nuclear. Considere-se por exemplo a influência dos estados de partícula independente ocupados sobre o grau de triaxialidade da deformação de núcleos transicionais. O efeito definitivamente está lá, e tem influência perceptível sobre as características de bandas rotacionais. Não exatamente como o esperado... Outro caso é o do colapso das correlações de emparelhamento em alto spin. Frequentemente um resultado é sugestivo, mas não é conclusivo. Novas variáveis necessitam ser medidas, ou é necessária maior precisão experimental.

No capítulo 2 encontra-se uma introdução geral aos modelos nucleares mais frequentemente utilizados nos artigos. Por razões de concisão, e por tratarem-se de trabalhos fundamentalmente experimentais os modelos são tratados de maneira algumas vezes superficial. O objetivo principal é introduzir um mínimo de conceitos fundamentais que facilite a leitura dos artigos. Lamentamos que nem sempre isto tenha sido possível devido aos compromissos clareza-concisão e clareza-completude. Detalhes adicionais podem ser encontrados nos próprios artigos e formulações mais abrangentes nas referências. No Capítulo 3 encontra-se uma introdução à intrumentação e ao método experimental. O Capítulo 4 é uma discussão introdutória que sistematiza os artigos agrupando-os por regiões de massa. No caso de trabalhos ainda não publicados faz-se uma descrição mais completa. O Capítulo 6 apresenta as conclusões gerais. Os artigos constituintes desta obra encontram-se ao final no Apêndice.

Capítulo 2

Modelos Nucleares

2.1 Modelos de partícula independente e coletivos

2.1.1 Modelo de camadas esférico e deformado

A força nuclear possui uma parte repulsiva de curto alcance ($\approx$ 0.4 fm). No entanto em um núcleo típico a distância média entre dois núcleons é muito superior à aquela, e portanto sentem apenas o efeito de uma cauda atrativa. Isto sugere que, ao menos como primeira aproximação, o núcleo possa ser descrito em termos de movimentos de partículas independentes em um campo médio atrativo devido a todos os outros núcleons. Esta é uma abordagem muito produtiva tendo obtido historicamente grande sucesso, como por exemplo a "explicação" dos números mágicos com a inclusão da interação spin-órbita.

Inicialmente considerava-se um núcleo com potencial esfericamente simétrico (como por exemplo o potencial de Woods-Saxon) com parâmetros ajustados para reproduzir os dados experimentais. No entanto para núcleos afastados de camadas fechadas, o modelo só funciona adequadamente assumindo-se um potencial de partícula única deformado. Dentre as várias versões para o potencial deformado destaca-se por sua importância histórica o modelo de Nilsson [1]. A hamiltoniana de Nilsson tem como base o oscilador harmônico deformado (axialmente simétrico), ao qual são adicionados termos de spin-órbita e órbita-órbita. Os números quânticos assintóticos de Nilsson ($[Nn_z\Lambda]\Omega^\pi$) são frequentemente utilizados para classificar as configurações.

2.1.2 Modelo rotacional

Núcleos deformados apresentam característica bandas rotacionais. As energias dos estados da banda do estado fundamental de um núcleo deformado par-par, por exemplo, é bem descrita pela fórmula:

$$E(I) = \frac{I(I+1)}{2\mathcal{J}}$$

onde $\mathcal{J}$ é o momento de inércia. No modelo rotacional extremo este é um parâmetro constante. Na prática os momentos de inércia podem ser variáveis e dependem do momento angular e da configuração do cabeça de banda. Definem-se os momentos de inércia cinemático $\mathcal{J}^{(1)}$ e dinâmico $\mathcal{J}^{(2)}$ através de:

$$\mathcal{J}^{(1)} = \frac{2I-1}{E_\gamma}$$

$$\mathcal{J}^{(2)} = \frac{4\hbar}{\Delta E_\gamma}$$

Onde E_γ é a energia da transição E2 a partir do estado de spin I, e ΔE_γ é a diferença de energia entre duas transições E2 consecutivas. Para um rotor rígido $\mathcal{J}$ é constante e $\mathcal{J}^{(1)} = \mathcal{J}^{(2)} = \mathcal{J}$.

O modelo rotacional pode ser complementado com os modelos de camadas formando o modelos tipo rotor mais partículas.

2.2 Parametrização da forma nuclear

Para descrever a deformação (de quadrupolo) nuclear é usual escrever a equação de superfície de acordo com a convenção de Lund [2] (omitindo-se deformações de multipolaridade mais elevada):

$$R(\theta,\varphi) = R_0 \left\{ 1 + \beta_2 \cos\gamma Y_2^0(\theta,\varphi) - \beta_2 \sin\gamma \frac{1}{\sqrt{2}} \left[Y_2^2(\theta,\varphi) + Y_2^{-2}(\theta,\varphi) \right] \right\}$$

onde R representa o raio polar, Y_l^m são harmônicos esféricos e os parâmetros β_2e γ são os parâmetros de elongação (quadrupolar) e grau de triaxialidade respectivamente. Por simplicidade (e na ausência ou irrelevância da deformação de hexadecapolo β_4) define-se $\beta = \beta_2$.

Nesta convenção o parâmetro angular γ é válido entre os ângulos de $-120°$ e $60°$ e indica trambém o caráter de coletividade da rotação. A rotação é sempre assumida em torno do eixo x'. Por exemplo: $\gamma = 0°$ para um núcleo de deformação prolata axialmente simétrica em torno do eixo z', rodando portanto coletivamente em torno do eixo perpendicular ao eixo de simetria. Os ângulos de $\gamma = -120°$, $-60°$ e $60°$ também correspondem a formas axialmente simétricas, prolata não-coletiva (rodando *intrinsecamente* em torno de eixo de simetria), oblata coletiva e oblata não-coletiva, respectivamente. O máximo de triaxialidade ocorre para ângulos $\gamma = -90°$, $-30°$ e $30°$, enquanto que o máximo momento de inércia irrotacional ocorre para $\gamma = -30°$ correspondendo também ao máximo de coletividade.

Os núcleos esféricos correspondem a $\beta = 0$. Os núcleos afastados de números mágicos (ou camadas fechadas) tendem a desenvolver deformações significativas ($\beta \approx 0.3$) e são usualmente axialmente simétricos. Os núcleos transicionais tem deformação β intermediária

mas podem desenvolver deformações triaxiais significativas. Para núcleos superdeformados a equação de superfície acima não é uma aproximação muito boa. Nestes núcleos a razão entre eixos do elipsóide está em torno de $2:1:1$, correspondendo grosso modo a $\beta \approx 0.6$.

2.3 Modelos de *Cranking*

A imagem usual que fazemos de um núcleo rotacional é a de um elipsóide deformado, axialmente simétrico, rodando em torno de um eixo perpendicular ao eixo de simetria. Se a velocidade angular de rotação puder ser considerada aproximadamente constante, podemos supor que, em um referencial com essa mesma velocidade angular, o potencial médio nuclear (seja auto-consistente, ou o potencial central empírico do modelo de camadas) pode ser representado como uma função da posição, *independente* do tempo. Como este referencial é não inercial, o movimento das partículas neste potencial será afetado de forças centrífuga e de Coriolis, modificando o seu espectro. Esta é basicamente a origem dos modelos de *Cranking*.

2.3.1 A Hamiltoniana de *Cranking*

Nos modelos de cranking considera-se um referencial em rotação com velocidade angular constante ω em torno de um eixo fixo (convencionalmente o eixo $x' = x$). A hamiltoniana de *Cranking* ou intrínseca H_ω é dada por:

$$H_\omega = H - \omega J_x$$

Onde H é a soma de Hamiltonianas de partícula única com campo médio deformado e J_x é a componente do momento angular na direção do eixo de rotação. A hamiltoniana de cranking é diagonalizada obtendo-se a função de onda Φ_ω que é um determinante de Slater. A energia deve ser minimizada no referencial intrínseco. O valor médio do operador H_ω, isto é, $\langle H_\omega \rangle = \langle \Phi_\omega | H_\omega | \Phi_\omega \rangle$, é definido como routhiano total E' ou energia no referencial intrínseco:

$$E' = \langle H_\omega \rangle = \langle H \rangle - \omega \langle J_x \rangle$$

A energia no referencial de laboratório é dada por $E = \langle H \rangle$ e define-se o *alinhamento* total como $I_x = \langle J_x \rangle = -\frac{dE'}{d\omega}$. A velocidade angular é obtida de acordo com princípios variacionais (para uma dedução veja-se por exemplo a ref. [3]):

$$\omega = \frac{dE}{dI_x}$$

Emparelhamento

As correlações de emparelhamento são incluídas através da utilização de um tratamento de BCS. Devido às correlaçoes de emparelhamento, as partículas não se encontram em órbitas independentes. O estado fundamental é um *condensado* de pares, como em um superfluido, com momento angular total nulo. Para contornar esta dificuldade, introduz-se o conceito de quasipartículas, que são entidades com características híbridas de partícula e buraco. As quasipartículas são excitações do condensado, considerado como o vácuo de quasipartículas, e são independentes.

Assumindo-se um campo de emparelhamento de monopolo com elementos de matriz constantes Δ, os routhianos de quasipartícula são obtidos a partir da solução do problema de autovalores [4]:

$$\begin{pmatrix} (h-\lambda-\omega j_x)_{\alpha i \alpha' i'} & \Delta\delta_{ii'} \\ \Delta\delta_{ii'} & -(h-\lambda-\omega j_x)_{\alpha i \alpha' i'} \end{pmatrix} \begin{pmatrix} U_i^{\alpha\mu} \\ V_i^{\alpha\mu} \end{pmatrix} = e'_{\alpha\mu} \begin{pmatrix} U_i^{\alpha\mu} \\ V_i^{\alpha\mu} \end{pmatrix}$$

Onde o potencial químico λ fixa o número total de partículas, e h, a hamiltoniana de partícula única contém o potencial deformado. No contexto do modelo de camadas (*Cranked Shell Model* - CSM [5]) é, por exemplo, a hamiltoniana do oscilador harmônico modificado. U e V são as amplitudes de partícula e buraco respectivamente.

Os estados de quasipartícula $|\alpha\mu\rangle$ são classificados por meio de dois números quânticos (π, α) de simetria: paridade (subentendida na equação acima) e *signature* α (simetria de rotação de 180° em torno do eixo x), definida através das equações:

$$e^{-i\pi j_x} |\alpha\mu\rangle = e^{-i\pi\alpha} |\alpha\mu\rangle$$

$$\alpha = \pm\frac{1}{2}$$

2.3.2 Diagramas de quasipartículas

Devido à duplicação do espaço (correspondente a partículas e buracos), os diagramas de quasipartícula (qp): $e'\times\omega$, tem simetria de reflexão em torno do eixo de energia zero, cada estado correspondendo a um estado simétrico de *signature* $-\alpha$ e routhiano $-e'$. O condensado (vácuo de qp) é representado pela ocupação de todos os estados de energia negativa. As excitações elementares correspondem à desocupação de um nível de energia negativa e a ocupação do nível simétrico correspondente, mas somente metade da energia de excitação (e demais quantidades) deve ser contabilizada.

O alinhamento i_x (ou projeção do momento angular no eixo de rotação) de qp é dado pela inclinação no gráfico de $e'\times\omega$:

$$i_x = -\frac{de'}{d\omega}$$

Figura 2.1: Diagrama de quasipartículas.

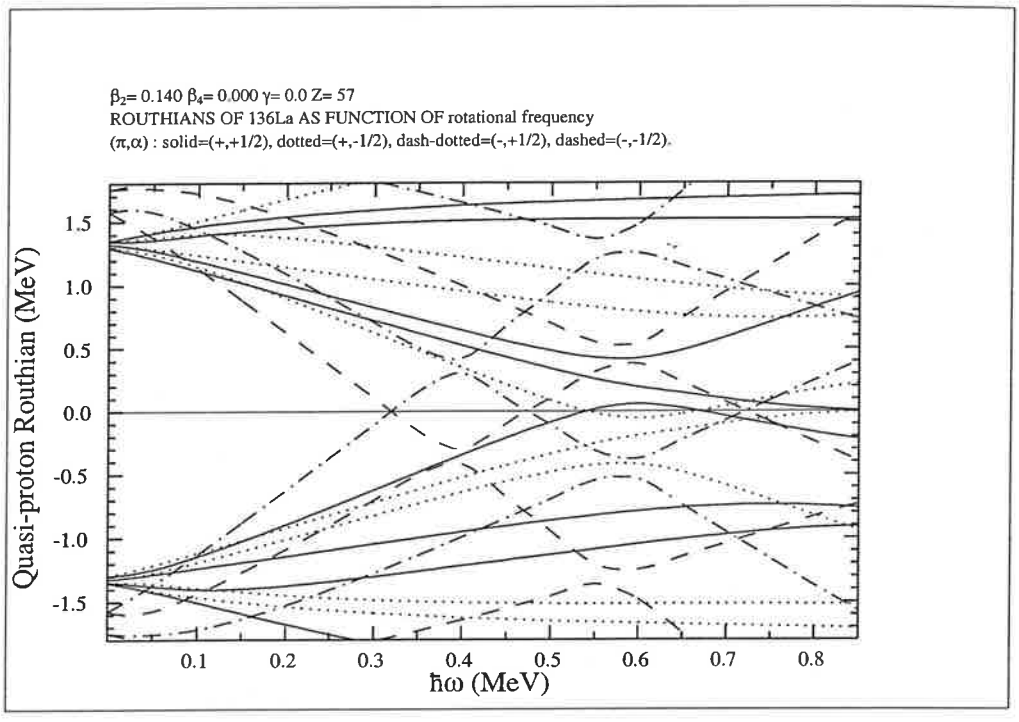

A figura 2.1 mostra um exemplo de diagrama de *qp* (prótons no ^{136}La). Como se trata de um núcleo ímpar em número de prótons, o estado de energia mínima já contem a excitação de 1 quasipróton (o vácuo corresponde a um núcleo par). Para a frequência de $\hbar\omega = 0.2$ MeV, por exemplo, o estado de energia mínima é a excitação do nível de $(\pi, \alpha) = \left(-, +\frac{1}{2}\right)$ para o de $(\pi, \alpha) = \left(-, -\frac{1}{2}\right)$, com energia de excitação $e' \tilde{\approx} 0.5$ MeV, neste caso um estado da subcamada intrusa $h_{11/2}$.

A interação de "Coriolis" $(-\omega j_x)$ tende a alinhar o momento angular de *qp* com a direção do eixo de rotação (x). A partir de uma certa velocidade de rotação, torna-se energeticamente favorável o alinhamento do momento angular de um par de *qp* com o eixo de rotação ao invés de mantê-lo emparelhado participando do *condensado*. Na figura 2.1 isto ocorre para um par de quasiprótons da subcamada $h_{11/2}$ do caroço par-par à frequência de $\hbar\omega \approx 0.4$ MeV. Isto corresponde ao *cruzamento* da banda do estado fundamental, que se denomina banda **g**, com a banda do *par quebrado,* ou banda **s** (Stockholm). No entanto na banda $\pi h_{11/2}$ do núcleo Z-ímpar de La $(Z = 57)$, este primeiro cruzamento encontra-se bloqueado, devido ao princípio de exclusão de Pauli. Outros cruzamentos podem occorrer a frequências mais altas.

O diagrama da figura 2.1 corresponde a uma deformação fixa dada pelos parâmetros β_2, β_4, e γ. Para núcleos transicionais faz-se importante estudar também o comportamento dos

Figura 2.2: Diagrama de quasipartículas em função de γ.

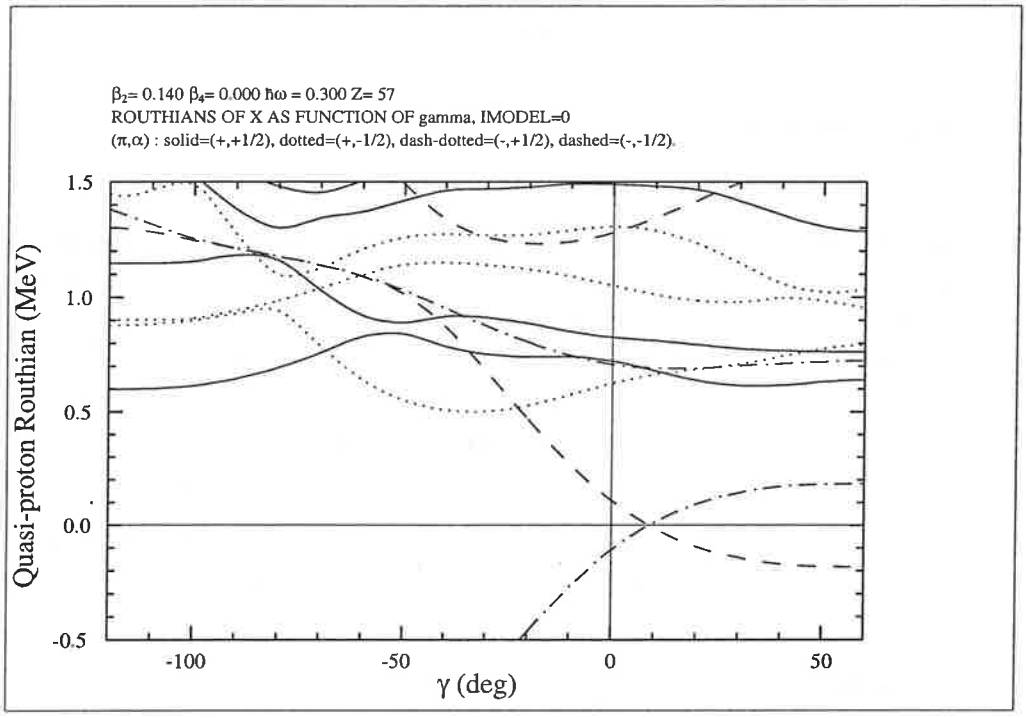

níveis de *qp* em função de γ. A figura 2.2 mostra um diagrama de *qp* para o ^{136}La em função de γ para uma velocidade angular de rotação fixa ($\hbar\omega = 0.3$MeV). Nota-se, por exemplo, que o quasipróton $h_{11/2}$ exerce uma tendência polarizadora no sentido de γ positivo, onde as duas *signatures* se desacoplam, apresentando alto valor de *signature splitting* (isto é, a diferença de energia entre os estados de *signatures* opostas). Este resultado ilustra o efeito da forte anisotropia da distribuição de massa de órbitas de alto-j.

2.3.3 Superfícies de Routhiano Total

Cálculos sistemáticos detalhados de Superfícies de Routhiano Total (TRS) [6] são frequentemente utilizados para prever as deformações nucleares de equilíbrio. Estes cálculos são baseados em um procedimento de Strutinski (gota líquida + correções de camada). O modelo de camadas utilizado é baseado no potencial de Woods-Saxon. Os parâmetros são otimizados para cada região de massa. A energia é minimizada com relação ao parâmetro de deformação de hexadecapolo β_4. À frequência de rotação zero os parâmetros de emparelhamento Δ_p e Δ_n auto-consistentes são calculados dentro do modelo de BCS, mas decrescem gradualmente com a frequência seguindo uma fórmula analítica pré-estabelecida. Os resultados são apresentados na forma de curvas de nível em um plano de coordenadas

polares $\beta_2 \times \gamma$ para cada configuração *yrast* definida através da paridade e *signature* de quasiprótons e quasinêutrons. É possível ainda o cálculo de TRS para a primeira excitação (*yrare*) de cada tipo. O modelo é muito bem sucedido em geral, inclusive para os casos de superdeformação, tornando-se um difundido padrão na literarura.

2.3.4 Transformação de dados experimentais para o sistema intrínseco

Para permitir a comparação com os cálculos de *Cranking*, os resultados experimentais são transformados para o sistema intrínseco. A velocidade angular é estimada a partir de dois estados (presumindo-se uma transição E2 intra-banda, com $\Delta I = 2$) através de diferenças finitas, e deve ser considerada como a velocidade média entre os dois estados.

$$\omega(I) = \frac{E(I+1) - E(I-1)}{I_x(I+1) - I_x(I-1)}$$

Para os alinhamentos normalmente utiliza-se a fórmula *semiclássica*:

$$I_x(I) = \sqrt{(I+1/2)^2 - K^2}$$

Onde K é a projeção (média) do momento angular total sobre o eixo intrínseco z' (perpendicular ao eixo de rotação x, usualmente o eixo de simetria cilíndrica da deformação). A rigor esta fórmula é uma correção usada no modelo de *Cranking*, tradicional. O modelo de *Tilted Axis Cranking*, na próxima seção, permitirá tratar bandas de alto K de forma mais rigorosa prescindindo desta relação.

O routhiano experimental é definido como:

$$E'(I) = \frac{1}{2}\left(E(I+1) + E(I-1)\right) - \omega(I) I_x(I)$$

Para se obter as quantidades experimentais correspondentes a quasipartículas (alinhamento i e routhiano e'), subtrai-se uma referência polinomial, ajustada em geral para reproduzir o alinhamento (I_{xg}) e o routhiano (E'_g) da banda do estado fundamental (g) do caroço par-par (ou vácuo de *qp*), na forma:

$$i = I_x - I_{xg}$$

$$e' = E' - E'_g$$

$$I_{xg}(\omega) = \omega J_0 + \omega^3 J_1$$

$$E'_g = -\frac{\omega^2}{2}J_0 - \frac{\omega^4}{4}J_1 + \frac{\hbar^2}{8J_0}$$

onde J_0 e J_1 são os parâmetros de Harris.

Havendo excitações de várias quasipartículas, o alinhamento i e o routhiano e' experimentais correspondem à soma das quantidades teóricas respectivas de todas elas.

No sistema de laboratório, *signature* é sempre um bom número quântico, e está associado ao valor do spin I do estado nuclear através de:

$$I = \alpha + 2n$$

Onde n é um número inteiro. Em um núcleo de A ímpar, α pode assumir os valores $+\frac{1}{2}$ e $-\frac{1}{2}$ enquanto que em um núcleo par α pode assumir convencionalmente os valores -1 e 0 (ou equivalentemente 1 e 0).

2.4 *Tilted Axis Cranking (TAC)*

O modelo de TAC [7] pode ser considerado uma generalização do modelo de *Cranking*. No modelo de *Cranking* tradicional a rotação de um núcleo deformado ocorre em torno de um dos eixos principais do tensor de inércia. No modelo de TAC, considera-se que o eixo de rotação pode ter uma orientação arbitrária em relação aos eixos principais. Inicialmente o modelo surgiu para a interpretação da estrutura das bandas de alto K em núcleos com simetria axial (onde K é a projeção do momento angular total sobre o eixo de simetria), obtendo considerável sucesso[8] [9] [10]. O desenvolvimento das consequências formais do modelo paralelamente à observação experimental de bandas com características rotacionais em núcleos quase esféricos na região de A≈200 [11] [12] [13] [14] [15] resultou no reconhecimento do mecanismo denominado *shears bands* [16] ou rotação magnética [17] [18]. O modelo prevê a ocorrência do fenômeno em outras diversas regiões de massa. Muitos casos já foram confirmados (para uma compilação recente vide ref. [19]).

Existem diversas variantes do modelo de TAC. Aqui serão discutidos apenas aspectos gerais e fundamentais. A hamiltoniana de TAC (H') autoconsistente é (convencionando-se rotação em torno do eixo z) [20]:

$$H' = H - \omega J_z$$

No contexto do cálculo variacional, o routhiano $E' = \langle H' \rangle$ é um extremo. O vetor velocidade angular é paralelo ao vetor momento angular total:

$$\vec{\omega} = (\omega_x, \omega_y, \omega_z) = (0, 0, \omega)$$

$$\vec{J} = (\langle J_x \rangle, \langle J_y \rangle, \langle J_z \rangle)$$

pois:

$$\langle [H', J_x] \rangle = i\omega \langle J_y \rangle$$

$$\langle [H', J_y] \rangle = -i\omega \langle J_x \rangle$$

e, como os membros do lado esquerdo correspondem à pequenas variações de E', sua estacionaridade implica em:

$$\langle J_x \rangle = \langle J_y \rangle = 0$$

ou seja:

$$\vec{\omega} \| \vec{J}$$

e ainda o momento angular total: $J = \langle J_z \rangle$.

Para uma família de soluções autoconsistentes $|\omega\rangle$ para diferentes valores de ω, valem as relações canônicas:

$$\frac{dE'}{d\omega} = -J$$

$$\frac{dE}{dJ} = \omega$$

Estas fórmulas permitem a comparação dos cálculos com os resultados experimentais analogamente ao descrito na seção 2.3.4. A fórmulas são semelhantes ao modelo de *Cranking* tradicional para $K = 0$, o qual é um caso particular do modelo de TAC denominado PAC (*principal axis cranking*). Para este tipo de soluções o valor de *signature* (α) é um bom número quântico. Os estados intrínsecos de quasipartícula descrevem bandas rotacionais quadrupolares ($\Delta I = 2$). Outras soluções existem para rotação uniforme mesmo quando o eixo de rotação (ou, equivalentemente, o de momento angular total) não coincide com um eixo principal, formando ângulos significativamente distintos de zero com cada um deles. Neste caso a simetria de *signature* é quebrada no referencial intrínseco. Os estados intrínsecos não podem ser mais classificados por este número quântico, e descrevem bandas dipolares ($\Delta I = 1$), sem *signature splitting*. Se o momento angular se encontra num plano formado por dois eixos principais a solução de TAC se denomina *Planar*. Uma dimensão extra, o ângulo θ (ou de *tilting*) com o eixo principal de maior elongação, é introduzida e influi por exemplo sobre o diagrama de quasipartículas. Existem ainda soluções de tipo *Aplanar* que requerem mais um ângulo de Euler (φ) para sua parametrização. Estas soluções são responsáveis pelo aparecimento de bandas dipolares *quirais* degeneradas.

2.4.1 Bandas de alto K

Quando uma subcamada de alto-j se encontra quase completamente cheia, seus estados de quasipartícula tem componente predominante de buraco. A anisotropia da distribuição de massa das órbitas de buraco tende a alinhar seu momento angular com o eixo maior de deformação nuclear. As bandas rotacionais sobre configurações deste tipo se chamam *fortemente acopladas* ou de *alto-K*. Elas aparecem em núcleos fortemente deformados (em geral axialmente simétricos) e se caracterizam como bandas dipolares (M1) com cabeça de banda de spin $I = K$. K é a projeção do momento angular total no eixo de simetria, e pode ser considerado approximadamente como um bom número quântico. No modelo de TAC para uma banda deste tipo o ângulo de *tilting* é dado com boa aproximação pela fórmula: $\cos\theta = \frac{K}{I}$ e $I = \mathcal{J}\omega$ [10]. Desta forma o ângulo θ em função de ω apresenta o comportamento de uma bifurcação de Hopf. Esta não é no entanto a forma geral de uma solução de TAC de tipo planar. O modelo apresenta diversas surpresas do ponto de vista de modelos tradicionais, algumas delas apresentadas a seguir.

2.4.2 Rotação Magnética

Este é um outro tipo de solução originada no modelo de TAC.

A rotação magnética [17] pode ser diferenciada da rotação usual pela origem da quebra de isotropia do sistema nuclear, que é a própria condição de possibilidade da ocorrência de rotação de um sistema quântico. No caso da rotação usual, a definição de um eixo de orientação (relativamente ao momento angular total) está associada à deformação (basicamente quadrupolar) da distribuição de massa (ou carga elétrica) do núcleo. Já no caso da rotação magnética, a distribuição de corrente elétrica no núcleo é a que é responsável pela definição do eixo de orientação. Tanto uma quanto outra forma de rotação apresentam-se experimentalmente através de um espectro de transições intensas regularmente espaçadas, de caráter quadrupolar elétrico E2 (no caso usual), ou dipolar magnético M1 (no caso magnético). Os rotores magnéticos apareçem em regiões de núcleos quase esféricos (próximos de números mágicos). É ainda necessário que as camadas de prótons e nêutrons apresentem-se uma quase-preenchida e a outra um pouco além de preenchida, ou seja, com nível de Fermi próximo de órbitas com caráter de buraco ou partícula, respectivamente. No nível de excitação mais baixo, o momento angular das partículas acopla-se perpendicularmente ao dos buracos. O momento angular e a energia de excitação crescem gradativamente à medida que os momentos angulares de partículas e buracos se alinham lembrando o fechar de uma tesoura de tosa (daí também a denominação *shears bands*). Como os fatores giromagnéticos de prótons e nêutrons tem sinais opostos, os momentos magnéticos tendem a somar-se construtivamente na direção perpendicular ao momento angular total. Daí originam-se a orientação e as fortes transições M1. Na região de massa $A \approx 200$, as partículas e buracos em órbitas de alto momento angular $\pi h_{9/2}, i_{13/2}$ e $\nu i^{-1}_{13/2}$ participam. Na região de massa $A \approx 100$, as configurações intrusas que formam as lâminas da tesoura são basicamente $\pi g^{-2}_{9/2}$ e $\nu h^{2}_{11/2}$. O fechar das lâminas permite gerar apenas mais 5 unidades de momento

angular. No entanto, quasi-nêutrons nas órbitas de paridade normal (+) também participam, e orientam-se, dependendo do sinal de seu momento de quadrupolo, paralela ou perpendicularmente à configuração fortemente anisotrópica $\nu h^2_{11/2}$, contribuindo para a geração de momento angular. As bandas podem ser regulares (quanto ao espaçamento das transições no espectro) ou irregulares, dependendo do tipo de acoplamento.

Cabe mencionar ainda que a comprovação dos casos de rotação magnética envolve também a medida de vidas médias das transições gama, uma vez que somente a medida do momento de quadrupolo de transição permite aferir com confiabilidade a deformação nuclear.

2.4.3 Bandas quirais

Uma outra previsão do modelo de TAC, a existência de bandas *quirais* [21], cuja configuração no sistema intrínseco quebra a simetria de reflexão por um plano qualquer. Nas regiões de núcleos transicionais de $A \approx 130$, por exemplo, quasi-prótons e quasi-nêutrons (da subcamada de alto-j $h_{11/2}$) têm características predominantes de partícula e de buraco, respectivamente. Este fato, associado a uma região de núcleos pouco deformados e susceptíveis à polarização do parâmetro de deformação gama pode gerar formas triaxiais. O acoplamento do momento angular de partículas e buracos em um núcleo ímpar-ímpar triaxial tende a ser perpendicular, com os buracos alinhando-se paralelamente ao eixo principal maior do elipsóide, e as partículas alinhando-se ao eixo principal menor. Já o eixo de maior momento de inércia (para fluxo irrotacional) é o eixo principal intermediário, favorecendo portanto a rotação coletiva em torno deste eixo em altos spins. Desta maneira o sistema intrínseco do núcleo em rotação tem uma quiralidade definida pela orientação dos momentos angulares de partícula, de buraco e coletivo em três direções mutuamente ortogonais. Como a orientação é definida por vetores axiais, a paridade é preservada. Experimentalmente a existência deste tipo de configuração se verifica através da observação de duas bandas rotacionais dipolares magnéticas de mesma paridade praticamente degeneradas.

2.5 Modelo de camadas de larga escala

O avanço na velocidade dos computadores permitiu a realização de cálculos de modelo de camadas com interação residual de larga escala (*Large Scale Shell Model* - LSSM). É possível por exemplo o cálculo completo com até 8 partículas nas camadas pf (1.963.461 estados), para a região do ^{48}Cr [23] [22]. O acordo entre o cálculo teórico e os resultados experimentais é impressionante, inclusive no que diz respeito a transições eletromagnéticas. O núcleo de ^{48}Cr em particular é considerado o melhor "rotor", no meio da camada $f_{7/2}$. O modelo acrescenta inteligibilidade portanto à interessante interrelação entre graus de liberdade de partícula única e coletivos naquela região de massa.

Capítulo 3

Instrumentação e métodos

3.1 Espectrômetros gama

3.1.1 Detectores de alta resolução e Supressores Compton

Os detectores de GeHP possuem tipicamente resolução intrínseca de 1.9 a 2.5 keV (para o raio γ de decaimento do ^{60}Co de 1.33 MeV) para eficiências relativas de fotopico de 20 a 100% (de um cintilador de NaI(Tl) padrão de $3' \times 3'$). Como a eficiência absoluta de fotopico do cintilador padrão é de cerca de 20%, pode-se avaliar que grande parte da interação gama com detectores de GeHP dá-se através de espalhamento Compton, inútil para efeitos de determinação da energia do raio gama. Para detectores de 20% de eficiência relativa, por exemplo, a razão fotopico/total é de cerca de 15%.

A razão fotopico/total pode ser melhorada com a utilização de supressores Compton, que consistem de um cintilador de NaI(Tl) ou BGO (Germanato de Bismuto) que envolve o detector de alta resolução, e detecta o raio gama espalhado neste último. O sistema eletrônico veta os eventos correspondentes, permitindo somente a aquisição de eventos "limpos". O advento dos supressores Compton permitiu reduzir a grande quantidade de eventos espúrios devidos ao fundo de espalhamento contínuo. Isto é particularmente importante para medidas de coincidência $\gamma - \gamma$, para as quais importa aquela razão elevada ao quadrado. Um resultado prático deste avanço tecnológico foi a descoberta da banda superdeformada do ^{152}Dy com o espectrômetro TESSA3 de Daresbury [24] em 1986, que consistia de 12 detectores de GeHp com supressão Compton.

3.1.2 Sistemas de multidetectores de alta resolução

Os trabalhos discutidos nesta obra foram realizados com diversos sistemas diferentes, parte deles descritos resumidamente nesta subseção. Todos estes sistemas se utilizam de supressores Compton. Maiores detalhes encontram-se nas referências.

O espectrômetro HERA do Lawrence Berkeley Laboratory (Berkeley, CA, EUA).

Este sistema contava com 20 detectores de GeHP de cerca de 20% de eficiência, em geometria de detecção 4π. Os supressores Compton eram de BGO, mas possuíam um "bico" de NaI(Tl) de maior eficiência na detecção de raios gama de baixa energia, retroespalhados. Os detectores se encontravam a cerca de 20 cm do alvo, permitindo espaço para a montagem de um filtro de multiplicidades com 40 detectores cintiladores de BGO. O sistema encontrava-se instalado na caverna número 5 do Cyclotron de 88 polegadas do LBL. Este sistema foi desativado no final de 1992 para dar lugar ao sistema GAMMASPHERE (*www-gam.lbl.gov*) que conta hoje com mais de 100 detectores de GeHP de cerca de 90% de eficiência, vários deles segmentados, com supressores Compton.

O espectrômetro GASP dos Laboratori Nazionali di Legnaro (Legnaro, Itália).

Este sistema possui 40 detectores de GeHP de cerca de 90% de eficiência a cerca de 27 cm do alvo (na configuração I), também em geometria de detecção 4π [25]. Os detectores são dispostos em 7 anéis a ângulos aproximados de 30°, 60°, 72°, 90°, 108°, 120°, e 150° em relação à direção do feixe. O espaço interior da esfera de detectores de alta resolução acomoda um filtro de multiplicidades de BGO com 80 elementos. O sistema pode ser utilizado em outra configuração (II) mais compacta, sem utilização do filtro de multiplicidades, para as experiências em que é mais importante aumentar a eficiência de detecção. O espectrômetro é montado junto ao sistema acelerador Tandem-Linac dos LNL.

O Pequeno Espectrômetro de Radiação Eletromagnética com Rejeição de Espalhamento - PERERE (LAFN, IFUSP)

Este sistema possui 4 detectores de GeHP, 2 deles de 20% de eficiência e 2 de 60%, a 8.5 cm e 12 cm do alvo, respectivamente. Atualmente podem ser utilizados 8 cintiladores de NaI(Tl), 7 deles de 3 e 1 de 4 polegadas de diâmetro como filtro de multiplicidades. O sistema é montado na canalização 30°A do acelerador Pelletron do Laboratório Aberto de Física Nuclear (LAFN - IFUSP).

3.1.3 Sistemas de detecção ancilares

Sistemas de detecção ancilares são sistemas que auxiliam na seleção de eventos do espectrômetro gama de alta resolução. Um exemplo são os filtros de multiplicidade, já mencionados na subseção anterior, que selecionam eventos de alta multiplicidade (número de raios gama emitidos em dada reação nuclear), em geral associados à população de estados de mais alto spin.

O sistema de partículas carregadas ISIS (GASP, LNL)

O sistema ISIS [26] consiste de 40 detectores telescópicos ($\Delta E - E$) de barreira de superfície, em geometria de detecção 4π. A eficiência de detecção varia conforme a experiência e a partícula a ser detectada. Para prótons a eficiência típica é de 60% e para partículas α é de 25%.

O espectrômetro de massa de recuo CAMEL (GASP, LNL)

O espectrômetro de massa de recuo ou RMS CAMEL [27] permite identificar a massa A do núcleo residual formado na reação nuclear em coincidência com os raios gama detectados no sistema GASP. A resolução do sistema acoplado GASP-CAMEL é melhor do que 1/300 e a eficiência de transmissão típica é de 1% para reações com emissão de partículas carregadas e alvos relativamente espessos.

O Sistema Ancilar de Cintiladores Plásticos - SACI (LAFN - IFUSP)

Este sistema [28] possui 11 detectores telescópicos ($\Delta E - E$) tipo *phoswich*, dispostos na geometria de um dodecaedro (com a entrada do feixe por uma das faces). Permite a identificação de partículas carregadas em coincidência com raios gama detectados no sistema PERERE. O sistema cobre um ângulo sólido de cerca de 75% de 4π e a eficiência de detecção típica é de 40% para prótons e 15% para partículas α.

3.1.4 Os conceitos de *poder de resolução* e *limite observacional* de um espectrômetro

Dois fatores principais caracterizam a qualidade de um espectrômetro gama. O primeiro deles é a *eficiência de fotopico*, que afeta o número total de contagens de interesse, e o segundo o *poder de resolução*, que afeta a razão pico/fundo (ou sinal/ruído) através da seleção de eventos. Estes dois fatores definem *limites observacionais* do espectrômetro, definidos como a fração mínima da seção de choque total que pode ser observada em uma experiência com um mínimo de contagens (N_{min}), ou com um mínimo da fração pico/fundo (f_{min}) (limites estatístico e de fundo, respectivamente).

O *poder de resolução* (R) do espectrômetro pode ser definido como o aumento da razão pico/fundo associado à condição de coincidência (janela) com uma transição γ, e é estimado por:

$$R = \left(\frac{SE_\gamma}{\Delta E_\gamma} PT \right)$$

Onde PT é a fração pico/total dos detectores de GeHp com supressão Compton; ΔE_γ é a resolução em energia experimental, incluindo efeitos de alargamento Doppler da radiação; e SE_γ é a separação média entre picos sucessivos das cascatas de raios γ.

Figura 3.1: O sistema Saci-Perere do LAFN (IFUSP, DFN).

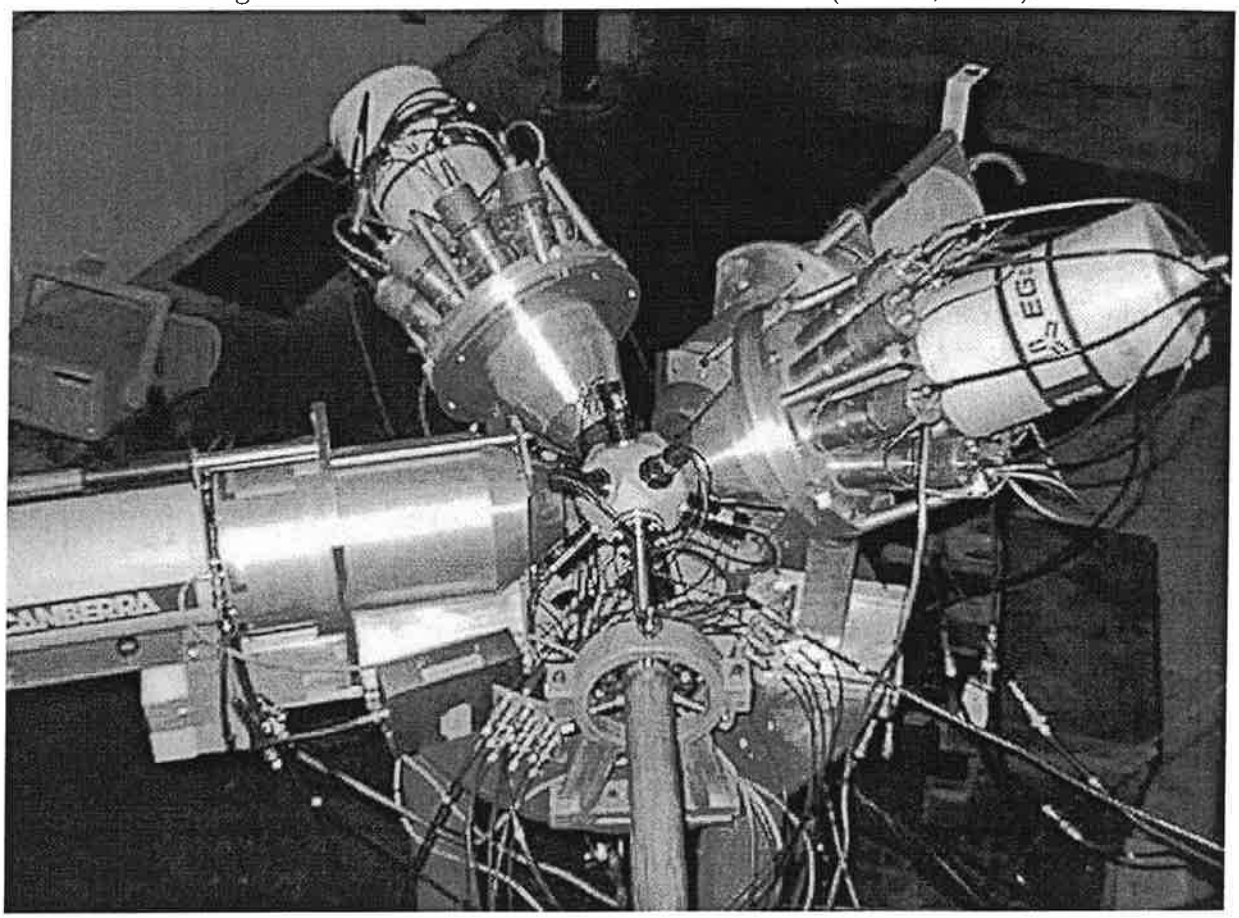

O *limite observacional estatístico* (α_e) e o *limite observacional de fundo* (α_f) são dados por:

$$\alpha_e = \frac{N_{min}}{N\varepsilon_0(k\varepsilon_t)^F}$$

$$\alpha_f = \frac{f_{min}}{R_0(kR)^F}$$

Onde: ε_t é a eficiência total de fotopico; ε_0 e R_0 são a eficiência e o poder de resolução do sistema ancilar, respectivamente; N é o número total de eventos (reações nucleares) produzidos na experiência; F é o nível de coincidência (*fold*: número de raios γ detectados) usada na análise e k é a fração do pico incluída em cada janela (*gate*). Em geral toma-se $k = 0.75$, $N_{min} = 100$ e $f_{min} = 0.2$, e N correspondente a uma experiência de cerca de 5 dias de aquisição de dados (tipicamente da ordem de 10^{10} eventos).

O ponto ótimo de um espectrômetro está associado ao ponto de cruzamento dos dois limites observacionais em função de F. A figura 3.2 mostra o cálculo dos limites observacionais dos espectrômetros utilizados para efeitos de comparação. Para o espectrômetro Perere foram realizadas correções para número reduzido de detectores. Na verdade os limites observacionais variam substancialmente com a experiência específica, e a figura deve ser tomada apenas como uma estimativa típica de caráter ilustrativo.

3.2 Técnicas experimentais

3.2.1 Reações de Fusão-Evaporação

Reações de fusão-evaporação com íons pesados são o método mais utilizado para a população de estados de alto spin [29]. Neste tipo de reação alvo e feixe fundem-se completamente formando um *núcleo composto* com alta energia de excitação (da ordem de dezenas de MeV) e momento angular (30-60$\hbar$), que decai subsequentemente por evaporação de partículas ou fissão. A secção de choque de fusão ($\sigma(l)$) em função do momento angular l tem a forma aproximada de uma ditribuição triangular até l_{max}, correspondente à soma dos raios nucleares multiplicada pelo momento linear.

O decaimento do núcleo composto é descrito pelo modelo estatístico introduzido por Weisskopf [30], segundo o qual cada estado decai, independentemente de sua formação, em um dos canais de saída abertos, de acordo com a hipótese de Bohr em que a memória sobre os detalhes do canal de entrada é perdida.

O processo de fissão é relativamente raro exceto para regiões de massa elevada e alto momento angular. A observação de transições discretas após a fissão é dificultada devido à grande variedade de canais abertos e à alta velocidade dos produtos formados.

Nos processos de evaporação, prótons e nêutrons tendem a carregar pouco momento angular devido à barreira centrífuga. Nêutrons evaporados reduzem a energia de excitação

Figura 3.2: Limites observacionais de espectrômetros gama. O ponto ótimo dos espectrômetros se encontra no cruzamento das linhas de α_e (crescentes) e α_f (decrescentes) em função de F. Nos espectrômetros HERA e GASP já foi levado em conta o efeito dos respectivos filtros de multiplicidades. O efeito dos detectores ancilares Saci e ISIS corresponde à detecção de 1 próton em coincidência.

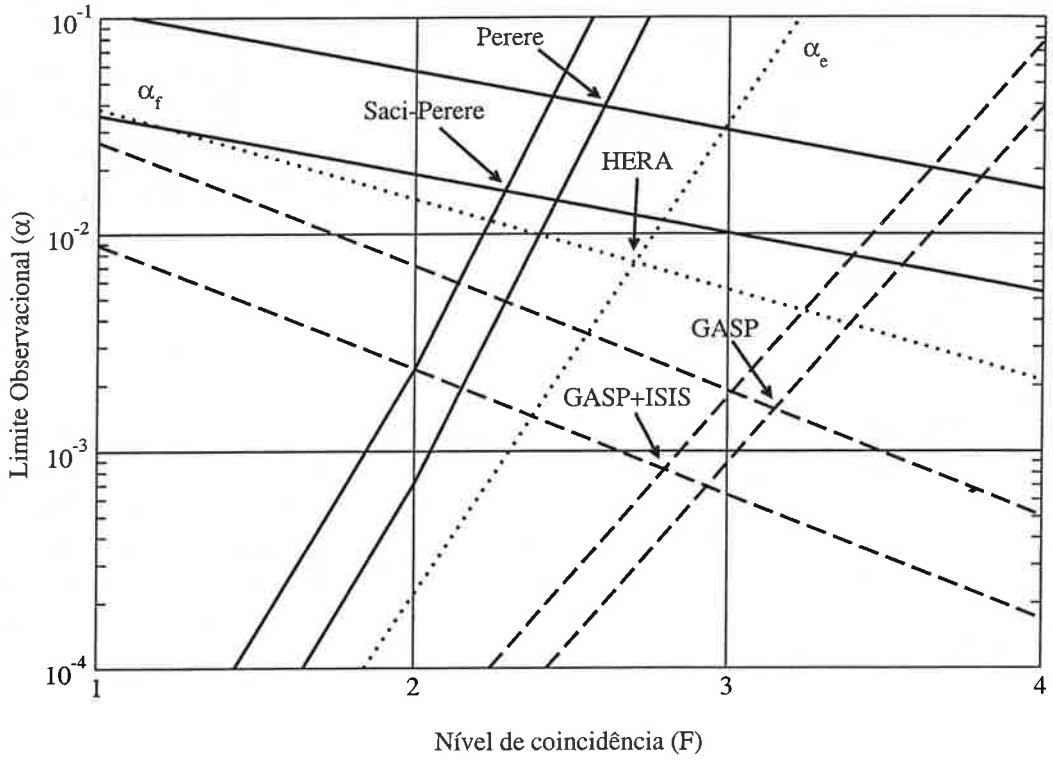

em passos de 4-10 MeV, e prótons um pouco mais devido à barreira coulombiana. Partículas α por outro lado carregam também significativa quantidade de momento angular, mas são raramente evaporadas para massas acima de $A \approx 110$. Após a emissão de algumas partículas o sistema se encontra próximo à linha *yrast* (a qual corresponde aos estados de menor energia de excitação para um dado valor de momento angular) o que inibe a emissão de partículas adicionais. O sistema passa então a evaporar raios γ, inicialmente do tipo "estatístico" de multipolaridade E1 que carregam pouco momento angular, e "tipo-*yrast*", E2, paralelos à linha *yrast*. Quando a densidade de níveis do sistema se reduz começa a ser possível a individualização de transições γ discretas. Os esquemas de níveis dos núcleos residuais podem então ser construídos com auxílio das técnicas de coincidência.

3.2.2 Coincidências temporais

Em uma experiência típica com secção de choque total de 1 b e corrente de feixe da ordem de 1 pnA (nA de partículas), ocorrem da ordem de 10^5 reações por segundo (ou seja, uma a cada $10\mu s$ em média). Para cada uma delas são evaporadas cerca de 3 a 5 partículas (p, n, e α) e cascatas de 15 a 30 raios γ dentro de um intervalo de tempo típico na faixa de 1ps a 1ns. A grande diferença entre as escalas de tempo envolvidas permite distinguir as partículas correspondentes a um único evento. Detectores de Ge hiperpuro não tem resposta particularmente rápida. Sua resolução é afetada pela alta variação dos tempos de formação de pulsos detectados em diferentes partes do cristal. A resolução temporal típica em situação experimental de um detector de GeHp é de $\approx 20ns$, mas é suficiente para discriminar raios gama *coincidentes* (dentro da escala de tempo de uma cascata γ) dos *aleatórios* basicamente originados por reações nucleares distintas.

As medidas de coincidência requerem uma eletrônica de pulsos sofisticada, com utilização de amplificadores rápidos e discriminadores de tempo de fração constante (CFD). Para detectores de GeHP constuma-se utilizar a técnica de ARC-*timing* (*Amplitude and Rise-time Compensated Timing*) [31], para minimizar os efeitos da variação da forma do pulso deste tipo de detector. Detectores de partículas carregadas por outro lado são em geral muito mais rápidos. Com cintiladores plásticos, por exemplo os telescópios tipo *Phoswich* utilizados no sistema Saci do LAFN -IFUSP, consegue-se uma resolução temporal inferior a 1ns.

3.2.3 Distribuições e correlações angulares

A medida de distribuições ou correlções angulares é importante por permitir a medida das diferenças de momentos angulares entre os estados nucleares.

Logo após a reação de fusão, o momento angular do núcleo composto se encontra orientado no plano perpendicular à direção do feixe, a qual constitui um eixo de quantização conveniente. A distribuição dos subestados magnéticos do momento angular apresenta uma forma *oblata*, isto é, na qual somente valores próximos a $m = 0$ são populados. A

subsequente evaporação de partículas, tipicamente 3-5 nêutrons, tende a alargar muito pouco esta distribuição, uma vez que cada partícula carrega em média 0.5-1 unidades de momento angular. Os raios γ subsequentemente emitidos apresentarão uma distribuição angular correspondente a esta orientação inicial [32]. Em uma cascata de transições *stretched*, isto é, nas quais a variação do spin I dos estados é igual à multipolaridade L da radiação ($\Delta I = L$), a distribuição angular permanece praticamente a mesma para todos os raios γ da cascata.

A maior parte das transições normalmente observadas em um experimento é de tipo M1(+δE2) ou E2, e em alguns casos E1. Transições de multipolaridade mais alta tendem a ser muito mais lentas, e ocorrer fora da *janela de coincidência*. A observação da distribuição angular de uma dada transição permite determinar sua multipolaridade. Para medidas em vários ângulos e suficientemente precisas é possível determinar a razão de mistura E2/M1 (δ). Na prática porém costuma ser conveniente a realização de correlações angulares $\gamma - \gamma$ ou DCO (*directional correlation from oriented states*) [33]. Como estas medidas envolvem a coincidência entre dois detectores, são medidas muito mais seletivas (com melhor razão pico/fundo) do que distribuições angulares simples.

3.2.4 Método da atenuação do efeito Doppler

O método da atenuação do efeito Doppler (DSAM) [34] permite a determinação de vidas médias de estados nucleares de cerca de 1ps ou inferiores. Neste método o núcleo residual recua em um substrato de poder de freamento $\frac{dE}{dx}(v)$ conhecido. Durante o tempo de freamento, da ordem de 1ps, os raios gama são emitidos em vôo e sofrem deslocamento Doppler. Sua energia E_γ dependente da velocidade de recuo instantânea $v(t)$ no instante t em que ocorre a emissão: $E_\gamma(v(t)) \simeq E_0(1 + \frac{v(t)}{c}\cos\theta)$, onde E_0 é a energia do raio γ emitida em repouso, c é a velocidade da luz e θ é o ângulo entre a direção da velocidade e a direção do detector. A forma da linha no espectro γ é portanto alargada, e contém informação sobre o instante de decaimento do estado. A medida das vidas médias envolve a simulação de Montecarlo de diversas trajetórias de recuo e tempos de emissão dos estados, e comparação com o espectro experimental. A simulação, e portanto a própria medida, é dependente de modelos para as transições não resolvidas que alimentam os estados, influindo negativamente sobre a incerteza e até mesmo a confiabilidade da medida.

Devido à alta estatística proporcionada pelos de sistemas de muitos detectores, tornou-se possível a realização de medidas de DSAM em coincidência. É possível desta forma examinar o decaimento de um estado em coincidência com a transição que o popula diretamente, eliminando a possibilidade de alimentação lateral. Além disso, foi desenvolvido um método alternativo, denominado NGTB (*narrow gate on transition below*) [35], que também elimina a influência da alimentação lateral. Neste método observa-se a redução da cauda na forma de uma linha do espectro gama, quando esta é observada em coincidência com uma transição inferior na cascata, sobre a qual colocou-se uma janela *estreita*, selecionando portanto preferencialmente eventos em que houve freamento total antes de

sua emissão. Com estes métodos medidas de DSAM mais precisas e de maior confiabilidade tornaram-se possíveis.

3.2.5 Método da distância de recuo (RDM ou RDDS)

Este método é usado para a medida de estados de vidas médias acima de 1ps até $\approx$ 1ns. Utiliza-se um dispositivo denominado *Plunger* que permite variar a distância entre o alvo e um anteparo (*Stopper*) em vácuo. O anteparo tem a função de frear completamente o núcleo residual. Desta forma, parte do decaimento ocorre em vôo com velocidade v constante, e parte após o tempo máximo $t_{max} = \frac{d}{v}$ onde d é a distância entre as duas superfícies. Desta forma, para cada transição são observados dois picos no espectro gama com energias separadas pelo deslocamento Doppler: $\Delta E_\gamma = E_\gamma(v) - E_0$. A proporção entre as áreas dos dois picos varia em função da distância, trazendo informação sobre a vida média dos estados. Também neste caso os resultados são dependentes de modelos, e beneficiam-se com a utilização de dados de coincidência $\gamma - \gamma$.

Capítulo 4

Regiões de massa

4.1 Região de $A \approx 45$

4.1.1 Vidas médias do ^{46}Ti e a técnica de janela estreita em transição subjacente

Medidas de vidas médias de estados nucleares de núcleos desta região constituem um bom teste para os cálculos de LSSM [23] [22]. Os resultados dos cálculos tem sido muito precisos, incentivando a realização de medidas também cada vez mais precisas e confiáveis. Uma das técnicas desenvolvidas para obtenção de vidas médias com maior confiabilidade é a de NGTB. Neste contexto a precisão com que é conhecida a curva de perda de energia de íons em sólidos passa a ter maior relevância.

O núcleo de ^{46}Ti foi estudado com a finalidade de testar, não somente as previsões do modelo teórico, mas também a própria técnica de NGTB e as parametrizações de perda de energia em diferentes substratos. Para este fim, foi estudada forma de linha de transições da banda *yrast* do ^{46}Ti, populada com alta intensidade na reação de ^{28}Si a 115 MeV e alvo de ^{24}Mg em dois substratos diferentes, Au e Pb. Foi utilizado o espectrômetro GASP dos LNL em associação com o sistema de detecção de partículas carregadas ISIS. O programa de análise (DBLS) foi desenvolvido pelo Prof. R.V. Ribas do IFUSP, a partir do programa *Lineshape* (J.C. Wells e N.R. Johson, de Oak Ridge), de maneira a permitir a análise simultânea de até 7 espectros em ângulos diferentes (adequado portanto ao sistema GASP).

A tabela 4.1 mostra a comparação dos resultados obtidos para as vidas médias dos estados do ^{46}Ti nas duas experiências (uma com substrato de Au, e a outra Pb), ambas com utilização da técnica de NGTB, medidas prévias disponíveis na literatura, e cálculos recentes de LSSM. A tabela mostra que os resultados das duas experiências são compatíveis, mas as vidas médias com substrato de Pb parecem sistematicamente menores (cerca de 10%) do que as obtidas com substrato de Au. Como a perda de energia em alvos de Au é bem conhecida e largamente utilizada na literatura, é provável que o valor da perda de

Tabela 4.1: Comparação entre resultados experimentais e teóricos para as vidas médias (em ps) da banda *yrast* do ^{46}Ti. Os estados são indicados por spin e paridade I^{π} na primeira coluna. E_{γ} é a energia da transição γ que depopula o estado. τ(Mg/Au) e τ(Mg/Pb) são os resultados das meias vidas obtidas com alvo de ^{24}Mg em substrato de Au e Pb respectivamente. Ambas tem incertezas de cerca de 5%. τ(NDS) indica os valores previamente disponíveis na literatura (*Nuclear Data Sheets*), e τ(LSSM) são as previsões de *Large Scale Shell Model*.

$I^{\pi}(\hbar)$	E_{γ}(keV)	τ(Mg/Au)	τ(Mg/Pb)	τ(NDS)	τ(LSSM)
14^{+}	1820	1.08	1.07	0.87(3)	1.20
12^{+}	1975	0.42	0.37	0.74(7)	0.42
10^{+}	1345	1.66	1.55	1.21(6)	1.87
8^{+}	1597	0.51	0.45	0.71(9)	0.57
6^{+}	1289	1.35	1.20	1.43(13)	1.50

energia em Pb seja na verdade cerca de 10% menor do que o calculado pela parametrização tradicional de Northcliffe e Schilling [36], utilizada no programa. Além disso, nota-se que os resultados dos cálculos de LSSM concordam, dentro de desvios de cerca de 10%, com os valores experimentais para substrato de Au, atestando a boa confiabilidade de ambos.

4.2 Regiões de $A \approx 100$ e $A \approx 130$

Estas duas regiões de massa apresentam aspectos semelhantes no que se refere à deformação e sua relação com órbitas de subcamadas intrusas. São regiões de transição com deformação intermediária no que se refere ao parâmetro β (tipicamente na faixa de $0.1 < \beta < 0.25$). Nestas regiões os parâmetros de deformação, particularmente o parâmetro de triaxialidade (γ) são fortemente influenciados pelas partículas de valência em órbitas de alto-j devido à forte anisotropia da função de onda. No caso da região de massa $A \approx 130$, o potencial químico de nêutrons se encontra ao redor da metade da subcamada intrusa $h_{11/2}$, enquanto que o de prótons se encontra na parte inferior da mesma subcamada. Desta forma quasi-nêutrons e quasi-prótons apresentam tendências polarizadoras opostas, os primeiros favorecendo formas oblatas e os segundos prolatas. No caso da região de $A \approx 100$, o potencial químico de nêutrons se encontra próximo à metade da subcamada intrusa $h_{11/2}$enquanto que o de prótons ao redor da metade da subcamada $g_{9/2}$. Os papéis de quasiprótons e quasinêutrons são portanto invertidos em relação à região de massa $A \approx 130$. Os núcleos ímpar-ímpar destas regiões são portanto interessantes devido à competição em spin relativamente baixo das tendências polarizadoras de prótons e nêutrons podendo resultar em formas triaxiais. Recentemente ocorre um renascimento do interesse científico destas regiões devido às previsões de manifestações da quiralidade do sistema intrínseco nuclear.

Capítulo 4

Regiões de massa

4.1 Região de $A \approx 45$

4.1.1 Vidas médias do ^{46}Ti e a técnica de janela estreita em transição subjacente

Medidas de vidas médias de estados nucleares de núcleos desta região constituem um bom teste para os cálculos de LSSM [23] [22]. Os resultados dos cálculos tem sido muito precisos, incentivando a realização de medidas também cada vez mais precisas e confiáveis. Uma das técnicas desenvolvidas para obtenção de vidas médias com maior confiabilidade é a de NGTB. Neste contexto a precisão com que é conhecida a curva de perda de energia de íons em sólidos passa a ter maior relevância.

O núcleo de ^{46}Ti foi estudado com a finalidade de testar, não somente as previsões do modelo teórico, mas também a própria técnica de NGTB e as parametrizações de perda de energia em diferentes substratos. Para este fim, foi estudada forma de linha de transições da banda *yrast* do ^{46}Ti, populada com alta intensidade na reação de ^{28}Si a 115 MeV e alvo de ^{24}Mg em dois substratos diferentes, Au e Pb. Foi utilizado o espectrômetro GASP dos LNL em associação com o sistema de detecção de partículas carregadas ISIS. O programa de análise (DBLS) foi desenvolvido pelo Prof. R.V. Ribas do IFUSP, a partir do programa *Lineshape* (J.C. Wells e N.R. Johson, de Oak Ridge), de maneira a permitir a análise simultânea de até 7 espectros em ângulos diferentes (adequado portanto ao sistema GASP).

A tabela 4.1 mostra a comparação dos resultados obtidos para as vidas médias dos estados do ^{46}Ti nas duas experiências (uma com substrato de Au, e a outra Pb), ambas com utilização da técnica de NGTB, medidas prévias disponíveis na literatura, e cálculos recentes de LSSM. A tabela mostra que os resultados das duas experiências são compatíveis, mas as vidas médias com substrato de Pb parecem sistematicamente menores (cerca de 10%) do que as obtidas com substrato de Au. Como a perda de energia em alvos de Au é bem conhecida e largamente utilizada na literatura, é provável que o valor da perda de

Figura 4.1: Esquema de níveis do ^{105}Rh.

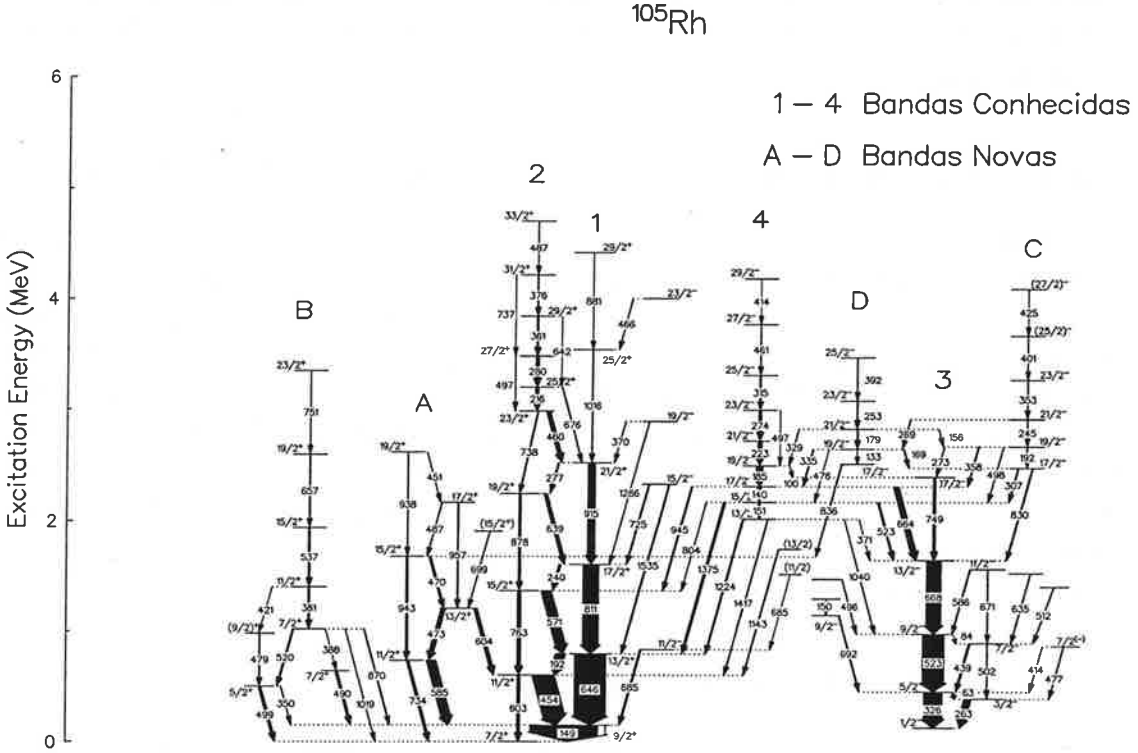

ocorra rotação magnética. Seria prematuro no entanto propor um mecanismo deste tipo sem antes realizar medidas de vidas médias das transições intra-banda. Apesar do alvo utilizado na nossa experiência ter espessura suficiente para frear completamente o recuo do núcleo residual, devido à baixa velocidade inicial do recuo e ao alto poder de freamento do Molibdênio metálico, não foi possível estabelecer um limite suficientemente restritivo para as vidas médias pela técnica de DSAM. Seria necessário a realização de uma nova experiência, preferivelmente com a reação inversa (feixe de ^{100}Mo sobre alvo composto de ^{11}B/Pb para conseguir a sensibilidade necessária para diferenciar um mecanismo de rotação tradicional do de rotação magnética.

Por outro lado, assumindo que a deformação e a triaxialidade permaneçam significativas em spins altos, seria possível a ocorrência de bandas *quirais*. Experimentalmente este fenômeno se manifestaria através da observação de um par de bandas dipolares magnéticas degeneradas. Este não é o caso, porém, das bandas observadas no ^{105}Rh ou nos isótopos de Ag estudados neste experimento.

4.2.2 Núcleos ímpar - ímpar $^{130-136}$La, $^{136-138}$Pr e ^{140}Tb

Os isótopos ímpar - ímpar de $^{130-136}$La, $^{136-138}$Pr foram investigados no Lab. Pelletron a partir do final dos anos 80 [43] [44] [45] [40]. Os primeiros isótopos estudados, $^{130-134}$La e ^{136}Pr, foram interpretados no contexto do CSM. Os valores de *signature splitting* indicavam forma prolata levemente triaxial para estes núcleos. Os resultados já indicavam dificuldades no procedimento usado na época para o cálculo da deformação de equilíbrio pelo método proposto por Frauendorf e May [42]. O advento dos cálculos de TRS [6] porém permitiu abandonar aquele tipo de abordagem. No ^{138}Pr, os resultados experimentais [45] já sugeriam a forma oblata para a banda de configuração $\pi[431]1/2^+ \otimes \nu h_{11/2}$. Cálculos posteriores de PSM (Projected Shell Model) indicam a forma oblata para todas as configurações neste núcleo [46].

As bandas de configuração $\pi h_{11/2} \otimes \nu h_{11/2}$:

As bandas formadas pelo acoplamento de quasipróton e quasinêutron, ambos da subcamada $h_{11/2}$ são *yrast* nos isótopos ímpar-ímpar dessa região. Os momentos angulares j das duas quasipartículas de valência se acopla de forma "perpendicular" nesta configuração, gerando cabeças de banda com $I = 7-8\hbar$. Esta configuração parece ter uma influência estabilizante sobre os núcleos γ-*soft*, e a sistemática mostra grande semelhança desta banda em diferentes núcleos. O núcleo de ^{140}Tb foi estudado recentemente em um experimento [47] com o espectrômetro GASP dos LNL, permitindo estender a sistemática desta configuração para região de alta deficiência em nêutrons, nos isótonos de $N = 75$.

O valor de *signature splitting* nestas bandas é em geral tomado como indicador do grau de triaxialidade da deformação nuclear, devido à relação dessa grandeza com a diferença de energia intrínseca dos routhianos de quasipartícula independente. Porém, quando o

valor de *signature splitting* não é muito elevado, outros fatores (além da triaxialidade) podem ter influência importante. De fato, o fenômeno denominado inversão de *signature*, isto é, quando as energias relativas dos estados de *signature* oposta estão invertidos em relação às expectativas teóricas (a interação de Coriolis sobre uma partícula de j puro favorece a *signature* $\alpha_{fav} = jmod(2)$), ocorre em algumas regiões de massa. Alguns autores sustentam que o fenômeno está associado com a interação residual próton-nêutron. Um estudo sistemático realizado por Yunzuo Liu e co-autores [48] aponta para inversão de *signature* em baixo spin para todos os núcleos da região de $A \approx 130$, à semelhança do que ocorre na região de $A \approx 160$. No entanto, para chegar a esta conclusão as atribuições de spins dos estados foi modificada em muitos casos em relação às dos trabalhos originais, com base em argumentos de sistemática. De acordo com aquele trabalho, os pontos de inversão de *signature* (o valor do spin I onde se cruzam as energias de excitação das duas *signatures*) se dá em torno de $I = 17\hbar$ ou acima. No ^{136}La porém, a inversão ocorre excepcionalmente em spin muito baixo: $I \approx 10.5\hbar$ [40]. Note-se que o ponto de inversão é independente da atribuição de spins em sentido absoluto.

Bandas quirais

Este fenômeno, em que a simetria direita-esquerda é quebrada no sistema intrínseco nuclear, é mencionado aqui devido ao seu grande interêsse atual.

Os núcleos ímpar-ímpar de a região de massa $A \approx 130$ são propícios para a ocorrência de bandas quirais. Quasiprótons e quasinêutron da subcamada $h_{11/2}$ tem carcterísticas predominantemente de partícula e de buraco, respectivamente, tendendo a acoplar-se perpendicularmente, conforme mencionado acima. A distribuição de matéria das quasi-partículas de valência assim dispostas tende a induzir a triaxialidade nuclear. A rotação coletiva tende a reforçar a tendência para a triaxialidade, estabelecendo-se favoravelmente em torno do eixo y' (de maior momento de inércia irrotacional) do elipsóide triaxial, e formando o terceiro eixo, definidor da quiralidade intrínseca do sistema, juntamente com os eixos de momento angular das quasipartículas.

A recente observação de bandas M1 quase degeneradas em diversos núcleos da região é uma notável corroboração destas previsões [49]. Os pares de bandas quase degeneradas tem diferenças energéticas que sugerem a existência de vibrações quirais.

4.2.3 Vidas médias de ^{133}Ce, ^{135}Pr, ^{135}Nd através de RDM

As vidas médias dos núcleos de ^{133}Ce [50], ^{135}Pr [51] e ^{135}Nd [52] foram medidas pela técnica da distância de recuo (RDM), cada um em um laboratório diferente: Lab. Pelletron (IFUSP), Lab. Tandar (Argentina), e Lawrence Berkeley Laboratory (EUA), respectivamente. São trabalhos independentes mencionados nesta única subseção apenas por terem em comum a técnica de medida.

No trabalho sobre o ^{133}Ce, foi utilizado um *Plunger* projetado e construído no Brasil. Foram medidos estados de bandas de 1 e 3 quasipartículas e os resultados comparados com

cálculos de rotor triaxial mais quasipartícula, modelo geométrico de Donau e Frauendorf e IBFM.

No trabalho sobre ^{135}Pr foram medidos estados da banda *yrast* $\pi h_{11/2}$, e os resultados foram comparados com cálculos de TRS e com medidas da literatura referentes ao caroço (núcleo de ^{134}Ce). Os cálculos de TRS preveem pontos de mínimo de energia em deformações com parâmetros β semelhantes, mas com γ muito diferentes, devido à ação polarizadora da partícula ímpar ($\pi h_{11/2}$), resultando em momentos de quadrupolo de transição (Q_t) distintos. O valor de Q_t experimental porém é muito semelhante para os dois núcleos. As curvas de nível de routhiano total por outro lado também são semelhantes para os dois núcleos, e mostram que a variação em função de γ é muito pequena, podendo ser influenciada por fatores normalmente desconsiderados nesse tipo de cálculo, particularmente no caso do núcleo par-par (devido à ausência da partícula polarizadora). Assim sendo, é possível que as deformações nucleares sejam efetivamente semelhantes para os dois núcleos, e próximas ao resultado do cálculo de TRS para o núcleo de ^{135}Pr.

O trabalho sobre o ^{135}Nd foi realizado com o *Plunger* de Bonn, montado no interior do espectrômetro HERA do LBL. O movimento do *Plunger* era comandado por meio de 3 *inch worms* simétricos independentes. Foram medidas vidas médias de estados de spin mais baixo da banda altamente deformada e que decaem para estados de deformação normal.

4.2.4 Vidas médias do ^{134}Pr

As vidas médias de duas bandas duplamente desacopladas no núcleo de ^{134}Pr [53] foram medidas com o espectrômetro GASP dos LNL (Itália). Uma das bandas, de configuração $\pi(h_{11/2})^3 \otimes \nu(f_{7/2}, h_{9/2})$ foi medida pela técnica DBLS, e a outra, de configuração $\pi(h_{11/2})^3 \otimes \nu i_{13/2}$, pela técnica de *Fractional Doppler Shift*, resultando em momentos de quadrupolo de transição de $Q_t \simeq 4$ e $Q_t \simeq 6$ eb (altamente deformada), respectivamente. O trabalho confirma a importância do efeito polarizador da quasipartícula $\nu i_{13/2}$ sobre a deformação nuclear β.

4.3 Região de nêutron-deficientes de $A \approx 145$

Esta é uma região γ-*soft* próxima à linha de instabilidade por emissão de prótons. A expansão das fronteiras do "mundo conhecido" frequentemente nos obriga a reajustes ou revisões de modelos, quando não a revoluções. Diversos núcleos desta região puderam ser estudados com o sistema GASP+ISIS+RMS (LNL), a partir da reação de ^{54}Fe +^{92}Mo a 240 MeV. O objetivo inicial consistia na observação de estados de alto spin do emissor de prótons β-atrasado ^{141}Dy, para o qual se esperava uma inversão de posição dos estados cabeça de banda de configuração de quasi-nêutron $h_{11/2}$ (normal) e $i_{13/2}$ (altamente deformado) de acordo com cálculos de superfície de energia total [54] e sistemáticas [55]. Apesar de não ter sido possível identificar estados deste núcleo na experiência, resultados surpreendentes foram obtidos para os núcleos de ^{143}Dy e ^{143}Tb.

4.3.1 Ambiguidade em configuração do ^{143}Dy

Estados excitados deste núcleo foram relatados pela primeira vez na ref. [56]. O uso dos sistemas ancilares (ISIS + RMS) foi essencial na identificação das transições γ deste núcleo. O uso de coincidências γ triplas possibilitou a apuração do intrincado esquema de níveis. O resultado mais interessante foi a observação de uma banda de paridade positiva de alto momento de inércia dinâmico, semelhante às bandas altamente deformadas de configuração $\nu i_{13/2}$ dos isótonos de $N = 77$: ^{137}Nd, ^{139}Sm, e ^{141}Gd. Cálculos de TRS porém indicam uma interpretação alternativa para a configuração da banda do ^{143}Dy, baseada em orbitas de nêutron de $N_{osc} = 4$ acopladas a um par quebrado de prótons $h_{11/2}$. O comportamento previsto pelo modelo de TRS para o alinhamento de quasipartículas em função da velocidade angular de rotação é qualitativamente consistente com os resultados experimentais para as bandas de paridade positiva deste conjunto de isótopos. Uma diferenciação experimental clara entre as duas configurações seria em princípio possível pela medida do fator giromagnético nuclear, o qual acusaria a presença ou ausência do par quebrado de prótons. No entanto as dificuldades experimentais envolvidas neste tipo de medida são enormes, talvez podendo ser resolvidas com os espectrômetros da próxima geração.

Esta discussão ilustra o papel do número atômico Z na estabilização da deformação nuclear concomitantemente à configuração do nêutron de valência.

4.3.2 Enigma no ^{143}Tb

O núcleo de ^{143}Tb, canal de evaporação de 3p, o mais intenso da mesma reação, teve seu esquema consideravelmente aprimorado com aquela experiência [57]. Trata-se de um bom exemplo de um núcleo transicional em que estruturas de diferentes deformações co-existem (triaxiais e oblatas) em função das forças polarizadoras dos núcleons de valência.

A banda *yrast* $\pi h_{11/2}$ apresenta *signature splitting* indicativo de alto grau de triaxialidade, conforme esperado a partir de cálculos de TRS ($\gamma = -27°$). A sistemática de isótonos de $Z = 59$ a 65 mostra *signature splitting* constante para a banda desta configuração, independentemente do número atômico. Isto aponta para um interessante efeito de compensação de tendências: à medida que o potencial químico de quasi-prótons sobe relativamente à subcamada $h_{11/2}$, níveis de alinhamento menor tendem a ser populados, o que, para deformação γ constante deveria resultar em menor *signature splitting*. Por outro lado, estes níveis mais altos tendem a favorecer a triaxialidade onde há maior *signature splitting*.

Tanto esta banda como de modo geral as demais estruturas observadas neste núcleo podem ser interpretadas e compreendidas dentro de modelos de *Cranking*, e encontram correspondência na sistemática da região. Uma excessão enigmática encontra-se na banda na banda *yrare* em spin baixo de paridade negativa e *signature* $\alpha = +1/2$ e sua "parceira" de *signature* oposta em spin elevado (bandas 1b e 1a na ref. [57]). Não há bandas que se assemelhem a estas na sistemática de núcleos vizinhos. As interpretações aventadas, tais como excitação do segundo estado de quasipróton $h_{11/2}$ (D), ou acoplamento da partícula

desemparelhada à vibração gama, apresentam sérias dificuldades. Bandas *yrare* foram observadas no ^{121}Xe [58], mas diferem em relação ao ^{143}Tb pela presença, neste último, do prematuro cruzamento. Não há portanto, até o momento, um modelo estrutural que formeça uma explicação abrangente. Além disso, é digno de nota que, na região de spin elevado ($I \geq 47/2$), as bandas 1a e 2a (de mesma paridade e *signature*) se apresentam praticamente degeneradas. Isto pode indicar a manifestação de alguma simetria mais profunda, como no caso das bandas dipolares *quirais* degeneradas. No caso do ^{143}Tb, no entanto tratam-se de bandas quadrupolares e não dipolares, o que aponta, no mínimo, para uma origem distinta para o mecanismo da quebra de simetria.

4.4 Região de $A \approx 160$

Esta é uma região onde encontram-se os melhores núcleos rotacionais de deformação *normal* axialmente simétrica. Devido à grande estabilidade da deformação nuclear, esta região constitui um bom campo de testes para o detalhamento de modelos nucleares.

4.4.1 Emparelhamento no ^{168}Yb

Desde a previsão de "colapso" do emparelhamento em alto spin por Mottelson e Valatin em 1960 tem-se procurado evidências experimentais que revelassem de forma clara a intensidade do campo de emparelhamento e sua relação com o momento angular de rotação. Infelizmente não se trata de um problema simples, já que o núcleo é em geral um sistema mesoscópico, no sentido de que o número de partículas não é suficientemente grande (ou macroscópico) para que se defina uma *transição de fase* e se possa desprezar a presença de flutuações estatísticas, nem suficientemente pequeno (ou microscópico) para que se possa individualizar todos os seus graus de liberdade. Por esta razão trata-se de um campo controvertido até hoje e diferentes enfoques foram propostos.

Na referência [59] discute-se o problema em uma abordagem simplificada, na qual toma-se o espectro experimental de excitações relativas do sistema intrínseco em comparação com o espectro de excitações de quasipartículas (ou com emparelhamento forte) e o de excitações de partícula-buraco (com emparelhamento desprezível), em função da velocidade angular de rotação. As duas condições extremas são interpoladas de maneira pouco rigorosa, mas a correspondência entre os resultados experimentais e teóricos para vários isótopos de Yb é muito sugestiva.

Inferências baseadas somente no espectro de energia no entanto são pouco conclusivas. Do ponto de vista experimental, a forma mais direta para a medida da intensidade da *deformação* do campo de emparelhamento, análoga à deformação de quadrupolo da distribuição de carga nuclear, é a medida da seção de choque de transferência de pares de partículas (prótons ou nêutrons), análoga à medida da probabilidade de transição reduzida B(E2) para determinação da deformação. No entanto estas medidas são extremamente difíceis de executar com estados de alto spin.

4.4.2 Alto K em $^{166-168}$Yb

Bandas de K alto são raras na região de $A \approx 160$. As órbitas de projeção Ω alta disponíveis para prótons são: $\pi[404]7/2$ e $\pi[523]7/2$ que se acoplam gerando momento angular 7 e paridade negativa [7^-], e para nêutrons: $\nu[505]11/2^-(h_{11/2})$. O espectrômetro HERA de Berkeley posibilitou a observação de bandas fortemente acopladas nos três isótopos de Yb mencionados [10]. Tratam-se de bandas muito fracamente populadas, particularmente nos isótopos pares. Suas intensidades relativas são comparáveis às de bandas superdeformadas. O modelo de TAC verificou-se adequado para a descrição destas bandas, levando à atribuição de configurações pouco usuais com a participação de nêutrons da subcamada $i_{13/2}$ e com ângulos de inclinação (*tilting*) na faixa de 45° a 65°.

4.5 Região de $A \approx 190$

Esta é uma região de massa de núcleos pouco deformados, em geral de forma oblata, no primeiro mínimo. Bandas M1 regulares constituídas pelo mecanismo de *shears* foram observadas, particularmente em isótopos de Hg e Pb. O segundo mínimo, superdeformado ($\beta \approx 0.5$), aperece em energias de excitação e momentos angulares menores do que na região de $A \approx 150$. Como consequência, grande número de bandas superdeformadas foram descobertas em isótopos de Hg, Pb, Tl e Au, Bi e Po.

4.5.1 Superdeformação em ^{193}Hg e ^{191}Au

Na referência [60] sobre o ^{193}Hg foram observadas pela primeira vez evidências do decaimento gama entre duas bandas SD. Os autores sugeriam que o decaimento poderia ser através de transições E1 (relacionadas a correlações octupolares) ou M1 (relacionada a acoplamento forte). No trabalho do LBL [61], verificou-se que o decaimento se dava nos dois sentidos entre duas bandas E2, tratando-se portanto de transições M1. Além disso, transições de baixa energia foram observadas, constituindo provavelmente as transições M1 esperadas entre as bandas SD.

A banda do ^{191}Au foi a banda SD mais fracamente populada que pôde ser observada com o espectrômetro HERA do LBL [62]. Sua intensidade relativa é de cerca de 0.15% do canal, verdadeiramente no limite daquele espectrômetro. Trata-se da única banda observada em isótopo de Au até hoje. É uma banda *idêntica* (transições a um quarto de intervalo) à banda SD *yrast* do ^{192}Hg, em relação à qual apresenta cerca de 1 unidade de alinhamento.

4.5.2 Bandas *Shears* no ^{193}Pb

Antes do surgimento do modelo de TAC, diversas bandas M1 já haviam sido observadas [11] [12] [13] [14] em núcleos fracamente deformados na região de massa $A \approx 190$. Estas bandas eram na ocasião denominadas *oblatas*. O modelo de TAC permitiu compreender

o mecanismo de formação do momento angular, denominado de *shears*, responsável pelo surgimento de tais bandas.

O núcleo de ^{193}Pb foi estudado [15] com os sistemas HERA e GAMMASPHERE (*Early Implementation*), este último constituído de 36 detectores de alta resolução com supressão Compton. Quatro bandas de intensas transições M1 foram observadas, três delas conectando-se aos estados esféricos, permitindo a comparação direta com cálculos. Duas delas (as mais regulares) apresentaram bom acordo com os cálculos de TAC.

Capítulo 5

Conclusões

Somente conclusões de caráter geral são apresentadas aqui uma vez que conclusões específicas são encontradas nos próprios artigos e na discussão introdutória apresentada no capítulo anterior.

A estrutura nuclear de estados de spin elevado foi investigada em diversas regiões de massa. Os resultados são interpretados por meio de diversos modelos nucleares permitindo em grande parte a sua compreensão. O acordo entre resultados teóricos e experimentais no entanto nunca é perfeito estimulando esforços para a elaboração de modelos mais detalhados ou mais abrangentes. As previsões dos modelos por sua vez são estimulantes para o desenvolvimento de equipamentos e técnicas para a realização de novas experiências. O trabalho insere-se em um contexto amplo para a compreensão da estrutura nuclear de forma sistemática. As descobertas neste campo podem muitas vezes ser transpostas para situações análogas em outras áreas da física, contribuindo para a evolução da ciência como um todo.

Referências Bibliográficas

[1] S.G. Nilsson, Mat. Fys. Medd. Dan. Vid. Selsk. **29** (1955) No. 16.

[2] G. Andersson *et al.*, Nucl. Phys. **A268**, 205 (1976).

[3] P. Ring & P. Schuck, *The Nuclear Many-Body Problem*, Springer-Verlag New York Inc., eds. W. Beiglböck, M. Goldhaber, E.H. Lieb, W. Thirring, ISBN 0-387-09820-8, (1980).

[4] R. Bengtsson & S. Frauendorf, Nucl. Phys. **A327**, 139 (1979).

[5] R. Bengtsson, S. Frauendorf, F.R. May, At. Data and Nucl. D. Tables **35**, 15 (1986).

[6] R. Wyss, J. Nyberg, A. Johnson, R. Bengtsson, and W. Nazarewicz, Phys. Lett. B **215**, 211 (1988).

[7] S. Frauendorf, Nucl. Phys. **A557**, 259c (1993).

[8] P.M. Walker *et al.*, Phys. Rev. Lett. **67**, 433 (1991).

[9] A. Brockstedt *et al.*, Nucl. Phys. **A571**, 337 (1994).

[10] * J.R.B. Oliveira *et al.*, Phys. Rev. C **50**, 1360 (1994).

[11] J.R. Hughes *et al.*, Phys. Rev. C **47**, R1337 (1993).

[12] B. Cederwall *et al.*, Phys. Rev. C **47**, R243 (1993).

[13] J.A. Becker *et al.*, Nucl. Inst. Meth. **B79**, 313 (1993).

[14] J.R. Hughes *et al.*, Phys. Rev. C **48**, R2136 (1993).

[15] * G. Baldsiefen *et al.*, Phys. Rev. C **54**, 1106 (1996).

[16] S. Frauendorf, J. Reif, G. Winter, Nucl. Phys. **A601**, 41 (1996).

[17] S. Frauendorf, Z. Phys. **A358**, 163 (1997).

[18] S. Frauendorf, J. Reif, Nucl. Phys. **A621**, 736 (1997).

[19] Amita, Ashok Kumar Jain, Balraj Singh, At. Data and Nucl. D. Tables **74**, 283 (2000).

[20] S. Frauendorf, Nucl. Phys. **A677**, 115 (2000).

[21] S. Frauendorf, Jie Meng, Nucl. Phys. **A617**, 131 (1997).

[22] E. Caurier *et al.*, Phys. Rev. Lett. **75**, 2466 (1995).

[23] E. Caurier, A.P. Zuker, A. Poves, G. Martínez-Pinedo, Phys. Rev. C **50**, 225 (1994).

[24] P.J. Twin *et al.*, Phys. Rev. Lett. **57**, 811 (1986).

[25] D. Bazzacco, *Proceedings of the International Conference on Nuclear Structure at High Angular Momentum*, Ottawa, 1992, Report. No. AECL 10613, Vol. 2, p. 376.

[26] E. Farnea *et al.*, Nucl. Inst. Meth. **A 400**, 87 (1998).

[27] P. Spolaore *et al.*, Nucl. Inst. Meth. **A 238**, 381 (1985).

[28] J.A. Alcántara-Núñez, Dissertação de Mestrado, IFUSP (1999).

[29] R.M. Diamond & F.S. Stephens, Ann. Rev. Nucl. Part. Sci. **30**, 85 (1980).

[30] J. M. Blatt & V. F. Weisskopf, *Theoretical Nuclear Physics*, New York: Willey (1952).

[31] *Modular Pulse-processing Electronics and Semiconductor Radiation Detectors*, EG&G ORTEC, 1997/98.

[32] K.S. Krane, R.M. Steffen & R.M. Wheller, Nucl. Data Table **II**, 351 (1973).

[33] J.E. Draper, Nucl. Inst. Meth. **A 247**, 481 (1986).

[34] T.K. Alexander, J.S. Forster, *Advances in Nuclear Physics*, M. Baranger, E. Vogt (Eds.), Plenum Press, New York, 1978, p. 197.

[35] F. Brandolini, R.V. Ribas, Nucl. Inst. Meth. **A 417**, 150 (1998).

[36] L.C. Northcliffe & R.F. Schilling, Nucl. Data Tables **7**, (1970).

[37] * F. R. Espinoza-Quiñones *et al.*, Phys. Rev. C **55**, 1548 (1997).

[38] * F. R. Espinoza-Quiñones *et al.*, Phys. Rev. C **52**, 104 (1995).

[39] * F. R. Espinoza-Quiñones *et al.*, Phys. Rev. C **55**, 2787 (1997).

[40] * E. W. Cybulska *et al.*, Acta Physica Polonica B **32**, 929 (2001).

[41] Ts. Venkova *et al.* Eur. Phys. J. A **6**, 405 (1999).

[42] S. Frauendorf & F.R. May, Phys. Lett. **125B**, 245 (1983).

[43] * J.R.B. Oliveira *et al.,* Phys. Rev. C **39**, 2250 (1989).

[44] * J.R.B. Oliveira *et al.,* Phys. Rev. C **45**, 2740 (1992).

[45] M.A. Rizzutto *et al.,* Z. Phys. **A 344**, 221 (1992).

[46] M.A. Rizzutto *et al.*, Nucl. Phys. **A569**, 547 (1994).

[47] * M.A. Rizzutto *et al.*, Phys. Rev. C **62**, 027302 (2000).

[48] Yunzuo Liu, Jingbin Lu,Yingjun Ma, Shangui Zhou, Hua Zheng, Phys. Rev. C **54**, 719 (1996).

[49] K. Starosta *et al.,* Phys. Rev. Lett. **86**, 971 (2001).

[50] * L.G.R. Emediato *et al.,* Phys. Rev. C **55**, 2105 (1997).

[51] * S. Botelho *et al.,* Phys. Rev. C **58**, 3276 (1998).

[52] * P.Willsau *et al.,* Phys. Rev. C **48**, R494 (1993).

[53] * M.N. Rao *et al.,* Phys. Rev. C **58**, R1367 (1998).

[54] Jing-ye Zang & N. Xu, Phys. Rev. C **43**, 2449 (1991).

[55] F. G. Kondev *et al.,* Phys. Rev. C **60**, 011303 (1999).

[56] * J.R.B. Oliveira *et al.,* Phys. Rev. C **62**, 064301 (2000).

[57] * F. R. Espinoza-Quiñones *et al.,* Phys. Rev. C **60**, 054304 (1999).

[58] C.-B. Moon *et al.,* Eur. Phys. J. A **4**, 107 (1999).

[59] * J.R.B. Oliveira *et al.,* Phys. Rev. C **47**, R926 (1993).

[60] D.M. Cullen *et al.,* Phys. Rev. Lett. **65**, 1547 (1990).

[61] * P. Fallon *et al.,* Phys. Rev. Lett. **70**, 2690 (1993).

[62] * D.T. Vo *et al.,* Phys. Rev. Lett. **71**, 340 (1993).

[*] ***Constante do Apêndice***

APÊNDICE

Artigos publicados organizados por regiões de massa

Regiões de $A \approx 100$ e $A \approx 130$

- F. R. Espinoza-Quiñones *et al.*, Phys. Rev. C **52**, 104 (1995).
- F. R. Espinoza-Quiñones *et al.*, Phys. Rev. C **55**, 1548 (1997).
- F. R. Espinoza-Quiñones *et al.*, Phys. Rev. C **55**, 2787 (1997).
- E. W. Cybulska *et al.*, Acta Physica Polonica B **32**, 929 (2001).
- J.R.B. Oliveira *et al.*, Phys. Rev. C **39**, 2250 (1989).
- J.R.B. Oliveira *et al.*, Phys. Rev. C **45**, 2740 (1992).
- M.A. Rizzutto *et al.*, Phys. Rev. C **62**, 027302 (2000).
- L.G.R. Emediato *et al.*, Phys. Rev. C **55**, 2105 (1997).
- S. Botelho *et al.*, Phys. Rev. C **58**, 3276 (1998).
- P.Willsau *et al.*, Phys. Rev. C **48**, R494 (1993).
- M.N. Rao *et al.*, Phys. Rev. C **58**, R1367 (1998).

Região de $A \approx 145$

- J.R.B. Oliveira *et al.*, Phys. Rev. C **62**, 064301 (2000).
- F. R. Espinoza-Quiñones *et al.*, Phys. Rev. C **60**, 054304 (1999).

Região de $A \approx 160$

- J.R.B. Oliveira *et al.*, Phys. Rev. C **50**, 1360 (1994).
- J.R.B. Oliveira *et al.*, Phys. Rev. C **47**, R926 (1993).

Região de $A \approx 190$

- G. Baldsiefen *et al.*, Phys. Rev. C **54**, 1106 (1996).
- P. Fallon *et al.*, Phys. Rev. Lett. **70**, 2690 (1993).
- D.T. Vo *et al.*, Phys. Rev. Lett. **71**, 340 (1993).

Band structures in ^{108}Ag

F. R. Espinoza-Quiñones, E. W. Cybulska, L. G. R. Emediato, C. L. Lima,
N. H. Medina,* J. R. B. Oliveira, M. N. Rao, R. V. Ribas, M. A. Rizzutto, W. A. Seale, and C. Tenreiro†
Laboratório Pelletron, Depto. de Física Nuclear, Instituto de Física, Universidade de São Paulo, Caixa Postal 20516, 01452-990, São Paulo, Brazil
(Received 24 February 1995)

The ^{108}Ag nucleus has been studied by in-beam γ spectroscopy with the heavy-ion fusion-evaporation reaction ^{100}Mo(^{11}B,3$n\gamma$) at 39 MeV. Excitation functions, γ-γ-t coincidences, angular distributions, and DCOQ ratios were measured. A level scheme has been constructed and various bands have been identified with characteristics similar to those in other $A \approx 100$ nuclei. Total Routhian surface calculations predict prolate axially symmetric shapes with collective and noncollective character and satisfactorily account for most of the experimental results.

PACS number(s): 21.10.Re, 23.20.Lv, 27.60.+j

I. INTRODUCTION

In recent years, the influence of the high-j intruder orbits on the deformation of γ-soft nuclei has been studied in various mass regions such as $A \approx 100$, 130, 150, and 190. In each of these regions the Fermi levels for the protons and the neutrons are in different parts of an intruder subshell. In odd-odd nuclei, this leads in general to conflicting tendencies of the proton and neutron intruder quasiparticles, one of these being coupled mainly to the rotational axis and the other to the deformation axis. Several interesting phenomena have emerged in this context, such as triaxiality, shape transitions, shape coexistence, oblate bands, etc. The phenomenon of signature inversion, first observed in $A \approx 150$ odd nuclei at high spin, is also seen in odd-odd nuclei at relatively low spins and, despite several attempts, has not been fully understood [1]. In the $A \approx 100$ odd-odd nuclei, the active intruder orbits are near the top of the $\pi g_{9/2}$ and the bottom of the $\nu h_{11/2}$ subshells. The former orbits are oblate driving, while the latter are strongly prolate driving and favor increased elongations.

In this paper we present an investigation of ^{108}Ag by a heavy-ion induced reaction. Various bands were identified which resemble previously observed structures in neighboring odd-odd Ag isotopes. In particular, the $\pi g_{9/2} \otimes \nu h_{11/2}$ band, which has been systematically seen in the ^{102,104,106}Ag [2–4] and the corresponding Rh isotones [5] and also in the present work in ^{108}Ag. In both ^{106}Ag and ^{108}Ag the ($I^\pi = 1^+$) ground state and the ($I^\pi = 6^+$) isomeric states have been assigned $\pi g_{9/2} \otimes \nu d_{5/2}$ configuration. Similar bandlike structures (based on this 6^+ state) were observed in both nuclei. Another band resembles the $\pi(p_{1/2}, f_{5/2})$ bands seen in odd-A Ag isotopes [6,7] and thus has been tentatively assigned the $\pi(p_{1/2}, f_{5/2}) \otimes \nu h_{11/2}$ configuration. Total Routhian surface (TRS) calculations of the Strutinsky type with a cranked Woods-Saxon potential with pairing were performed and indicate a stabilization of the quadrupole deformation around $\beta_2 = 0.16$, $\gamma = 0°$ (prolate collective) for all configurations containing at least one $h_{11/2}$ quasineutron excitation. For the $\pi g_{9/2} \otimes \nu d_{5/2}$ configuration an equilibrium deformation around $\beta_2 = 0.1$, $\gamma = -120°$ (prolate, noncollective) is predicted and can probably be associated with the 6^+ isomer bandhead. In addition a structure was observed with characteristics of high-K bands (probably $K = 8$).

II. EXPERIMENTAL PROCEDURE

High-spin states in ^{108}Ag were populated by the ^{100}Mo(^{11}B,3$n\gamma$) reaction. The beam was provided by the Pelletron Accelerator of the University of São Paulo. The target used was a ~ 20 mg/cm^2 metallic self-supporting foil of enriched ^{100}Mo.

The γ-ray measurements included excitation functions, angular distributions, and γ-γ coincidences and were obtained with HPGe detectors having $\sim 20\%$ efficiencies and energy resolutions of 2.1–2.4 keV at 1332 keV. The excitation functions were obtained by varying the beam energy in steps of 5 MeV from 35 to 50 MeV. The peak cross section of the desired (^{11}B,3n) reaction is near the Coulomb barrier (34 MeV) and substantial contribution from the 4n channel was observed, which is in reasonable agreement with the statistical model calculations (PACE). A beam energy of 39 MeV was chosen for the other measurements. This energy was the best compromise between the enhancement of population of high-spin states and the competition from the 4n channel. The 4n channel (^{107}Ag) has a well-established decay scheme [6,4], permitting the identification of its γ rays. Other very weak channels such as 2$n\alpha$ and 4np were also observed.

*Present address: Istituto Nazionale di Fisica Nucleare, Sezione di Padova, Padova, Italy.
†Present address: Facultad de Ciencias, Depto. de Física, Universidad de Chile, Santiago de Chile, Chile.

The coincidence data were obtained with two BGO Compton suppressed HPGe detectors placed at ±50° and two HPGe detectors at ±140° to the beam direction. At least one of a set of one 4 in. × 4 in. NaI(Tl) and seven 3 in. × 3 in. detectors placed, respectively, above and below the target, was required to trigger for an accepted γ-γ coincidence event. The angular distribution data were taken using a Compton suppressed HPGe detector positioned at four angles varying from 0° to +90° and a second HPGe detector at −90° was used as a monitor. Due to the complexity of the singles spectra, it was possible to obtain reliable angular distributions only for the strong M1 transitions of the yrast band.

The total number of γ-γ coincidence events was about 7×10^7 and the data were gain matched and sorted into two-dimensional arrays. A symmetrized $E_\gamma \times E_\gamma$ matrix was constructed and the analysis of the data was performed using PANORAMIX [8] and VAXPAK [9] codes.

TABLE I. Energies, spin assignments, relative intensities, and DCOQ ratios for the γ-ray transitions in the ^{100}Mo(^{11}B,3n)^{108}Ag reaction at 39 MeV. The γ-ray energies are accurate to ± 0.3 keV. E_i and E_f are the energies of the initial and final states corresponding to each transition.

E_γ [keV]	E_i [keV]	E_f [keV]	$I_i^\pi \rightarrow I_f^\pi$	I_γ	DCOQ ratio
35.3	533.8	498.5	(8$^-$) → (7$^-$)	10.0(20)	
54.8	420.7	366.3		4.0(10)	
58.5	498.5	440.1	(7$^-$) → (6$^-$)	23.6(9)	
75.5	366.3	290.8			
75.5	290.8	215.0			
75.0	810.1	735.3	(8$^+$) → (7$^+$)	9.0(20)	
103.1	523.8	420.7		10.4 (5)	0.96 (10)
117.8	919.4	802.0	(8$^+$) → (7$^+$)	5.6 (4)	0.62 (14)
122.6	498.5	376.2	(7$^-$) → (7$^+$)	1.7 (4)	
148.2	523.9	376.1	(6$^+$) → (7$^+$)	4.1 (5)	0.42 (12)
153.9	687.7	533.8	(9$^-$) → (8$^-$)	81.5 (9)	0.64 (9)
157.6	533.8	376.2	(8$^-$) → (7$^+$)	4.2 (7)	
157.9	523.8	366.3		1.9 (4)	0.69 (14)
183.5	1674.2	1490.2	(10$^+$) → (9$^+$)	1.5 (4)	
215.5	215.0	0.0	3$^+$ → 1$^+$	7.3 (5)	1.00 (18)
233.3	2908.9	2675.5	(13$^+$) → (12$^+$)	13.1 (6)	0.71 (6)
234.0	2536.9	2302.9	(12$^-$) → (11$^-$)	4.8 (6)	
240.4	2908.9	2668.6	(13$^+$) → (12$^+$)	7.3 (5)	0.70 (10)
249.2	2675.5	2426.8	(12$^+$) → (11$^+$)	4.0 (6)	0.59 (17)
255.4	366.3	110.9		10.7 (5)	0.61 (8)
261.8	2536.9	2275.1	(12$^-$) → (11$^-$)	3.0 (5)	
263.4	3172.3	2908.9	(14$^+$) → (13$^+$)	17.7 (6)	0.69 (6)
265.3	376.2	110.9	(7$^+$) → 6$^+$	19.9 (7)	0.63 (11)
278.2	802.0	523.8	(7$^+$) → (6$^+$)	4.9 (5)	0.46 (16)
304.5	2675.5	2371.1	(12$^+$) → (11$^+$)	4.2 (6)	
310.7	2847.6	2536.9	(13$^-$) → (12$^-$)	6.3 (6)	0.57 (15)
322.4	3494.7	3172.3	(15$^+$) → (14$^+$)	14.5 (7)	0.75 (9)
329.2	440.1	110.9	(6$^-$) → 6$^+$	100.0 (9)	0.84 (9)
340.8	3188.4	2847.6	(14$^-$) → (13$^-$)	6.2 (6)	0.83 (18)
344.7	1435.7	1091.0	(11$^-$) → (10$^-$)	48.4 (9)	0.59 (9)
359.1	735.3	376.2	(7$^+$) → (7$^+$)	5.9 (7)	
361.0	2302.9	1942.4	(11$^-$) → (12$^-$)	2.2 (6)	
378.0	3872.7	3494.7	(16$^+$) → (15$^+$)	10.9 (5)	0.86 (20)
387.5	498.5	110.9	(7$^-$) → (6$^+$)	10.5 (7)	0.67 (10)
393.2	2536.9	2143.7	(12$^-$) → (11$^-$)	8.3 (7)	0.62 (14)
395.6	919.4	523.8	(8$^+$) → (6$^+$)	32.3 (9)	0.91 (14)
403.3	1091.0	687.7	(10$^-$) → (9$^-$)	72.7 (9)	0.70 (9)
412.9	523.8	110.9	(6$^+$) → 6$^+$	16.4 (8)	0.90 (12)
417.7	3606.1	3188.4	(15$^-$) → (14$^-$)	5.8 (6)	
425.8	802.0	376.2	(7$^+$) → (7$^+$)	7.2 (7)	0.93 (27)
434.3	810.1	376.2	(8$^+$) → (7$^+$)	13.0 (9)	
440.5	4313.2	3872.7	(17$^+$) → (16$^+$)	5.5 (7)	0.68 (17)
496.5	3172.3	2675.5	(14$^+$) → (12$^+$)	5.6 (9)	
501.6	2444.0	1942.4	(13$^-$) → (12$^-$)	15 (3)	0.62 (9)
502.0	2143.7	1641.7	(11$^-$) → (10$^-$)	6 (1)	0.58 (21)
506.7	1942.4	1435.7	(12$^-$) → (11$^-$)	41.8 (9)	0.53 (8)
532.6	4092.1	3559.5	(16$^-$) → (15$^-$)	6.4 (9)	
537.4	2908.9	2371.1	(13$^+$) → (11$^+$)	5.3 (9)	
550.9	2994.9	2444.0	(14$^-$) → (13$^-$)	10.3 (9)	0.65 (9)
557.0	1091.0	533.8	(10$^-$) → (8$^-$)	5.3 (8)	
570.8	1490.2	919.4	(9$^+$) → (8$^+$)	7.2 (9)	
564.6	3559.5	2994.9	(15$^-$) → (14$^-$)	7.0 (9)	0.59 (14)
573.6	4179.7	3606.1	(16$^-$) → (15$^-$)	4.7 (9)	
585.4	3494.7	2908.9	(15$^+$) → (13$^+$)	3.6 (9)	
595.1	2536.9	1942.4	(12$^-$) → (12$^-$)	6.0 (9)	
623.7	734.6	110.9	(7$^+$) → (6$^+$)	5.7 (9)	
688.2	1490.2	802.0	(9$^+$) → (7$^+$)	6.3 (9)	
692.0	2064.1	1372.3	(10$^+$) → (9$^+$)	5.4 (9)	
697.0	2371.1	1674.2	(11$^+$) → (10$^+$)	3.2 (9)	
699.2	810.1	110.9	(8$^+$) → 6$^+$	5.3 (9)	
700.1	3872.7	3172.3	(16$^+$) → (14$^+$)	4.0 (9)	
722.0	1098.2	376.2	(8$^+$) → (7$^+$)	12.2 (13)	
748.0	1435.6	687.4	(11$^-$) → (9$^-$)	15.4 (11)	0.90 (12)
754.8	1674.2	919.4	(10$^+$) → (8$^+$)	37.7 (12)	1.08 (18)
818.0	4313.2	3494.7	(17$^+$) → (15$^+$)	3.4 (8)	
851.2	1942.3	1090.8	(12$^-$) → (10$^-$)	9.5 (11)	0.82 (17)
880.9	2371.1	1490.2	(11$^+$) → (9$^+$)	5.0 (9)	
895.3	2536.9	1641.7	(12$^-$) → (10$^-$)	5.2 (9)	
934.6	1669.9	735.3	(9$^+$) → (7$^+$)	4.4 (11)	
936.6	2426.8	1490.2	(11$^+$) → (9$^+$)	4.2 (9)	
954.0	1641.5	687.4	(10$^-$) → (9$^-$)	9.5 (9)	0.73 (13)
965.9	2064.1	1098.2	(10$^+$) → (8$^+$)	4.6 (9)	
977.2	1787.3	810.1	(10$^-$) → (8$^-$)	6.7 (9)	
987.0	1098.2	110.9	(8$^+$) → 6$^+$	5.6 (12)	
992.0	4179.7	3188.4	(16$^-$) → (14$^-$)	1.7 (7)	
994.4	2668.6	1674.2	(12$^+$) → (10$^+$)	15.5 (12)	1.00 (19)
996.1	1372.3	376.2	(9$^+$) → (7$^+$)	5.7 (12)	
999.3	2371.6	1372.3	(11$^+$) → (9$^+$)	5.4 (10)	
1001.3	2675.5	1674.2	(12$^+$) → (10$^+$)	18.6 (11)	0.89 (16)
1008.5	2444.1	1435.6	(13$^-$) → (11$^-$)	11.0 (10)	0.93 (14)
1041.0	2710.9	1669.9	(11$^+$) → (9$^+$)	5.3 (12)	
1052.5	2995.0	1942.3	(14$^-$) → (12$^-$)	7.0 (11)	
1052.8	2143.3	1090.8	(11$^-$) → (10$^-$)	2.5 (5)	
1096.8	4092.0	2995.0	(16$^-$) → (14$^-$)	3.0 (9)	
1101.8	2536.6	1435.6	(12$^-$) → (11$^-$)	3.8 (9)	
1108.0	1641.5	533.5	(10$^-$) → (8$^-$)	3.0 (9)	
1115.2	3559.5	2444.1	(15$^-$) → (13$^-$)	4.7 (9)	
1117.3	2904.6	1787.3	(12$^+$) → (10$^+$)	4.3 (8)	
1184.0	2275.1	1091.0	(11$^-$) → (10$^-$)	4.8 (8)	

Background subtracted gate spectra were generated, and efficiency corrected relative intensities of the γ rays were extracted. Typical examples of coincidence spectra are shown in Fig. 1. The energy and efficiency calibration for the spectra were made using ^{152}Eu and ^{133}Ba lines. The intensities of γ rays in Table I were extracted from the γ-γ coincidence data and represent the sum of the efficiency corrected areas of the transitions (placed in the level scheme) in coincidence with each gate of energy E_γ.

The multipolarities for most of the γ rays were obtained applying the DCOQ method (directional correlation from oriented states referred to quadrupole transitions) [10]. An $E_\gamma(\pm 50°) \times E_\gamma(\pm 140°)$ matrix was constructed to extract multipolarity information from the two coincidence intensities $N_{12}(\gamma_1 \rightarrow \pm 50°, \gamma_2 \rightarrow \pm 140°)$ and $N_{21}(\gamma_2 \rightarrow \pm 50°, \gamma_1 \rightarrow \pm 140°)$. The DCOQ$(\gamma_1, \gamma_2)$ ratios (N_{21}/N_{12}) corrected for relative efficiencies of detectors at $\pm 140°$ and $\pm 50°$ are referred to quadrupole transition gate (γ_2) and reflect the multipolarity and mixing ratio of γ_1. The sum of gates on several quadrupole transitions was used in order to determine the DCOQ ratios of weak γ-ray transitions. The theoretical DCOQ ratio depends on the pair of fixed observation angles, multipole character of the transition γ_1, the ΔI involved, and on the orientation of the spin of the initial state of the cascade. For cascades of predominantly stretched transitions there is very little dependence on the particular state depopulated by transition γ_1 [11]. Therefore the DCOQ ratios for transitions with pure multipolarities (L) can be estimated from the values of L and ΔI. Table II shows the ratios calculated specifically for the present measurements. It should be pointed out that $\Delta I = 1$ transitions could give DCOQ ratios less than or greater than 0.85 for $\delta < 0$ or $\delta > 0$, respectively. Also, $\Delta I = 0$ transitions could give a DCOQ ratio between 0.81 and 1.03 for large mixing ratios.

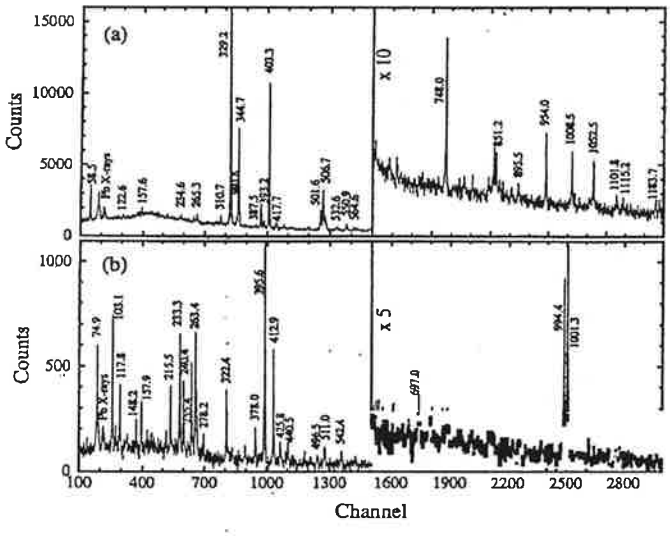

FIG. 1. Background-subtracted γ-γ coincidence spectra of the ^{100}Mo(^{11}B,3n)^{108}Ag reaction at 39 MeV gated by (a) the 153.9 keV line and (b) the 754.8 keV line.

TABLE II. Theoretical DCOQ ratios for mixing ratio δ=0. L is the multipolarity of the γ ray involved and ΔI is the spin change in the transition.

L	ΔI	DCOQ ratio
1	0	1.03
1	1	0.85
2	0	0.81
2	1	0.98
2	2	1.00

III. EXPERIMENTAL RESULTS

A. Level scheme

The level scheme of ^{108}Ag, shown in Fig. 2, was constructed on the basis of the γ-γ coincidence relations and intensity-energy balances. The relative intensities of the γ rays belonging to ^{108}Ag and the measured DCOQ ratios are listed in Table I, together with the level energies and their proposed spins and parities. Six structures with rotational band characteristics can be observed in the level scheme. Negative parity bands with strong $M1$ and weak $E2$ transitions and a small staggering (e.g., band 1) are typical of this mass region. On the other hand, bands 3, 4, and 5, show strong $E2$ with very weak $M1$'s transitions and a large staggering (200–400 keV).

In ^{108}Ag, the spin and parity of the $I^\pi = 1^+$ ground

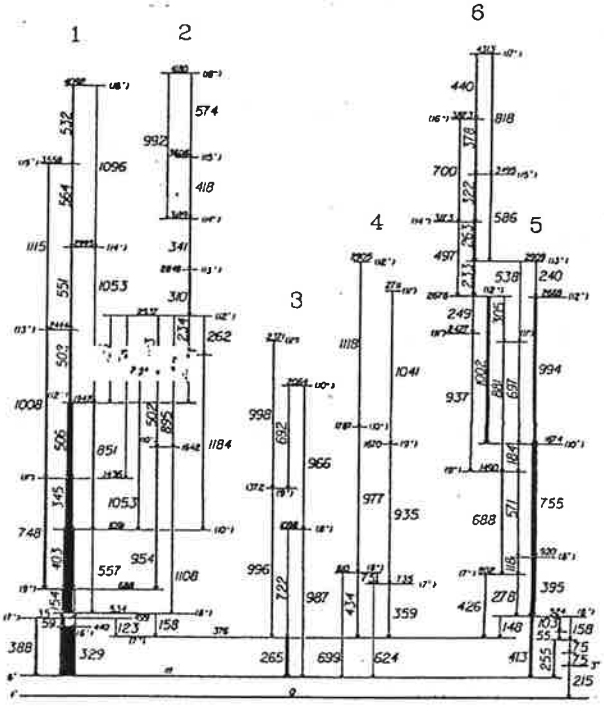

FIG. 2. The level scheme of ^{108}Ag obtained from the ^{100}Mo(^{11}B,3$n\gamma$) reaction at 39 MeV.

TABLE III. The assigned K values and configurations in ^{108}Ag. The signature splittings listed were taken at $\hbar\omega$=0.35 MeV.

Band	K	(π, α)	Configuration	$\Delta e'_{exp}$ (keV)
1	4	(-,0); (-,-1)	$aA; bA$	60
2	4	(-,0); (-, 1)	$aAEF; bAEF$	0
3	0	(+,0); (+, 1)	$aG; aH(aG; bG)$	250
4	0	(+,0); (+, 1)	$aE; aF(aE; bE)$	350
5	0	(+,0); (+, 1)	$gA; hA$	180
6	8	(+,0); (+, 1)	$gacA$	0

state and of the two isomeric states at 110.9 keV ($I^\pi = 6^+$) and at 215 keV ($I^\pi = 3^+$) are well known from atomic beam resonance [12], from the β decay properties to Pd and Cd isotopes [13] and from $(p, n\gamma)$ reactions [14]. The assignments of the other spins in the level scheme were made on the basis of the DCOQ ratios and the systematics for this mass region. The 533.8-keV level of the negative parity band 1 decays through two low energy γ rays of 35 and 59 keV. A similar decay has been also observed in other Ag and Rh isotopes [2,3,5]. Taking into account electron conversion coefficients, the intensity balance shows that the 35- and 59-keV transitions are necessarily of $M1$ nature. The DCOQ ratio indicates a dipole of $\Delta I = 1$ type for the 388-keV transition. Since this transition populates the 6^+ isomer at 110.9 keV we propose $I^\pi = 7^-$ for the 498.5 keV level, and $I^\pi = 6^-$ for the 440.1 keV level. This choice of spins is also consistent with the similar level scheme of ^{106}Ag [2]. The remaining attributions of the spins in band 1 were based on angular distributions, DCOQ ratios, and rotational band characteristics.

In the case of band 2, according to the DCOQ ratios, the transitions of 954, 502, and 393 keV are of type $\Delta I = 0$ or 1. Therefore the maximum spin of the 2536.9 keV level is $I = 12$. The value of $I = 12$ was chosen in order to maintain band 2 nearest to the yrast line. The DCOQ ratio for the 265-keV γ ray which feeds the 6^+ isomer (the bandhead of band 3) indicates a change of no more than one unit of spin. Besides this, the proposed spins for the levels of band 3 were chosen in analogy to a similar structure in ^{106}Ag. The bandhead of band 5 (6^+) at 523.8 keV and the spins of the levels in band 4 were inferred from theoretical arguments (see discussion). The other spins in bands 5 and 6 were attributed relative to this 6^+

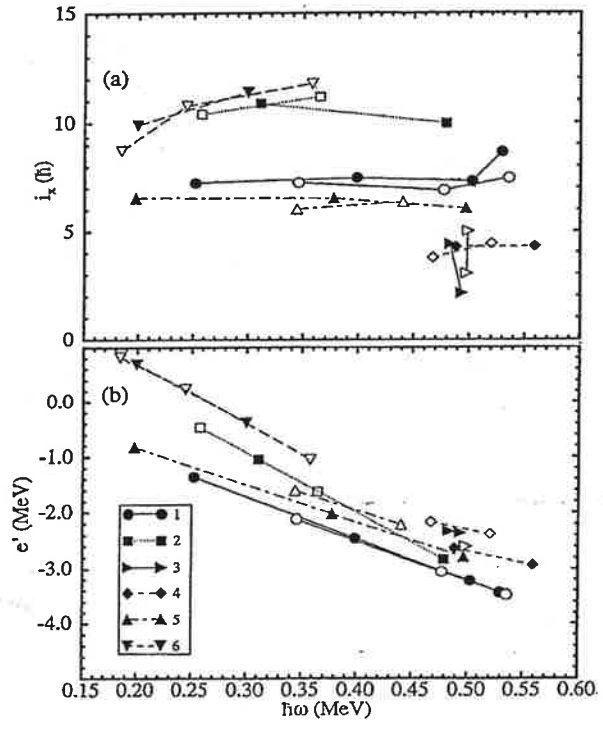

FIG. 3. Experimental quasiparticle (a) alignments and (b) Routhians for the six rotational bands of ^{108}Ag. The solid symbols correspond to α=0 and the open ones to α=1. The following symbols are used for the bands: circles band 1, squares band 2, diamonds band 4, triangles right, up and down bands 3, 5, and 6, respectively.

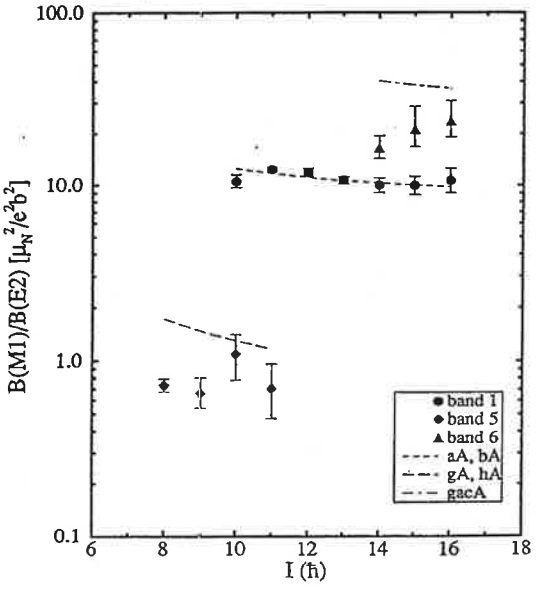

FIG. 4. Experimental and calculated $B(M1)/B(E2)$ ratios for bands 1, 5, and 6 in ^{108}Ag. The calculations were made using the deformation parameters $\beta_2 = 0.16$, $\beta_4 = 0$, $\gamma = 0°$ and $K = 4, 2$, and 8 for bands 1, 5, and 6, respectively. Circles band 1, diamonds band 5, and triangles up band 6.

bandhead and are consistent with the DCOQ results.

The experimental Routhians and alignments (Fig. 3) were calculated following the procedure described in [15,16] with the Harris parameters of $\mathcal{J}_0 = 3.6\ \hbar^2\text{MeV}^{-1}$ and $\mathcal{J}_1 = 29.8\ \hbar^4\text{MeV}^{-3}$, giving a nearly constant alignment for band 1. The K values used, experimental signature splittings, and proposed configurations are given in Table III.

The experimental in-band branching ratios $I_\gamma(\Delta I = 1)/I_\gamma(\Delta I = 2)$ from each level of spin I can provide valuable information regarding the intrinsic configuration of the band. The intensities I_γ were obtained from the spectra gated by the transitions populating the level of interest. Experimental reduced transition probability ratios can be obtained as

$$\frac{B(M1; I \to I-1)}{B(E2; I \to I-2)} = 0.693\ \frac{1}{1+\delta^2}\ \frac{[E_\gamma(I \to I-2)]^5}{[E_\gamma(I \to I-1)]^3}\ \frac{I_\gamma(I \to I-1)}{I_\gamma(I \to I-2)}.$$

The results obtained for bands 1, 5, and 6 ($\delta = 0$) can be seen in Fig. 4, together with theoretical estimates (described in the Discussion). No reliable results were obtained for the other bands due to the poor statistics.

IV. THEORETICAL CALCULATIONS AND RESULTS

A. Quasiparticle Routhians

Figure 5 shows the quasiparticle Routhians calculated from the cranked shell model based on a deformed Woods-Saxon potential including monopole pairing interaction [17]. The diagrams are specific for $Z = 47$ and $N = 61$. The states are classified by the two remaining symmetries, parity and signature (π, α). The signature splitting for each configuration can be read off the diagrams. The aligned angular momentum (i_x) can be obtained from the derivative of the Routhian with respect to the rotational frequency: $i_x = -de'/d\omega$. Table IV shows the correspondence between the letter code used to specify the various quasiparticle states, parity, signature, Nilsson labels, and spherical shell model states most closely related.

It can be seen that the first band crossing occurs around $\hbar\omega = 0.35$ MeV and corresponds to the alignment of the first two $h_{11/2}$ quasineutrons (A and B) with the axis of rotation. The next crossing corresponds to the breaking of the first $g_{9/2}$ quasiproton pair (ab), around $\hbar\omega = 0.48$ MeV. The signature splitting between the a and b quasiprotons is small, which reflects the fact that the quasiprotons are weakly coupled to the rotational axis.

The deformation parameters used ($\beta_2 = 0.16$, $\beta_4 = 0$, $\gamma = 0°$) were chosen in accordance with the TRS calculations (see next section), and are appropriate, in general, to the bands which present at least one $\nu h_{11/2}$ quasineutron excitation.

TABLE IV. The letter code used to denote the quasiparticle states.

j shell	$[Nn_z\Lambda]\Omega$	Parity	$\alpha = -\frac{1}{2}$	$\alpha = +\frac{1}{2}$
$\nu h_{11/2}$	$[550]\frac{1}{2}$	-	A	B
$\nu h_{11/2}$	$[541]\frac{3}{2}$	-	C	D
$\nu g_{7/2}$	$[413]\frac{5}{2}$	+	E	F
$\nu d_{5/2}$	$[402]\frac{5}{2}$	+	G	H
$\pi g_{9/2}$	$[413]\frac{1}{2}$	+	b	a
$\pi g_{9/2}$	$[404]\frac{9}{2}$	+	d	c
$\pi g_{9/2}$	$[422]\frac{5}{2}$	+	f	e
$\pi(p_{1/2}, f_{5/2})$	$[301]\frac{1}{2}$	-	h	g

B. Equilibrium deformations

Standard total Routhian surface calculations were performed for the least excited configurations of ^{108}Ag. The calculations employ a deformed Woods-Saxon potential and a monopole pairing residual interaction [17,18]. The results are summarized in Fig. 6 which show the contour plots for the total energy in the intrinsic frame (mini-

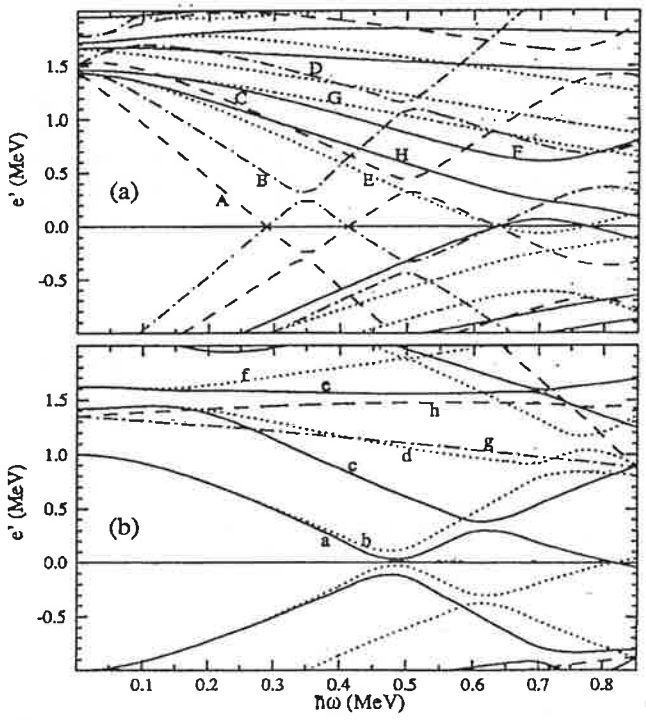

FIG. 5. Quasiparticle Routhians as a function of rotational frequency in ^{108}Ag for (a) neutrons and (b) protons ($\beta_2 = 0.16$, $\beta_4 = 0$, $\gamma = 0°$). The following convention is used for the levels: solid line ($\pi = +, \alpha = +\frac{1}{2}$), dotted line ($\pi = +, \alpha = -\frac{1}{2}$), dashed-dotted line ($\pi = -, \alpha = +\frac{1}{2}$), dashed line ($\pi = -, \alpha = -\frac{1}{2}$).

mized with respect to β_4) as a function of the deformation parameters β_2 and γ. The equilibrium deformation is indicated by the position of a thick dot.

Figures 6(a,b) show the results for the yrast configuration aA at two different rotational frequencies. The equilibrium is stable at a prolate-collective shape ($\gamma \approx 0°$) for a wide frequency range ($\hbar\omega = 0.2 - 0.5$ MeV) where the calculations were performed. The results are essentially the same for the theoretically unfavored signature $\alpha = 1$ (bA).

Figure 6(c) shows the result for the gA configuration (the positive parity configuration with the lowest excitation energy). The energy minimum is close to the one for the aA configuration but is very shallow with respect to γ. It fluctuates slightly around $\gamma = 0°$ as a function of frequency according to our calculations. The same is true for the unfavored signature configuration hA.

Figures 6(d,e,f) show the results for the aG configuration at three different frequencies. Below $\hbar\omega = 0.4$ MeV the energy minimum remains close to $\beta_2 = 0.1$, $\gamma = -120°$, representing a noncollective prolate state with about $6\hbar$ of angular momentum aligned with the symmetry axis. Above $\hbar\omega = 0.4$ MeV the configuration changes adiabatically into the $aABG$ configuration which contains the first aligned pair of $h_{11/2}$ quasineutrons (AB). As a consequence of the strong driving forces of the AB pair, the equilibrium deformation becomes prolate collective ($\beta_2 = 0.16$, $\gamma = 0°$). As a result of the collective rotation and the combined alignment of the four quasiparticles, the total spin for this configuration is at least $16\hbar$. A band based on this configuration is unlikely to be populated by the reaction used in this paper due to the limitation in the input angular momentum. This calculation is representative of other configurations containing one positive parity quasineutron and a $g_{9/2}$ quasiproton, viz., aE, aF, aH. This is rather surprising since the $g_{9/2}$ quasiproton has also a rather strong shape driving force. Oblate- or triaxial-collective deformations were previously expected for these positive parity configurations [7]. On the other hand it is possible to conclude from these calculations that the strong β_2 and γ driving properties of the $\nu h_{11/2}$ intruder orbit apparently tend to stabilize the equilibrium deformation around $\beta_2 = 0.16$, $\gamma = 0°$, rather independently of the other quasiparticles present.

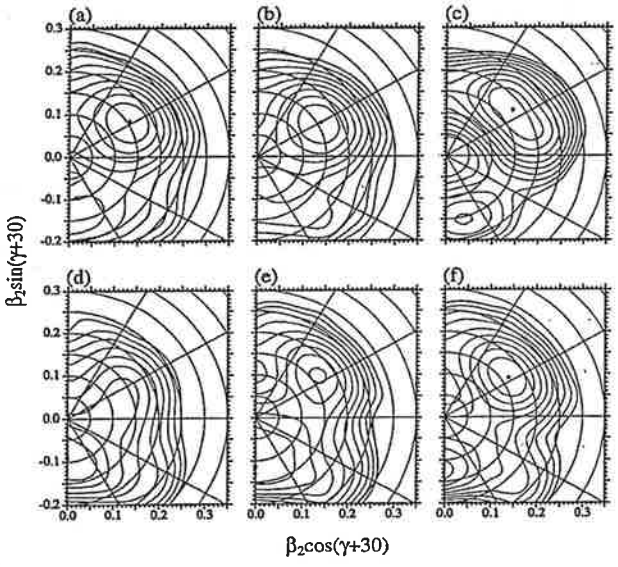

FIG. 6. Total Routhian surfaces for ^{108}Ag. (a) aA configuration, $\hbar\omega$=0.251 MeV (β_2=0.156, β_4=0.001, $\gamma = 2.2°$). (b) aA configuration, $\hbar\omega$=0.377 MeV (β_2=0.158, β_4=0.002, $\gamma = 0.0°$). (c) gA configuration, $\hbar\omega$=0.377 MeV (β_2=0.180, β_4=0.013, $\gamma = 6.5°$). (d) aG configuration, $\hbar\omega$=0.314 MeV (β_2=0.092, β_4=0.006, $\gamma = -120.0°$). (e) aG configuration, $\hbar\omega$=0.377 MeV (β_2=0.114, β_4=0.009, $\gamma = -120.0°$). (f) aG configuration, $\hbar\omega$=0.440 MeV (β_2=0.166, β_4=0.000, $\gamma = 3.2°$). The thick dots indicate the position of the equilibrium deformation.

C. Estimated branching ratios $B(M1)/B(E2)$

The theoretical branching ratios $B(M1)/B(E2)$ between in-band $\Delta I = 1$ and $\Delta I = 2$ transitions from each band state can be estimated from the geometrical model proposed by Dönau and Frauendorf [16]. In this semiclassical model the $M1$ transitions are assumed to originate from the precession of the magnetic moment vector around the total angular momentum vector. The intensity of the radiation is therefore proportional to the component of the magnetic moment vector perpendicular to the spin axis. Effective g factors are used to relate the angular momentum of each quasiparticle configuration to its magnetic moment vector. The estimates are then made from assumptions with respect to the orientation of the angular momentum of each quasiparticle, parametrized by the alignment and the projection onto the symmetry axis (K). The effective g factors are obtained from the Schmidt estimates, with an attenuation factor of 0.7 for the spin g-factors g_s [19].

The calculated branching ratios for the relevant configurations of ^{108}Ag can be compared to the experimental results in Fig. 4 (see also Sec. V). The deformation parameters used were $\beta_2 = 0.16$, $\beta_4 = 0$, $\gamma = 0°$, and the alignments of each quasiparticle were obtained from Fig. 5. For the aA and bA configurations, a $K = 4$ projection was assumed, arising essentially from the $g_{9/2}$ quasiproton (a, b). The $h_{11/2}$ quasineutron A is almost fully aligned ($i_x = 5.2\hbar$). In this situation the perpendicular components of the magnetic moments of the two quasiparticles tend to add, since the neutron g factor is negative and the proton positive, leading to rather high $M1$ transitions. The estimates shown for the gA, hA configurations are actually upper limits, calculated assuming the g factor of a pure $f_{5/2}$ ($g = 0.548$) component for the g, h quasiparticles and $K = 2$. For a fully rotation-aligned $\pi p_{1/2} \otimes \nu h_{11/2}$ configuration no $M1$ transitions are expected. The actual states g, h are of mixed $p_{1/2}, f_{5/2}$ parentage. For the $K = 8$ band ($gacA$), with a pair of $g_{9/2}$ quasiprotons (ac) coupled to the deformation

axis, very large $B(M1)/B(E2)$ ratios are calculated. A value of $K = 7$ would reduce the $B(M1)/B(E2)$ values by roughly 50%.

V. DISCUSSION

A. Bands 1 and 2

Band 1 is the yrast band and presents strong $M1$ transitions and weak $E2$ crossovers. The signature splitting is ≈ 60 keV at $\hbar\omega = 0.35$ MeV, decreasing as the frequency increases. This type of semidecoupled band is characteristic of a "conflicting" coupling between two intruder-orbit quasiparticles in odd-odd nuclei. We assign the $\pi g_{9/2} \otimes \nu h_{11/2}$ (aA and bA) configurations for this band, which corresponds to the lowest two quasiparticle excitations available. Bands with this configuration have been observed in other odd-odd Ag isotopes [2–4]. TRS calculations [see Fig. 6(a)] predict nearly axially symmetric prolate equilibrium deformations and a signature splitting of ≈ 35 keV (around $\hbar\omega = 0.35$ MeV), essentially the splitting between the a and b quasiproton orbits of opposite signatures [see Fig. 5(b)]. However, the theoretically favored signature is $\alpha = 0$ while experimentally it is $\alpha = -1$ (the same is true for the other odd-odd Ag and Rh isotopes cited in Sec. I). The quasiproton Routhians show signature inversion (with very small splitting) for γ between $-10°$ and $20°$. Indeed the TRS minima show a weak tendency toward positive γ values insufficient, though, to produce signature inversion.

For $\gamma \approx 0°$ the angular momenta of the two quasiparticles are nearly perpendicular to each other. This results, according to the geometrical model, in rather large $B(M1)/B(E2)$ ratios as shown in Fig. 4. The alignment expected for this configuration comes mostly from the quasineutron, which contributes with $5.2\hbar$, while the deformation aligned quasiproton contributes with about $2.7\hbar$, in reasonable agreement with the experimental result of $7.3\hbar$ [Fig. 3(a)]. The first neutron and proton crossings, AB and ab, respectively, are blocked for this configuration. The next two crossings expected are the BC (at $\hbar\omega = 0.51$ MeV) and the EF (around $\hbar\omega = 0.7$ MeV). We believe that the BC crossing is responsible for the upbend observed around $\hbar\omega = 0.53$ MeV [Fig. 3(a)]. Band 2 has negligible signature splitting and presents a gain in alignment of about $3.8\hbar$ relative to band 1. This is close to the expected alignment ($i_x = 4.2\hbar$) from the EF quasiparticles. On the other hand, the BC quasiparticles would contribute with an alignment of about $6.9\hbar$, therefore we tentatively assign the $aAEF$ and $bAEF$ configurations for band 2. The calculated splitting between the above configurations is ≈ 20 keV, around $\hbar\omega = 0.35$ MeV. The extrapolated crossing frequency between band 2 and band 1 lies above the upbend in band 1, which is qualitatively consistent with the present assignment. A band with similar characteristics to band 2 has been observed in ^{106}Ag by Popli *et al.* [2] and Jerrestam *et al.* [4]. The latter authors seem to suggest a $\pi g_{9/2} \otimes \nu(h_{11/2})^2(g_{7/2}, d_{5/2})$ configuration for this band. However, our calculations predict too large an alignment ($i_x = 6.8\ \hbar$) relative to band 1 for this configuration.

B. Bands 3 and 4

Both bands 3 and 4 present large signature splitting (250 keV and 350 keV, respectively), strong $E2$ transitions, and weak or absent $M1$ transitions. The 6^+ isomer has been interpreted as $[\pi(g_{9/2})^{-3} \otimes \nu d_{5/2}]_{6^+}$ coupled to the ^{110}Sn core [14]. This would correspond to the aG, $\alpha = 0$ configuration (and aH for the favored signature $\alpha = 1$). We believe that this state is the bandhead of band 3. A similar band has also been observed above the 6^+ isomer of ^{106}Ag. The equilibrium deformation for this configuration is calculated to be around $\beta_2 = 0.1$, $\gamma = -120°$, i.e., slightly prolate, noncollective (Fig. 6) for frequencies below 0.4 MeV which might be interpreted as the $I = 6$ bandhead. Above 0.4 MeV the miminum is shifted to $\beta_2 = 0.16$, $\gamma = 0°$ (prolate, collective) as a result of the alignment of the prolate-driving AB quasineutrons. For the latter deformation a small signature splitting, an alignment of $13\hbar$, and strong $M1$ transitions as in the case of band 1, are expected, in evident contradiction with the experiment. Experimentally, band 3 is observed at $\hbar\omega \approx 0.47$ MeV. TRS calculations show that, as the frequency approaches 0.4 MeV, the total energy minimum becomes shallow, extending toward oblate-collective deformations. Oblate or triaxial deformations could account for an increase in signature splitting between the $g_{9/2}$ quasiprotons and for the absence of strong $M1$ transitions. The AB crossing is also shifted to larger frequencies and therefore no contribution to the alignment is expected from the AB quasiparticles. However, no clear explanation is available for the steady increase in alignment of band 3, which might be an indication of either deformation changes or quasiparticle alignment. More detailed calculations as well as experimental results are necessary to resolve these difficulties.

Similar TRS results are obtained for the aH (the unfavored signature of band 3), bG, bH, aE, aF, bE, and bF configurations, since the natural parity (+) quasineutron orbits present a rather weak dependence on β_2 and γ. We tentatively assign the aE and aF (aE, bE would also be possible) configurations to the favored and unfavored signatures of band 4. The spin of the levels in band 4 were chosen to be consistent with this assignment.

C. Bands 5 and 6

Band 5 shows a rather constant alignment of 6–$6.5\hbar$ in the frequency range from 0.2 to 0.5 MeV and a large signature splitting (200 keV). The absence of the neutron AB crossing (predicted to be at $\hbar\omega \approx 0.35$ MeV) and the large alignment is a clear indication of the presence of a $h_{11/2}$ quasineutron (A) in the configuration of this band. The signature splitting of 200 keV is close

to those calculated for both the $(p_{1/2}, f_{5/2})$ (g,h) and the second $g_{9/2}$ (c,d) quasiproton excitations. The calculated signature splitting of the latter configuration is strongly dependent on frequency, while the experimental one is constant. In addition, at low spins the experimental $B(M1)/B(E2)$ ratios are rather small (around 0.6 $\mu_N{}^2/e^2b^2$). For a fully aligned (doubly decoupled) pure $\pi p_{1/2} \otimes \nu h_{11/2}$ configuration no $M1$ transitions are expected at all $[B(M1)/B(E2) = 0]$. However, admixtures from $p_{1/2}$, $f_{5/2}$, and $p_{3/2}$ are present in the first two negative parity quasiproton excitations (g,h), increasing the effective g factor and the quasiparticle angular momentum projection along the symmetry axis (K). Figure 4 shows the theoretical estimates for the limit of pure $\pi f_{5/2} \otimes \nu h_{11/2}$ $(K = 2)$ configuration (dashed line). On the other hand, the presence of the $g_{9/2}$ quasiproton would lead to $M1$ transitions an order of magnitude stronger. In view of the above arguments we propose gA, hA for the 1 and 0 signatures of band 5, respectively. Also in the odd isotopes (^{105}Ag, ^{107}Ag) [7,6], admixed $\pi p_{1/2}$ bands have been observed with similar characteristics. We estimate $I = 6\hbar$ for the bandhead assuming $I = I_x = i_{x\pi} + i_{x\nu} \approx 0.5 + 5.5 = 6\hbar$ for this rotation aligned band.

Band 6 decays to band 5 around $I = 12\hbar$. The experimental signature splitting is negligible and the experimental $B(M1)/B(E2)$ ratios surprisingly show an increase of more than an order of magnitude relative to band 5, which points toward a major configuration change. The above-mentioned characteristics of band 6 indicate a large K value. A $(\pi g_{9/2})^2$ configuration is known to produce $K^\pi = 8^+$ isomers in neighboring even-even Cd isotopes [20,21], and related high-K bands in odd Cd isotopes [22]. The possibility of the coupling of $[\pi {g_{9/2}}^2]_{K=8}$ to the configuration of band 6 was considered, and provides a possible explanation for the negligible signature splitting and in particular, the large $B(M1)/B(E2)$ ratios observed (this configuration is labeled $gacA$ in Fig. 4). However, it is puzzling that such a presumably large change in K value from band 6 to band 5 does not result in an observable delay in the interband transitions. The experimental setup of this paper is sensitive to lifetimes above 20 ns.

VI. CONCLUSION

A level scheme for the states populated in a heavy ion reaction has been proposed for ^{108}Ag. Six bandlike structures are observed. Tentative configuration assignments were proposed for each band by combining low-lying quasiproton excitations of $g_{9/2}$, $(p_{1/2}, f_{5/2})$ parentage, with quasineutron excitations of $h_{11/2}$, $g_{7/2}$, $d_{5/2}$. Similar structures have been observed by previous experiments in other nearby odd-odd or odd-A Ag isotopes. Most of the band structures observed can be understood within the cranked shell model. A weakly deformed prolate shape is predicted by TRS calculations for the configurations containing at least one $h_{11/2}$ quasineutron excitation. This prediction seems to be consistent with the data presently available. The band developed above the 6^+ isomer appears to have characteristics of triaxial or oblate shapes and cannot be fully understood with the present TRS calculations which predict only prolate axially symmetric shapes at moderate rotational frequencies. More detailed calculations with parameters optimized specifically for the ^{108}Ag region might clarify these matters.

ACKNOWLEDGMENTS

This work was partially supported by the Conselho Nacional de Desenvolvimento Científico e Tecnológico (CNPq), Coordenação de Aperfeiçoamento de Pessoal de Nível Superior (CAPES), and Fundação de Amparo à Pesquisa do Estado de São Paulo (FAPESP).

[1] T. Komatsubara, K. Furuno, T. Hosoda, J. Mukai, T. Hayakawa, T. Morikawa, Y. Iwata, N. Kato, J. Espino, J. Gascon, N. Gjørup, G.B. Hagemann, H.J. Jensen, D. Jerrestam, J. Nyberg, G. Sletten, B. Cederwall, and P.O. Tjøm, Nucl. Phys. **A557**, 419c (1993), and references therein.

[2] R. Popli, F.A. Rickey, L.E. Samuelson, and P.C. Simms, Phys. Rev. C **23**, 1085 (1981).

[3] J. Tréherne, J. Genevey, S. André, R. Béraud, A. Charvet, R. Duffait, A. Emsallem, M. Meyer, C. Bourgeois, P. Kilcher, J. Sauvage, F.A. Beck, and T. Byrski, Phys. Rev. C **27**, 166 (1983).

[4] D. Jerrestam, W. Klamra, J. Gizon, F. Lidén, L. Hildingsson, J. Kownacki, Th. Lindblad, and J. Nyberg, Nucl. Phys. **A577**, 786 (1994).

[5] R. Duffait, A. Charvet, K. Deneffe, R. Beraud, A. Emsallem, M. Meyer, T. Ollivier, J. Tréherne, A. Gizon, F. Beck, and T. Byrski, Nucl. Phys. **A454**, 143 (1986).

[6] R. Popli, J.A. Grau, S.I. Popik, L.E. Samuelson, F.A. Rickey, and P.C. Simms, Phys. Rev. C **20**, 1350 (1979).

[7] H.J. Keller, S. Frauendorf, U. Hagemann, L. Käubler, H. Prade, and F. Stary, Nucl. Phys. **A444**, 261 (1985).

[8] V.R. Vanin and M. Aïche, Nucl. Instrum. Methods Phys. Res. Sect. A **284**, 452 (1989).

[9] W.T. Milner, VAXPAK programs, Oak Ridge National Laboratory (1986).

[10] K.S. Krane, R.M. Steffen, and R.M. Wheeler, Nucl. Data Tables **11**, 351 (1973).

[11] J.E. Draper, Nucl. Instrum. Methods Phys. Res. Sect. A **247**, 481 (1986).

[12] G.K. Rochester and K.F. Smith, Phys. Lett. **8**, 266 (1964).

[13] O.C. Kistener and A.W. Sunyar, Phys. Rev. **143**, 918 (1966).

[14] T. Hattori, M. Adachi, and H. Taketani, J. Phys. Soc. Jpn. **41**, 1830 (1976).

[15] R. Bengtsson and S. Frauendorf, Nucl. Phys. **A237**, 139 (1979).
[16] F. Dönau and S. Frauendorf, in *Proceedings International Conference on High Spin Properties of Nuclei*, Oak Ridge, 1982, edited by N.R. Johnson (Harwood, New York, 1983) Nucl. Sci. Res. Ser., Vol **4**, p. 143.
[17] R. Wyss, J. Nyberg, A. Johnson, R. Bengtsson, and W. Nazarewicz, Phys. Lett. B **215**, 211 (1988).
[18] W. Nazarewicz, J. Dudek, R. Bengtsson, T. Bengtsson, and I. Ragnorsson, Nucl. Phys. **A435**, 397 (1985).
[19] S. Frauendorf, Phys. Lett. **100B**, 219 (1981).
[20] I. Thorslund, C. Fahlander, J. Nyberg, S. Juutinen, R. Julin, M. Piiparinen, R. Wyss, A. Lampinen, T. Lönnroth, D. Müller, S. Törmänen, and A. Virtanen, Nucl. Phys. **A564**, 285 (1993).
[21] S. Juutinen, R. Julin, M. Piiparinen, P. Ahonen, B. Cederwall, C. Fahlander, A. Lampinen, T. Lönnroth, A. Maj, S. Mitarai, D. Müller, J. Nyberg, P. Šimeček, M. Sugawara, I. Thorslund, S. Törmänen, A. Virtanen, and R. Wyss, Nucl. Phys. **A573**, 306 (1994).
[22] S. Juutinen, P. Šimeček, C. Fahlander, R. Julin, J. Kumpulainen, A. Lampinen, T. Lönnroth, A. Maj, S. Mitarai, D. Müller, J. Nyberg, M. Piiparinen, M. Sugawara, I. Thorslund, S. Törmänen, and A. Virtanen, Nucl. Phys. **A577**, 727 (1994).

Rotational structures in ^{107}Ag

F. R. Espinoza-Quiñones, E. W. Cybulska, J. R. B. Oliveira, R. V. Ribas, N. H. Medina, M. N. Rao, M. A. Rizzutto, L. G. R. Emediato, W. A. Seale, and S. Botelho
Laboratório Pelletron, Instituto de Física, Universidade de São Paulo, São Paulo, Brazil
(Received 3 September 1996)

The ^{107}Ag nucleus has been investigated with the ^{100}Mo(^{11}B,$4n\gamma$) reaction at 39 MeV beam energy. Gamma-gamma coincidences and angular correlations were measured. The ground state band has been extended to higher spins and a three-quasiparticle rotational band has been established. The results were interpreted within the cranked shell model and total Routhian surface predictions. [S0556-2813(97)03103-8]

PACS number(s): 21.10.Re, 23.20.Lv, 25.70.Gh, 27.60.+j

The structure of nuclei and their rotational behavior in the $A \approx 100$ mass region have been extensively studied in recent years. The ^{107}Ag nucleus is a good example of the influence of high-j intruder orbital on the deformation of γ-soft nuclei. The active intruder orbitals, in this region, are near the top of the $\pi g_{9/2}$ and the bottom of the $\nu h_{11/2}$ subshells, resulting in driving forces towards oblate shapes for the former and prolate for the latter one. High-spin states in ^{107}Ag have been previously studied by ^{104}Ru(^{6,7}Li,$xn\gamma$) [1], ^{96}Zr(^{14}N,$3n\gamma$) [2], and ^{94}Zr(^{17}O,$p3n\gamma$) [3] reactions and five rotational bands have been identified. The $\pi g_{9/2}$ yrast band based on $9/2^+$ isomeric state, crosses with two three-quasiparticle bands [$\pi g_{9/2} \otimes (\nu h_{11/2})^2$ and $\pi g_{9/2} \otimes \nu g_{7/2} \otimes \nu h_{11/2}$]. Another three-quasiparticle band has been observed around $I^\pi = 29/2^+$ in ^{107}Ag in [3]. The low-spin states belonging to the band based on $1/2^-$ ground state have been previously known through the Coulomb excitation and were also observed in fusion-evaporation reactions [1,2] but no linking transitions to the other structures were reported. In this paper we confirm the existence of this ground state band and extend it to higher spins where a crossing with a new bandlike structure is also observed. Also, new linking transitions are being reported, which connect the new structure to the already established states.

High-spin states in ^{107,108}Ag were populated by the ^{100}Mo(^{11}B,xn) reaction at 39 MeV beam energy, where the two strongest channels (^{107,108}Ag) have approximately equal cross sections. The results obtained in ^{108}Ag have been published elsewhere [4]. The beam was provided by the Pelletron accelerator of the University of São Paulo. The γ-ray measurements for the ^{107}Ag nucleus included excitation functions, γ-γ coincidences, and directional correlation (DCO) ratios. The experimental setup and analysis are described in [4]. The spin assignment of the levels was obtained from DCO ratios derived by gating on known dipole or quadrupole transitions. A partial level scheme of ^{107}Ag is shown in Fig. 1 where the contribution of the present work is in the region delimitated by the dashed-line frame.

The previously known bands (labeled 1, 2, and 4) have been observed and are in agreement with [1–3] but only the first few states in band 3 [3] were seen in the present work. The ground state band, labeled 5, known from literature [1,2] up to spin $I^\pi = 9/2^-$ was extended to higher spins and crosses with a three-quasiparticle band (labeled 6) around $I^\pi = 15/2^-$. It was not possible to extract the DCO ratios for γ rays in band 6 due to the poor statistics. The comparison between the experimental alignments and the ones extracted from the cranked shell model calculations helped to propose the spins of this band. The γ-ray sequence (190, 300, and 485 keV) built on the 2542 keV, $I^\pi = 19/2^-$ state, confirms the placement in the level scheme given by Popli [2], but is in disagreement with that given by Jerrestam [3]. The DCO ratios for the 372 keV transition confirms the indication given by above references of spin $I = 13/2$ for the 1926 keV level.

The experimental Routhians and alignments, shown in Fig. 2, were calculated following the procedure described in [5,6] with Harris parameters of $\mathcal{J}_0 = 8.9\ \hbar^2 \mathrm{MeV}^{-1}$ and $\mathcal{J}_1 = 15.7\ \hbar^4 \mathrm{MeV}^{-3}$ taken from ^{105}Ag [7]. The cranked shell model (CSM) [8] calculations, based on the deformed Woods-Saxon potential, were performed for $Z = 47$ and $N = 60$, using $\beta_2 = 0.16$ and $\gamma = 0°$.

Band 1 is the yrast band and presents strong $E2$ crossovers and weak $M1$ transitions. The aligned angular momentum is $i_x \approx 1.5\hbar$ while the signature splitting is large, $\approx$ 250 keV at $\hbar\omega = 0.3$ MeV. The $\pi g_{9/2}$ configuration was assigned to this band, which corresponds to the lowest quasiproton excitation available. Yrast bands with this configuration have been observed in other odd-Z nuclei in this mass region [7,9]. The lowest three-quasiparticle configurations in ^{107}Ag are expected to be a combination of the $g_{9/2}$ quasiproton with the lowest two quasineutron configurations, i.e., $\pi g_{9/2} \otimes [\nu h_{11/2}]^2$ and $\pi g_{9/2} \otimes \nu h_{11/2} \otimes \nu(g_{7/2}, d_{5/2})$. All configurations containing at least one $h_{11/2}$ quasineutron are expected to have a large alignment, $i_x > 5\hbar$. In the case of the first configuration assigned to band 2 the alignment is $i_x \approx 12\hbar$, while the second one with $i_x \approx 10\hbar$ was attributed to band 4.

Band 5 shows a large signature splitting ($\approx$ 180 keV) and a rather constant alignment of 0–0.5$\hbar$ in the frequency range from 0.2 to 0.35 MeV. The CSM calculations predict a large signature splitting (200 keV) for the normal parity $\pi p_{1/2}$ configuration, with (−,1/2) being the favored branch, in agreement with the experimental observations. Furthermore, the experimental $B(M1)/B(E2)$ ratio is $0.026(3)(\mu_N/e\ \mathrm{b})^2$ for the $5/2^-$ level, which is in agreement with the theoretical

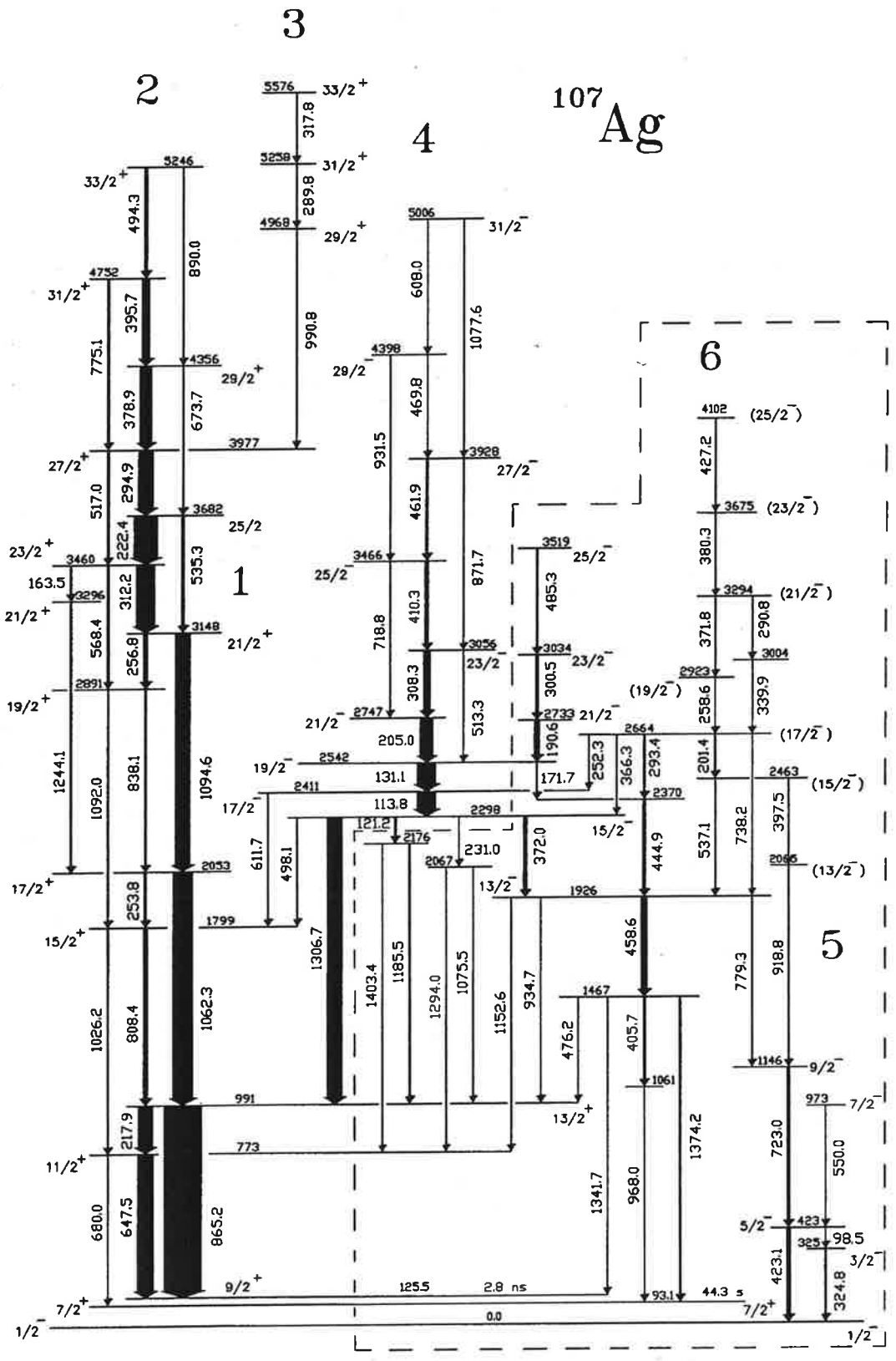

FIG. 1. A partial level scheme of ^{107}Ag obtained from the ^{100}Mo(^{11}B,4$n\gamma$) reaction at 39 MeV. The contribution of the present work is indicated by the dashed-line frame. All the energies are given in keV.

estimate of 0.02 $(\mu_N/e\ \mathrm{b})^2$ for the $\pi p_{1/2}$ configuration, using the semiclassical model of Dönau and Frauendorf [6]. We propose, therefore, a $\pi p_{1/2}$ configuration for band 5. Total Routhian surface calculations for the $\pi p_{1/2}$ configuration show that the equilibrium deformation is at $\beta_2 \approx 0.16$ and $\gamma = 0°$ corresponding to a prolate collective shape.

The experimental signature splitting of band 6 is negligible and no $E2$ crossover transitions were observed. This

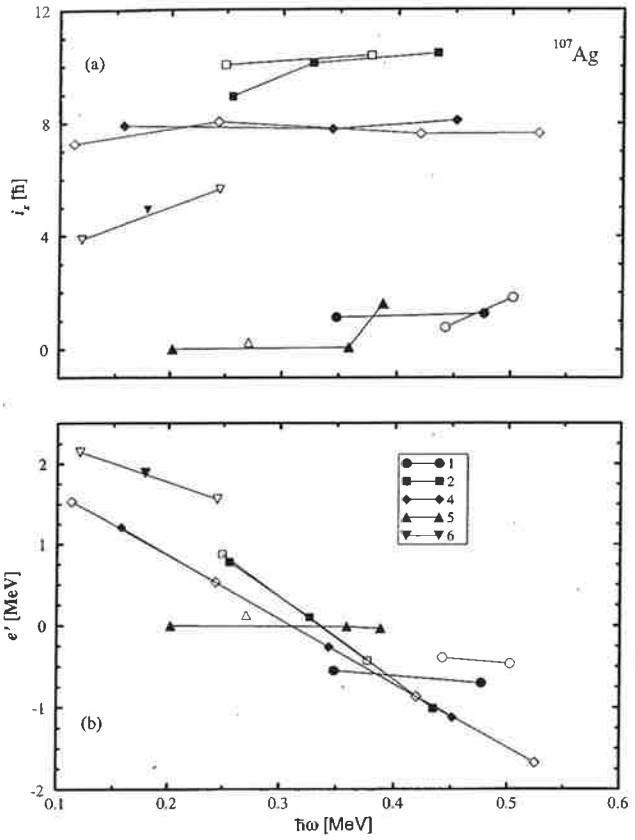

FIG. 2. Experimental quasiparticle (a) alignments and (b) Routhians for the five rotational bands of ^{107}Ag. The solid symbols correspond to $\alpha = 1/2$ and the open ones to $\alpha = -1/2$. The following symbols are used: circles, band 1; squares, band 2; diamonds, band 4; triangles up, band 5; and triangles down, band 6.

band presents a gain in alignment of about $4\hbar$ relative to band 5, which is close to the expected $i_x = 3\hbar$ for $[\pi g_{9/2}]^2$ quasiparticles. The possibility of coupling the $[\pi g_{9/2}]^2_{K=8}$ to the configuration of band 5 was considered, and provides a possible explanation for the very small signature splitting. In addition, the experimental lower limit for the $B(M1)/B(E2)$ ratio for the $21/2^-$ level in band 6 is $5(\mu_N/e\,\mathrm{b})^2$ and is consistent with the theoretical estimates, which predict increasing values from 7 to 13 $(\mu_N/e\,\mathrm{b})^2$ in the spin range of 21/2 to 25/2 for the $\pi p_{1/2} \otimes \pi[g_{9/2}]^2$ configuration. This type of configuration is known to produce $K=8$ in the neighboring even-even and odd-N nuclei [10–12]. A band with similar characteristics to band 6 has been observed also in odd-odd ^{108}Ag [4], for which a $\pi(p_{1/2}, f_{5/2}) \otimes \nu h_{11/2} \otimes \pi[g_{9/2}]^2$ configuration was suggested. The above-mentioned large K value is expected to result in an isomeric bandhead (e.g., ^{109}Cd [12]). However a lifetime of less than about 20 nsec would not be observed with the experimental setup of the present experiment. On the other hand, the theoretical $B(M1)/B(E2)$ ratios for the $\pi p_{1/2} \otimes \nu(h_{11/2})^2$ configuration are very small, of the order of 0.01 $(\mu_N/e\,\mathrm{b})^2$. Furthermore, the alignment of two quasineutrons is not expected to modify the equilibrium shape which is already prolate collective for band 5, and therefore the same signature splitting would continue in band 6. Similar results would be obtained also with any other combination of two low lying quasineutrons. In view of the above arguments, we tentatively assign the $\pi(p_{1/2}, f_{5/2}) \otimes \pi[g_{9/2}]^2$ configuration to band 6.

In conclusion, the present investigation of ^{107}Ag has confirmed and extended the $\pi p_{1/2}$ band to higher spins and also a new three-quasiparticle side band, crossing with the former one was observed. Linking transitions from this new three-quasiparticle band to the yrast and the ground state bands were also established.

This work was partially supported by the Conselho Nacional de Desenvolvimento Científico e Tecnológico (CNPq), Coordenação de Aperfeiçoamento de Pessoal de Nível Superior (CAPES), and Fundação de Amparo à pesquisa do Estado de São Paulo (FAPESP).

[1] H. W. Schuh, D. Hippe, L. Cleemann, J. Eberth, R. Vorwerk, K. U. Zell, and P. V. Brentano, Z. Phys. A **293**, 301 (1979).

[2] R. Popli, J. A. Grau, S. I. Popik, L. E. Samuelson, F. A. Rickey, and P. C. Simms, Phys. Rev. C **20**, 1350 (1979).

[3] D. Jerrestam, W. Klamra, J. Gizon, F. Lidén, L. Hildingsson, J. Kownacki, Th. Lindblad, and J. Nyberg, Nucl. Phys. **A577**, 786 (1994).

[4] F. R. Espinoza-Quiñones, E. W. Cybulska, L. G. R. Emediato, C. L. Lima, N. H. Medina, J. R. B. Oliveira, M. N. Rao, R. V. Ribas, M. A. Rizzutto, W. A. Seale, and C. Tenreiro, Phys. Rev. C **52**, 104 (1995).

[5] R. Bengtsson and S. Frauendorf, Nucl. Phys. **A237**, 139 (1979).

[6] F. Dönau and S. Frauendorf, in *Proceedings of the International Conference on High Spin Properties of Nuclei*, Oak Ridge, Tennessee, 1982, Nuclear Science Research Series Vol. 4, edited by N. R. Johnson (Harwood, New York, 1983), p. 143.

[7] H. Keller, S. Frauendorf, U. Hagemann, L. Käubler, H. Prade, and F. Stary, Nucl. Phys. **A444**, 261 (1985).

[8] R. Wyss, J. Nyberg, A. Johnson, R. Bengtsson, and W. Nazarewicz, Phys. Lett. B **215**, 211 (1988).

[9] H. Dejbakhsh, R. P. Schmitt, and G. Mouchaty, Phys. Rev. C **37**, 621 (1988).

[10] I. Thorslund, C. Fahlander, J. Nyberg, S. Juutinen, R. Julin, M. Piiparinen, R. Wyss, A. Lampinen, T. Lönnroth, D. Müller, S. Törmänen, and A. Virtanen, Nucl. Phys. **A564**, 285 (1993).

[11] S. Juutinen, R. Julin, M. Piiparinen, P. Ahonen, B. Cederwall, C. Fahlander, A. Lampinen, T. Lönnroth, A. Maj, S. Mitarai, D. Müller, J. Nyberg, P. Šimeček, M. Sugawara, I. Thorslund, S. Törmänen, A. Virtanen, and R. Wyss, Nucl. Phys. **A573**, 306 (1994).

[12] S. Juutinen, P. Šimeček, C. Fahlander, R. Julin, J. Kumpulainen, A. Lampinen, T. Lönnroth, A. Maj, S. Mitarai, D. Müller, J. Nyberg, M. Piiparinen, M. Sugawara, I. Thorslund, S. Törmänen, and A. Virtanen, Nucl. Phys. **A577**, 727 (1994).

Rotational bands and shape changes in ^{105}Rh

F. R. Espinoza-Quiñones, E. W. Cybulska, J. R. B. Oliveira, R. V. Ribas, M. N. Rao, M. A. Rizzutto, N. H. Medina, L. G. R. Emediato, W. A. Seale, and S. Botelho
Laboratório Pelletron, Instituto de Física, Universidade de São Paulo, São Paulo, Brazil
(Received 3 February 1997)

The ^{105}Rh nucleus has been studied by in-beam γ spectroscopy with the heavy-ion fusion-evaporation reaction ^{100}Mo(^{11}B, $\alpha 2n\gamma$) at 39 MeV. Gamma-gamma-t coincidences and directional correlation ratios were measured. Four rotational bands have been identified with similar characteristics to those in other $A\approx 100$ odd-proton nuclei. The positive-parity yrast band based on the $\pi g_{9/2}$ configuration and the negative-parity $\pi p_{1/2}$ band, showing large signature splittings, exhibit band crossings at the frequencies of 0.38 MeV and 0.48 MeV, respectively. Experimental Routhians and alignments as well as $B(M1)/B(E2)$ ratios were extracted. The structure of the bands was interpreted within the framework of the cranked shell model and total Routhian surface calculations. [S0556-2813(97)01706-8]

PACS number(s): 21.10.Re, 23.20.Lv, 25.70.Gh, 27.60.+j

I. INTRODUCTION

In the $A\approx 100$ mass region, the proton Fermi level spans the upper half of the $\pi g_{9/2}$ intruder subshell as Z increases from 40 to 50. Over this range, the γ-deformation tendencies of this relatively high-j shell vary smoothly from triaxial collective to prolate noncollective forms [1], while the β_2 deformation decreases from about 0.3 to nearly 0. On the other hand, the neutron Fermi level ($N\approx 60$) lies below or near the bottom of the $\nu h_{11/2}$ high-j shell with a driving force towards $\gamma \geqslant 0°$. The normal-parity quasiparticle states in this region originate from the $\pi(p_{1/2}, p_{3/2}, f_{5/2})$ and $\nu(g_{7/2}, d_{5/2})$ subshells, which do not modify significantly the γ deformations. The equilibrium deformation of the nucleus will depend on the interplay of the driving forces when two or more high-j quasiparticles are involved. The $\pi g_{9/2}$ bands in the odd Rh and Ag isotopes (with proton Fermi level in the middle of the subshell) show large signature splitting. When one or two $h_{11/2}$ quasineutrons are coupled to that configuration, resulting in two-quasiparticle (odd-odd ^{102,104}Rh [2] and ^{106,108}Ag [3,4] nuclei) and three-quasiparticle bands (^{103}Rh [5] and ^{105,107}Ag [3,6,7]), respectively, the signature splitting is either small or disappears and the $B(M1)/B(E2)$ ratios become relatively large. This could indicate a transition from triaxial to prolate collective shape [8]. Another type of band, with no signature splitting and very large $B(M1)/B(E2)$ ratios, has been observed also in this mass region. The interpretation for these bands is usually given by assuming a high-K configuration, which contains two $g_{9/2}$ quasiprotons, e.g., ^{109}Cd [9], ^{103}Rh [5], and ^{107,108}Ag [4,10]. An accurate description of this type of bands [11] falls beyond the scope of the standard total Routhian surface (TRS) predictions and cranked shell model (CSM) and will not be attempted here.

The nuclear structure of the ^{105}Rh nucleus is very interesting to study, because it should present many of the above-mentioned phenomena. However, it is a very difficult nucleus to be produced in a fusion evaporation reaction, because it lies on the neutron-rich side of the stability line and is therefore hindered by a lack of suitable target-projectile combinations. Previous to the present work, the only information on the structure of this nucleus was based on the β-decay measuremnts in ^{105}Ru [12], particle transfer reactions [13], and an unpublished work with the ^{96}Zr(^{12}C, $p2n\gamma$) reaction [14], in which several positive-parity levels with spin up to $17/2\hbar$ were suggested, but no γ-ray transitions were reported. The spin of the ground state is known to be $7/2^+$ with the configuration of $\pi g_{9/2}$, while the configuration of the $1/2^-$ isomeric state is of a $\pi p_{1/2}$ parentage [12]. In this work, we present the results of an investigation of ^{105}Rh with ^{100}Mo(^{11}B,$\alpha 2n\gamma$) reaction as a by-product of ^{108}Ag [4]. Four rotational bands were identified in ^{105}Rh and they resemble closely those seen in ^{103}Rh [5].

II. EXPERIMENTAL PROCEDURE

High-spin states of ^{105}Rh were populated by the ^{100}Mo(^{11}B, $\alpha 2n\gamma$) reaction at 39 MeV beam energy. The beam was provided by the Pelletron accelerator of the University of São Paulo. The target used was ≈ 20 mg/cm^2 metallic self-supporting foil of enriched ^{100}Mo. The γ-ray measurements included excitation functions, γ-γ-t coincidences, and directional correlation (DCO) ratios. The coincidence data were obtained with two Compton-suppressed HPGe detectors placed at $\pm 50°$ and two HPGe detectors at $\pm 140°$, and a multiplicity filter composed of eight NaI(Tl) detectors was placed above and below the target. These data were gain matched and sorted into two-dimensional arrays. A symmetrized $E_\gamma \times E_\gamma$ matrix was constructed containing about 70×10^6 coincident events and the analysis of data was performed using the PANORAMIX code [15]. In order to obtain the multipolarities of the γ transitions using the DCO method, separate $E_\gamma(\pm 50°)\times E_\gamma(\pm 140°)$ matrices were also constructed and the analyses of data were performed using the VAXPAK codes [16]. A $E_\gamma \times t$ matrix was used to search for delayed γ rays in a 20–500 ns time interval. The symmetrized $E_\gamma \times E_\gamma$ matrix was used to establish the level scheme of ^{105}Rh. Background-subtracted gate spectra were generated from this matrix. Examples of spectra constructed from the sum of gates are shown in Fig. 1. The γ-ray tran-

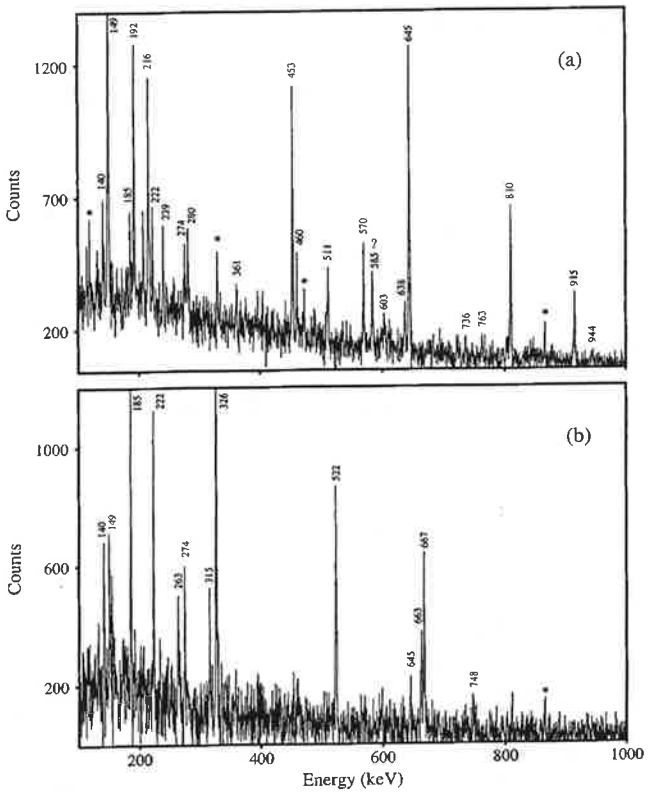

FIG. 1. Sum of background-subtracted γ-γ-coincidence spectra of the ^{100}Mo(^{11}B,$\alpha 2n$)^{105}Rh reaction at 39 MeV showing transitions in positive- and negative-parity bands. The spectra in (a) and (b) were constructed from the sum of gates on the 149.2-, 453.3-, 645.3-, 809.9-, and 914.8-keV γ rays and from 140.4-, 185.2-, 326.1-, 522.4-, 667.6-, and 662.9-keV γ rays, respectively. The (*) indicate known contaminants from the ^{107,108}Ag nuclei; question marks are for unplaced γ rays.

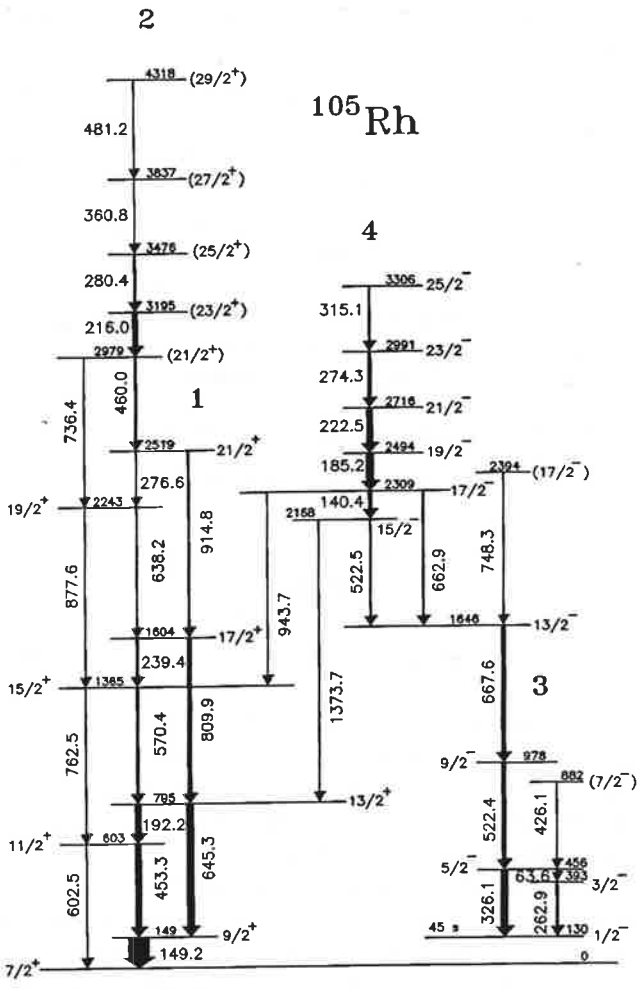

FIG. 2. The level scheme of ^{105}Rh obtained from the ^{100}Mo (^{11}B,$\alpha 2n\gamma$) reaction at 39 MeV.

sitions belonging to ^{105}Rh were identified by setting gates on the known 149.2 and 326.1 keV γ rays [13]. The DCOQ ratios are referred to a quadrupole transition gate and reflect the multipolarity of coincident γ rays. The sum of gates on several quadrupole transitions was used in order to determine the DCOQ ratios of weak γ-ray transitions. The theoretical DCOQ ratios are 1.0 if the transitions involved are of the quadrupole character. For $\Delta I=1$ transitions, the DCOQ ratios are less than 0.85. It should be noted that $\Delta I=0$ transitions could give DCOQ ratios between 0.81 and 1.03 for large mixing ratios.

III. EXPERIMENTAL RESULTS

The level scheme of ^{105}Rh, shown in Fig. 2, was constructed up to $I^{\pi}=(29/2^{+})$ at an excitation energy of 4318 keV on the basis of the γ-γ coincidence relations, considering intensity-energy balances. The energies and the relative intensities for all γ-ray transitions assigned to ^{105}Rh were extracted from coincidence spectra and are listed in Table I. The table also contains the level energies with their proposed spins and parities, as well as the measured DCOQ ratios. The observed levels are grouped into four structures with rotational band characteristics, labeled 1–4 for purposes of discussion. In the present study, the bands based on the $7/2^{+}$ ground state (band 1) and on the $1/2^{-}$ isomeric state at 130 keV level (band 3) were confirmed and extended to $I^{\pi}=21/2^{+}$ and $I^{\pi}=17/2^{-}$, respectively. Furthermore, two new sidebands (2 and 4) were observed and are firmly established by the γ-γ coincidences, as shown in Fig. 1. The yrast, positive-parity band (band 1) shows the $E2$ transitions slightly stronger than the $M1$ below the band crossing, but above it (band 2) only the $M1$ transitions were observed. The negative-parity band (band 3), however, is characterized by strong $E2$ and very weak or unobserved $M1$ transitions. At higher energies and spins, band 3 is strongly fed by band 4 which presents similar characteristics to band 2.

The assignment of spins and parities in bands 1, 3, and 4 was based on the DCO ratios, rotational band characteristics, and the systematics of odd-Z nuclei in this mass region. In the case of band 2, the positive parity was corroborated by the CSM calculations (see Sec. IV), while the $\Delta I=1$ sequence of spins based on the $(21/2^{+})$, 2979 keV level was chosen mainly on the basis of a close similarity with the ^{103}Rh nucleus [5]. However, this choice is not a unique one, since a sequence of spins 23/2, 25/2, 27/2, 29/2, and 31/2 is also possible.

The experimental Routhians (e') and alignments (i) for the four bands in ^{105}Rh as a function of the rotational frequency ($\hbar\omega$) are shown in Fig. 3 and were calculated fol-

TABLE I. Energies, spin assignments, relative intensities (I_γ), and DCOQ ratios (R_{DCOQ}) for the γ-ray transitions in the ^{100}Mo(^{11}B,$\alpha 2n$)^{105}Rh reaction at 39 MeV. The γ-ray energies are accurate to $\pm$ 0.3 keV. E_i and E_f are the energies of the initial and final states corresponding to each transition.

E_γ [keV]	E_i [keV]	E_f [keV]	$I_i^\pi \rightarrow I_f^\pi$	I_γ	R_{DCOQ}
63.6	455.7	392.5	$5/2^- \rightarrow 3/2^-$	2.4(8)	
140.4	2308.6	2168.1	$17/2^- \rightarrow 15/2^-$	19.9(15)	0.7(2)
149.2	149.2	0.0	$9/2^+ \rightarrow 7/2^+$	100.0(12)	0.7(1)
185.2	2493.8	2308.6	$19/2^- \rightarrow 17/2^-$	37.6(13)	0.8(2)
192.2	794.5	602.5	$13/2^+ \rightarrow 11/2^+$	31.7(13)	0.7(2)
216.0	3195.4	2979.4	$(23/2^+) \rightarrow (21/2^+)$	26.1(15)	
222.5	2716.3	2493.8	$21/2^- \rightarrow 19/2^-$	32.5(15)	0.8(1)
239.4	1604.4	1364.9	$17/2^+ \rightarrow 15/2^+$	14.8(12)	
262.9	392.5	129.6	$3/2^- \rightarrow 1/2^-$	13.3(15)	0.6(2)
274.3	2990.6	2716.3	$23/2^- \rightarrow 21/2^-$	19.0(12)	0.7(3)
276.6	2519.4	2242.6	$21/2^+ \rightarrow 19/2^+$	3.1(12)	
280.4	3475.8	3195.4	$25/2^+ \rightarrow 23/2^+$	13.9(12)	
315.1	3305.7	2990.6	$25/2^- \rightarrow 23/2^-$	11.1(10)	
326.1	455.7	129.6	$5/2^- \rightarrow 1/2^-$	36.2(9)	1.1(1)
360.8	3836.6	3475.8	$(27/2^+) \rightarrow (25/2^+)$	7.6(7)	
426.1	881.8	455.7	$7/2^- \rightarrow 5/2^-$	2.4(5)	
453.3	602.5	149.2	$11/2^+ \rightarrow 9/2^+$	29.3(7)	0.7(2)
460.0	2979.4	2519.4	$(21/2^+) \rightarrow 21/2^+$	14.4(7)	
481.2	4317.8	3836.6	$(29/2^+) \rightarrow (27/2^+)$	<1.0	
522.4	978.1	455.7	$9/2^- \rightarrow 5/2^-$	21.4(24)	1.0(1)
522.5	2168.1	1645.7	$15/2^- \rightarrow 13/2^-$	9.6(10)	
570.4	1364.9	794.5	$15/2^+ \rightarrow 13/2^+$	15.1(10)	0.7(2)
602.5	602.5	0.0	$11/2^+ \rightarrow 7/2^+$	7.0(9)	
638.2	2242.6	1604.4	$19/2^+ \rightarrow 17/2^+$	8.1(24)	
645.3	794.5	149.2	$13/2^+ \rightarrow 9/2^+$	34.6(10)	1.0(1)
662.9	2308.6	1645.7	$17/2^- \rightarrow 13/2^-$	12.3(14)	1.0(1)
667.6	1645.7	978.1	$13/2^- \rightarrow 9/2^-$	20.8(9)	1.0(1)
736.4	2979.4	2242.6	$21/2^+ \rightarrow 19/2^+$	3.1(4)	
748.3	2394.0	1645.7	$(17/2^-) \rightarrow 13/2^-$	4.5(15)	0.9(3)
762.5	1364.9	602.5	$15/2^+ \rightarrow 11/2^+$	5.7(7)	
809.9	1604.4	794.5	$17/2^+ \rightarrow 13/2^+$	20.4(9)	1.0(2)
877.6	2242.6	1364.9	$19/2^+ \rightarrow 15/2^+$	3.1(6)	
914.8	2519.2	1604.4	$21/2^+ \rightarrow 17/2^+$	10.5(6)	1.0(3)
943.7	2308.6	1364.9	$17/2^- \rightarrow 15/2^+$	2.8(6)	
1373.7	2168.1	794.5	$15/2^- \rightarrow 13/2^+$	2.8(4)	

lowing the procedure described in [17,18] with Harris parameters of $\mathcal{J}_0 = 4\hbar^2$ MeV^{-1} and $\mathcal{J}_1 = 40\hbar^4$ MeV^{-3} taken from ^{102}Ru [19]. The low-lying collective bands 1 and 3 show a large signature splitting ($\Delta e' \approx$ 200 keV) and an alignment of about $3\hbar$ and $2\hbar$, respectively. Around the frequencies of 0.40 MeV and 0.48 MeV, a band crossing is observed in bands 1 and 3, respectively. Above these crossings, bands 2 and 4 exhibit a gain in alignment of $8\hbar$ and $5\hbar$ relative to bands 1 and 3, respectively, an absence of signature splitting, and enhancement of $M1$ transitions.

Experimental ratios of reduced transition probabilities $[B(M1)/B(E2)]$ are indicators of the deformation parameters γ and β_2 and can also give insight into the structure of ıe band. All the experimental data for these ratios were ɔbtained from the spectra gated by the transitions populating

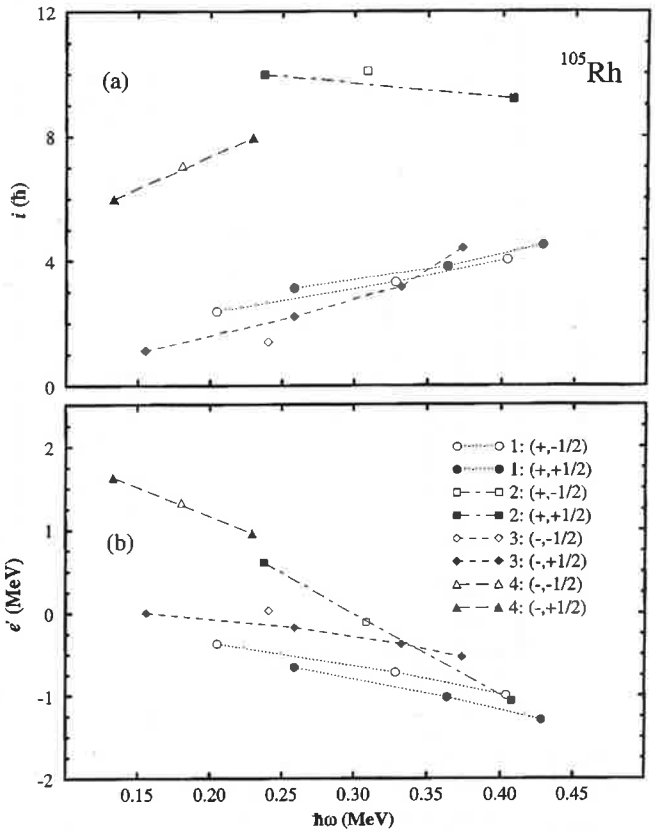

FIG. 3. Experimental quasiparticle (a) alignments and (b) Routhians as a function of the rotational frequency $\hbar\omega$ for the rotational bands labeled 1–4 in ^{105}Rh. The solid symbols correspond to $\alpha = +\frac{1}{2}$ and the open ones to $\alpha = -\frac{1}{2}$. The following symbols are used for the bands: circles, band 1; squares, band 2; diamonds, band 3; and triangles, band 4.

the level of interest. The experimental $B(M1)/B(E2)$ ratios for band 1 in ^{105}Rh are shown in Fig. 4, together with the lower and upper limits for bands 2, 4, and 3, respectively, as well as the theoretical estimates using the geometrical model of Dönau and Frauendorf [18].

IV. THEORETICAL CALCULATIONS

A. CSM calculations

The quasiparticle Routhians, calculated with the cranked shell model, based on a deformed Woods-Saxon potential including pairing interactions [20] are shown in Fig. 5. The calculations were performed for $Z=45$ ($\beta_2=0.19$, $\beta_4=0.0$, $\gamma=-30°$) and $N=60$ ($\beta_2=0.19$, $\beta_4=0.0$, $\gamma=0°$) at fixed deformations, which were indicated by the TRS predictions for the $\pi g_{9/2}$ and $\pi g_{9/2} \otimes (\nu h_{11/2})^2$ configurations in ^{105}Rh. The various quasiparticle states are classified by parity and signature (π, α) and the slopes of the trajectories are directly related to the aligned angular momentum (i). In order to simplify notation a letter code was used. For the protons, the first available $g_{9/2}$ orbitals are labeled by lower case letters a, b, c, d, e, and f, and the $\pi p_{1/2}$ orbitals are labeled by g and h, while, for the neutrons, the first available $h_{11/2}$ orbitals are A, B, C, and D, and for $\nu g_{7/2}$ and $\nu d_{5/2}$ orbitals are E, F, and G, H, respectively.

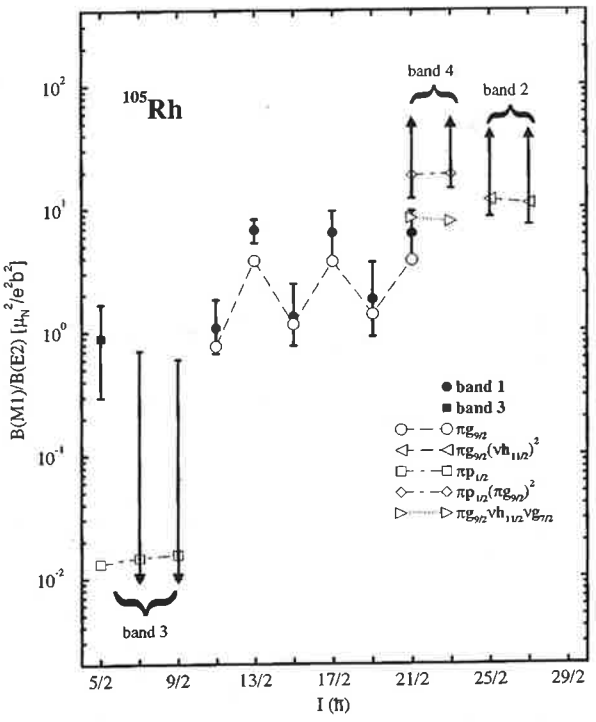

FIG. 4. Reduced transition probabilities in ^{105}Rh. The experimental $B(M1)/B(E2)$ ratios are given by solid symbols: circles, band 1; and squares, band 3, and upper or lower limits, shown for some levels in bands 2, 3, and 4 in ^{105}Rh. Calculated values are given by open symbols connected by dashed, dotted, and dot-dashed lines. The estimates were made using the equilibrium deformation $\beta_2 = 0.19$, $\beta_4 = 0$, $\gamma = -30°$, and $K = 7/2$ for $\pi g_{9/2}$ bands (circles). For the remaining bands the deformation parameters $\beta_2 = 0.19$, $\beta_4 = 0$, $\gamma = 0°$ and $K = 7/2$, 1/2 , 17/2, and 7/2 were assumed for $\pi g_{9/2} \otimes (\nu h_{11/2})^2$ (left-pointing triangles), $\pi p_{1/2}$ (squares), $\pi p_{1/2} \otimes (\pi g_{9/2})^2$ (diamonds), and $\pi g_{9/2} \otimes \nu(h_{11/2}, g_{7/2})$ (right-pointing triangles) configurations, respectively.

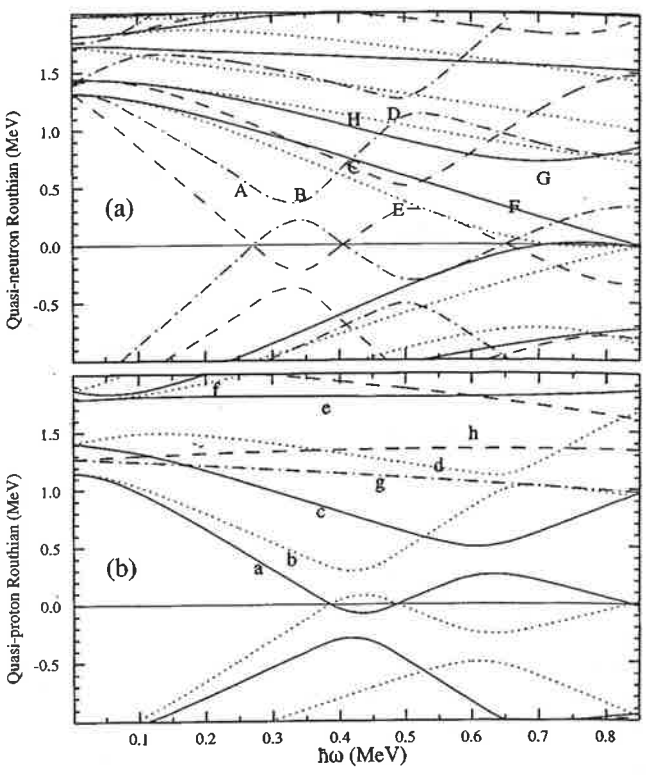

FIG. 5. Quasiparticle Routhians as a function of rotational frequency for neutrons (a) calculated at $\beta_2 = 0.19$, $\beta_4 = 0$, $\gamma = 0°$ and protons (b) calculated at $\beta_2 = 0.19$, $\beta_4 = 0$, $\gamma = -30°$ in ^{105}Rh. The following convention is used for the levels: solid line $(\pi = +, \alpha = +\frac{1}{2})$, dotted line $(\pi = +, \alpha = -\frac{1}{2})$, dot-dashed line $(\pi = -, \alpha = +\frac{1}{2})$, and dashed line $(\pi = -, \alpha = -\frac{1}{2})$. The configurations are labeled by letters.

The lowest available one-quasiproton excitations correspond to a and b $(\pi g_{9/2})$ configurations, which show a large energy splitting and are assigned to the two signature branches of the yrast band (band 1). The first two negative-parity quasiproton excitations (g, h) are an admixture of $p_{1/2}$, $f_{5/2}$, and $p_{3/2}$ and also have a large signature splitting, where the g $(-,\frac{1}{2})$ configuration corresponds to the favored $E2$ stretched cascade (band 3). Bands with these configurations have been previously observed in other odd-Z nuclei of this mass region. Moreover, as the rotational frequency increases, a band crossing of the yrast band is observed around $\hbar\omega = 0.40$ MeV and corresponds to the alignment of the first two $h_{11/2}$ quasineutrons (A and B), resulting in a net gain in angular momentum of about $10\hbar$. The next band crossing corresponds to the breaking of the first $g_{9/2}$ quasiproton pair (ab) and would occur around $\hbar\omega = 0.43$ MeV, but is blocked in the yrast band (a and b configurations).

B. TRS calculations

Total Routhian surface calculations were performed in order to get a quantitative estimate of the equilibrium deformation and to follow the nuclear shape evolution, as a function of the rotational frequency. The calculations employed the Strutinsky shell-correction formalism, deformed Woods-Saxon potential, and a monopole pairing residual interaction [20,21]. The nucleus ^{105}Rh is very γ soft and its energy minimum is very shallow below the band crossing, extending toward oblate-collective deformations, as shown in Fig. 6. There is a strong indication for configuration-dependent triaxiality in the one-quasiproton configurations $g_{9/2}$ [Fig. 6(a)] and $p_{1/2}$ [Fig. 6(c)].

The result for yrast configuration a $(\pi g_{9/2})$ at $\hbar\omega = 0.317$ MeV is shown in Fig. 6(a). For this configuration, a very large negative γ deformation ($\gamma \approx -30°$) and a large signature splitting (250 keV at $\hbar\omega \approx 0.32$ MeV) are predicted below $\hbar\omega = 0.4$ MeV. The signature splitting of 250 keV is close to that extracted from band 1. Above this frequency, the three-quasiparticle configuration containing two $h_{11/2}$ quasineutron (aAB) becomes yrast, with a resulting prolate-collective shape ($\gamma \approx 0°$), as shown in Fig. 6(b). This configuration is predicted to have a small signature splitting (≈ 50 keV at $\hbar\omega \approx 0.45$ MeV), comparable to the experimental value for band 2. The γ-deformation change from triaxial- to prolate-collective shape is due to the strong driving force of the $(\nu h_{11/2})^2$ quasineutrons, which also results in an alignment gain of $10\hbar$. Since $h_{11/2}$ quasineutrons dominate the nuclear shape ($\gamma \approx 0°$) and the energy splitting of the $g_{9/2}$ quasiproton tends to zero around $\gamma = 0°$, the small signature splitting ($\approx$ 50 keV) of the three-quasiparticle configuration is essentially between the a and b quasiproton states.

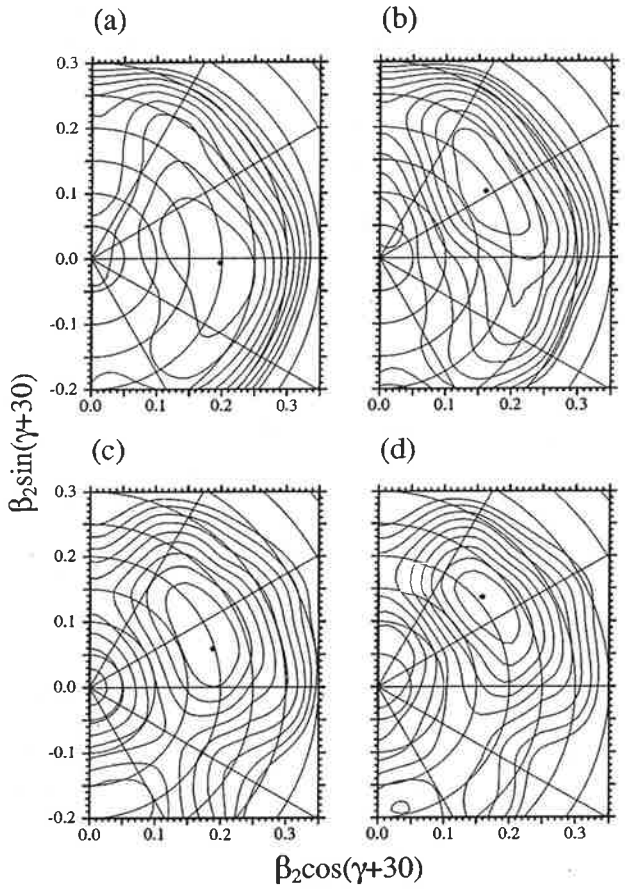

FIG. 6. Total Routhian surface calculations for one- and three-quasiparticle configurations in ^{105}Rh. (a) a configuration, $\hbar\omega=0.317$ MeV; minimum at $\beta_2=0.197$, $\beta_4=0.008$, $\gamma=-32°$. (b) aAB configuration, $\hbar\omega=0.444$ MeV; minimum at $\beta_2=0.190$, $\beta_4=0.009$, $\gamma=2.2°$. (c) g configuration, $\hbar\omega=0.317$ MeV; minimum at $\beta_2=0.197$, $\beta_4=0.010$, $\gamma=-12.6°$. (d) gAB configuration, $\hbar\omega=0.444$ MeV; minimum at $\beta_2=0.210$, $\beta_4=0.009$, $\gamma=9.3°$ (the thick dots indicate the position of the equilibrium deformation).

The situation is similar when examining the g ($\pi p_{1/2}$) configuration. The equilibrium deformation remains almost unchanged at a triaxial-collective shape ($\gamma\approx-12°$) for frequencies below $\hbar\omega=0.40$ MeV, as shown in Fig. 6(c). Around $\hbar\omega=0.30$ MeV the energy splitting between the favored (g) and unfavored (h) signatures is $\approx$180 keV, which is close to that observed for band 3. As a consequence of the additional strong driving forces of the AB pair, the energy minimum is pulled towards positive γ values ($\gamma\approx10°$) for the gAB configuration, as shown in Fig. 6(d). Such a deformation change does not affect significantly the signature splitting value corresponding to the $\pi p_{1/2}$ configuration. At $\hbar\omega=0.381$ MeV, this value is around 300 keV for the $\pi p_{1/2}\otimes(\nu h_{11/2})^2$ configuration, which is in complete disagreement with that for band 4.

C. Estimated branching ratios $B(M1)/B(E2)$

In the semiclassical model of Dönau and Frauendorf [18], the $M1$ transitions are assumed to originate from the precession of the perpendicular component of the magnetic moment around the total angular momentum vector. Using this approach the branching ratios $B(M1)/B(E2)$, between inband $\Delta I=1$ and crossover $\Delta I=2$ transitions from each band state, were estimated for the one- and three-quasiparticle configurations of ^{105}Rh and compared with the experimental results in Fig. 4. Effective g factors were used to relate the angular momentum of each quasiparticle configuration to its magnetic moment vector and were obtained from the Schmidt estimates, with an attenuation factor of 0.7 for the spin g factors [22]. The deformation parameters used were obtained from the TRS calculations for each configuration and the proton and neutron alignments were derived from the quasiparticle Routhians in Fig. 5. In the case of the $\pi g_{9/2}$ yrast band, a $K=7/2$ projection and a correction for large experimental signature splittings (200 keV) were used, while for the $\pi g_{9/2}\otimes(\nu h_{11/2})^2$ band, the $K=7/2$ projection was assumed to come essentially from the $g_{9/2}$ quasiproton. A pair of aligned $h_{11/2}$ quasineutrons ($i\approx10\hbar$) coupled to the $g_{9/2}$ quasiproton with a relatively large K value is responsible for the enhancement of $M1$ transitions, as seen in band 2. The calculations for band 3 were performed assuming a pure $p_{1/2}$ configuration with the g factor=0.03 and $K=1/2$. In the case of a pure $p_{3/2}$ ($g=1.97$) the $B(M1)/B(E2)$ ratios would increase by a factor of about 100. For the high-K $\pi p_{1/2}\otimes(\pi g_{9/2})^2$ band (gac) with a pair of $g_{9/2}$ quasiprotons coupled to the deformation axis, large $B(M1)/B(E2)$ ratios are in agreement with the experimental lower limits for band 4. Another three-quasiparticle $\pi g_{9/2}\otimes\nu(h_{11/2},g_{7/2})$ configuration (aAE and bAE) could be considered; however, the theoretical $B(M1)/B(E2)$ ratios result in smaller values than those for the experimental lower limits for band 4.

V. DISCUSSION

Band 1 is the yrast band with strong $M1$ and $E2$ transitions. The observed large signature splitting of 200 keV, according to the CSM and TRS calculations, corresponds to the lowest one-quasiproton excitations (a and b) with a large negative γ value ($\gamma\approx-30°$). The calculated $B(M1)/B(E2)$ ratios using $\Delta e'=200$ keV and $K=7/2$ are in very good agreement with the experimental results and thus the $\pi g_{9/2}$ configuration was assigned to band 1.

The three-quasiparticle band 2 is characterized by strong $M1$ transitions and is built on the second $(21/2^+)$ state of the yrast band, as shown in Fig. 1. The difference between the two structures 1 and 2 is clearly exhibited in the rotating frame (see Fig. 3) where band 2 has negligible signature splitting and a gain in alignment of about $8\hbar$ relative to band 1. These characteristics are expected for a $\pi g_{9/2}\otimes(\nu h_{11/2})^2$ configuration (aAB and bAB). TRS and CSM calculations indicate that the first band crossing occurs around $\hbar\omega=0.40$ MeV and corresponds to an alignment of a pair of $h_{11/2}$ quasineutrons (AB). This phenomenon causes a change in γ deformation from triaxial- to prolate-collective shapes. Since the signature splitting corresponds to the splitting between the two quasiprotons (a and b), it decreases as γ increases from $-30°$ to $0°$. On the basis of the geometrical model, the enhancement of the $M1$ transitions is caused by a coherent superposition of the magnetic moments of a strongly coupled proton ($g_{9/2}$) and of the two aligned neutrons ($h_{11/2}$).

On the other hand, band 3 is characterized by strong $E2$, weak, or unobserved $M1$ transitions, and a large signa-

ture splitting (200 keV). The $\pi p_{1/2}$ configuration (g and h) is expected to have a very large signature splitting with g being the lower branch, while the other one (h) should be weakly populated and difficult to observe experimentally. These properties were also seen in other odd-Z nuclei in this mass region. TRS calculations suggest triaxial-collective shape ($\gamma \approx -12°$) and a large signature splitting (180 keV) for this configuration. In addition, at $I^{\pi}=5/2^{-}$ the experimental $B(M1)/B(E2)$ ratio is rather small (roughly $1.0\mu_N^2/e^2\,\mathrm{b}^2$). The theoretical $B(M1)/B(E2)$ ratio was calculated for a pure $\pi p_{1/2}$ configuration and is two orders of magnitude smaller. However, admixtures from $p_{1/2}$, $p_{3/2}$, and $f_{5/2}$ are present in the first two negative-parity quasiproton excitations (g, h), increasing the effective g factor and the quasiparticle angular momentum projection along the symmetry axis (K), resulting in larger $B(M1)/B(E2)$ ratios, comparable with the experimental ones.

The three-quasiparticle band 4 decays preferentially to band 3, around $I^{\pi}=17/2^{-}$. The experimental signature splitting in band 4 is negligible and no $E2$ crossover transitions were observed. Essentially three types of configurations were considered for this band: namely, $\pi p_{1/2}\otimes(\nu h_{11/2})^2$, $\pi g_{9/2}\otimes(\nu h_{11/2},g_{7/2})$, and $\pi p_{1/2}\otimes\pi[(g_{9/2})^2]_{K=8}$. In the first case, the coupling of the $(\nu h_{11/2})^2$ to the $\pi p_{1/2}$ configuration is expected to give a fairly large signature splitting, of the same order of magnitude as for band 3, in contradiction with the experimental results. Similar results would be obtained with any other combination of two low-lying $(h_{11/2},g_{7/2})$ quasineutrons. For the second type of configuration $\pi g_{9/2}\otimes\nu(h_{11/2},g_{7/2})$, a small signature splitting would be expected. In addition, the experimental lower limits for the $B(M1)/B(E2)$ ratios for the $21/2^{-}$ and $23/2^{-}$ levels are around $13\mu_N^2/e^2\,\mathrm{b}^2$ in disagreement with the theoretical results ($\approx 9\mu_N^2/e^2\,\mathrm{b}^2$). On the other hand, for the third configuration $\pi p_{1/2}\otimes\pi(g_{9/2})^2$, the theoretical estimates ($\approx 18\mu_N^2/e^2\mathrm{b}^2$) are consistent with the experimental lower limits; see Fig. 4. Furthermore, this band presents a gain in alignment of about $5\hbar$ relative to band 3, which is the expected value for $(\pi g_{9/2})^2$ quasiparticles. The large K value provides also a possible explanation for the negligible signature splitting observed experimentally [11]. It should be noted that $K\approx 8$ usually implies an isomeric state for the bandhead. However, a lifetime of less than about 20 nsec cannot be measured with the experimental setup of the present experiment. Bands with this type of configuration have been observed already in this mass region in nuclei such as odd-N ^{109}Cd [23], odd-odd ^{108}Ag [4], and odd-Z ^{103}Rh [5]. In view of the above arguments, the $\pi p_{1/2}\otimes\pi[(g_{9/2})^2]_{K=8}$ configuration was tentatively assigned to band 4.

VI. CONCLUSION

A level scheme for the states populated in a heavy-ion reaction has been proposed for the ^{105}Rh nucleus. Four rotational bands were observed, which are consistent with the systematics of the odd-Z nuclei in the $A=100$ mass region. Most of the band structures were interpreted within the framework of the CSM and TRS. Triaxial deformation could explain the large signature splitting in the one-quasiproton configurations and the absence of strong $M1$ transitions. A shape change, between the yrast and the three-quasiparticle bands, above the crossing frequency of $\hbar\omega=0.4$ MeV, occurs due to the alignment of a pair of $h_{11/2}$ quasineutrons which induce the disappearance of the signature splitting and the enhancement of $M1$ transitions. The data presently available indicate that the negative, three-quasiparticle band can be ascribed to a high-K configuration [coupling the $(\pi g_{9/2})^2$ to the $(\pi p_{1/2})$ band]. This type of high-K band appears also in other nuclei in this mass region.

ACKNOWLEDGMENTS

The authors would like to acknowledge financial support from the Brazilian Conselho Nacional de Desenvolvimento Científico e Tecnológico (CNPq).

[1] G. A. Leander, S. Frauendorf, and F. R. May, *Proceedings of the Conference on High Angular Momentum Properties of Nuclei*, Oak Ridge, 1982, edited by N. R. Johnson (Harwood, New York, 1983), p. 281.

[2] R. Duffait, A. Charvet, K. Deneffe, R. Beraud, A. Emsallem, M. Meyer, T. Ollivier, J. Treherne, A. Gizon, F. Beck, and T. Byrski, Nucl. Phys. **A454**, 143 (1986).

[3] D. Jerrestam, W. Klamra, J. Gizon, F. Lidén, L. Hildingsson, J. Kownacki, Th. Lindblad, and J. Nyberg, Nucl. Phys. **A577**, 786 (1994).

[4] F. R. Espinoza-Quiñones, E. W. Cybulska, L. G. R. Emediato, C. L. Lima, N. H. Medina, J. R. B. Oliveira, M. N. Rao, R. V. Ribas, M. A. Rizzutto, W. A. Seale, and C. Tenreiro, Phys. Rev. C **52**, 104 (1995).

[5] H. Dejbakhsh, R. P. Schmitt, and G. Mouchaty, Phys. Rev. C **37**, 621 (1988).

[6] H. J. Keller, S. Frauendorf, U. Hagemann, L. Käubler, H. Prade, and F. Stary, Nucl. Phys. **A444**, 261 (1985).

[7] D. Jerrestam, W. Klamra, J. Gizon, B. Fogelberg, S. J. Freeman, H. J. Jensen, S. Mitarai, G. Sletten, and I. Thorslund, Nucl. Phys. **A579**, 256 (1994).

[8] S. Frauendorf, in *Proceedings of the International Symposium on In-Beam Nuclear Spectroscopy*, Debrecen, edited by Z. S. Dombrádi and T. Fényes (Akadémiai Kiadó, Budapest, 1984), p. 711.

[9] S. Juutinen, R. Julin, M. Piiparinen, P. Ahonen, B. Cederwall, C. Fahlander, A. Lampinen, T. Lönnroth, A. Maj, S. Mitarai, D. Müller, J. Nyberg, P. Šimeček, M. Sugawara, I. Thorslund, S. Törmänen, A. Virtanen, and R. Wyss, Nucl. Phys. **A573**, 306 (1994).

[10] F. R. Espinoza-Quiñones, E. W. Cybulska, J. R. B. Oliveira, R. V. Ribas, N. H. Medina, M. N. Rao, M. A. Rizzutto, L. G. R. Emediato W. A. Seale, and S. Botelho, Phys. Rev. C **55**, 1548 (1997).

[11] S. Frauendorf, Nucl. Phys. **A557**, 259c (1993).

[12] R. N. Saxena, V. P. Esteves, and F. C. Zawislak, J. Phys. G **5**, 1169 (1979).

[13] *Table of Isotopes*, 7th ed., edited by C. Michael Lederer and Virginia S. Shirley (John Wiley & Sons, New York, 1978), p. 469.

[14] J. A. Grau, L. E. Samuelson, P. C. Simms, S. I. Popik, and F. A. Rickey, Bull. Am. Phys. Soc. **21**, 95 (1976).

[15] V. R. Vanin and M. Aïche, Nucl. Instrum. Methods Phys. Res. A **284**, 452 (1989).

[16] W. T. Milner, Computer codes VAXPAK, Oak Ridge National Laboratory, 1986.

[17] R. Bengtsson and S. Frauendorf, Nucl. Phys. **A237**, 139 (1979).

[18] F. Dönau and S. Frauendorf, in *Proceedings International Conference on High Spin Properties of Nuclei*, Oak Ridge, 1982, edited by N. R. Johnson, Nuclear Science Research Series Vol. 4 (Harwood, New York, 1983), p. 143.

[19] D. R. Haenni, H. Dejbakhsh, R. P. Schmitt, and G. Mouchaty, Phys. Rev. C **33**, 1543 (1986).

[20] R. Wyss, J. Nyberg, A. Johnson, R. Bengtsson, and W. Nazarewicz, Phys. Lett. B **215**, 211 (1988).

[21] W. Nazarewicz, J. Dudek, R. Bengtsson, T. Bengtsson, and I. Ragnarsson, Nucl. Phys. **A435**, 397 (1985).

[22] S. Frauendorf and F. R. May, Phys. Lett. **125B**, 245 (1983).

[23] S. Juutinen, P. Šimeč, C. Fahlander, R. Julin, J. Kumpulainen, A. Lampinen, T. Lönnroth, A. Maj, S. Mitarai, D. Müller, J. Nyberg, M. Piiparinen, M. Sugawara, I. Thorslund, S. Törmänen, and A. Virtanen, Nucl. Phys. **A577**, 727 (1994).

Vol. 32 (2001) *ACTA PHYSICA POLONICA B* No 3

HIGH SPIN STRUCTURES IN $A \approx 100$ AND 140 MASS REGIONS*

E.W. Cybulska, J.R.B. Oliveira, M.A. Rizzutto, R.V. Ribas
N.H. Medina, W.A. Seale, M.N. Rao, F.R. Espinoza-Qui†
J.A. Alcántara-Núñez and F. Falla-Sotelo

Instituto de Física, Universidade de São Paulo
São Paulo, Brazil.

(Received October 31, 2000)

High spin structures were studied in the ^{105}Rh and ^{136}La nuclei using the ^{100}Mo(^{11}B,$\alpha 2n$)^{105}Rh and ^{128}Te(^{11}B,xn)^{136}La reactions respectively. DCO ratios, α–γ–γ and γ–γ coincidences were measured. Four new bands were identified in ^{105}Rh and three in ^{136}La. The results were interpreted with the CSM.

PACS numbers: 23.90.+w

1. Introduction

In the $A \approx 100$ and 130–140 mass regions the neutron and proton, which occupy high-j subshells show similar characteristics. Valence nucleons which lie at the top of the subshell exert a driving force towards a collectively rotating oblate shape, while those at the bottom tend towards collective prolate deformations. The competition between driving forces results in a variety of nuclear shapes and shape transitions. The Gamma Spectroscopy Group of the University of São Paulo has been studying the odd and odd–odd nuclei for $Z = 45$, 47, 57 and 59. The results of this research have been presented in references [1] and [2]. Recently, a renewal of interest in these mass regions has appeared due to the theoretical predictions based on the Tilted Axis Cranking model, which indicate a possible existence of chiral bands in triaxial nuclei ($A \approx 130$) [3] and magnetic rotational bands [4], which appear in nearly spherical nuclei such as in the $A \approx 100$ regions.

* Presented at the XXXV Zakopane School of Physics "Trends in Nuclear Physics", Zakopane, Poland, September 5–13, 2000.

† Permanent Address: Centro de Engenharia e Ciências Exatas, Universidade Estadual do Oeste do Paraná, Toledo, PR, Brazil.

Experimentally the former are observed as two nearly degenerate bands with strong M1 and E2 transitions, while the latter as bands with very strong M1 and very weak E2 transitions. In view of the above, we have returned to study the La isotopes and also to repeat the ^{105}Rh measurements with an improved apparatus.

2. Experimental details and results

The beam was provided by the 9 MV Pelletron Tandem. The experimental setup consists of 4 GeHP Compton suppressed detectors (PERERE). Two of the detectors with 60 % efficiency were placed at 37° and 260° while the remaining ones with 20 % efficiency were set at 100° and 323° with respect to the beam. For experiments where the neutron channels are the strongest, such as ^{136}La, a multiplicity filter of 8 NaI(Tl) was placed close to the target chamber. In order to identify the charged particle evaporation channels (such as ^{105}Rh) a 4π particle ancillary scintillator system SACI was built in this laboratory. This detector consists of 11 phoswhich plastic $E - \Delta E$ telescope scintillators housed in an aluminium casing of a semi-regular polyhedral shape, with 12 pentagonal and 20 triangular sides. The BC-400 plastic 0.1mm thick was used for the ΔE and a BC-444 plastic 10 mm thick for the E detector. The overall geometrical efficiency of this system is 76 %.

The ^{100}Mo(^{11}B, $\alpha 2n$)^{105}Rh reaction was used at 43 MeV beam energy, with a thick isotopically enriched target. The α–γ–γ coincidences and the DCO ratios were measured. The level scheme, Fig. 1, shows four previously known bands (1–4) [2], three of them (1, 2 and 4) extended to higher spins and four new bands A to D observed for the first time. The spins were assigned on the basis of DCO measurements and systematics.

The ^{136}La was produced in a ^{128}Te(^{11}B, xn)^{136}La reaction at 48 MeV beam energy. A thick, isotopically enriched target, on a lead backing was used. The γ–γ coincidences and the DCO ratios were measured. Prior to this work, the nucleus ^{136}La was investigated using $(p, 3n)$ reaction [5], where the spin of 8^+ or 7^+ was assigned to the 114 ms isomeric state. Figure 2(a) shows the level scheme of the present work, composed of three bands, tentatively placed on the 114 ms isomeric state. Since the ^{136}La level scheme is very similar to that of its isotone ^{138}Pr [1] and to the other odd–odd La and Pr isotopes, the assignment of the spins to the levels and of the band configurations was based on the systematics of this mass region, as well as Cranking Shell Model (CSM) predictions and the measured DCO ratios.

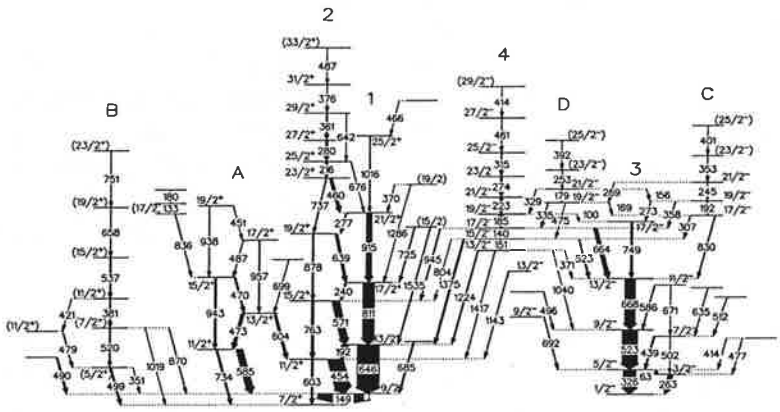

Fig. 1. ^{105}Rh level scheme showing the new bands A to D. The bands 1, 2 and 4, known from [2], were extended to higher spins.

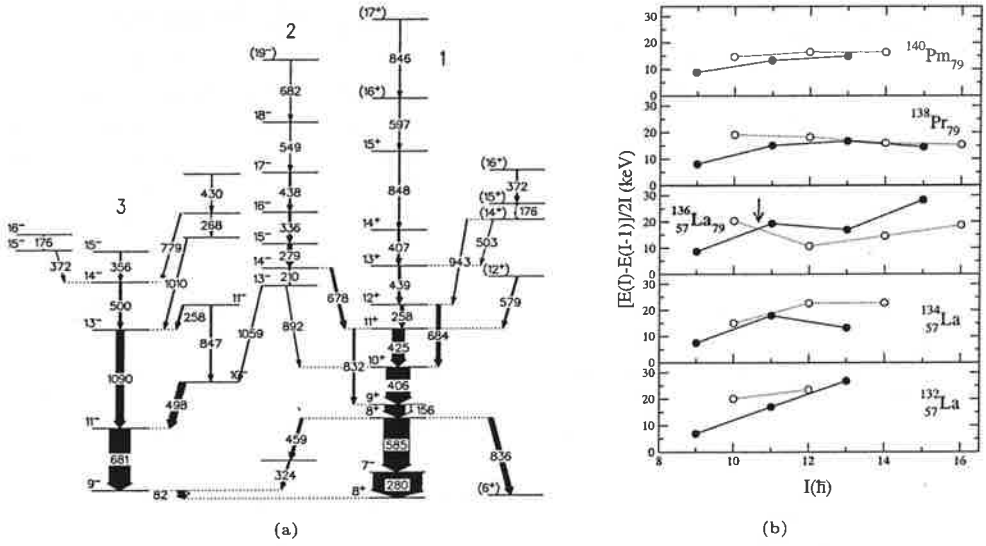

Fig. 2. (a) — ^{136}La level scheme. Bands 1, 2 and 3 were assigned the $\pi h_{11/2} \otimes \nu h_{11/2}$, $\pi[413]_{5/2} \otimes (\pi h_{11/2})^2 \otimes \nu h_{11/2}$, and $\pi[411]_{1/2} \otimes \nu h_{11/2}$ configurations, respectively. (b) — systematics of the transition energies for the $\pi h_{11/2} \otimes \nu h_{11/2}$ band. The signature inversion point in ^{136}La is indicated by an arrow.

3. Discussion

Band A in ^{105}Rh is similar to the bands based on the $7/2^+[413]$ proton state coupled to the $2^+\gamma$-phonon of the core observed in ^{107,109}Rh [6]. This can be considered as an indication of triaxiality in ^{105}Rh, contrary to the calculations presented in [6]. A possible configuration for band B is $\pi 1/2^+[431]$,

but unlike in ^{107}Rh [6], the $3/2^+$ bandhead was not observed. The M1 bands in ^{105}Rh (2, 4, D and C) are candidates for magnetic rotation.

The experimental Routhians in ^{136}La exhibit a rather large and constant signature splitting of $\Delta e' = 105$ keV in the yrast band, and none in band 2. The CSM calculations performed with deformation parameters $\beta_2 = 0.14$ and $\beta_4 = 0.0$ as a function of γ-deformation for $\hbar\omega = 0.45$ MeV indicate two possibilities consistent with the observed signature splitting of band 1: a nearly oblate shape ($\gamma = -50°$) for the coupling of an $\alpha_n = -\frac{1}{2}$ neutron with the two proton signatures ($\alpha_p = \pm\frac{1}{2}$); or a nearly prolate ($\gamma = -5°$) for an $\alpha_p = -\frac{1}{2}$ proton with the two neutron signatures ($\alpha_n = \pm\frac{1}{2}$). Precise measurements of M1 + E2 mixing ratio would be helpful in order to resolve this ambiguity.

A careful examination of band 1 in the ^{136}La level scheme shows a clear signature inversion between $I^\pi = 10^+\hbar$ and $I^\pi = 11^+\hbar$, as indicated by an arrow in figure 2(b). Signature inversion has been observed [7] also for neutron deficient nuclei, such as ^{134}Pr and ^{124}La, but never below a spin of 17 $\hbar$.

4. Conclusion

The use of the SACI-PERERE array permitted the establishment of 4 new rotational bands in ^{105}Rh level scheme and an extension to higher spins of 3 other bands. Lifetime measurements for the M1 bands are necessary in order to confirm their magnetic rotation character. The level scheme for ^{136}La was established, showing three rotational bands in agreement with the sytematics of $A = 130$–140 mass region. Signature inversion was observed at very low spins in ^{136}La in contrast to the other nuclei in this region. In the present work no evidence for chiral bands was observed.

This work was supported by the Fundação de Amparo à Pesquisa do Estado de São Paulo (FAPESP) and Conselho Nacional de Desenvolvimento Científico e Tecnológico (CNPq), Brazil.

REFERENCES

[1] M.A. Rizzutto *et al.*, *Nucl. Phys.* **A569**, 547 (1994) and references therein.
[2] F.R. Espinoza-Quiñones *et al.*, *Phys. Rev.* **C55**, 2787 (1997) and references therein.
[3] S. Frauendorf, *Z. Phys.* **A358**, 163 (1997).
[4] S. Frauendorf, Lie Meng, *Nucl. Phys.* **A617**, 131 (1997).
[5] Morek *et al.*, *Nucl. Phys.* **A433**, 159 (1985).
[6] Ts. Venkova *et al.*, *Eur. Phys. J.* **A6**, 405 (1999).
[7] Yunzuo Liu *et al.*, *Phys. Rev.* **C54**, 719 (1996).

Rotational band structure in odd-odd ^{132}La

J. R. B. Oliveira, L. G. R. Emediato, M. A. Rizzutto, R. V. Ribas, W. A. Seale, M. N. Rao, N. H. Medina, S. Botelho, and E. W. Cybulska
Laboratório Pelletron, Departamento de Física Nuclear, Instituto de Física, Universidade de São Paulo, 01498-São Paulo, SP, Brazil
(Received 3 January 1989)

The level scheme of ^{132}La was obtained with in-beam gamma spectroscopy techniques using fusion evaporation reactions with ^{10,11}B, ^{14}N beams and isotopic targets of Te and Sn. Two rotational band structures were seen. One band, assigned to the $\pi h_{11/2}\otimes\nu h_{11/2}$, shows a smaller signature splitting as compared to the isotones ^{134}Pr and ^{136}Pm, indicating a slight reduction of triaxiality. The other band has been tentatively assigned the $\pi[422]\frac{3}{2}^{+}\otimes\nu h_{11/2}$ configuration, and shows no signature splitting indicating a near prolate shape.

I. INTRODUCTION

The prediction that nuclei in the $A\approx130$ mass region are γ soft and that their shapes are influenced by quasiparticles in high-j orbitals[1,2] has resulted in a recent surge of interest in the study of odd-odd nuclei in this region.[3–5] The doubly-odd nuclei in this region are particularly interesting, in that they permit investigation of the competition between the relatively strong shape driving forces caused, on the one hand, by the neutron quasiparticle situated in the upper part of the $h_{11/2}$ shell and, on the other, by the proton quasiparticle at the lower part of the same high-j shell. Experimental results up to now indicate nonaxial deformations as a result of this competition.

We present here the results of an investigation of in-beam spectroscopy of ^{132}La, using fusion-evaporation reactions with beams provided by the Pelletron Tandem Accelerator of the University of São Paulo. Prior to our investigation, the available information on the level structure of ^{132}La was from the beta decay of ^{132}Ce (Refs. 6 and 7). The ground-state spin of ^{132}La was known to be $J^{\pi}=2^{-}$. A metastable state ($J^{\pi}=6^{-}$; $T_{1/2}=24.3$ min.) was known to exist at 188 keV excitation, which decays to the ground state with the emission of a 53-keV $M3$ γ ray, followed by a 135-keV $M1$ transition.

II. EXPERIMENTAL PROCEDURES AND RESULTS

Cross-beam reactions, namely, ^{124}Te(^{11}B,3n)^{132}La and ^{126}Te(^{10}B,4n)^{132}La, and excitation functions for the second reaction, were used to identify the γ rays belonging to ^{132}La. The targets were prepared by pressing enriched tellurium powder (96.21% of ^{124}Te and 98.69% of ^{126}Te) onto a lead foil, forming targets 10 and 4 mg/cm^2 thick, respectively. In the second experiment, with the ^{126}Te(^{10}B,4n)^{132}La reaction, two HpGe detectors were used at 55° for the γ-γ-t coincidences, which were sorted on line onto a 1024×1024 $E_\gamma\times E_\gamma$ array. A symmetric, background subtracted matrix was generated, using the technique described in Ref. 8. The angular distributions were measured for the ^{126}Te(^{10}B,4n)^{132}La reaction at a beam energy of 45 MeV. Spectra were obtained at seven angles between $-10°$ and 90°. A third experiment was also performed using the ^{122}Sn(^{14}N,4n)^{132}La at 55 MeV, in order to search for low-energy γ rays.

The γ intensities, taken from the singles spectra, and corrected for detector efficiency, together with the angular distribution results, are given in Table I. Figure 1 shows typical gate spectra.

Two bands were observed, both of them characterized by strong $M1$ transitions and much weaker $E2$ crossovers. The stronger band is presented in Fig. 2, together with the recent results of other isotones,[4] ^{134}Pr and ^{136}Pm, showing a striking similarity between these three bands, except for the lowest transition of $\approx$90 keV. In our study of the first two reactions (^{124}Te+^{11}B; ^{126}Te+^{10}B), copper absorbers were used to suppress Pb x rays, which also hindered greatly the observation of the γ rays of energies below 100 keV. Thus, the third reaction referred to above was performed with a self-supporting, enriched ^{122}Sn target and sufficient aluminum absorber to attenuate specifically the Sn x rays (25, 28 keV). In addition, the beam was stopped in a shielded Faraday cup away from the target. Besides confirming the results from the other two reactions, a 67-keV γ ray was observed (Fig. 1), satisfying all the coincidence requirements for the (8^{+}) to (7^{+}) transition. No γ ray of $\approx$90 keV was seen in our spectra.

The complete level scheme based on the present work is shown in Fig. 3. There are three self-coincident gammas: 161, 293, and 455 keV. The placements of these and the other gammas in the decay scheme were made on the basis of relative intensities in the gated above and gated below spectra, the energy and intensity balance, crossover transitions, and the measured multipolarities. Nearly all of the strong γ rays seen in the various coincidence spectra have been placed in this level scheme. A few weak lines, viz., 233, 351, and 411 keV, appear in some isolated gates, and it was not possible to establish consistent placement for these γ rays in the present scheme.

The level populated by the 169-keV transition pertain-

TABLE I. Energies, intensities, and angular distribution results for the gamma transitions in the ^{126}Te(^{10}B,4n)^{132}La reaction at 45 MeV. For the 67-keV transition, the intensity is from the ^{122}Sn(^{14}N,4n)^{132}La reaction at 55 MeV. The relative intensities are from singles spectra, corrected for detector efficiency, and normalized to the 169-keV transition. The energies are accurate to ±0.2 keV, except those quoted as integers which are accurate to ±1 keV.

E (keV)	I_{rel} (%)	Assignment	a_2/a_0	a_4/a_0
67.1	26.7(1.3)	$(8^+)\rightarrow(7^+)$		
151.0	13.5(1.0)		−0.314(70)	+0.008(90)
161.1[a]	107.6(6.0)	$(9^+)\rightarrow(8^+)$	−0.329(56)	−0.030(49)
169.3	100.0(6.2)	$(7^-)\rightarrow(6^-)$	−0.576(64)	−0.005(40)
202.7	91.9(5.6)		−0.580(82)	−0.0046(50)
227.3	26.7(1.1)	$(8^-)\rightarrow(7^-)$	−0.60(10)	+0.030(80)
230.6	11.2(1.8)		−0.35(11)	+0.09(11)
232.6	22.6(2.4)		−0.51(10)	0.072(85)
279.0	53.7(3.5)		+0.290(17)	−0.073(21)
289.0	12.0(3.4)	$(9^-)\rightarrow(8^-)$		
293.8[a]	90.7(5.1)	$(11^+)\rightarrow(10^+)$	−0.392(24)	−0.026(20)
		$(10^+)\rightarrow(9^+)$		
312.4	17.4(1.3)	$(7^+)\rightarrow(7^-)$	+0.290(31)	−0.018(36)
320.2	24.8(1.9)		+0.216(31)	+0.001(37)
351.5[b]	23.5(3.1)			
380.4	6.0(0.8)	$(10^-)\rightarrow(9^-)$	−0.318(57)	−0.259(66)
386.5	12.7(1.3)	$(13^+)\rightarrow(12^+)$		
392.6	16.7(1.5)	$(12^+)\rightarrow(11^+)$	−0.513(74)	+0.052(72)
396.0	8.3(1.2)	$(8^-)\rightarrow(6^-)$		
454.6[a]	7.2(0.7)	$(14^+)\rightarrow(13^+)$		
		$(10^+)\rightarrow(8^+)$		
481.7	30.6(2.2)	$(7^+)\rightarrow(6^-)$	−0.226(59)	−0.037(56)
516.0[b]	30.7(3.0)	$(9^-)\rightarrow(7^-)$	+0.119(85)	−0.031(99)
587.9	5.6(2.1)	$(11^+)\rightarrow(9^+)$		
669.8[b]	23.5(3.6)	$(10^-)\rightarrow(8^-)$		
687	1.8(0.7)	$(12^+)\rightarrow(10^+)$		
778	<1	$(13^+)\rightarrow(11^+)$		
841	<2	$(14^+)\rightarrow(12^+)$		

[a]Gamma ray placed twice in the level scheme.
[b]Unresolved doublet with contaminant.

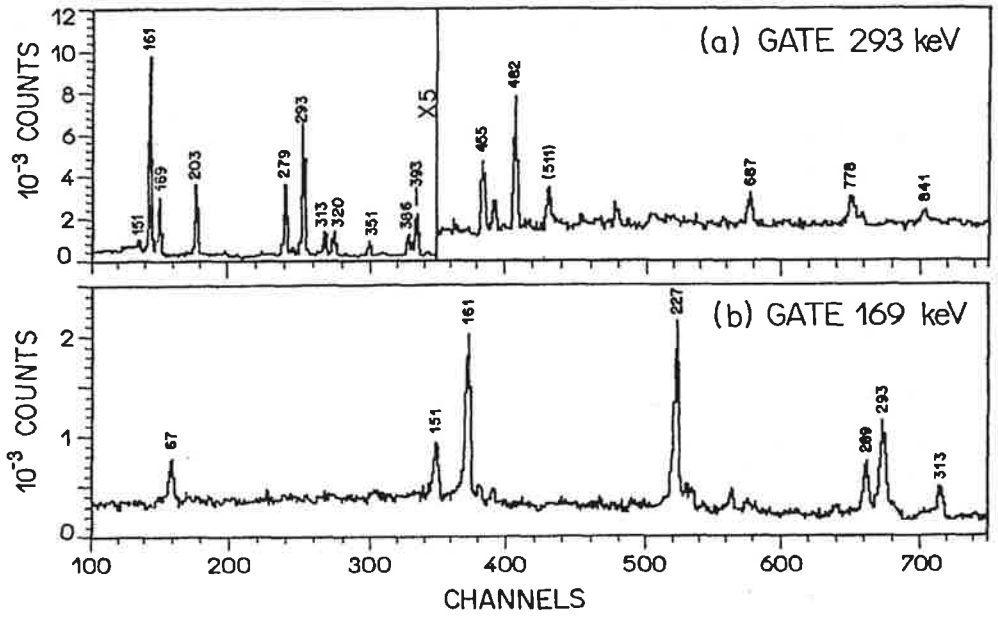

FIG. 1. Typical γ-γ coincidence spectra used to determine the level scheme of ^{132}La. (a) Gate on the 293-keV transition, data from ^{126}Te(^{10}B,4n)^{132}La at 48 MeV. (b) Gate on the 169-keV transition, data from ^{122}Sn(^{14}N,4n)^{132}La at 55 MeV.

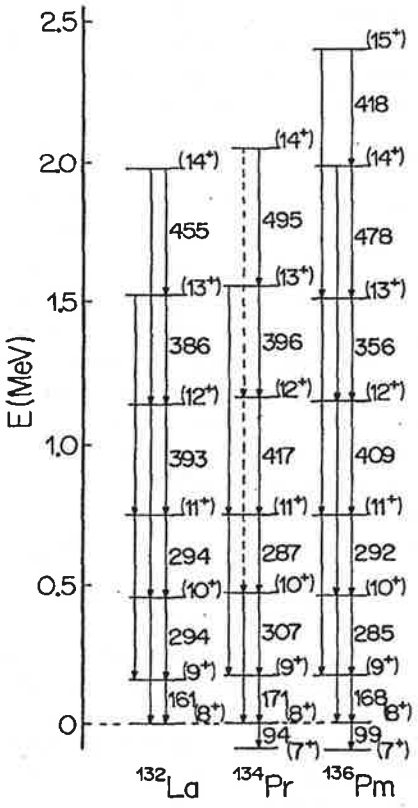

FIG. 2. Comparison of the $\pi h_{11/2}\otimes\nu h_{11/2}$ band in the isotones ^{132}La, ^{134}Pr, and ^{136}Pm.

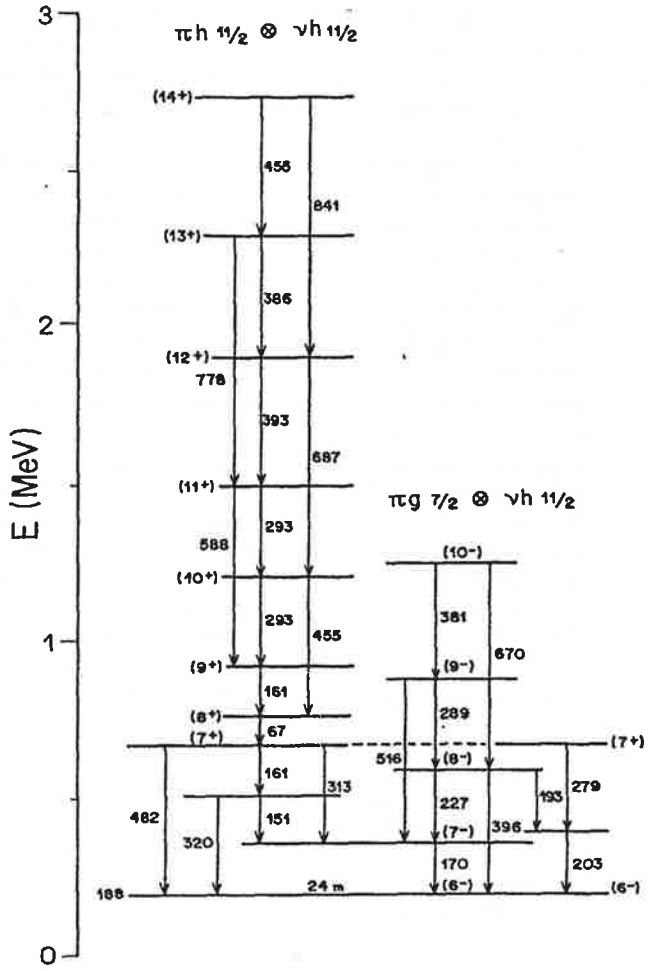

FIG. 3. The complete level scheme of ^{132}La based on the present work.

ing to a second weaker band is assumed to be the known 6^- (24 min) isomer at 188-keV excitation in ^{132}La, since no gammas were observed to depopulate this level, from the in-beam coincidence spectra. Further, the decay spectra taken off-beam show a strong 135-keV gamma decaying with the half-life of the known 6^- isomeric state.

III. EXPERIMENTAL ALIGNMENTS AND ROUTHIANS

In the neighboring N-odd and Z-odd nuclei, such as ^{131}Ce (Ref. 9) and ^{131}La (Ref. 10), the observed yrast bands (bandhead $\frac{9}{2}^-$ and $\frac{11}{2}^-$, respectively) are built on a $h_{11/2}$ neutron strongly coupled to the core and a decoupled $h_{11/2}$ proton, respectively, suggesting thus a $\pi h_{11/2}\otimes\nu h_{11/2}$ configuration for the strongest band in ^{132}La. The assignment of (8^+) to the spin and parity of the bandhead, populated by the 161-keV transition, is consistent with a perpendicular coupling between neutron and proton. The observed bandhead $I=(8^+)$ belongs to the unfavored component of the band, which for the aforementioned configuration corresponds to the signature $\alpha=0$ ($I=\alpha$ mod2).

The experimental alignment i_x and the Routhian e' were extracted from the data, using the procedure described in Ref. 11:

$$e'(\omega)=E'(\omega)-E'_g(\omega)\ ,$$

where

$$E'(\omega)=[E(I+1)+E(I-1)]/2-\omega I_x$$

and

$$E'_g(\omega)=-\omega^2(J_0/2)-\omega^4(J_1/4)+1/(8J_0)\ .$$

The Harris parameters J_0 and J_1 are obtained from the least-squares fit of the angular momentum alignment to the experimental data in the frequency range below the first crossing:

$$i_x(\omega)=I_x(\omega)-I_{xg}(\omega)=I_x(\omega)-(\omega J_0+\omega^3 J_1)\ ,$$

where I_x is given by

$$I_x=[(I+\tfrac{1}{2})^2-\langle K\rangle^2]^{1/2}\ .$$

In ^{132}La, the Fermi level for protons should lie around $\Omega_p=\frac{1}{2}$ while the Fermi level for the neutron is around $\Omega_n=\frac{9}{2}$ of the $h_{11/2}$ shell, resulting in $K=5$ according to

the Gallagher-Moszkowski rule.[12] The assignment of the angular momentum projection $\langle K \rangle$ could usually be corroborated comparing the experimental $B(M1)/B(E2)$ values, with the semiclassical formalism of Dönau and Frauendorf.[13] In the present case, however, the crossover $E2$ transitions are very weak and because of the double placements of some of the γ rays involved, only two experimental values could be obtained, and thus this procedure did not lead to a $\langle K \rangle$ value with reasonable confidence. The $\langle K \rangle = 5$ value was used in the calculations of the alignment and the Routhian, which are shown in Fig. 4. The Harris parameters[14] extracted from the data are $J_0 = 11.3\hbar^2$ MeV^{-1} and $J_1 = 41.7\hbar^4$ MeV^{-3}. The alignment i_x is constant up to a frequency of 0.4 MeV, as would be expected for the $\pi h_{11/2} \otimes \nu h_{11/2}$ band, since the first neutron and proton orbitals are blocked. The magnitude of i_x (5.6$\hbar$) shows good agreement with the other isotones and is comparable with the sum of alignments in neighboring nuclei of odd-N (1.8$\hbar$) (Ref. 9) and odd-Z (4.5$\hbar$) (Ref. 10). The observed signature splitting of 25 keV is about half the value seen in ^{134}Pr and ^{136}Pm (Ref. 4) and 60% of that observed in ^{128,130}La (Ref. 15).

As mentioned earlier, the bandhead of the second band

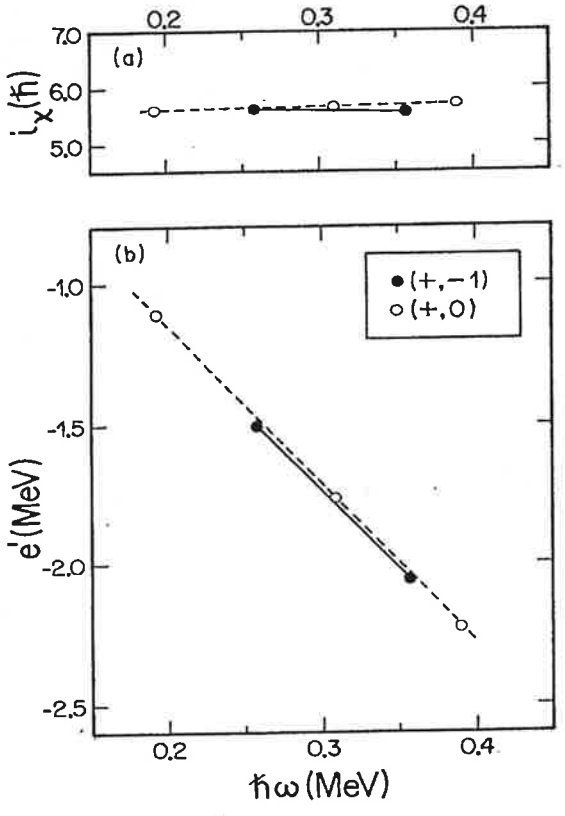

FIG. 4. (a) The experimental alignment and (b) Routhians for the $\pi h_{11/2} \otimes \nu h_{11/2}$ band of ^{132}La. The open and solid circles are the favored ($\alpha = -1$) and unfavored ($\alpha = 0$) components of the band, respectively. The Harris parameters used were $J_0 = 11.3\hbar^2$ MeV^{-1} and $J_1 = 41.7\hbar^4$ MeV^{-3}.

was assumed to be the 6^- isomer in ^{132}La. The proton Fermi level is near the Nilsson orbital $[422]\frac{3}{2}^+$ of mixed $g_{7/2}$ and $d_{5/2}$ parentage. Thus a possible configuration for this band would be a $\pi[422]\frac{3}{2}^+ \otimes \nu h_{11/2}$ with

$$I^\pi = K = \Omega_p + \Omega_n = \tfrac{3}{2}^+ + \tfrac{9}{2}^- = 6^-$$

for the bandhead. In ^{131}La (Ref. 10), the $\pi h_{11/2}$ bandhead ($I^\pi = \frac{11}{2}^-$) lies 305 keV above the ground state $\pi g_{7/2}$ ($I^\pi = \Omega = \frac{3}{2}^+$), thus it is not unreasonable to expect the $\pi h_{11/2} \otimes \nu h_{11/2}$ bandhead to lie above the $\pi[422]\frac{3}{2}^+ \otimes \nu h_{11/2}$ bandhead in ^{132}La. Although there are very few points, the experimental Routhian indicates no signature splitting of this negative-parity band.

As can be seen from Fig. 3, the $\pi h_{11/2} \otimes \nu h_{11/2}$ band decays to the 6^- isomeric state through the emission of a 67-keV γ ray followed by a 482-keV transition, which shows a negative anisotropy $a_2/a_0 = -0.23$, thus indicating $\Delta I = 1$ character. In addition, correct intensity balance (in the 482 keV gate) for the (8^+) state could be obtained only if the 67-keV γ ray corresponds to an $M1$ transition [$\alpha_T(M1) = 3.37$, $\alpha_T(E1) = 0.68$]. Thus we assign $J^\pi = (7^+)$ to the level fed by the 67-keV γ ray. This assignment is also consistent with the systematics in the $N = 75$ isotones shown in Fig. 2. A spin of (7^+) for this level would imply that the 313-keV transition has a $\Delta I = 0$ dipole character, in agreement with the measured anisotropy $a_2/a_0 = +0.23$.

IV. THEORETICAL CALCULATIONS AND DISCUSSION

Theoretical calculations were made within the framework of the triaxial cranking shell model.[16] The total single quasiparticle Hamiltonian includes a pairing term together with the cranking term given by

$$H = H_0 - \omega J_x + H_{\text{pair}} .$$

A modified oscillator potential was used in the intrinsic Hamiltonian H_0 as in Ref. 17. The calculations were performed at a fixed rotational frequency of $\hbar\omega = 250$ keV, deformation parameters $\beta = 0.2, \epsilon_4 = 0$, and pairing strengths $\Delta_p = \Delta_n = 1.2$ MeV. The Fermi levels for protons and neutrons were adjusted to give the correct value of the mean particle numbers ($Z = 57$, $N = 75$) at a deformation of $\gamma = 0°$. The calculated Routhians, corresponding to the first $h_{11/2}$ excited quasiparticle states as a function of γ (in the Lund convention[17]), are presented in Fig. 5 for both protons and neutrons. The results show a preference of $\gamma = -60°$ for the first favored quasineutron and $\gamma > 0°$ for the first favored quasiproton. The experimentally observed signature splitting is found to correspond to the splitting of the two neutron signatures at $\gamma \approx -15°$. The bands based on the unfavored signature of the proton are not seen, since they lie high above the yrast line due to the large splitting.

The total Routhian (E'_{tot}) was calculated using the methods of Frauendorf and May,[18] in which a phenomenological contribution from the core is added to the quasiparticle Routhians. The V_{po} parameter (the prolate

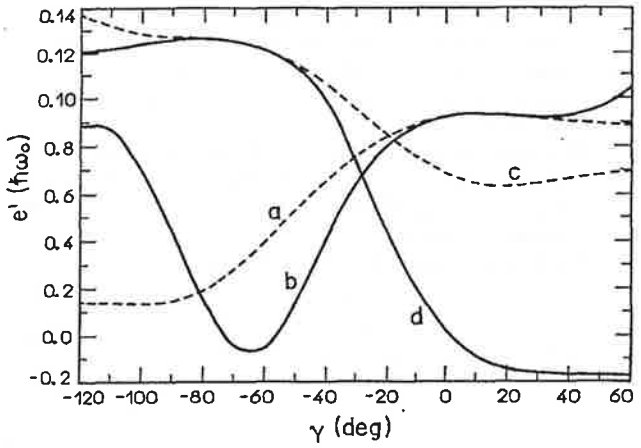

FIG. 5. Calculated Routhians for the first $h_{11/2}$ quasiparticle states in ^{132}La. (a,b) neutrons, (c,d) protons. The dashed lines are for the signature $\alpha=+\frac{1}{2}$ and the solid lines are for $\alpha=-\frac{1}{2}$.

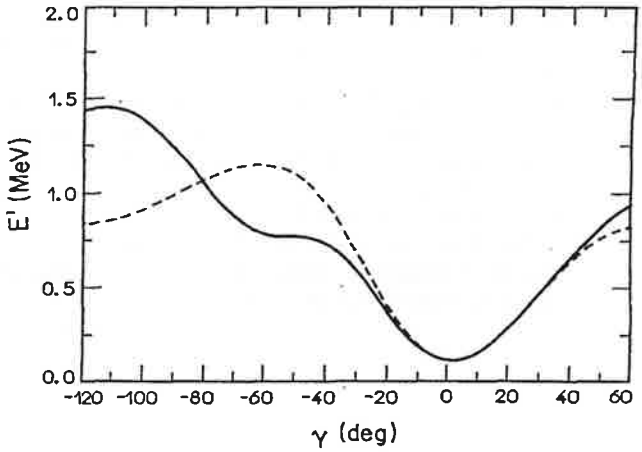

FIG. 6. The total Routhians as a function of the gamma deformation. The dashed line is for the signature $\alpha=0$ and the solid line is for the signature $\alpha=-1$ of the $\pi h_{11/2}\otimes\nu h_{11/2}$ configuration.

to oblate potential energy difference) was taken as -400 keV.[2] The results show minima at $\gamma\approx0°$ (Fig. 6) for both signatures where the splitting is very small (2–3 keV). The calculations are insensitive to the exact values of the pairing strengths and deformation parameters β and ϵ_4. Usually the V_{po} parameter is adjusted to reproduce the experimental splitting. This procedure fails in the present case as the equilibrium value of γ is around 0°, where the corresponding contribution to the prolate-oblate energy term $V_{po}\cos(3\gamma)$ to the total Routhian has an extremum.

The observed signature splitting in ^{132}La in the $\pi h_{11/2}\otimes\nu h_{11/2}$ band is half as much as in the isotones with $Z=59$ and 61. This reduction is expected as the proton Fermi level is lower in ^{132}La ($Z=57$), thus producing a larger driving force towards positive values of γ.[1] In ^{128,130}La (Ref. 15) the experimental signature splitting in this band is about 40 keV. The reason for the reduction in ^{132}La is less obvious. On the one hand, as the neutron Fermi level rises within the high-j shell, the splitting around $\gamma=0°$ tends to reduce, while the equilibrium γ deformation could change towards a region of larger signature splitting.

V. CONCLUSIONS

High-spin states of ^{132}La were measured for the first time, and a level scheme was proposed. Two rotational bands were identified.

In the doubly-odd nuclei ^{132}La, ^{134}Pr, and ^{136}Pm, the $\pi h_{11/2}\otimes\nu h_{11/2}$ bands show very similar characteristics. The smaller signature splitting in ^{132}La may indicate a slight reduction of triaxiality as compared to the other two isotones. The second weaker band, with the 6^- isomer as the bandhead, probably has the configuration $\pi[422]\frac{3}{2}^+\otimes\nu h_{11/2}$. No signature splitting was observed in this band, indicating $\gamma\approx0°$.

ACKNOWLEDGMENTS

The authors wish to thank Dr. C. L. Lima, University of São Paulo, Brazil, and Dr. A. J. Kreiner, Comisión Nacional de Energía Atomica (CNEA), Buenos Aires, Argentina for helpful discussions. This work was partially supported by the Fundação de Amparo à Pesquisa do Estado de São Paulo and by the Conselho Nacional de Desenvolvimento Científico e Tecnológico.

[1] G. A. Leander, S. Frauendorf, and F. R. May, in *Proceedings of the Conference on High Angular Momentum Properties of Nuclei, Oak Ridge, 1982,* edited by N. R. Johnson (Harwood Academic, New York, 1983), p. 281.

[2] Y. S. Chen, S. Frauendorf, and G. A. Leander, Phys. Rev. C **28**, 2437 (1983).

[3] E. S. Paul, C. W. Beausang, D. B. Fossan, R. Ma, W. F. Piel, Jr., N. Xu, and L. Hildingsson, Phys. Rev. C **36**, 1853 (1987).

[4] C. W. Beausang, L. Hildingsson, E. S. Paul, W. F. Piel, Jr., P. K. Weng, N. Xu, and D. B. Fossan, Phys. Rev. C **36**, 1810 (1987).

[5] S. Shi, C. W. Beausang, D. B. Fossan, R. Ma, E. S. Paul, N. Xu, and A. J. Kreiner, Phys. Rev. C **37**, 1478 (1988).

[6] C. Gerschel and M. N. Perrin, C.R. Acad. Sci. Ser. B **269**, 220 (1969).

[7] B. Harmatz and T. W. Handley, Nucl. Phys. **A191**, 497 (1972).

[8] G. Palameta and J. C. Waddington, Nucl. Instrum. **A234**, 476 (1985).

[9] R. Ma, E. S. Paul, C. W. Beausang, S. Shi, N. Xu, and D. B. Fossan, Phys. Rev. C **36**, 2322 (1987).

[10] E. S. Paul, C. W. Beausang, D. B. Fossan, R. Ma, W. F. Piel, Jr., N. Xu, L. Hildingsson, and G. A. Leander, Phys. Rev. Lett. **53**, 984 (1987).

[11] R. Bengtsson and S. Frauendorf, Nucl. Phys. **A327**, 139

(1979).
[12]C. J. Gallagher and S. A. Moszkowski, Phys. Rev. **111**, 1282 (1958).
[13]F. Dönau and S. Frauendorf, in *Proceedings of the Conference on High Angular Momentum Properties of Nuclei, Oak Ridge, 1982,* edited by N. R. Johnson (Harwood Academic, New York, 1983), p. 143.
[14]S. M. Harris, Phys. Rev. **138**, B509 (1965).
[15]R. Ma, E. S. Paul, S. Shi, C. W. Beausang, W. F. Piel, Jr., N. Xu, D. B. Fossan, T. Chapuran, D. P. Balamuth, and J. W. Arrison, Phys. Rev. C **37**, 1926 (1988).
[16]R. Bengtsson and J. D. Garrett, in *Proceedings of the Nordic Winter School on Nuclear Physics, Hemsedal, Norway, 1983,* Vol. 2 of *Collective Phenomena in Atomic Nuclei,* edited by T. England, J. Rekstad, and J. S. Vaagen (World-Scientific, Singapore, 1984).
[17]G. Andersson, S. E. Larsson, P. Moller, S. G. Nilsson, I. Ragnarsson, S. Aberg, R. Bengtsson, J. Dudek, B. Nerlo-Pomorska, K. Pomorski, and Z. Szymanski, Nucl. Phys. **A268**, 205 (1976).
[18]S. Frauendorf and F. R. May, Phys. Lett. **125B**, 245 (1983).

Semidecoupled band structure in odd-odd ^{134}La and ^{136}Pr

J. R. B. Oliveira,* L. G. R. Emediato, E. W. Cybulska, R. V. Ribas, W. A. Seale, M. N. Rao, N. H. Medina, M. A. Rizzutto, S. Botelho, and C. L. Lima

Laboratório Pelletron, Departamento de Física Nuclear, Instituto de Física, Universidade de São Paulo, São Paulo, Brazil

(Received 13 December 1991)

The level schemes of the isotones ^{134}La and ^{136}Pr were obtained with in-beam gamma spectroscopy techniques using fusion evaporation reactions with ^{10}B, ^{14}N, and ^{16}O beams and enriched targets of ^{126,128}Te and ^{123}Sb. Rotational bands assigned to the $\pi h_{11/2} \otimes \nu h_{11/2}$ configuration were seen in both nuclei. Another band seen in ^{136}Pr was tentatively assigned to the $\pi[413]\frac{5}{2} \otimes \nu h_{11/2}$ configuration. A beginning of a backbend seems to show up in this band.

PACS number(s): 23.20.Lv, 27.60.+j

I. INTRODUCTION

In recent years many articles have appeared on the study of odd-odd nuclei in the γ-soft, $A \sim 130$ mass region [1–4]. The doubly-odd nuclei in this region are particularly interesting in that they permit investigation of the competition between the relatively strong shape driving forces caused, on the one hand, by the neutron quasiparticle situated in the upper part of the $h_{11/2}$ shell and, on the other hand, by the proton quasiparticle at the lower part of the same high-j shell, which may result in triaxial equilibrium shapes. For small values of γ, the signature splitting of the $\pi h_{11/2}$ orbital is very large, in contrast to nearly zero splitting for a neutron in a high-Ω orbital. Thus, a semidecoupled band structure, with the proton in the favored signature orbital, showing a small signature splitting due to the neutron is expected for this configuration. Indeed, yrast bands with these characteristics have been found in several odd-odd nuclei in this region.

We present here the results of an investigation of in-beam gamma spectroscopy of the $N = 77$ isotones, ^{134}La and ^{136}Pr, using fusion-evaporation reactions with beams provided by the Pelletron Tandem Accelerator of the University of São Paulo. Prior to our investigation the available information on the level structure of ^{136}Pr came from the beta decay of ^{136}Nd [5]. The ground state and a 9.4 ns isomeric state at 40.1 keV of ^{136}Pr are both known to have spin $J^\pi = 2^+$. During the present work a paper on the high-spin spectroscopy of Pr nuclei was published by Dragulescu *et al.* [6]. The ^{134}La nucleus has been previously studied with the ^{133}Cs$(\alpha, 3n)$ and ^{136}Ba$(p, 3n)$ reactions [7], but no bands were identified.

*Present address: Lawrence Berkeley Laboratory, Nuclear Science Division 70A-3307, 1 Cyclotron Rd., Berkeley, CA 94720.

II. EXPERIMENTAL PROCEDURES AND RESULTS

Crossed-beam reactions, ^{123}Sb$(^{16}$O$, 3n)$ and ^{126}Te$(^{14}$N$, 4n)$, and excitation functions were used to identify the gamma rays belonging to ^{136}Pr. The targets, about 10 mg/cm^2 thick, were made of enriched ^{123}Sb (99%) and ^{126}Te (98.7%) powder compressed onto a lead foil. In the case of the ^{134}La nucleus, the gamma rays from the ^{128}Te$(^{10}$B$, 4n)$ reaction were identified through comparison with the $(\alpha, 3n)$ reaction [7]. The target was of enriched ^{128}Te (99.2%) 0.93 mg/cm^2 thick, evaporated onto a 1 mg/cm^2 gold foil. Two HPGe detectors were used for the γ-γ-t coincidences. The data were sorted on-line into a 1024×1024 channel, $E_\gamma \times E_\gamma$ array. A symmetrized background-subtracted matrix was generated using the technique described in Ref. [8]. The angular distributions were measured for the ^{123}Sb$(^{16}$O$, 3n)^{136}$Pr and ^{128}Te$(^{10}$B$, 4n)^{134}$La reactions at beam energies of 64 and 44 MeV, respectively. In most of the cases the A_4/A_0 values were ≈ 0 within errors. Due to the complexity of the singles spectra the quality of the angular distributions only permitted determination of the predominant multipole character of the transitions. The gamma intensities, taken from the singles spectra and corrected for detector efficiency together with the angular distribution results, are given in Tables I and II. Figure 1 shows typical gated spectra for ^{136}Pr and ^{134}La, respectively.

A. ^{136}Pr level scheme

The level scheme of ^{136}Pr, based on the present work, is shown in Fig. 2. The principal features are two bands showing small staggering, strong $M1$ transitions, and much weaker $E2$ crossovers. Both bands depopulate to an isomeric level of 92 ± 1 ns, the more intense band through two strong-dipole transitions (245 and 209 keV), while the weaker one through a 314 keV gamma ray. The latter band shows an indication of a backbend. The half-life of the isomeric state was determined by the deconvolution of the time spectrum.

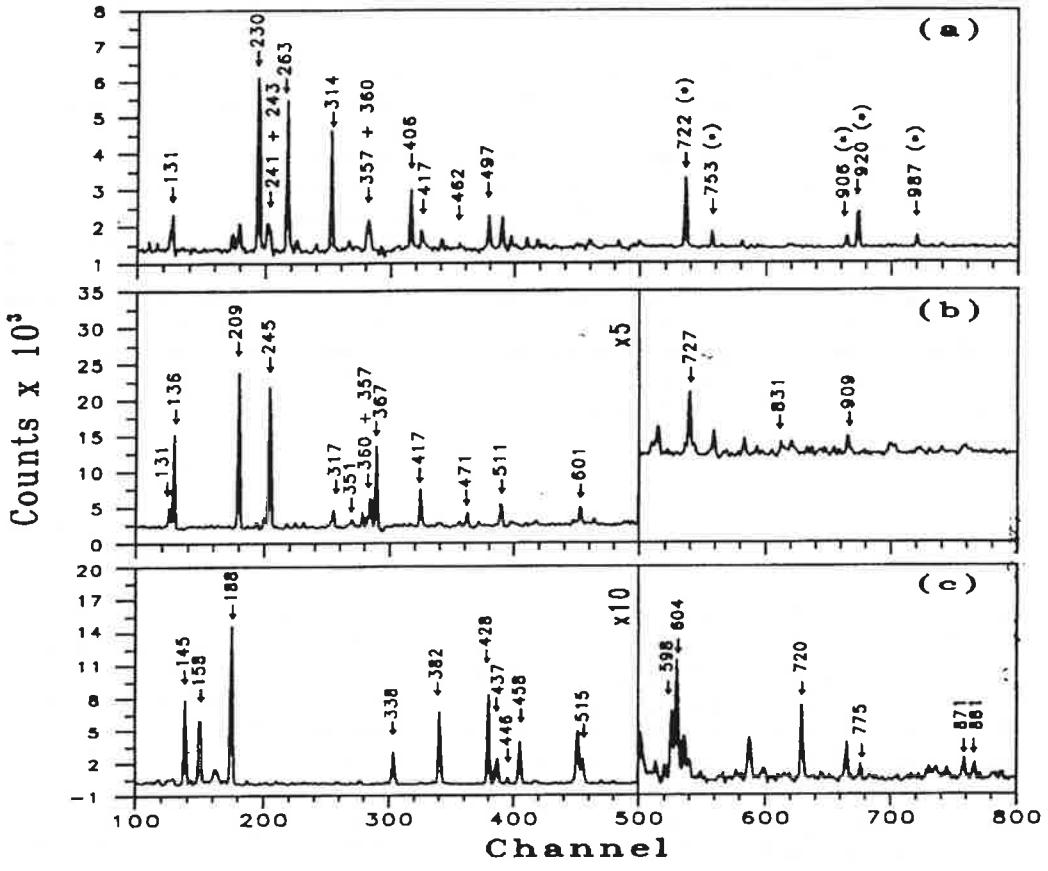

FIG. 1. Typical gamma-gamma coincidence spectra. (a) ^{136}Pr: sum of 314, 230, 405, and 497 keV gates; (b) ^{136}Pr: sum of 209, 245, 136, and 367 keV gates; (c) ^{134}La: sum of 145, 381, 338, and 437 keV gates; (*): gammas of ^{136}Pr which could not be placed consistently in the level scheme.

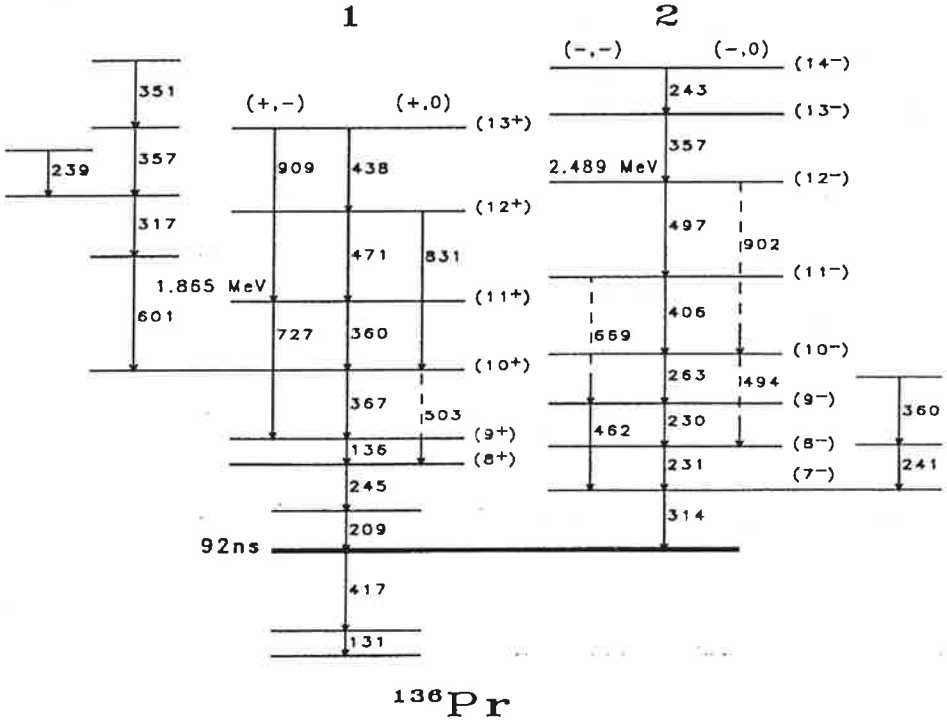

FIG. 2. The level scheme of ^{136}Pr based on the present work.

The present level scheme and that proposed by Dragulescu *et al.* [6] are essentially in agreement up to a relative excitation energy of 1.865 MeV for the stronger band and up to 2.489 MeV for the weaker one. On the basis of the observed crossover transitions of 831 and 909 keV, we have been able to extend the first band to a higher excitation energy. However we differ in the configurations and the spin assignments for both bands, as will be discussed below.

B. ^{134}La level scheme

The level scheme of ^{134}La (Fig. 3) shows a band with striking similarity to the yrast band in ^{136}Pr. The present level scheme agrees well with the relevant part of that proposed by Morek *et al.* [7] based on the $(\alpha, 3n)$ reaction, up to a relative excitation energy of 1.97 MeV, except for the 775 and 604 keV transitions which were not observed in the $(\alpha, 3n)$ work. In addition our placement of the crossover 871 keV line differs from that of Ref. [7]. There are also quite a few lines seen in both investigations, which although correlated, could not be placed consistently in the present level scheme. No isomeric state was observed in the range of 50 to 500 ns in this nucleus.

TABLE I. Gamma-ray energies, relative intensities, and spin assignments for ^{136}Pr.

E_γ (keV)[a]	I_R (%)	A_2/A_0	$I_i \rightarrow I_f$
131.2	132.5(1.6)	−0.16(1)	
136.7	44.6(8.0)	−0.29(2)	$(9^+) \rightarrow (8^+)$
209.7	117.6(1.2)	−0.47(1)	
230.8[c]	29.3(1.0)	−0.53(3)	$(8^-) \rightarrow (7^-)$
238.8	20.2(1.0)	−0.07(5)	
240.5	9.1(2.0)	−0.37(6)	
243[b]	3.3(0.2)		$(14^-) \rightarrow (13^-)$
245.0	100.0(1.2)	−0.31(1)	
263.1	8.9(0.9)	−0.43(19)	$(10^-) \rightarrow (9^-)$
313.9	31.8(1.1)	−0.33(3)	
317.4	8.8(1.4)	−0.42(11)	
351.1	9.2(1.5)	−0.26(13)	
357.7[c]	4.9(0.9)		
360.2[c]	16.6(1.0)	−0.74(16)	$(11^+) \rightarrow (10^+)$
367.0	39.5(1.1)	−0.65(6)	$(10^+) \rightarrow (9^+)$
405.4	6.5(1.4)	−0.39(7)	$(11^-) \rightarrow (10^-)$
417.8	192.2(13.0)	−0.11(17)	
438[b]	1.4(0.1)	−0.65(6)	$(13^-) \rightarrow (12^-)$
462[b]	3.0(0.1)		$(9^-) \rightarrow (7^-)$
471.7	5.5(1.0)	−0.57(14)	$(12^+) \rightarrow (11^+)$
494[b]	1.6(0.1)		$(10^-) \rightarrow (8^-)$
497[b]	3.5(0.1)		$(12^-) \rightarrow (11^-)$
501.9	6.1(1.0)		$(10^+) \rightarrow (8^+)$
601.7	17.7(2.0)	−0.82(14)	
669[b]	2.0(0.2)		$(11^-) \rightarrow (9^-)$
727.0	18.4(2.0)		$(11^+) \rightarrow (9^+)$
830.0	5.6(1.3)		$(12^+) \rightarrow (10^+)$
903	< 1		$(12^-) \rightarrow (10^-)$
909	< 2		$(13^+) \rightarrow (11^+)$

[a]Energy uncertainties of 0.5 keV except for very weak transitions.
[b]Intensities obtained from coincidence spectra.
[c]Doublets.

TABLE II. Gamma-ray energies, relative intensities, and multipolar characters for ^{134}La .

E_γ (keV)	I_R (%)	A_2/A_0	$I_i \rightarrow I_f$
145.0	100.(8)	−0.310(40)	$(9^+) \rightarrow (8^+)$
158.4	116.(7)	−0.340(29)	
187.8		−0.232(49)	
229.4	30.(3)		
257.9	26.(3)	−0.31(10)	
277[a]			
307.2	61.(5)	−0.441(75)	
338.0	53.(3)	−0.21(25)	$(11^+) \rightarrow (10^+)$
381.6	83.(4)	−0.380(53)	$(10^+) \rightarrow (9^+)$
407[a]			
427.9	114.(6)	−0.228(46)	
434.1 }			$(13^+) \rightarrow (12^+)$
436.5 }	31.7(7)		$(12^+) \rightarrow (11^+)$
445.9[b]	35.(4)		$(14^+) \rightarrow (13^+)$
458.1	75.(5)	−0.052(56)	
719.			
774.7	4.(2)		$(12^+) \rightarrow (10^+)$
870.8	20.(2)	+0.39(27)	$(13^+) \rightarrow (11^+)$
880.5	6.(2)		$(14^+) \rightarrow (12^+)$

[a]Contaminated with 444 keV from ^{133}La.
[b]Doublet.

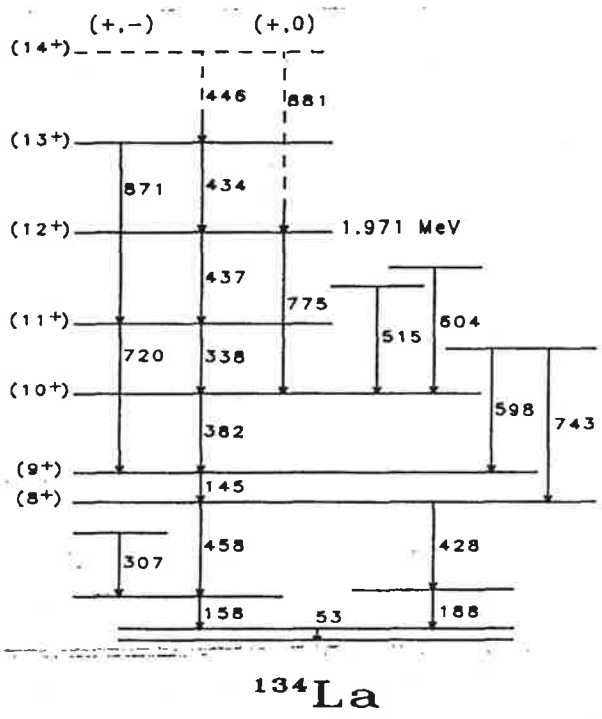

FIG. 3. The level scheme of ^{134}La based on the present work.

III. THEORETICAL CALCULATIONS

Theoretical calculations were made within the framework of the triaxial cranking shell model [9]. The total single particle Hamiltonian includes a cranking term together with a pairing term given by

$$H = H_0 - \omega J_x + H_{\text{pair}}. \quad (1)$$

A modified oscillator potential was used in the intrinsic Hamiltonian H_0 as in Ref. [10]. The deformation parameters used were $\beta = 0.165$, $\varepsilon_4 = 0$. The value of β was extracted from the relation $\beta = \sqrt{1224/E_\gamma(15/2^- \rightarrow 11/2^-)}$ applied to the first $E2$ transition of the $\pi h_{11/2}$ bands of the nearby odd-proton nuclei, which are expected to be axially symmetric (Fig. 4, $\gamma = 0°$). Although this formula was deduced for the energy of the first 2^+ states of even-even nuclei [11], it is also valid if complete decoupling of the rotation aligned $h_{11/2}$ proton is assumed. This is nearly the case, since the level spacing of the $\pi h_{11/2}$ bands closely follows the spacing of the ground-state bands of the even-even neighbors in this mass region. The pairing strengths used were $\Delta_p = 1.28$ MeV and $\Delta_n = 1.12$ MeV, typical values for this region. The Fermi levels were adjusted to give the correct mean value of the number of protons and neutrons (Z=57, 59 and N=77) at a deformation of $\gamma = 0°$. The calculated Routhians corresponding to the first excited quasiparticle states as a function of γ (in the Lund convention [10]) are presented in Fig. 4 for both protons and neutrons. The results show a preference of $\gamma = -60°$ for the first favored $h_{11/2}$ quasineutron and $\gamma > 0°$ for the first favored $h_{11/2}$ quasiproton.

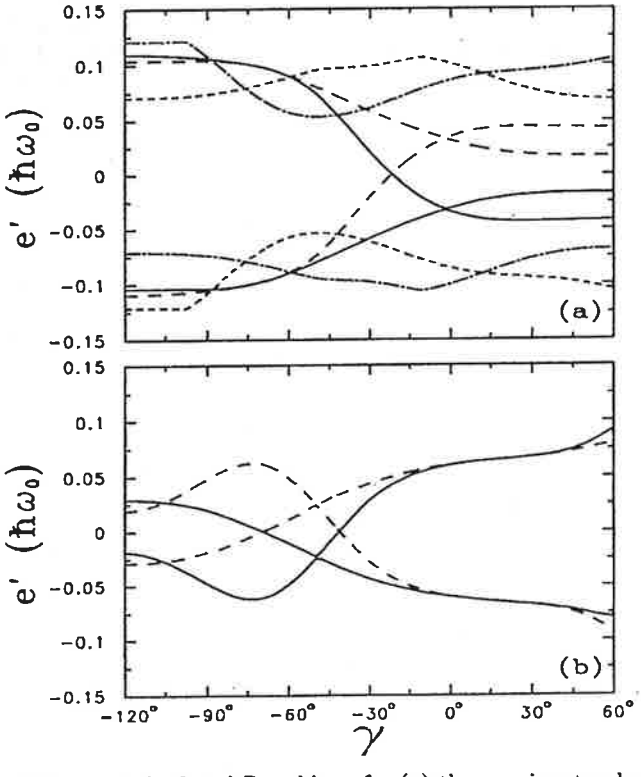

FIG. 4. Calculated Routhians for (a) the quasiproton levels at $\hbar\omega = 0.038\hbar\omega_0$, $\beta = 0.165$, $\Delta_n = 0.16\hbar\omega_0$, $\Delta_p = 0.14\hbar\omega_0$. The solid and dashed lines are for $\pi h_{11/2}$ favored ($\alpha = -\frac{1}{2}$) and unfavored ($\alpha = +\frac{1}{2}$) components, respectively. The dash-dotted and dotted lines represent the $\pi[413]\frac{5}{2}$ levels. (b) The same as (a) for the first $h_{11/2}$ quasineutron.

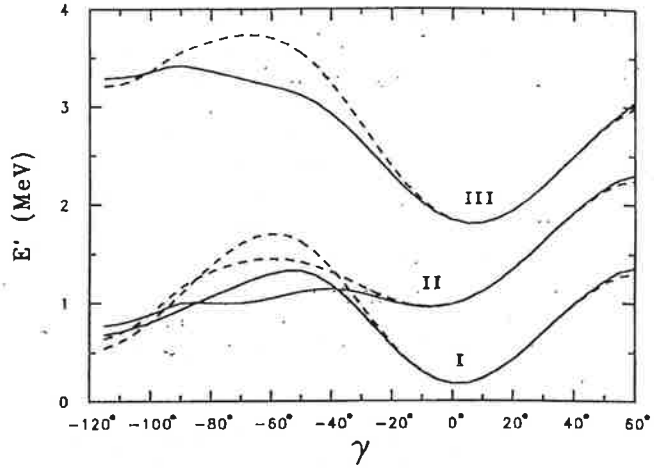

FIG. 5. The total Routhians as a function of the gamma deformation. The dashed line is for the signature $\alpha = 0$ and the solid line for the signature $\alpha = -1$. I, the $\pi h_{11/2} \otimes \nu h_{11/2}$ configuration at $\hbar\omega = 0.03\hbar\omega_0$; II, the $\pi[413]\frac{5}{2} \otimes \nu h_{11/2}$ two-quasiparticle configuration at $\hbar\omega = 0.03\hbar\omega_0$; and III, the $\pi[413]\frac{5}{2} \otimes \pi h^2_{11/2} \otimes \nu h_{11/2}$ four-quasiparticle configuration at $\hbar\omega = 0.038\hbar\omega_0$.

The total Routhian (E'_{tot}), Fig. 5, was calculated using the method of Frauendorf and May [12], in which a phenomenological contribution from the core is added to the quasiparticle Routhians.

IV. DISCUSSION

The experimental alignment i_x and the Routhian e' were extracted from the data, using the procedure described in Refs. [13, 2]. The Harris parameters $\mathcal{J}_0$ and $\mathcal{J}_1$ are obtained from the least squares fit of the angular momentum alignment to the experimental data in the frequency range below the first crossing.

A. The $\pi h_{11/2} \otimes \nu h_{11/2}$ bands

In the neighboring odd-neutron nucleus ^{133}Ce, the observed yrast band with a bandhead spin of $9/2^-$ [14] is built on a $h_{11/2}$ neutron strongly coupled to the core ($\Omega_n = 9/2$), while the yrast bands in the odd-proton nuclei, ^{133}La [15] and ^{135}Pr [16], with bandhead spins of $11/2^-$ are due to a decoupled $h_{11/2}$ proton ($\Omega_p = 1/2$). This suggests a $\pi h_{11/2} \otimes \nu h_{11/2}$ configuration for the yrast band in ^{134}La and ^{136}Pr. The assignment of (8^+) to the spin and parity of the bandheads is based on a perpendicular coupling between neutron and proton as discussed by Kreiner [17]. The observed bandheads, $I = (8^+)$, belong to the unfavored component of the band, which for the above configuration corresponds to the signature $\alpha = 0$ [$I = \alpha$ mod(2)]. We point out here that Dragulescu *et al.* [6] explain the structure of the odd-odd Pr nuclei as

due to the $2d_{3/2}$, $3s_{1/2}$, and $1h_{11/2}$ neutron coupled to the $2d_{5/2}$, $1g_{7/2}$, and $1h_{11/2}$ proton. In particular they assign for the $\Delta J = 1$ bands seen in ^{136}Pr a $[\pi d_{5/2} \otimes \nu h_{11/2}^{-1}]$ configuration, giving rise to a negative-parity band. Unfortunately the section which refers to the ^{136}Pr nucleus in their article is very sketchy.

In this mass region the Fermi level for the neutron is around $\Omega_n = 9/2$, while that for the proton is around $\Omega_p = 1/2$ or $3/2$ of the $h_{11/2}$ shell. However, cranking shell model calculations predict that $\Omega_p = 1/2$ is by far the nearest to the Fermi level, resulting in $K = \Omega_p + \Omega_n = 5$ according to the Gallagher-Moszkowski rule [18]. The assignment of the angular momentum projection $< K >$ is usually corroborated by comparing the experimental $B(M1)/B(E2)$ values with the predictions of the semiclassical formalism of Dönau and Frauendorf [19]. The experimental $B(M1)/B(E2)$ ratios are obtained from the measured $M1/E2$ branching ratios as

$$\frac{B(M1; I \rightarrow I-1)}{B(E2; I \rightarrow I-2)} = 0.693 \frac{E_\gamma^5(E2)}{E_\gamma^3(M1)} \frac{I_\gamma(M1)}{I_\gamma(E2)}, \qquad (2)$$

where the $E2/M1$ mixing ratio δ for the dipole transition is assumed negligible. A reasonable agreement between the experimental and calculated $B(M1)/B(E2)$ ratios is obtained using $< K >= 5$ for both ^{134}La and ^{136}Pr. The calculated alignments and Routhians are shown in Figs. 6 and 7.

The fitting of the three parameter function

$$I_x(\omega) = i_x + \omega \mathcal{J}_o + \omega^3 \mathcal{J}_1, \qquad (3)$$

to the experimental values of I_x led to very small values of $\mathcal{J}_o$ with uncertainties greater than the value itself for both ^{134}La and ^{136}Pr. In fact, the inclusion of this parameter did not improve the quality of the fit. Thus we simply assumed $\mathcal{J}_o = 0$. The values of $\mathcal{J}_1$ and i_x from the

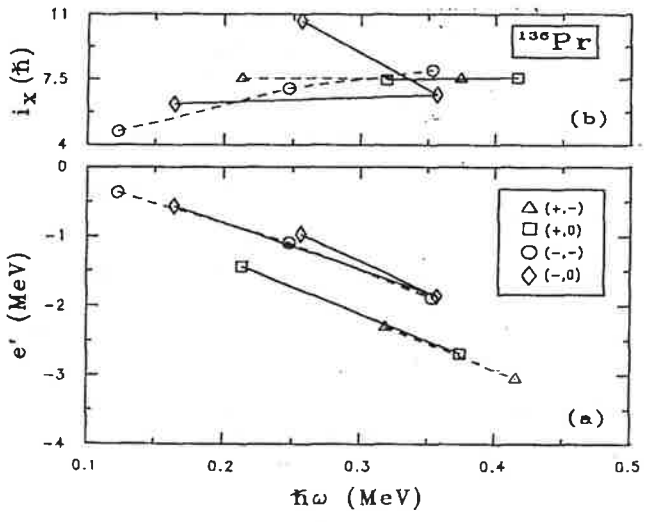

FIG. 6. (a) The experimental alignments and (b) Routhians for the $\pi h_{11/2} \otimes \nu h_{11/2}$ and $\pi[413]\frac{5}{2} \otimes \nu h_{11/2}$ bands in ^{136}Pr. The dashed and solid lines are the favored ($\alpha = -1$) and unfavored ($\alpha = 0$) components of the band, respectively. The Harris parameters used were $\mathcal{J}_0 = 0.0\hbar^2$ MeV^{-1} and $\mathcal{J}_1 = 64.4\hbar^4$ MeV^{-3}.

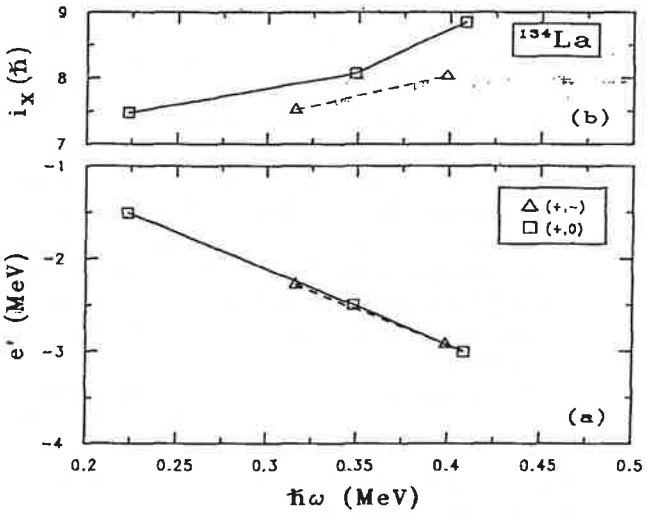

FIG. 7. (a) The experimental alignments and (b) Routhians for the $\pi h_{11/2} \otimes \nu h_{11/2}$ band in ^{134}La. The same Harris parameters were used as in Fig. 6.

fitting of the remaining two parameter curve were very similar for both nuclei: $\mathcal{J}_1 = 65.9\hbar^{-4}$ MeV^{-3}, $i_x = 7.35\hbar$ for ^{134}La and $\mathcal{J}_1 = 54.6\hbar^{-4}$ MeV^{-3}, $i_x = 7.50\hbar$ for ^{136}Pr. In both nuclei, the alignment i_x is constant up to a frequency of 0.4 MeV, as would be expected for the $\pi h_{11/2} \otimes \nu h_{11/2}$ band since the first neutron and proton orbitals are blocked. A moderate signature splitting is extracted from the data, 40 keV for ^{136}Pr and about 50 keV for ^{134}La. The observed signature splitting is found to correspond to the splitting of the two neutron signatures at $\gamma = -15°$ to $-25°$, Fig. 4, depending on the rotational frequency, for both ^{134}La and ^{136}Pr. The bands based on the unfavored signature of the proton are not seen since they lie high above the yrast line due to the large splitting. The results of the total Routhian calculations for these bands show minima at $\gamma \sim 0°$, where the calculated splitting is about 2 to 5 keV, much smaller than the experimental values. A similar situation was also reported in the articles about ^{132}La [2] and ^{138}Pm [1].

B. The $\pi[413]\frac{5}{2} \otimes \nu h_{11/2}$ band

In ^{136}Pr a second, near yrast band, was observed. Another Nilsson orbital for protons near the Fermi energy in this region is the $[413]\frac{5}{2}$. A possible configuration for this band is the $\pi[413]\frac{5}{2} \otimes \nu h_{11/2}$ with bandhead values of $K = 2$ or 7. The value of $< K >= 2$, although favored by the Gallagher-Moszkowski rule, is unlikely as it would not result in a near yrast configuration. A low K value could not explain the extremely weak $E2$ crossover transitions in this band. Thus a value $< K >= 7$ was used in the calculations. Using the same reference configuration parameters of the yrast band, the experimental alignment and Routhians were obtained. The curve of i_x as a function of ω (Fig. 6) indicates the beginning of a backbend. The experimental crossing frequency ω_c can

be extracted from the mean value of the frequencies at which i_x starts to bend backward and again forward. Unfortunately, our observational limit is below the forward bend due to the relatively low angular momentum of the compound system. Thus we can only state an upper limit of 0.31 MeV for the crossing frequency which is close to the calculated value of 0.3 MeV for the crossing of the $h_{11/2}$ proton orbital, indicating that the $\pi h_{11/2}$ orbital is not blocked in contrast to the situation in the yrast band. In this context we point out that the band assigned to the $\pi[413]\frac{5}{2}^+$ configuration in ^{135}Pr [16] exhibits nearly collective prolate shape, with the first backbend occurring at 0.32 MeV.

The experimental signature splitting could not be determined precisely (see Fig. 7) but it is certainly not large. Total Routhian calculations performed with the V_{po} parameter [12] of -1 MeV for the $\pi[413]\frac{5}{2} \otimes \nu h_{11/2}$ configuration show two competing equilibrium deformations, one at $\gamma \sim -70°$ and another near $\gamma = 0°$. However an oblate shape ($\gamma \sim -70°$) is unlikely as it would mean decoupling of the neutron implying strong $E2$ transitions, not observed experimentally.

We note here that Beausang *et al.* [1] have assigned the $\pi[413]\frac{5}{2}^+ \otimes \nu h_{11/2}$ configuration to a band in ^{138}Pm, which backbends at a rotational frequency of $\hbar\omega = 0.37$ MeV. At low frequencies this band consists of two sequences of stretched $E2$ transitions of opposite signature, in complete contrast with the second band seen in ^{136}Pr in the present work (strong $M1$ and very weak $E2$ transitions). The calculated total Routhians in ^{138}Pm [1] lead to equilibrium shape for this configuration at $\gamma \sim -65°$, i.e., collective oblate rotation. According to these authors a value of $\gamma \sim -40°$ is required in order to reproduce the observed crossing frequency of $\hbar\omega_c \sim 0.37$ MeV in the $\pi[413]\frac{5}{2} \otimes \nu h_{11/2}$ band. Above the crossing frequency the calculations of the total Routhians for both ^{136}Pr and ^{138}Pm show minima much closer to $\gamma \sim 0°$. Thus the behavior of the $\pi[413]\frac{5}{2} \otimes \nu h_{11/2}$ band in ^{136}Pr on the one hand, and ^{138}Pm on the other hand, seems to indicate that the addition of two protons at a neutron number of N=77 leads to a tendency towards oblate deformations.

V. CONCLUSIONS

The isotones ^{134}La and ^{136}Pr were investigated via (HI,xn) reactions. The yrast bands were assigned the $\pi h_{11/2} \otimes \nu h_{11/2}$ configuration. Cranking shell model calculations predict equilibrium deformations at $\gamma \sim 0°$ with signature splitting much smaller than the experimental values. In ^{136}Pr a second band was observed, showing the beginning of a backbend. The $\pi[413]\frac{5}{2} \otimes \nu h_{11/2}$ configuration was assigned to this band. The experimental crossing frequency of $\hbar\omega_c \leq 0.31$ MeV is well reproduced by the calculations for a prolate ($\gamma \sim 0°$) shape.

This work was partially supported by the Fundação de Amparo à Pesquisa do Estado de São Paulo and by the Conselho Nacional de Desenvolvimento Científico e Tecnológico.

[1] C.W. Beausang, P.K. Weng, R. Ma, E.S. Paul, W.F. Piel, Jr., N. Xu, and D.B. Fossan, Phys. Rev. C **42**, 541 (1990).
[2] J.R.B. Oliveira, L.G.R. Emediato, M.A. Rizzutto, R.V. Ribas, W.A. Seale, M.N. Rao, N.H. Medina, S. Botelho, and E.W. Cybulska, Phys. Rev. C **39**, 2250 (1989).
[3] C.W. Beausang, L. Hildingsson, E.S. Paul, W.F. Piel, N. Xu, and D.B. Fossan, Phys. Rev. C **36**, 1810 (1987).
[4] M.J. Godfrey, Y. He, I. Jenkins, A. Kirwan, P.J. Nolan, D.J. Thornley, S.M. Mullins, R. Wadsworth, and R.A. Wyss, J. Phys. G **15**, 671 (1989).
[5] E. Browne, J.M. Dairiki, and R.E. Doebler, in *Table of Isotopes*, edited by C.M. Lederer and V.S. Shirley (Wiley, New York, 1978).
[6] E. Drágulescu, M. Ivascu, M. Ionescu-Bujor, A. Iordáchescu, C. Petrache, D. Popescu, G. Semenescu, M. Duma, I. Gurgu, S. Baciu R.A. Meyer, V. Paar, S. Brant, D. Vorkapic, D. Vretenar, and H. Ajazaj, Rev. Roum. Phys. **32**, 486 (1987); **32**, 947 (1987).
[7] T. Morek, H. Beuscher, B. Bochev, T. Kutsarova, R.M. Lieder, M. Müller-Veggian, and A. Neskakis, Nucl. Phys. **A433**, 159 (1985).
[8] G. Palameta and J.C. Waddington, Nucl. Instrum. Methods A **234**, 476 (1985).
[9] G.A. Leander, S. Frauendorf, and F.R. May, in *Proceedings of the Conference on High Angular Momentum Properties of Nuclei, Oak Ridge, 1982*, edited by N.R. Johnson (Harwood Academic, New York, 1983), p. 281.
[10] G. Andersson, S.E. Larsson, G. Leander, P. Moller, S.G. Nilsson, I. Ragnarsson, S. Aberg, R. Bengtsson, J. Dudek, B. Nerlo-Pomorska, K. Pomorski, and Z. Szymanski, Nucl. Phys. **A268**, 205 (1976).
[11] J. Meyer-Ter-Vehn, Nucl. Phys. **A249**, 111 (1975).
[12] S. Frauendorf and F.R. May, Phys. Lett. **125B**, 245 (1983).
[13] R. Bengtsson and S. Frauendorf, Nucl. Phys. **A327**, 139 (1979).
[14] R. Ma, E.S. Paul, C.W. Beausang, S. Shi, N. Xu, and D.B. Fossan, Phys. Rev. C **36**, 2322 (1987).
[15] T. Morek, H. Beuscher, B. Bochev, D.R. Haenni, T. Kutsarova, R.M. Lieder, M. Mullet, and A. Neskakis, Nucl. Phys. **A391**, 269 (1082).
[16] T.M. Semkov, D.G. Sarantites, K. Honkanen, V. Abenante, L.A. Adler, C. Baktash, N.R. Johnson, I.Y. Lee, M. Oshima, Y. Schutz, Y.S. Chen, J.X. Saladin, C.Y. Chen, O. Dietzsch, A.J. Larabee, L.L. Riedinger, and H.C. Griffin, Phys. Rev. C **34**, 523 (1986).
[17] A.J. Kreiner and M.A.J. Mariscotti, J. Phys. G **6**, L13 (1980).
[18] C.J. Gallagher, Jr. and S.A. Moszkowski, Phys. Rev. **111**, 1282 (1958).
[19] F. Dönau and S. Frauendorf, in [9], p. 143. F. Dönau and S. Frauendorf, in [9], p. 143.

The $\pi h_{11/2} \otimes \nu h_{11/2}$ yrast band in odd-odd ^{140}Tb

M. A. Rizzutto
Departamento de Ciências Exatas e Tecnológicas, Faculdades Integradas de Guarulhos, Guarulhos, SP, Brazil

M. N. Rao, W. A. Seale, J. R. B. Oliveira, E. W. Cybulska, N. H. Medina, and R. V. Ribas
Instituto de Física, Universidade de São Paulo, São Paulo, SP, Brazil

F. R. Espinoza-Quiñones
Centro de Engenharia e Ciências Exatas, Universidade Estadual do Oeste do Paraná UNIOESTE, Toledo, PR, Brazil

D. Bazzacco, F. Brandolini, S. Lunardi, C. M. Petrache, Zs. Podolyák, C. Rossi-Alvarez, and C. A. Ur
Dipartimento di Fisica dell'Università and INFN, Sezione di Padova, Padova, Italy

G. de Angelis, D. R. Napoli, P. Spolaore, A. Gadea, D. De Acuña, M. De Poli, E. Farnea, D. Foltescu, M. Ionescu-Bujor,* and A. Iordachescu*
INFN, Laboratori Nazionali di Legnaro, Legnaro, Italy

A. Chatterjee and A. Saxena
Bhabha Atomic Research Center, Bombay, India

L. Sajo Bohus
Instituto de Fisica, Universidad Simon Bolivar, Caracas, Venezuela
(Received 13 April 2000; published 20 July 2000)

The $\pi h_{11/2} \otimes \nu h_{11/2}$ yrast band in the odd-odd nucleus ^{140}Tb has been populated by the ^{92}Mo (^{54}Fe, αpn) reaction at 240-MeV incident beam energy. No previous spectroscopic information was known in this nucleus. The present data fit nicely in the systematics of the $N=75$ isotones of La, Pr, Pm, Eu, and Tb ($Z=57$ to 65).

PACS number(s): 21.10.Re, 23.20.En, 23.20.Lv, 27.60.+j

In order to investigate neutron-deficient nuclei in the $A \approx 140$ mass region we have carried out a study of the ^{54}Fe + ^{92}Mo reaction at 240-MeV incident beam energy. The incident beam was obtained with the XTU tandem accelerator of the Legnaro National Laboratory, Legnaro, Italy. The multidetector array GASP [1], consisting of 40 high-efficiency Compton-suppressed HpGe detectors and the 80-element BGO multiplicity filter, was used for obtaining gamma-ray double and triple coincidence spectra. The 40-telescope Si ball (ISIS) [2] permitted information on the type and multiplicity of the charged particles emitted, while the recoil mass spectrograph [3] allowed mass identification. The target used was an ≈ 1 mg/cm^2 thick ^{92}Mo foil.

Due to the fact that the efficiency of charged particle detection of the ISIS ancillary detector is not 100%, the observed charged particle (type and multiplicity) gated spectra contain transitions from different channels. For example, events from $\alpha 2p$ (^{140}Gd), $\alpha 3p$ (^{139}Eu), $2\alpha p$ (^{137}Eu), and the $2\alpha 2p$ (^{136}Sm) channels will appear in αp (^{141}Tb) spectra, due to the escape from detection in the charged particle array of one or more protons and alpha particles. The αpn events will also appear in the αp spectra, as there was no neutron detection. Thus, one can represent each multiplicity gated γ-γ matrix as a weighted superposition of several individual channels, each with a weight proportional to the intensities of gamma rays representing the particular channel. This leads to a set of linear equations which may be solved to obtain linear combinations of the various spectra which then consist of transitions belonging only to the given channel of interest. We have used this technique to generate "cleaned" spectra consisting of transitions from each individual reaction channel corresponding to the various charged particle multiplicities.

To illustrate the resulting "cleaned" spectra in the present case, we show in Fig. 1(a) the αp-gated γ-γ total projected spectrum, obtained from the charged-particle (type and multiplicity)-γ-γ cube. The gamma-ray peaks corresponding to ^{140}Gd ($\alpha 2p$), ^{139}Eu ($\alpha 3p$), ^{137}Eu ($2\alpha p$), and ^{136}Sm ($2\alpha 2p$) channels can also be seen in this spectrum, in addition to the transitions in ^{141}Tb and ^{140}Tb nuclei produced in the αp and αpn channels. The ($\alpha 2p$) channel is the strongest of these four channels, while the other three are populated much more weakly. In Fig. 1(b) the contributions of the peaks from channels other than αp and αpn have been clearly suppressed by the procedure described above. For example, in Fig. 1(b) the strongest lines corresponding to γ ray transitions from the yrast band of ^{140}Gd ($\alpha 2p$ channel) have disappeared, while those belonging to ^{141,140}Tb (αp and αpn channels) are enhanced.

Of the various nuclei ($Z=63$ to 66; $N=75$ to 78) produced in this experiment, the $3p$ channel leading to ^{143}Tb

*Permanent address: Institute of Physics and Nuclear Engineering, Bucharest, Romania.

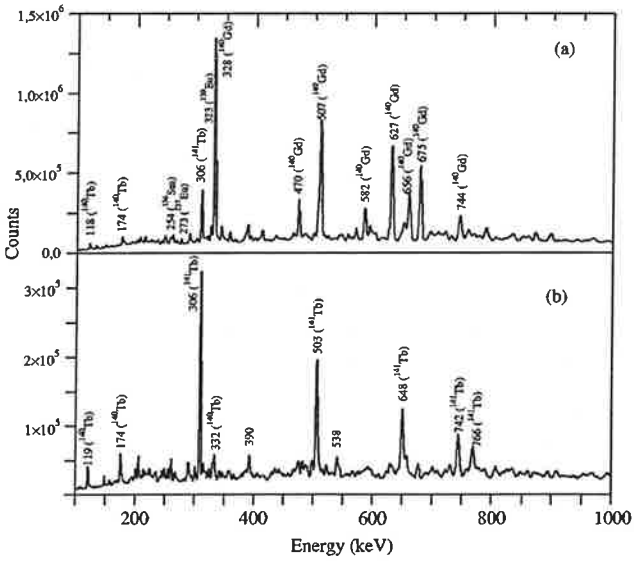

FIG. 1. (a) αp-gated γ-γ total projected spectrum. (b) "Cleaned" αp and αpn spectra from which the contributions of $x\alpha yp$ $(x,y \geq 2)$ channels have been removed.

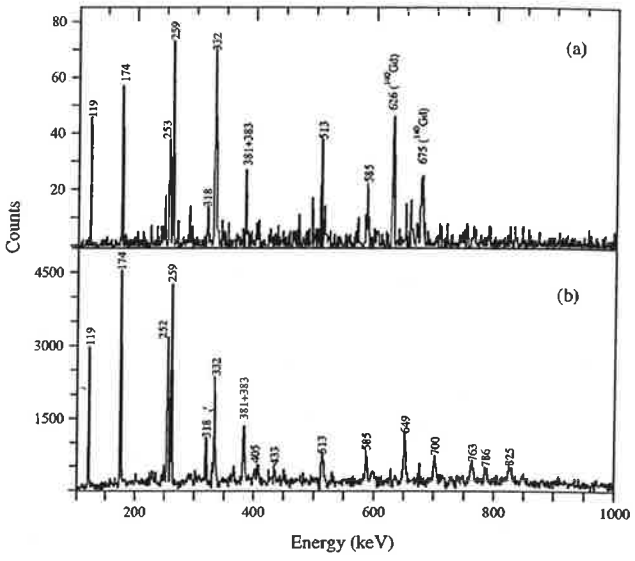

FIG. 2. (a) Sum of gates on several transitions assigned to ^{140}Tb starting with $(A=140)$-γ-γ cube. (b) Sum of gates on several transitions assigned to ^{140}Tb starting with the "cleaned" charged-particle (type and multiplicity)-γ-γ cube.

was the strongest one populated at the incident energy used and the results on the high-spin structures populated in ^{143}Tb were described in [4], where a more detailed description of the experiment and the analysis of data may be found. We report here the results on the αpn channel leading to the odd-odd nucleus ^{140}Tb. No data on high-spin states were known in ^{140}Tb previous to this work. In spite of the fact that the production cross section for this nucleus was about one tenth that of ^{143}Tb and about a third of the αp channel leading to ^{141}Tb, it was possible to unambiguously assign gamma transitions to ^{140}Tb nucleus by ruling out the possibility of these transitions belonging to ^{141}Tb, based on the mass-gated spectra. In Fig. 2(a) we present the spectrum of gamma rays, obtained as a sum of gates on several gamma transitions assigned to ^{140}Tb from an analysis of the mass-gated matrices. The spectrum in Fig. 2(b) was generated in a similar manner, except for the fact that we started with the "cleaned" charged-particle (type and multiplicity)-γ-γ cube, instead of the A-γ-γ cube, in order to obtain better statistics.

The level scheme of ^{140}Tb obtained from the present work is shown in Fig. 3, while Fig. 4 presents the $[\pi h_{11/2} \otimes \nu h_{11/2}]$ band in ^{140}Tb $(Z=65)$ compared with the corresponding bands in the odd-odd nuclei with $Z=57-63$, ^{132}La [5], ^{134}Pr [6–8], ^{136}Pm [6], and ^{138}Eu [9]. One can see the smooth behavior of the excitation energies among the 5 isotones above the level with a spin and parity assignment of (8^+). This smooth trend would continue down one more level, fed by the 118-keV γ ray in ^{140}Tb which could then be the assigned (7^+) spin and parity, based on the DCO ratio of the 118-keV transition [1.13 (20), see Table I]. This assignment would then be consistent with the smooth systematics of all the previous level schemes and spin assignments for the $[\pi h_{11/2} \otimes \nu h_{11/2}]$ bands in the $N=75$ doubly odd isotones. The only exception to this behavior would then be the level scheme of ^{134}Pr according to [8], where there is a cascade of two gamma rays viz., 306.5- and 94.3-keV deexciting the (8^+) level, instead of just a single γ ray of $M1$ multipolarity. No $(9^+ \rightarrow 7^+)$ transition has been observed in the $[\pi h_{11/2} \otimes \nu h_{11/2}]$ bands in any of these nuclei, except in the case of ^{134}Pr [8], where it was observed as a very weak 477.2-keV transition ($<0.5\%$) and with only a tentative placement in the level scheme. In addition there is disagreement in the placement of the 306.5-keV gamma ray between [6] and [8]. We also mention here that recently Liu *et al.* [10] have published a systematic study of spin assignments of low-lying levels in doubly odd nuclei around $A \approx 130$. The

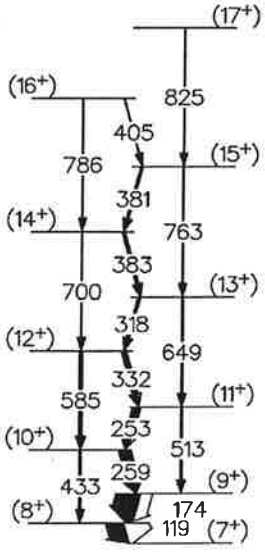

FIG. 3. The level scheme of ^{140}Tb obtained from the present work.

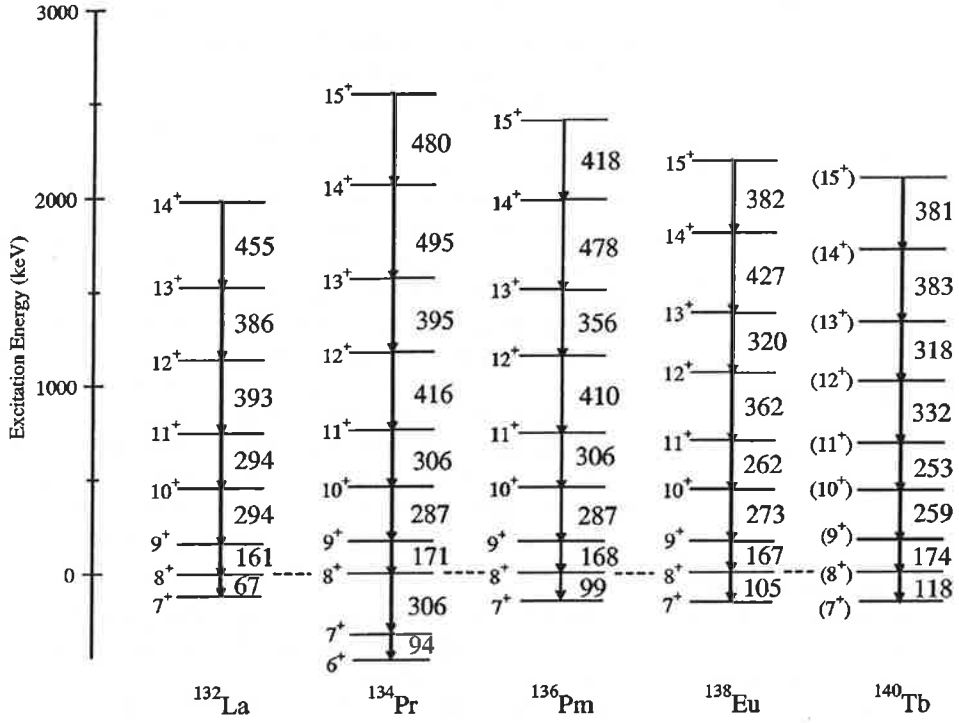

FIG. 4. The $[\pi h_{11/2} \otimes \nu h_{11/2}]$ bands in the odd-odd $N=75$ isotonic chain with $Z=57$–65.

authors base their conclusions on the argument that the excitation energy of the levels in the $[\pi h_{11/2} \otimes \nu h_{11/2}]$ bands, with the same assigned spin, in a chain of deformed doubly odd isotones (isotopes) varies with the proton (neutron) number in a smooth way, and a deviation from this smooth trend may imply a questionable spin assignment. They then go on to consider that the correct spin assignment is that which removes the deviation from the smooth trend. In the mass region of $A \approx 130$, these authors suggest that the spins of the levels of the $[\pi h_{11/2} \otimes \nu h_{11/2}]$ bands may differ by one unit from those shown in Fig. 4. Such a possibility cannot be confirmed or overruled from the present data.

The energy levels, transition energies, intensities and DCO ratios and tentative spin and parity assignments for the levels assigned to the ^{140}Tb nucleus are shown in Table I. The DCO ratios shown have been obtained with gates on dipole transitions, and as such, one would expect a value of 1.0 for a dipole and 2.0 for a quadrupole transition for the

TABLE I. Energy levels, transition energies, intensities, DCO ratios, and tentative spin and parity assignments for the levels assigned to the ^{140}Tb nucleus.

E_γ [keV]	E_i [keV]	E_f [keV]	$I_i^\pi \rightarrow I_f^\pi$	I_γ	DCO ratio
118.7	118.7	0	$(8^+) \rightarrow (7^+)$	100	1.13 (20)
173.7	292.4	118.7	$(9^+) \rightarrow (8^+)$	94	1.0 (1)
253.5	805.4	551.9	$(11^+) \rightarrow (10^+)$	27	0.94 (13)
259.5	551.9	292.4	$(10^+) \rightarrow (9^+)$	41	0.75 (8)
317.6	1454.7	1137.2	$(13^+) \rightarrow (12^+)$	10	1.03 (18)
331.8	1137.2	805.4	$(12^+) \rightarrow (11^+)$	19	0.68 (17)
380.8	2217.9	1837.1	$(15^+) \rightarrow (14^+)$	9	
382.6	1837.1	1454.7	$(14^+) \rightarrow (13^+)$	12	
405.0	2622.9	2217.9	$(16^+) \rightarrow (15^+)$	< 5	
433.2	551.9	118.7	$(10^+) \rightarrow (8^+)$	6	
513.0	805.4	292.4	$(11^+) \rightarrow (9^+)$	7	
585.3	1137.2	551.9	$(12^+) \rightarrow (10^+)$	12	1.89 (44)
649.3	1454.7	805.4	$(13^+) \rightarrow (11^+)$	5.5	
699.8	1837.1	1137.2	$(14^+) \rightarrow (12^+)$	5.1	
763.2	2217.9	1454.7	$(15^+) \rightarrow (13^+)$	5.9	
785.9	2622.9	1837.1	$(16^+) \rightarrow (14^+)$	< 5	
825.0	3042.9	2217.9	$(17^+) \rightarrow (15^+)$	< 4	

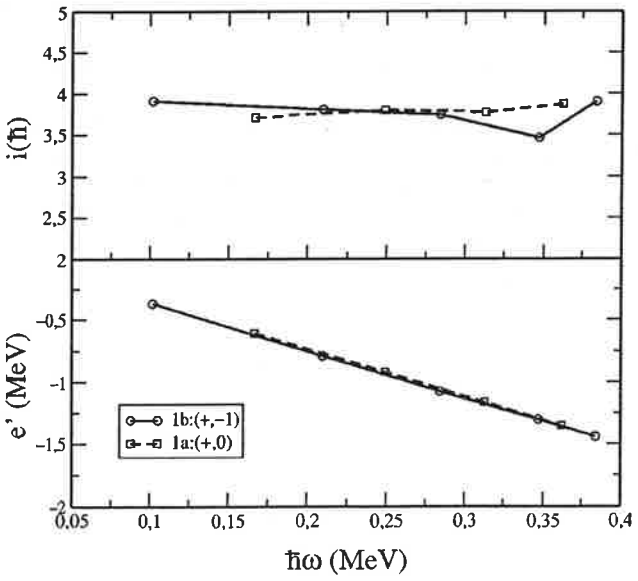

FIG. 5. The experimental alignments i_x and Routhians e' for the two signature components, viz. $\alpha = -1$ and 0 of the yrast band of ^{140}Tb.

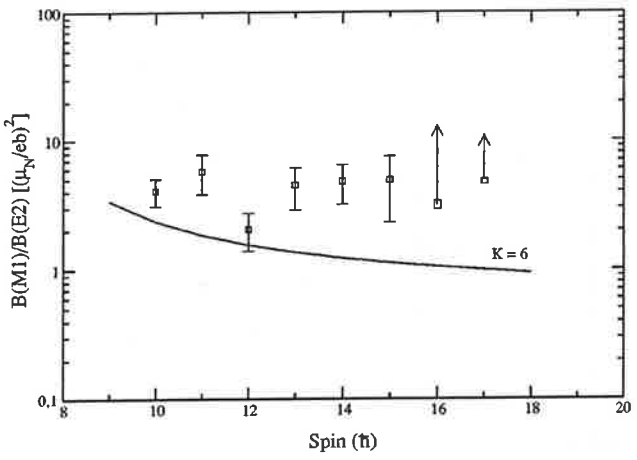

FIG. 6. The ratios of the reduced transition rates $B(M1)/B(E2)$ for the levels in the yrast band of ^{140}Tb.

GASP geometry [4]. The experimental alignments i_x and Routhians e' for the two signature components, viz., $\alpha = -1$ and 0 of the yrast band of ^{140}Tb were extracted by using a frequency-dependent reference $\mathcal{J}_{\text{ref}} = 20.0 + 67.0\omega^2$ ($\hbar^2$ MeV^{-1}), extracted from the data. These results have been presented in Fig. 5. The signature splitting is less than about 25 keV for rotational frequencies below $\hbar\omega = 0.3$ MeV, similar to that observed in the other isotones. This has been attributed to a small amount of triaxiality ($\gamma \approx -10°$ to $-15°$) in nuclei of this mass region.

From the intensities of $M1$ and $E2$ transitions in the band, the ratios of the reduced transition rates $B(M1)/B(E2)$ have been obtained, assuming that the $E2/M1$ mixing ratio δ for the $\Delta I = 1$ transitions is zero. It is found (Fig. 6) that the ratios of the reduced transition rates are about 4.0 $\pm 1.5(\mu_N/e\ \text{b})^2$. Similar values have been found for the other nuclei in the isotonic chain [6,9]. Also shown in Fig. 6 is the theoretical estimate of these ratios, obtained using the geometrical model [11], for the $\pi h_{11/2} \otimes \nu h_{11/2}$ configuration for $K = 6$ (corresponding to $\omega_n = 9/2$; $\omega_p = 3/2$). A value of $K = 7$ ($\omega_p = 5/2$) leads to very similar results.

In summary, the yrast band has been located in the doubly-odd ^{140}Tb for the first time. Its structure is very similar to corresponding bands in lighter doubly-odd isotones with two high-j quasiparticles, pointing to the stabilizing effect of these quasiparticles on the γ-soft cores.

We thank G. Manente for the preparation of the targets, and the staff of the XTU-Tandem of LNL for the smooth operation of the accelerator. This work was partially supported by the Fundação de Amparo à Pesquisa do Estado de São Paulo (FAPESP) and the Conselho Nacional de Desenvolvimento Científico e Tecnológico (CNPq), Brazil.

[1] D. Bazzacco, in Proceedings of the International Conference on Nuclear Structure at High Angular Momentum, Ottawa, 1992, Report No. AECL 10613, Vol. 2, p. 376.

[2] E. Farnea *et al.*, Nucl. Instrum. Methods Phys. Res. A **400**, 87 (1998).

[3] P. Spolaore, J. D. Larson, C. Signorini, S. Beghini, Z. Xi-Kai, and S. Hou-Zhi, Nucl. Instrum. Methods Phys. Res. A **238**, 381 (1985).

[4] F. R. Espinoza-Quiñones *et al.* Phys. Rev. C **60**, 054304 (1999).

[5] J. R. B. Oliveira, L. G. R. Emediato, M. A. Rizzutto, R. V. Ribas, W. A. Seale, M. N. Rao, N. H. Medina, S. Botelho, and E. W. Cybulska, Phys. Rev. C **39**, 2250 (1989).

[6] C. W. Beausang, L. Hildingsson, E. S. Paul, W. F. Piel, Jr., P. K. Weng, N. Xu, and D. B. Fossan, Phys. Rev. C **36**, 1810 (1987).

[7] C. M. Petrache, G. de Angelis, D. Bucurescu, M. Ivascu, D. Bazzacco, and S. Lunardi, Z. Phys. A **344**, 227 (1992).

[8] C. M. Petrache, D. Bazzacco, S. Lunardi, C. Rossi Alvarez, G. de Angelis, M. De Poli, D. Bucurescu, C. A. Ur, P. B. Semmes, and R. Wyss, Nucl. Phys. **A597**, 106 (1996).

[9] Y. Liang, K. Ahn, R. Ma, E. S. Paul, N. Xu, and D. B. Fossan, Phys. Rev. C **38**, 2432 (1988).

[10] Y. Liu, J. Lu, Y. Ma, S. Zhou, and H. Zheng, Phys. Rev. C **54**, 719 (1996).

[11] F. Dönau and S. Frauendorf, in *Proceedings of the Conference on High Angular Momentum Properties of Nuclei*, Oak Ridge, 1982, edited by N. R. Johnson (Harwood Academic, New York, 1983), p. 143; F. Dönau, Nucl. Phys. **A471**, 469 (1987).

Lifetime measurements in ^{133}Ce

L. G. R. Emediato, M. N. Rao, N. H. Medina, W. A. Seale, S. Botelho, R. V. Ribas,
J. R. B. Oliveira, E. W. Cybulska, F. R. Espinoza-Quiñones,
V. Guimarães, M. A. Rizzutto, and J. C. Acquadro
Laboratório Pelletron, Departamento de Física Nuclear, Instituto de Física, Universidade de São Paulo, São Paulo, Brazil
(Received 23 August 1996)

Lifetimes of low-lying levels in the one- and three-quasiparticle bands in ^{133}Ce have been measured using the recoil-distance Doppler-shift technique. The $E2$ transition strengths extracted for the negative parity yrast states are well described by the triaxial-rotor-plus-quasiparticle and the geometrical models, but the interacting-boson-plus-fermion predictions are too small by about a factor of 3. The $B(M1)$ values extracted for the levels in the positive parity three-quasiparticle band are consistent with the previous $\nu h_{11/2}\otimes\pi h_{11/2}\otimes\pi g_{7/2}$ configuration assignment to this band. [S0556-2813(97)05403-4]

PACS number(s): 21.10.Tg, 23.20.−g, 25.70.Gh, 27.60.+j

The yrast and low-lying excited bands in odd neutron nuclei in the light rare earth region have been reasonably well established in literature. On the other hand, experimental data on transition probabilities are scarce, especially in the side bands known from spectroscopic data. In most cases the configurations assigned to these side bands are tentative and information on lifetimes in these bands could lead to the confirmation of these assignments.

In this work we report on lifetime measurements in ^{133}Ce with the recoil-distance Doppler-shift (RDDS) technique. Data were obtained for both the $\nu h_{11/2}$ yrast band and the positive parity side band previously assigned to the $\nu h_{11/2}\otimes\pi h_{11/2}\otimes\pi g_{7/2}$ configuration [1].

Levels in ^{133}Ce were populated by the ^{120}Sn(^{16}O,3n) reaction at an incident energy of 70 MeV. The spectra were measured using a BGO Compton suppressed HPGe detector (22% efficiency, energy resolution ≈2.1 keV) at 0° to the beam, in coincidence with at least one of six 3''×3'' NaI(Tl) detectors in a plane perpendicular to the reaction plane. The target of enriched ^{120}Sn was prepared by evaporation of enriched metallic onto a thin Au backing which faced the incident beam. The thickness of the target (≈1.0 mg/cm^2) allowed the recoiling nuclei to escape with an average velocity of $v=0.008c$. The Pb stopper was of sufficient thickness (≈20 mg/cm^2) to stop all the recoils. The measurements were performed with a plunger device constructed in our laboratory [2]. Spectra were obtained for 13 different target-stopper distances from around 20 to 250 μm. The target-stopper flight distances were measured using the capacitance technique and also with a precision micrometer. Data for spectra at different flight distances were normalized using the 279 keV gamma line from the Coulomb excitation of the Au backing. This was possible by using a separate output from the HPGe detector without the coincidence condition with one of the 6 NaI detectors. Figure 1 shows typical spectra.

In the analysis of RDDS data it is usual to fit the ratio of the intensities of the shifted and unshifted components of a gamma line as a function of the flight distance. Instead the program LIFETIME [3], adjusts the lifetimes and the initial populations of the levels to obtain the best fits to the measured unshifted and shifted intensities independently, as functions of flight distances given a model for the time distribution of the side feeding intensities. This enables extraction of lifetimes even in cases where one of the components is difficult to extract within reasonable experimental uncertainties, as it turned out to be the case in the present work. The following corrections to the data were applied: position- and velocity-dependent changes in the solid angle subtended by the detector; effect of attenuation of alignment during flight; emission of gamma rays during the slowing-down time resulting in an energy distribution between the shifted and unshifted energies. The possibility that the measured zero target-stopper distance may not be the true zero was considered by adding a term d_0 to each flight distance. This d_0 term is treated as a variable parameter in the program. The value obtained for this real zero distance was 22.5

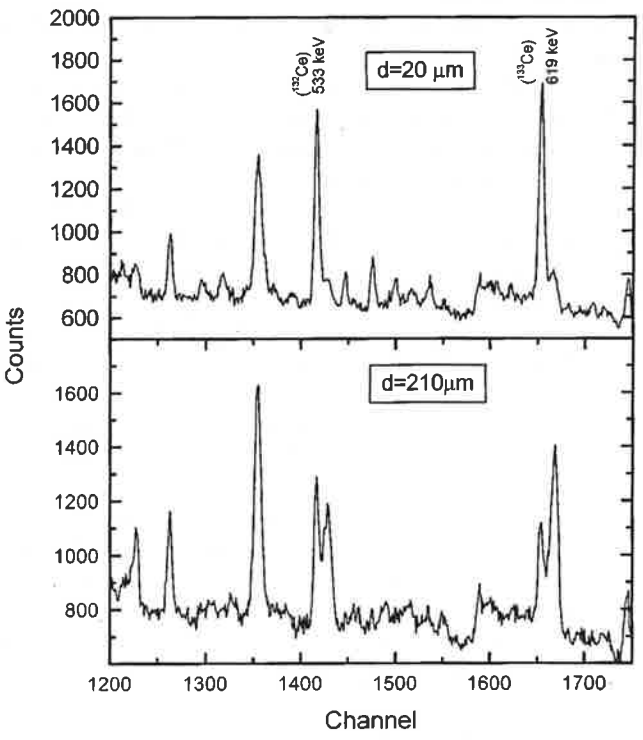

FIG. 1. Typical spectra for two target-stopper distances (20 and 210μ).

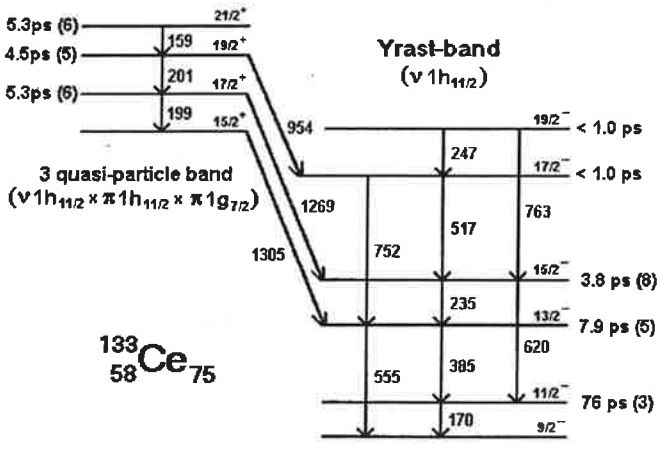

FIG. 2. Relevant portion of the level scheme of ^{133}Ce.

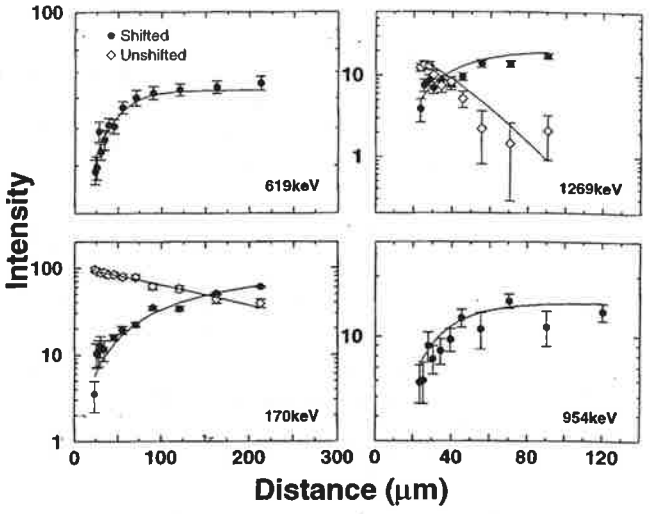

FIG. 3. Decay curves of ^{133}Ce.

± 1.0 μm. Transitions from levels with $\tau \sim 1$ ps appeared totally shifted at all distances, and this value is taken as an upper limit in such cases. In modeling the side feeding transitions, a one-step side feeding was assumed where necessary. The relative intensities of the gamma rays were taken from previous work [1], where the same reaction and incident energy were employed. A separate measurement of the spectrum with a thick target was made in order to verify that the relative intensities agreed with the previous work at least for the strong gamma lines. The side feeding intensities were obtained from these relative intensities as the difference between the total intensity feeding and depopulating a given level. No long-lived ($\tau > 1$ ps) side feeding transitions were needed in order to fit the decay and growth curves. The decay and growth curves for 14 transitions were fitted simultaneously. The total number of data points was 340 and the number of parameters (initial populations and transition probabilities) which were varied was 22. A reduced χ^2 of 2.1 was obtained for the overall best fit to all the decay curves. The uncertainties in the experimental data points (unshifted and shifted intensities) include statistical and fitting errors given by the peakfitting routine used [4]. The program LIFETIME uses the least-squares minimization routine MINUIT written by James and Roos [5] which includes the error routine MINOS. MINOS finds the true positive and negative errors (confidence intervals) of a parameter by examining the behavior of the χ^2 in the vicinity of its best value. The value of the parameter is varied in steps, both above and below its best value, and at each step, χ^2 is reminimized by varying all the remaining parameters. This process is continued until χ^2 increases by one unit.

Figure 2 shows the level scheme used to obtain the final results on the lifetimes, while samples of the resulting fits to the data are shown in Fig. 3.

At the incident energy used, the $3n$ and the $4n$ channels had about equal cross sections and thus it was possible to use the known [6,7] lifetimes in ^{132}Ce as a simultaneous check on the measurements. The results obtained for levels in the ground state band of ^{132}Ce are compared with earlier measurements in Table I.

The measured lifetimes for the levels in the yrast $\nu h_{11/2}$ band in ^{133}Ce are compared with the predictions of the triaxial rotor plus quasiparticle model (PTR) [8] in Table II.

Standard BCS parameters were used in the calculations; $\Delta = 0.92$ MeV, Fermi level $\lambda = 50.6$ MeV and $\hbar\omega_0 = 8.41$ MeV, while the VMI parameters for the even-even core were taken from the original work of Mariscotti *et al.* [9]; $\mathcal{J}_0 = 6.9$ $(\text{MeV})^{-1}$ and the stiffness constant $C = 0.0061$ $(\text{MeV})^3$ giving for the core softness $\sigma = 1/2C\mathcal{J}_0^3 = 0.25$. For the odd neutron the $N = 4$ and 5 shells were included and the κ and μ values were taken from standard tables ($N = 4$, $\kappa = 0.07$, $\mu = 0.39$; $N = 5$, $\kappa = 0.062$, $\mu = 0.43$). The deformation parameters ($\epsilon_2 = 0.165$, $\epsilon_4 = 0.019$) were taken from the systematics of potential energy surface calculations for the $N = 75$ isotones quoted in [10]. It was necessary to employ a small ($\gamma \approx -5°$) triaxiality parameter in order to reproduce reasonably well the experimental levels, but the calculated transition probabilities were insensitive to the exact γ value. We point out that the rather large signature splitting (≈ 70–100 keV) seen in the $\nu h_{11/2}$ yrast band has been taken as evidence for slightly triaxial shapes ($\gamma \approx -30°$) in nuclei of this region at low spins [1]. Also shown in Table II are the transition probabilities calculated with the geometrical model of Dönau and Frauendorf [11]. The calculations were done with the same deformation parameters as above. For the $\nu h_{11/2}[541]9/2^-$ configuration, $K = 9/2$, $g_n = -0.24$ and an alignment of $2\hbar$ were used. The collective g factor was taken to be Z/A.

While the results of both calculations are in close agreement with the measured $B(E2)$ values, the calculated $B(M1)$ values for the $13/2^-$ and the $15/2^-$ levels are about three times larger than the measured values. The experimental $B(M1)$'s were extracted assuming pure $M1$ transitions. $M1$ transitions in rotational bands in this mass region are, in

TABLE I. Lifetimes in ^{132}Ce. Values of τ are in ps.

J^π	E_γ (keV)	τ_{present}	$\tau_{\text{Ref. [4]}}$	$\tau_{\text{Ref. [5]}}$
2^+	325	59 ± 6	58 ± 9	57 ± 4
4^+	533	5.5 ± 0.6	–	5.4 ± 1.0
6^+	683	< 1	–	1.0 ± 0.5
8^+	787	< 1	1.0 ± 0.2	< 1

TABLE II. Lifetimes and reduced transition probabilities in the ^{133}Ce $\nu h_{11/2}$ yrast band: (a) triaxial-rotor-plus-quasiparticle model, and (b) geometrical model.

J_i^π	J_f^π	E_γ (keV)	τ (ps)	Expt.	Transition probabilites a	b	
$11/2^-$	$9/2^-$	170	76±3	65±2	104	27	b
$13/2^-$	$9/2^-$	555	7.9±0.5	17±3	27	27	a
	$11/2^-$	385		45±4	162	106	b
$15/2^-$	$11/2^-$	619	3.8±0.8	52±15	52	50	a
	$13/2^-$	235		56±15	209	175	b
$17/2^-$	$13/2^-$	752	≤1.0	≥65	72	68	a
	$15/2^-$	517		≥40	242	230	b
$19/2^-$	$15/2^-$	763	≤1.0	≥65	87	81	a

[a] $B(E2)$ in Weisskopf units (W.u.).
[b] $B(M1)$ in milli-Weisskopf units (mW.u.).

general, nearly pure. Furthermore, PTR calculations predict an $E2$ admixture of $<10\%$. We point out that the decay γ rays from both these levels (385 and 235 keV, respectively) have double placements in the level scheme [1]. For the 170-keV ($11/2^-$ to $9/2^-$) transition, the PTR predicts a larger and the geometrical model a smaller $B(M1)$ than the experimental value. It should be pointed out also that, in the geometrical model, the $B(M1)$ values [and the $B(E2)$ to a lesser extent] are very sensitive to K, which is indirectly related to triaxiality in a high-j single quasiparticle band. A value of $K\approx 2.5$ would result in a reasonable agreement with the experimental $B(M1)$ values, but the $B(E2)$ would be roughly a factor of 2 too large.

Reduced $E2$ transition probabilities in the yrast band of the even-odd Ce isotopes have also been calculated with the interacting-boson-plus-fermion model (IBFM) [12]. Even though the IBFM predictions reproduce the signature splittings observed in the low-energy region quite well, the calculated transition probabilities for the yrast transitions, read from Fig. 4 of [12], vary between 0.02 to 0.12 e^2 b^2 and thus are a factor of about 2–3 too low compared with the results of the present measurements. This is puzzling in the light of the fact that IBFM seems to reproduce rather well the measured $B(E2)$ values in the low-lying decoupled $\pi h_{11/2}$ yrast band in the proton odd neighbor ^{131}La [13].

The $M1$ transitions of the positive parity three-quasiparticle band, which has been previously assigned to the $\nu h_{11/2}\otimes\pi h_{11/2}\otimes\pi g_{7/2}$ configuration in [1], were relatively strong. Such an enhancement in $B(M1)$ values has been observed in the case of mixed neutron-proton configurations in other odd-N nuclei in this mass region. In addition, it was possible also to obtain experimental decay curves for the interband transitions (954 and 1269 keV) connecting the 3qp band to the levels of the yrast band. As a result, reliable lifetimes could be obtained for three of the lowest levels of the $K=15/2$ band. The lifetime of the 15/2 bandhead could not be determined as the interband 1305 keV transition was very weak. These results are presented in Table III. In contrast, the data on the $M1$ transitions in the negative parity three-quasiparticle $\nu h_{11/2}\otimes(\pi h_{11/2})^2$ band (not shown in Fig. 2) indicate that these transitions are extremely rapid ($\tau<1$ ps).

TABLE III. Lifetimes in the ^{133}Ce three-quasiparticle band.

J_i^π	J_f^π	E_γ (keV)	τ (ps)	Transition probabilities
$17/2^+$	$15/2^-$	1269	5.3±0.6	$B(E1)=23$ μW.u.
$19/2^+$	$17/2^-$	954	4.5±0.5	$B(E1)=42$ μW.u.
	$17/2^+$	201		$B(M1)=0.5$ W.u.
$21/2^+$	$19/2^+$	159	5.3±0.6	$B(M1)=1.1$ W.u.

The measured lifetimes of the $19/2^+$ and the $21/2^+$ levels of the 3qp band correspond to $B(M1)$ values of 0.5 and 1.1 W.u., respectively. The geometrical model [11] predicts a value of ≈0.5 W.u. for this configuration utilizing $K=15/2$, and the following input parameters for the $\nu h_{11/2}$, $\pi h_{11/2}$, and $\pi g_{7/2}$ quasiparticles, respectively; g factors: -0.24, 1.26, and 1.0; alignments: 2, 4, and 1$\hbar$. The last two quantities were obtained from experimental data. The triaxiality parameter was set to zero, as this band does not show any significant signature splitting.

Finally, the $B(E1)$ values extracted for the $19/2^+\rightarrow 17/2^-$ and the $17/2^+\rightarrow 15/2^-$ interband transitions are about 23 and 42 μW.u., respectively. Unfortunately data are not available in other odd-N nuclei of this mass region to compare with these $E1$ transition strengths.

To conclude, in ^{133}Ce, both triaxial-rotor-plus-quasiparticle and the geometrical models reproduce fairly well the measured reduced $E2$ transition probabilities in the $\nu h_{11/2}$ yrast band. However, the agreement between the experiment and the predictions is not good for the $B(M1)$ values. IBFM predictions for the $B(E2)$'s, on the other hand, are about 2–3 times smaller than the measured values. For the positive parity three-quasiparticle band, the experimental $B(M1)$ values are of the same order of magnitude as the geometrical model predictions.

This work was supported by Coordenação de Aperfeiçoamento de Pessoal de Nível Superior (CAPES), Conselho Nacional de Desenvolvimento Científico e Tecnológico (CNPq), and Fundação de Amparo à Pesquisa do Estado de São Paulo (FAPESP). The authors would like to thank J. C. Abreu and W. Engel for the preparation of the targets.

[1] R. Ma *et al.*, Phys. Rev. C **36**, 2322 (1987).
[2] L.G.R. Emediato, Ph.D. thesis, University of São Paulo, 1995.
[3] J.C. Wells, M.P. Fewell, and N.R. Johnson, Oak Ridge National Laboratory Report No. ORNL/TM-9105 (unpublished).
[4] W.T. Milner, ORNL VAXPAK Routines (unpublished).
[5] F. James and M. Roos, Comput. Phys. Commun. **10**, 343 (1975).
[6] A.J. Kirwan *et al.*, J. Phys. G **15**, 85 (1989).
[7] D. Husar *et al.*, Nucl. Phys. **A292**, 267 (1977).
[8] S.E. Larsson, G. Leander, and I. Ragnarsson, Nucl. Phys. **A307**, 189 (1978).
[9] M.A.J. Mariscotti, G. Scharff-Goldhaber, and B. Buck, Phys. Rev. **178**, 1864 (1969).
[10] E.S. Paul *et al.*, Phys. Rev. Lett. **61**, 42 (1988).
[11] F. Dönau and S. Frauendorf, in *Proceedings of the Conference on High Angular Momentum Properties of Nuclei*, Oak Ridge, 1982, edited by N.R. Johnson (Harwood Academic, New York, 1983), p. 143.
[12] H.C. Chiang and S.T. Hsieh, Phys. Rev. C **43**, 2445 (1991).
[13] N.V. Zamfir *et al.*, Z. Phys. A **344**, 21 (1992).

Lifetime measurements in ^{135}Pr

S. Botelho,* W. A. Seale, L. G. R. Emediato, J. R. B. Oliveira, M. N. Rao, R. V. Ribas, N. H. Medina, E. W. Cybulska, M. A. Rizzutto, and F. R. Espinoza-Quiñones
Laboratório Pelletron, Departamento de Física Nuclear, Instituto de Física, Universidade de São Paulo, São Paulo, Brazil

G. García-Bermúdez,† H. Somacal, and M. A. Cardona
Unidad de Actividad Fisica, Comisión Nacional de Energía Atômica, Buenos Aires, Argentina
(Received 20 February 1998)

Lifetimes of low-lying levels in the $\Delta I=2$ band built on the $\pi h_{11/2}$ state in the Z-odd nucleus ^{135}Pr were measured with the Doppler-shift recoil-distance technique. Reduced transition probabilities $B(E2)$ were extracted in order to calculate the deformation parameters. These values were compared to theoretical results of the total Routhian surface (TRS) calculations. While the quadrupole moments obtained for the $\pi h_{11/2}$ excited levels below the first backbend in ^{135}Pr are very similar to those of the ^{134}Ce core, TRS results predict a quadrupole moment of about 50% larger for the core. [S0556-2813(98)04311-8]

PACS number(s): 21.10.Tg, 23.20.−g, 27.60.+j

The mass region $A\simeq 130$ has been of both theoretical and experimental interest because nuclei in this region are expected to exhibit a soft behavior related to the shape asymmetry parameter γ. Various theoretical approaches can be applied to this mass region and, in general, some properties such as observed energy spacings can be reasonably well predicted by more than one model. The band structures in ^{133}Pr [1], ^{135}Pr [2], and ^{137}Pr [3] were determined in previous measurements and compared with cranked-shell model (CSM) predictions, with good agreement. They show some common features: (i) there is a negative-parity $\Delta I=2$ band built on the $\pi h_{11/2}$ orbit with strong $E2$ transitions connecting the levels; (ii) in the positive-parity rotational band based on the $\pi g_{7/2}$ Nilsson orbit, there are several $M1$ transitions in the low-spin part of the spectrum. More recently, Breitenbach *et al.* [4] have used the triaxial-rotor-plus-quasiparticle model to describe the levels in ^{133}Pr. In contrast, prior to this experiment, no lifetime measurements concerning the low-lying levels in the Pr nuclei were available in the literature. However, there are some results related to the even-even Ce isotopes. Husar *et al.* [5] measured the lifetimes in the yrast band of ^{130,132,134}Ce and observed a strong reduction of the $E2$ transition strengths with increasing neutron number. Kirwan *et al.* [6] measured the lifetimes in the yrast band of ^{132}Ce; a pronounced drop in collectivity was observed in the vicinity of the first backbend ($I=12^+$) due to the alignment of a pair of $h_{11/2}$ protons. Dewald *et al.* [7] determined the lifetimes for the $I=4^+-16^+$ states in ^{130}Ce using the coincidence plunger technique and concluded that the experimental $B(E2)$ values could be well reproduced by calculations based on the triaxial-rotor model (with $\beta_2=0.26$ and $\gamma=21°$) and the rotation-vibration model (with $\beta_2=0.25$).

In this Brief Report, lifetimes of low-lying levels below the backbend in the $\Delta I=2$ band built on the $\pi h_{11/2}$ state in ^{135}Pr [2] were measured with the Doppler-shift recoil-distance method (RDM). This method can be applied in the range of $\tau\approx 1$ ps to several hundred ps and permits the determination of model-free matrix elements for γ transitions in nuclei. The plunger apparatus employed in this experiment was described in detail by García-Bermúdez *et al.* [8]. The target-stopper separation was measured with a commercial electronic linear measurement instrument (TESATRONIC-TTA 60, supplied by TESA S. A., Switzerland) and was also continuously monitored during the runs by means of the capacitance technique of Alexander and Bell [9]. This technique also allows the measurement of the zero distance (d_0) through the extrapolation of the linear part of the curve showing the inverse of the capacitance as a function of the target-stopper distance. The value of the zero distance was obtained as (17.0 ± 0.2) μm. The quality of the target and stopper plays a critical role in RDM experiments. In principle, the shortest lifetime that is possible to measure depends on the zero distance that target and stopper can reach before touching. This distance is strictly related to the planarity of the target and stopper surfaces. The target consisted of $\simeq$1.1 mg/cm^2 of Sb evaporated onto a $\simeq$1.3 mg/cm^2 Au foil backing. The stopper was a thick, polished Pb foil of about 12 mg/cm^2, sufficient to stop both the recoil nucleus and the beam. The target was stretched according to the procedures proposed in [10].

The ^{121,123}Sb(^{16}O,4n)^{133,135}Pr reaction was performed at a beam energy of 76 MeV, supplied by the TANDAR accelerator facilities. Single γ-ray spectra were obtained with two HPGe detectors placed at 0° and 157° to the beam direction. The data analysis was performed for each detector, thus providing observation of the background region for the shifted γ-ray peaks, as well as giving two independent values for the recoil velocity. The detector at the forward angle (32% efficiency and energy resolution of 1.94 at 1333 keV) was positioned at 11.6 cm from the target, while the other detector (40% efficiency and energy resolution of 1.85 at 1333 keV) was at 15.6 cm from the target. The γ-ray spectra were ac-

*Present address: Departamento de Física, Centro das Ciências Exatas e Tecnológicas, Pontifícia Universidade Católica de São Paulo, São Paulo, Brazil.
†Also at the Carrera del Investigador Cientifico of the Consejo Nacional de Investigaciones Cientificas y Tecnologicas, Buenos Aires, Argentina.

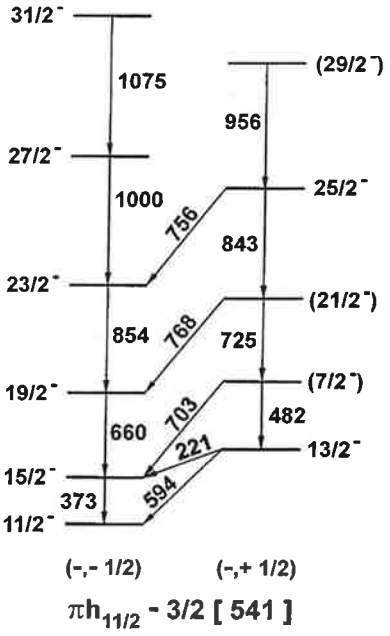

FIG. 1. Relevant portion of the rotational bands in ^{135}Pr, as proposed by Semkow *et al.* [2]. The bands are identified by (π, α) numbers. The Nilsson configurations at $\hbar\omega=0.0$ is $\pi h_{11/2}$ 3/2 [541]. The experimental lifetimes measured in this work are related to the 373, 660, and 854 keV transitions.

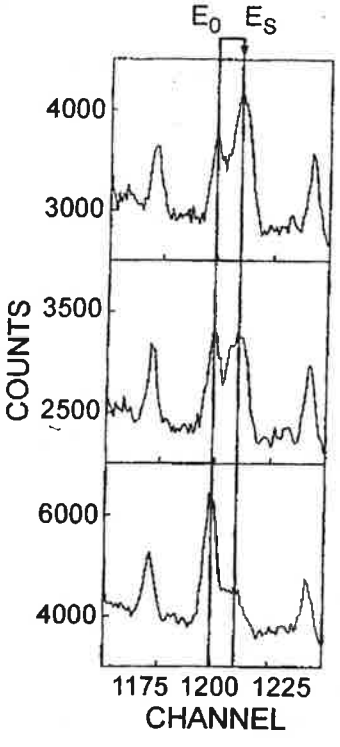

FIG. 2. Unshifted and shifted γ-ray peaks of the 373 keV transition at three target-stopper distances, respectively, from bottom to top (d=57, 247, and 797 μm).

quired for 16 target-stopper separations ranging from 17 to 797 μm, in runs of typically 3 h.

The relevant portion of the rotational band in ^{135}Pr, as proposed by Semkow *et al.* [2], is shown in Fig. 1. In the current experiment the lifetimes of the 373, 660, and 854 keV transitions, corresponding to the low-lying states of the $\pi h_{11/2}$ band, were measured for the first time. The 1000 keV γ ray is contaminated by a transition of the same energy in the ^{134}Pr nucleus, produced in a competing reaction. An illustrative spectrum, showing the intensities of the unshifted and shifted peaks at various target-to-stopper distances is presented in Fig. 2, for E_γ=373 keV.

The average recoil velocity relative to the velocity of light was determined experimentally from the separation of the shifted and unshifted peak centroids as $\beta=v/c$ =0.0096(5). In order to obtain the peak areas of the unshifted (I_0) and shifted (I_s) γ rays, it must be noted that the unshifted peaks present a width characterized by the intrinsic resolution of the detector, while the widths of the Doppler-shifted peaks are broadened due to the spread in the recoil velocities. The γ spectra for all distances were normalized using the 279.5 keV gamma line from the Coulomb excitation of the Au backing. The computer code LIFETIME [11] was used in order to correct the unshifted and shifted intensities as a function of flight distances for all of the usual perturbing effects [12] (such as changes of solid angle as a function of recoil velocity and particle-detector distance, effects of alignment attenuation, and emission of γ rays during the slowing down time resulting in an energy distribution between shifted and unshifted energies).

LIFETIME treats the initial distance d_0, the initial population of the feeding states, the transition rates of the interband, and the side-feeding transitions as variable parameters and performs a least-squares fit to the shifted and unshifted transition intensities. The side feeding was modeled by one-step transitions, and the associated parameters were included in the least-squares analysis. The relative intensities of the side feeding were given by the difference between the total intensity populating and depopulating a given level. The best fits obtained by LIFETIME are shown in Fig. 3. The measured lifetimes and $B(E2)$ values for the 373, 660, and 874 keV transitions are shown in Table I. The transition quadrupole moments in Table II have been deduced with the following equation:

$$B(E2)=\frac{5}{16\pi}Q_t^2\langle IK20|(I-2)K\rangle^2,$$

with K=3/2. The code TRS [13] was used for the purpose of obtaining relevant properties of specified configurations near the ground state by means of the energy minimization as a function of the deformation parameters β_2, β_4, and γ for each rotational frequency. This code performs calculations based on the Woods-Saxon potential, Strutinsky formalism (liquid drop with shell corrections), and self-consistent pairing. In Fig. 4, examples of total Routhian surfaces for some selected configurations of ^{135}Pr and ^{134}Ce are shown for two rotational frequencies, illustrating the equilibrium deformation below and above the backbending. For the ^{135}Pr nucleus, TRS predicts a neutron alignment between $\hbar\omega\simeq$0.35 and 0.40 MeV [Figs. 4(a) and 4(b)], while the experimental value [2] is at $\hbar\omega\simeq$0.46 MeV. The ^{135}Pr nucleus changes its deformation from $\gamma\simeq+30°$ (noncollective prolate shape) to a very large negative deformation γ $\simeq-30°$ (triaxial-collective shape). The neutron alignment (gain of $\simeq10\hbar$) in ^{134}Ce is predicted to occur between $\hbar\omega$

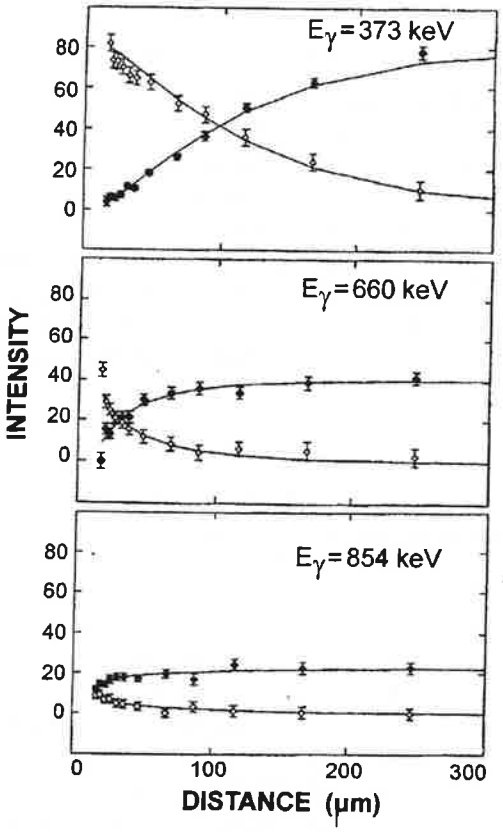

FIG. 3. Typical fits to the experimental intensities I_0 and I_s as a function of target-stopper distance. I_0 and I_s are the intensities of the unshifted and shifted components, respectively, of the 373, 660, and 854 keV transitions. Open circles denote the I_0 component while solid circles stand for I_s. The fit was performed by LIFETIME.

$\simeq 0.175$ and 0.234 MeV [Figs. 4(c) and 4(d)], while the experimental value (according to CSM calculations done based on the data of Ref. [5]) is $\hbar\omega \simeq 0.38$ MeV. The ^{134}Ce nucleus changes from $\gamma \simeq -27°$ (collective prolate) to $\gamma \simeq -85°$ (noncollective oblate) as a consequence of the neutron alignment. The most interesting feature extracted from the comparison between TRS predictions and the experimental results is related to the behavior of the quadrupole moment Q_t of the ^{135}Pr and the core ^{134}Ce. TRS predicts that the Q_t values of ^{135}Pr (2.2 e b) and those of ^{134}Ce (3.4 e b) should be very different. This is to be expected as the odd proton in ^{135}Pr polarizes the nuclear shape towards positive γ values. On the other hand, the experimental values for both nuclei are unexpectedly very similar, as can be seen in Table II. The term called Q_t^{TRS}, in Table II, was calculated from the following expression:

TABLE I. Lifetimes and reduced transition probabilities obtained in this work.

E_γ (keV)	τ_{expt} (ps)	$B(E2)_{\mathrm{expt}}$ (e^2 b^2)
373	33±2	0.33±0.02
660	3.4±0.9	0.19±0.05
854	1.33±0.07	0.134±0.007

TABLE II. Experimental values of the quadrupole moments, and those calculated by TRS for the ^{135}Pr and ^{134}Ce nuclei.

Nucleus	J^π	Q_t^{expt} (e b)	Q_t^{TRS} (e b)
^{135}Pr[a]	$15/2^-$	3.2±0.1	2.2
	$19/2^-$	2.4±0.3	
	$23/2^-$	1.98±0.05	
^{134}Ce[b]	2^+	3.3±0.2	3.4
	4^+	2.44±0.01	
	6^+	1.60±0.08	

[a]Spins and parities from Ref. [2].
[b]From Ref. [5].

$$Q_t = \frac{6ZeA^{2/3}}{(15\pi)^{1/2}} r_0^2 \beta_2 \left[1 + \frac{2}{7}\left(\frac{5}{\pi}\right)^{1/2} \beta_2\right] \cos(30° + \gamma),$$

where the β_2 and γ parameters were extracted from the TRS predictions.

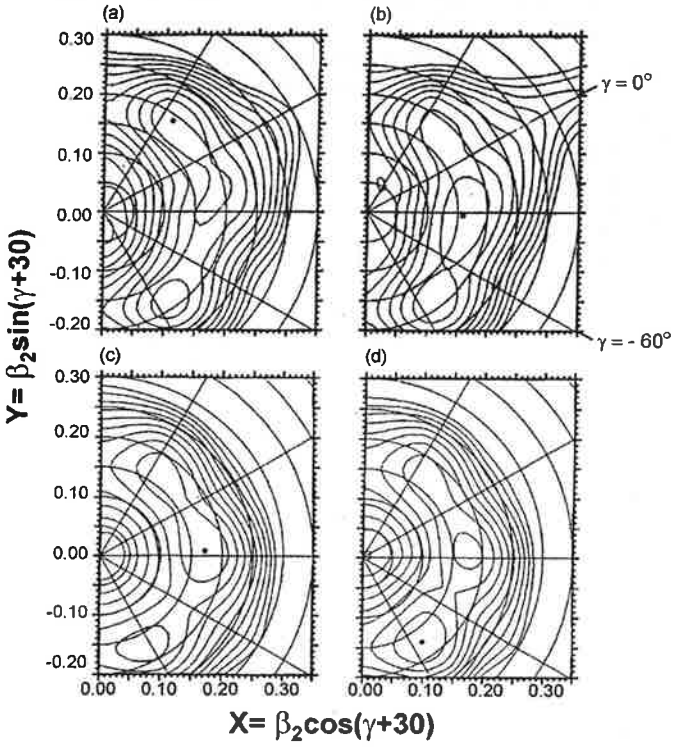

FIG. 4. Total Routhian surfaces in the (β_2, γ) plane for the ^{135}Pr (a), (b) and ^{134}Ce (c), (d) nuclei. The black dots show the location of minima. The contour lines stand for the total energy in the intrinsic frame as a function of the deformation parameter β_2 and γ. (a) $\hbar\omega = 0.350$ MeV, minimum at $\beta_2 = 0.190$, $\beta_4 = -0.018$, $\gamma \simeq 24°$; (b) $\hbar\omega = 0.408$ MeV, minimum at $\beta_2 = 0.159$, $\beta_4 = -0.019$, $\gamma \simeq -32°$. The neutron alignment for ^{135}Pr $(\nu h_{11/2})^2$ occurs between (a) and (b), driving the nucleus to a very large negative γ deformation (triaxial-collective shape); (c) $\hbar\omega = 0.175$ MeV, minimum at $\beta_2 = 0.172$, $\beta_4 = -0.017$, $\gamma \simeq -27°$; (d) $\hbar\omega = 0.234$ MeV, minimum at $\beta_2 = 0.172$, $\beta_4 = -0.009$, $\gamma \simeq -85°$. The neutron alignment ^{134}Ce $(\nu h_{11/2})^2$ occurs between (c) and (d), driving the nucleus to a very large negative γ deformation (noncollective oblate shape).

To conclude, the lifetimes of the low-lying levels (373, 660, and 854 keV) based on the $\pi h_{11/2}$ band in ^{135}Pr were measured and compared with the even-even core ^{134}Ce. Our experimental results for the quadrupole moments show that there is a decrease with frequency for the states below the backbend (Table I), very similar in magnitude and behavior to the quadrupole moments in ^{134}Ce measured by Husar *et al.* [5]. This may be due to changes in the deformation parameters (β_2, γ) because the band crossing has not occurred yet. The theoretical predictions of TRS indicate that the magnitude of Q_t should be different for ^{135}Pr and ^{134}Ce. Finally, we believe that the experimental results obtained in this work for ^{135}Pr encourage further measurements to investigate the electromagnetic transitions in the $A \simeq 130$ region.

The authors wish to thank the Fundação de Amparo à Pesquisa do Estado de São Paulo (FAPESP), Conselho Nacional de Pesquisa e Desenvolvimento (CNPq), Coordenadoria de Apoio ao Ensino Superior (CAPES), and the ICTP (Trieste) for financial support. Some of us (W.A.S., L.G.R.E., and S.B.) are grateful to the TANDAR/CNEA staff for their hospitality during our stay in Buenos Aires. We are also indebted to H. Grahmann, W. P. Engels, and J. C. Abreu for their help in manufacturing the targets.

[1] L. Hildingsson, C. W. Beausang, D. B. Fossan, and W. F. Piel, Jr., Phys. Rev. C **37**, 985 (1988).
[2] T. M. Semkow *et al.*, Phys. Rev. C **34**, 523 (1986).
[3] N. Xu, C. W. Beausang, R. Ma, E. S. Paul, W. F. Piel, Jr., and D. B. Fossan, Phys. Rev. C **39**, 1799 (1989).
[4] J. B. Breitenbach, J. L. Wood, M. Jarrio, R. A. Braga, H. K. Carter, J. Kormicki, and P. B. Semmes, Nucl. Phys. **A595**, 481 (1995).
[5] D. Husar, S. J. Mills, H. Gräf, U. Neumann, D. Pelte, and G. Seiler-Clark, Nucl. Phys. **A292**, 267 (1977).
[6] A. J. Kirwan, P. J. Bishop, D. J. G. Love, P. J. Nolan, D. J. Thornley, A. Dewald, A. Gelberg, K. Schiffer, and K. O. Zell, J. Phys. G **15**, 85 (1989).
[7] A. Dewald *et al.*, Nucl. Phys. **A545**, 822 (1992).
[8] G. García-Bermúdez, M. A. Cardona, and A. Filevich, Nucl. Instrum. Methods Phys. Res. A **292**, 367 (1990).
[9] T. K. Alexander and A. Bell, Nucl. Instrum. Methods **81**, 22 (1970).
[10] J. L. Gallant, Nucl. Instrum. Methods **81**, 27 (1970).
[11] J. C. Wells, M. P. Fewell, and N. R. Johnson, "LIFETIME: a Computer Program for Analyzing Doppler-Shift Recoil-Distance Nuclear Lifetime Data," Oak Ridge National Laboratory Report No. ORNL/TM-9105, 1985.
[12] R. J. Sturm and M. W. Guidry, Nucl. Instrum. Methods **138**, 345 (1976).
[13] R. Wyss, J. Nyberg, A. Johnson, R. Bengtsson, and W. Nazarewicz, Phys. Lett. B **215**, 211 (1988).

PHYSICAL REVIEW C VOLUME 48, NUMBER 2 AUGUST 1993

Lifetimes of the decay from superdeformed to normal deformed in ^{135}Nd

P. Willsau,[1] H. Hübel,[1] R. M. Diamond,[2] M. A. Deleplanque,[2] A. O. Macchiavelli,[2,*] J. R. Oliveira,[2,†] F. S. Stephens,[2] H. Kluge,[3] J. A. Becker,[4] E. A. Henry,[4] A. Kuhnert,[2,‡] and M. Stoyer

[1]*Institut für Strahlen- und Kernphysik, Universität Bonn, Nussallee 14-16, D-5300 Bonn, Germany*

[2]*Lawrence Berkeley Laboratory, Berkeley, California 94720*

[3]*Hahn-Meitner-Institut für Kernforschung, Glienicker Strasse 100, D-1000 Berlin, Germany*

[4]*Lawrence Livermore National Laboratory, Livermore, California 94550*

(Received 22 March 1993)

Lifetimes of low-spin members of the superdeformed band in ^{135}Nd have been determined by the Doppler-shift recoil-distance method. We find a quadrupole moment of $7.2^{+1.2}_{1.5}$ b for the 677 keV ($\frac{37}{2}$-$\frac{33}{2}$) transition in the band, confirming the large deformation previously measured by the Doppler-shift attenuation method. However, the quadrupole moment for the 620 keV transition deexciting the 3.324 MeV ($\frac{25}{2}$) state at the bottom of the band is much smaller. We conclude that the superdeformed potential-energy minimum disappears or the band drastically changes character at this point which causes the sudden depopulation.

PACS number(s): 21.10.Tg, 21.10.Re, 23.20.Js, 27.60.+j

The spectroscopy of rotational bands with very large prolate deformation—generally called superdeformed (SD) bands—has made rapid progress in recent years. A large number of such bands has been discovered in the mass 130, 150, and 190 regions. However, the investigation of the decay out of the SD potential-energy minimum has largely been unsuccessful up to now. The first case where some of the transitions linking the SD and normally deformed minima could be observed [1] was in ^{135}Nd; see partial level scheme of Fig. 1. In this nucleus, the SD band collects about 10% of the intensity flow near the bottom of the band and it was possible to find several connections to the normally deformed states, each with an intensity of about 1–2 %. In order to understand the decay mechanism of the SD bands, it is important to know the transition probabilities at the bottom of the band and, if possible, for the linking transitions. Doppler-shift attenuation method (DSAM) measurements [2] in the mass 150 region, and recoil-distance method (RDM) measurements [3] in the mass 190 region, find that the collectivity remains high in the SD band all the way down to the region where it decays out.

In a previous experiment [4] lifetimes were measured for states with spins $I \geq \frac{41}{2}$ in the SD band of ^{135}Nd using the DSAM. A constant average transition quadrupole moment of $Q_t = 7.4 \pm 1.0$ b was deduced from these data. It was also shown that the 677 keV ($\frac{37}{2}$-$\frac{33}{2}$) transition and all lower-spin transitions are emitted from fully stopped nuclei when a gold-backed target is employed. This suggests that the lifetimes (plus feeding times) at the bottom of the SD band are in the picosecond (or longer) range, requiring a RDM measurement.

In this Rapid Communication we report on a lifetime measurement of lower-spin states of the SD band in ^{135}Nd where it decays into the normally deformed states. The RDM was used to measure the lifetimes. From these data we determined transition probabilities, and for $E2$ transitions, both at the bottom of the band and for transitions in the decay out of the band, we deduced transition

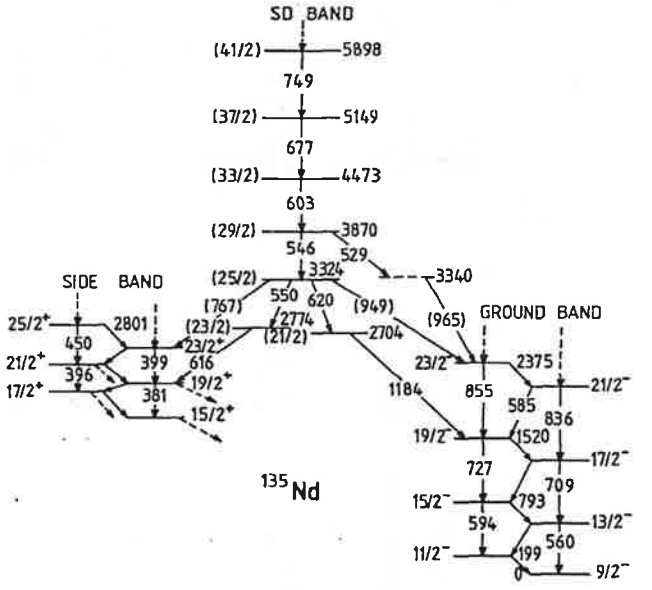

FIG. 1. Partial level scheme of ^{135}Nd showing the decay out of the SD band.

*Present address: Comision Nacional de Energia Atomica, 1429 Buenos Aires, Argentina.

†Present address: Universidade de Sao Paulo, Sao Paulo, SP, Brasil.

‡Present address: LIGO project, Caltech 102-33, Pasadena, CA 91125.

quadrupole moments. For comparison, the transition probabilities of several transitions in the normally deformed ground band were also determined. In the analysis of the previous DSAM experiment, the side-feeding intensities and a model for the side-feeding lifetimes had to be included. Furthermore, uncertainties in the stopping power enter and limit the accuracy of the results. It was, therefore, an additional aim of this experiment to obtain an independent determination of the deformation of the SD states in ^{135}Nd. Our experiment confirms the large deformation for the lower-spin members of the band. However, we find that the only observed $E2$ transition out of the 3.324 MeV state (lowest observed band member) has a considerably smaller Q_t than the in-band transitions. This implies either that the SD band terminates or that it drastically changes character at this point.

Excited states in ^{135}Nd were populated in the ^{100}Mo(^{40}Ar,$5n$) reaction at 175 MeV, the beam being provided by the 88-Inch cyclotron at the Lawrence Berkeley Laboratory. A self-supporting metallic molybdenum foil of 1 mg/cm^2 thickness, enriched in ^{100}Mo to 97%, was used as a target. Both the target and a gold-stopper foil with a thickness of 11.6 mg/cm^2 were stretched and mounted in the Bonn recoil-distance device [5]. The target-stopper distance was varied by three piezoelectric motors with a precision of ± 1 μm. The distance was monitored continuously by capacitance measurements. Gamma-ray coincidences were measured with the HERA array of 20 Compton-suppressed Ge detectors and an inner ball of 32 BGO scintillators. Approximately 115×10^6 coincidence events (at least 2 Ge and 2 BGO detector signals were required) were recorded at each of the five target-stopper distances of 10 (electrical contact), 20, 40, 76, and 146 μm. With the average recoil velocity $v/c=(2.43\pm0.05)\%$, determined from the energy separation of the shifted and unshifted peaks in the γ-ray spectra, these distances correspond to flight times of 1.37, 2.74, 5.5, 10.4, and 20.0 ps, respectively.

In the analysis, a large number of γ-γ coincidence matrices were created, each corresponding to a particular pair of angles for the Ge detectors, and a given target-stopper distance. This was done in order to keep the full energy resolution for the shifted peaks which appear at a different location in the spectra depending on the Ge angle to the beam. Therefore, the HERA detectors were separated into five groups, each corresponding to similar angles, whose average values were 37°, 51°, 90°, 123°, and 153°. With five target-stopper distances, a total of 75 matrices was created. In the sorting, multiplicity and total-energy cuts of $K>14$ and $H>1.6$ MeV, respectively, were applied. The resulting spectra contained predominantly ^{135}Nd: about 60% of the ^{134}Nd events, but only about 20% of the ^{135}Nd events were suppressed by these requirements. To obtain coincidence spectra, gates were set on several clean transitions above the states for which the lifetimes were to be determined. Therefore, side feeding into the levels of interest did not affect the analysis. Spectra with gates on different transitions, created from matrices with the same angle on the projection axis, were added to improve statistics.

Examples of the γ-ray coincidence spectra for three

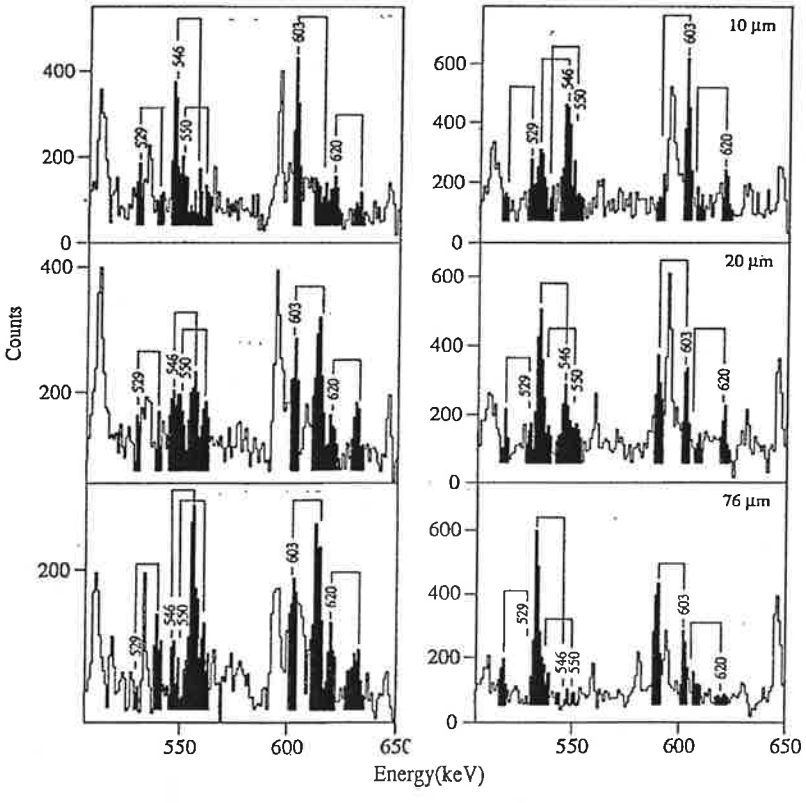

FIG. 2. Coincidence spectra over the range 500–650 keV measured in forward (left) and backward (right) detectors at three different target-stopper distances. The spectra are sums of gates at the shifted and unshifted positions of the transitions at 603 and 677 keV and the shifted positions of the transitions at 749, 817, 882, and 947 keV. Unshifted and shifted components are clearly separated. Areas in which peak intensities were fitted are shown in black.

different target-stopper distances measured at forward and backward angles are shown in Fig. 2. Peak areas were determined by a standard fitting routine taking the different widths of the shifted and unshifted components of the transitions into account. Contaminants in the spectra were identified in the following way: those at shifted positions were found by comparing spectra recorded at different Ge detector angles, those at non-shifted positions could be identified due to their different time behavior. In the cases presented in Table I, there were spectra at enough angles to disentangle the effects of the contaminants.

Theoretical lifetime curves were calculated and fitted to the experimental intensity ratios $R = I_{\text{unshift}}/(I_{\text{unshift}} + I_{\text{shift}})$ by a program supplied to us by Emling [6]. Examples are shown in Fig. 3. The transitions were treated within one fitting procedure; therefore, the ratios R had to be modified to take the different total intensities of the transitions into account. This was achieved by multiplying the ratios R of transition n by $I_{\text{total}}(n)/I_{\text{total}}(603\text{ keV})$. The in-band feeding times were calculated from the quadrupole moments measured in the previous experiment [4] using the DSAM. The lifetimes of the states with spins between $(\frac{25}{2})$ and $(\frac{37}{2})$ at the bottom of the superdeformed band and of several states in the normally deformed ground band in ^{135}Nd were obtained. The data for the SD band are summarized in Table I; those for the ground band will be given in detail in Ref. [7].

The lower part of the SD band in ^{135}Nd collects an intensity of about 10% of the total population of this nucleus. This was the first case where decay pathways to the normally deformed states were identified, and several branches were observed with intensities of the order of 1% each. The data from the previous experiment [4] in which a gold-backed target was used were reanalyzed and an additional transition of 965 keV could be tentatively placed into the level scheme (see Fig. 1). The ordering of the 529 keV and the 965 keV transitions was chosen due to the similar time behavior of the 529 keV and the 546 keV transitions observed in the RDM measurement. The intensities of the different decay pathways were carefully determined and with this information, transition probabilities were calculated for the SD and the linking transitions. For the $E2$ transitions, transition quadrupole moments can then be derived using the rotational model formula. These quantities are included in Table I. In addition, the quadrupole moments are displayed graphically in Fig. 4, where they are compared to the average Q_t value determined from the previous DSAM experiment [4] for the higher-spin transitions in the band. The lifetime of the 749 keV $(\frac{41}{2}\text{-}\frac{37}{2})$ transition in the SD band could not be determined in our experiment because it is already fully Doppler shifted at the closest target-stopper distance of 10 μm. This gives a lower limit for the transition quadrupole moment of 6.7 b, which is consistent with the previous DSAM experiment [4].

TABLE I. Lifetimes τ, transition probabilities λ, and quadrupole moments Q_t of superdeformed states in ^{135}Nd.

I_i ($\hbar$)	τ (ps)	E_γ (keV)	λ (ps^{-1})	Q_t (b)[a]
$\frac{41}{2}$	<0.22	749	>4.5	>6.7
$\frac{37}{2}$	$0.31^{+0.20}_{-0.08}$	676	$3.2^{+1.2}_{-1.2}$	$7.2^{+1.2}_{-1.5}$
$\frac{33}{2}$	$0.63^{+0.38}_{-0.12}$	603	$1.6^{+0.4}_{-0.6}$	$6.8^{+0.8}_{-1.4}$
$\frac{29}{2}$	$1.4^{+0.5}_{-0.6}$	546	$0.55^{+0.51}_{-0.18}$	$5.2^{+2.0}_{-1.0}$
		529	$0.16^{+0.16}_{-0.05}$	
$\frac{25}{2}$	$2.4^{+0.7}_{-0.9}$	620	$0.08^{+0.04}_{-0.03}$	$1.4^{+0.4}_{-0.3}$
		550	$0.13^{+0.13}_{-0.04}$	

[a]Deduced from transition probabilities using the rotational model formula with $K = \frac{1}{2}$ for the SD band.

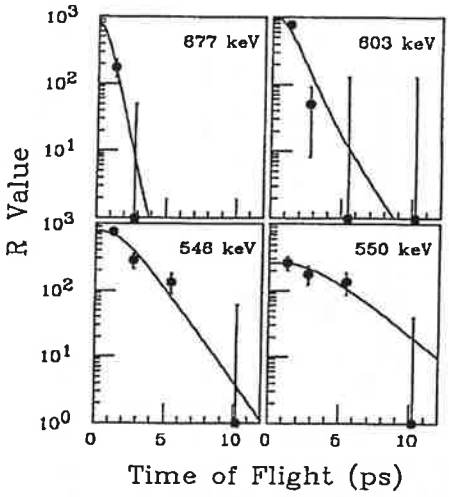

FIG. 3. Decay curves of four SD transitions in ^{135}Nd. The points are the normalized experimental data (see text); the curves represent the fits to the data.

The transition quadrupole moment of the 677 keV $(\frac{37}{2}\text{-}\frac{33}{2})$ transition, $Q_t = 7.2^{+1.2}_{-1.5}$ b, is in agreement with the previously determined [4] average value of $Q_t = 7.4 \pm 1.0$ b and confirms the large deformation of the SD band. Using the relation $Q_t = 0.004ZR^2[(c/a)^2 - 1]/(c/a)^{2/3}$, we deduce an axis ratio c/a of about 1.4 for the 677 keV transition in the SD band of ^{135}Nd, in good agreement with values for other SD bands in this mass region [8–11]. The drop in the Q_t values of the 603 and 546 keV transitions is not so significant, given the large experimental uncertainties. However, it is interesting to note that the dynamic moment of inertia of the SD band, which shows a rather smooth behavior over the whole frequency range, rises sharply at the bottom of the band. This fact was already interpreted [1] as a change in the internal structure of the band at this point. A smaller quadrupole moment of the 546 keV transition would support this interpretation.

A rather drastic change in the SD band is seen at the 3.324 MeV state. The only $E2$ transition observed so far deexciting this level is the 620 keV transition which has a quadrupole moment of $Q_t = 1.4 \pm 0.4$ b, indicating a drop in the $B(E2)$ value of more than an order of magnitude compared with the rest of the band. This Q_t value is even more than a factor of 2 smaller than the ones in the nor-

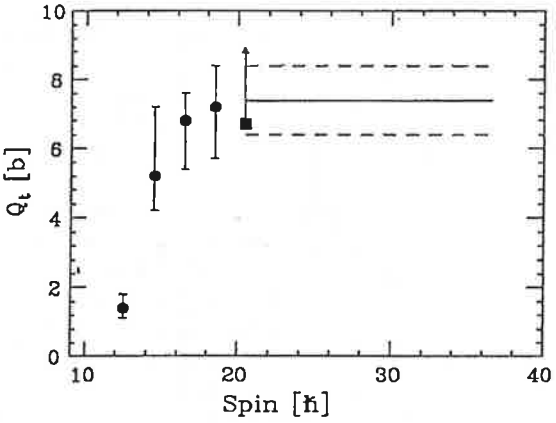

FIG. 4. Transition quadrupole moments Q_t of $E2$ transitions with energies 620, 546, 603, 677, and 749 (only lower limit) keV from this experiment (points with error bars). The lines give the average quadrupole moments and uncertainties for the higher spin transitions from a previous DSAM experiment [4].

mally deformed ground band [7]. The transition that would continue the SD band from this state would be expected around 490 keV, but no such transition is seen. In fact, any continuation of the band with the previous quadrupole moment and a transition energy greater than about 350 keV would be more intense than the observed 620 keV transition. No such transition is seen, indicating either that the band does not continue or that there is a large disruption in the energies of the band at this point. It is this disappearance of the in-band $E2$ strength that causes the fragmented decay out of the 3.324 MeV state.

The interesting aspect of this behavior is that it seems to be very similar to the usual decay out of SD bands. These bands generally depopulate quite suddenly over just one or two levels and there has been much speculation about what might cause this behavior. Simple models suggest that the deexcitation should be more gradual. We have here the first direct information about this deexcitation process, and it shows that the deexcitation is sudden. The discontinuity in the band may be connected to the disappearance of the SD potential-energy minimum—as our total Routhian surface calculations suggest—or to another drastic change in character of the band. Of course, it is not clear that ^{135}Nd is typical for the deexcitations of SD bands in general, but at least in this case we have learned that there is a sudden change in the structure of the band at the deexcitation point.

In conclusion, lifetimes of low-spin states of the SD band in ^{135}Nd have been determined using the RDM. The transition quadrupole moments within the SD band are in agreement with a previous experiment using a DSAM. However, the band is observed to change drastically at the 3.324 MeV state. The $B(E2)$ value for the 620 keV $E2$ transition depopulating this level is more than an order of magnitude smaller than that for the transitions in the SD band. This is probably related to the sudden depopulation of the SD band at this point.

One of us, P.W., wants to thank the Graduiertenförderung NRW for financial support. This work was supported by the Bundesminister für Forschung und Technologie BRD and by the U.S. Department of Energy under Contract No. W-7405-ENG-48 (LLNL) and by the Office of Energy Research, Division of Nuclear Physics of the U.S. Department of Energy under Contract No. DE-AC03-76SF00098 (LBL).

[1] E. M. Beck *et al.*, Phys. Rev. Lett. **58**, 2182 (1987).
[2] M. A. Bentley *et al.*, Phys. Rev. Lett. **59**, 2141 (1987).
[3] I. Y. Lee *et al.*, in *Proceedings of the International Conference on Nuclear Structure at High Angular Momentum, Ottawa, 1992* (Report No. AECL-10613), p. 21.
[4] R. M. Diamond *et al.*, Phys. Rev. C **41**, R1327 (1990).
[5] S. Heppner, Thesis, Univ. Bonn, 1991 (unpublished).
[6] H. Emling *et al.*, Nucl. Phys. **A419**, 187 (1984); private communication.
[7] P. Willsau, Thesis, Univ. Bonn, in preparation.
[8] A. J. Kirwan *et al.*, Phys. Rev. Lett. **58**, 467 (1987).
[9] Y.-J. He *et al.*, J. Phys. G **16**, 657 (1990).
[10] P. H. Regan *et al.*, Phys. Rev. C **42**, R1805 (1990).
[11] S. M. Mullins *et al.*, Phys. Rev. C **45**, 2683 (1992).

PHYSICAL REVIEW C

NUCLEAR PHYSICS

THIRD SERIES, VOLUME 58, NUMBER 3 SEPTEMBER 1998

RAPID COMMUNICATIONS

The Rapid Communications section is intended for the accelerated publication of important new results. Manuscripts submitted to this section are given priority in handling in the editorial office and in production. A Rapid Communication in **Physical Review C** *may be no longer than five printed pages and must be accompanied by an abstract. Page proofs are sent to authors.*

Influence of valence neutron configuration on quadrupole deformation in doubly-odd ^{134}Pr

M. N. Rao, R. V. Ribas, N. H. Medina, J. R. B. Oliveira, M. A. Rizzutto, and W. A. Seale
Instituto de Física, Universidade de São Paulo, São Paulo, Brazil

C. M. Petrache, D. Bazzacco, S. Lunardi, C. Rossi Alvarez, T. Scanferla, C. A. Ur, and R. Venturelli
Dipartimento di Fisica and INFN, Sezione di Padova, Padova, Italy

F. R. Espinoza-Quiñones
Departamento de Física-CCE, Universidade Estadual de Londrina, Londrina, Paraná, Brazil

Zs. Podolyák, D. De Acuña, G. de Angelis, M. De Poli, E. Farnea, A. Gadea, D. R. Napoli, and L. H. Zhu*
INFN, Laboratori Nazionali di Legnaro, Legnaro, Italy

A. Dewald, J. Gableske, and P. von Brentano
Institut für Kernphysik der Universität zu Köln, Köln, Germany

(Received 11 December 1997)

Lifetimes of levels in two doubly-decoupled bands of ^{134}Pr involving neutron intruder orbits have been measured using Doppler-shift techniques. The deduced transition quadrupole moments are consistent with total Routhian surface predictions for the suggested configurations of both bands. The negative-parity band with one neutron in the $i_{13/2}$ orbit has a much larger quadrupole deformation than the positive-parity band with a neutron in the $(f_{7/2}/h_{9/2})$ orbit, reflecting the strong polarizing effect of the $N=6$ intruder orbit on the nuclear shape. [S0556-2813(98)50109-4]

PACS number(s): 21.10.Tg, 21.10.Re, 25.70.Gh, 27.60.+j

The large amount of experimental information on deformed rotational bands in the $A=130$ region has revealed several structures with enhanced moment of inertia and quadrupole deformations of $\beta_2 \approx 0.3-0.4$. They correspond to an ellipsoidal nuclear shape with a major-to-minor axis ratio of 3:2. Cranking shell model (CSM) and total Routhian surface (TRS) calculations [1] indicate that many of these highly deformed (HD) rotational bands may be attributed to the occupation of the $N=6$ neutron intruder orbits, believed to have a strong polarizing effect on the shape of the nucleus. As a consequence, it is expected that the bands which involve two $i_{13/2}$ neutrons should be more deformed than those with only one neutron in the $i_{13/2}$ orbit. However, recent accurate quadrupole moment measurements of the yrast superdeformed (SD) band in ^{131}Ce and the yrast and two excited SD bands in ^{132}Ce using the Doppler-shift attenuation method [2] have yielded very similar deformations for these bands, leading to the conjecture that in the Ce isotopes the equilibrium deformation of highly deformed bands depends less on the $N=6$ intruder than on the greater stability of the SD core at the $Z=58$ shell gap. Very recently, the quadrupole moments of several highly deformed bands in Nd and Ce isotopes have been measured [3], which also showed no clear dependence on the number of occupied intruder orbits. Two bands of ^{134}Nd in which the $\nu i_{13/2}$ orbit becomes occupied at high spin do not show the expected increase in deformation, a fact which was explained through the compensation of the polarizing force of the $\nu i_{13/2}$ intruder orbit (which drives the nucleus towards larger deformation), by the rotation-induced shrinking effect at high spins (which drives the nucleus towards smaller deformation). The signifi-

*Permanent address: Institute of Atomic Energy, Beijing, China.

cance of intruder orbitals in determining the deformation has recently been called into question by the observation of strongly coupled structures based on a hole in the Nilsson [404]9/2 orbit in ^{129,131}Pr [4,5] and ^{133}Pr [6]. A recent systematic investigation of the high-spin spectra of nuclei in the $A\approx135$ region ($Z=57-61$, $N=72-78$), using the configuration-dependent shell-correction approach with the cranked Nilsson potential [7], has shown that the equilibrium deformation of the superdeformed bands is strongly dependent on the number of proton holes in the $g_{9/2}$ orbit.

In the odd-odd nuclei of the $A=130$ mass region the prevalent structures are the semi-decoupled deformed rotational bands built on $\pi h_{11/2}\otimes\nu h_{11/2}$, $\pi g_{7/2}/d_{5/2}\otimes\nu h_{11/2}$, and $\pi h_{11/2}\otimes\nu g_{7/2}$ configurations [8,9]. Above $N=72$, the occupation of the deformation driving $\nu(f_{7/2},h_{9/2})$ and $\nu i_{13/2}$ intruder orbits becomes possible. Bands tentatively assigned to configurations built on these orbits have indeed been observed in ^{130}La [10], ^{132}Pr [11–13], ^{134}Pr [8,12], ^{134}Pm [14], and ^{136}Pm [15]. They are predicted by TRS calculations to have an enhanced deformation. However, lifetime measurements to experimentally demonstrate that the observed doubly-decoupled bands have a larger deformation are very scarce. The only lifetime results are from a fractional Doppler shift analysis of a doubly-decoupled band in ^{134}Pm [14], where the authors conclude that in this band the odd neutron occupies the [541]1/2$^-$ orbit of mixed $h_{9/2}$ and $f_{7/2}$ parentage, based on the measured quadrupole moment. Measurements of transition quadrupole moments in the observed doubly-decoupled bands of other odd-odd nuclei of the $A=130$ mass region would help identify which of the available neutron intruder orbits are occupied in the bands of different nuclei.

The present article reports on lifetime measurements in ^{134}Pr based on Doppler-broadened line shapes and centroid shifts. The ^{134}Pr nucleus has one proton and one neutron outside the $Z=58$, $N=74$ subshells and thus the potential minimum at large deformation is shallower than in Ce ($Z=58$, $N=74$). As a consequence, core stabilization by shell gaps may be less effective in ^{134}Pr than in Ce nuclei, and the shape driving effect of the $\nu i_{13/2}$ intruder orbit may have a more pronounced influence.

The rotational bands in ^{134}Pr were populated through the ^{110}Pd (^{28}Si, $p3n$) reaction, by bombarding a Au-backed 1 mg/cm^2 ^{110}Pd target with a 130-MeV ^{28}Si beam provided by the XTU tandem accelerator of the Legnaro National Laboratories. The GASP array [16] with 40 Compton-suppressed HPGe detectors and the 80-element BGO inner ball was used for coincidence measurements. The multitelescope light-charged-particle detector array (ISIS) [17], consisting of 40ΔE-E Si telescopes, enabled the selection of the reaction channels associated with proton evaporation. Events were written on tape when three or more Ge detectors fired in coincidence with at least four BGO detectors. A total of 1.9×10^9 triple or higher-fold Compton-suppressed events was collected.

The Doppler-broadened line shapes for a cascade of six transitions in the positive-parity doubly-decoupled band were obtained for each of the seven rings of detectors (34°, 60°, 72°, 90°, 108°, 120°, and 146°) available in the GASP array. The spectra for the analysis were obtained from matrices constructed selecting the coincidences between the detectors of a specific ring and any other of the 40 detectors, regardless of the angle, by setting narrow gates on a few clean stopped transitions deexciting the lowest level of the band. This technique avoided as much as possible the presence of contaminant peaks near the Doppler broadened transitions.

The negative-parity doubly-decoupled band is weaker in intensity by at least a factor of 2 [12], and most of the transitions in this band, especially those with the higher energies, appear shifted and hence are faster. Furthermore, no deexciting transitions from this band that could be used as gates have been reported in the literature. Thus we have employed the centroid-shift analysis, which in this case is the more sensitive technique for extracting the quadrupole moment of the entire band. For this purpose γ-γ matrices have been produced in which each axis represents detectors belonging to the same ring. Since the transitions detected at 90° are not subject to Doppler shifts, all of the in-band transitions were used as gates on the 90° detectors, and the Doppler-shifted spectra of the band at the various angles were obtained from the θ versus 90° matrices. Finally, the spectra showing the Doppler-shifted transitions in the forward (34°) and the backward (146°) ring of detectors are obtained as a sum of gates on all the in-band transitions for the different angles from the 34° vs θ and 146° vs θ matrices. From the difference in Doppler shifts at the forward and backward angles the mean recoil velocity at which a given state decays is obtained as

TABLE I. Transition quadrupole moments and lifetimes for the positive-parity doubly-decoupled band in ^{134}Pr. The transition energies given are from the unshifted spectra at 90°. The relative intensities are from Ref. [8], renormalized to 100% for the lowest analyzed transition. $Q_{sf}=3.2\pm0.3$ eb.

E_γ (keV)	I_γ (%)	J^π	Q_t (eb)	τ (fs)
822.8	100(10)	21^+	3.76(10)	430(23)
882.4	53(6)	23^+	3.80(10)	296(16)
977.8	48(5)	25^+	4.48(24)	126(14)
1075.5	36(4)	27^+	3.94(20)	102(11)
1167.0	31(3)	29^+	3.71(20)	76(8)
1252.0	26(3)	31^+	3.57(24)	58(8)

TABLE II. Energies and lifetimes for the transitions in the negative-parity doubly-decoupled band in ^{134}Pr. The transition energies given are from the unshifted spectra at 90°. The relative intensities are from Ref. [12], renormalized to 100% for the lowest analyzed transition. $Q_t=6.3\pm0.4$ eb and $Q_{sf}=3.3\pm0.5$ eb.

E_γ (keV)	I_γ (%)	τ (fs)
948.7	100(7)	240(30)
1009.0	87(7)	167(21)
1064.6	77(7)	123(16)
1126.2	61(5)	87(11)
1202.0	43(4)	63(8)
1290.0	38(4)	48(6)
1385.0	34(3)	34(4)
1486.0	17(2)	24(3)

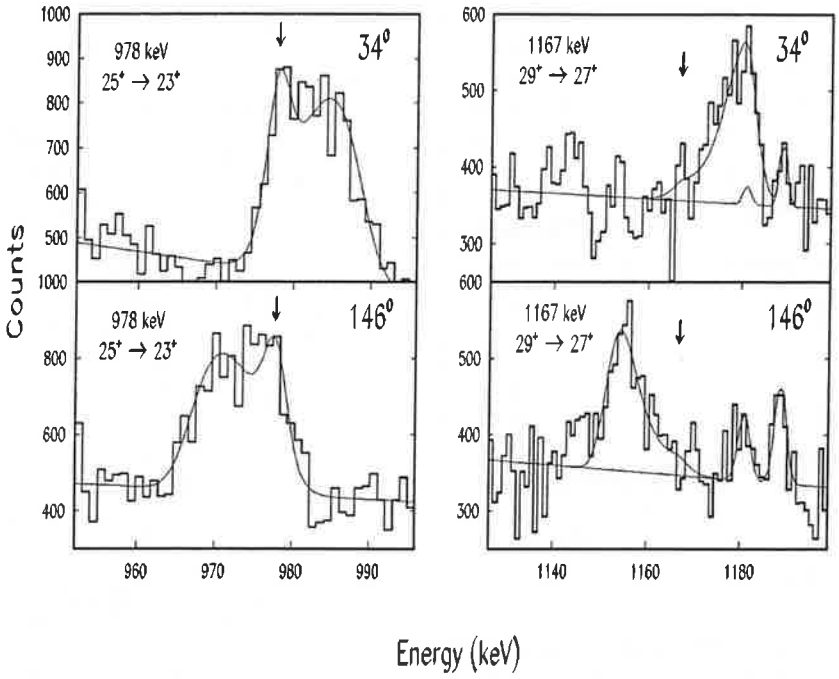

FIG. 1. Experimental and calculated line shapes for some transitions in the positive-parity doubly-decoupled band of ^{134}Pr for the forward and backward ring of detectors. The arrows indicate the positions of the unshifted peaks.

$$\bar{\beta}=[E_s(34°)-E_s(146°)]/2E_0\cos(34°).$$

The experimental results are then expressed in terms of the fractional Doppler shift as

$$F(\tau)=(\bar{\beta}/\beta_0),$$

where β_0 is the initial velocity of the recoiling nucleus.

The analysis of data was performed with the codes LINESHAPE [18] and FTAU [19]. Both codes are modified versions of the original program for Doppler broadened line shape analysis by Gascon *et al.* [20]. This code is based on the programs DECHIST and HISTAVER [21], which employ the formalism of Currie [22] to simulate the velocity history (including direction) of a series of recoiling nuclei, using Monte Carlo techniques. The LINESHAPE code includes the least-squares minimization routine MINUIT and the parameter error analysis routine MINOS, developed at CERN [23]. The code FTAU performs a two-dimensional χ^2 minimization of the experimental fractional Doppler shifts in terms of the assumed spin independent parameters for the in-band and side-feeding quadrupole moments.

Both the line-shape and the fractional Doppler shift calculations were performed assuming rotational-band side feeding for each of the levels of interest. The moment of inertia of the side-feeding cascades was varied from 40 to 55$\hbar^2$ MeV^{-1}, values found for the dynamical moments of inertia ($J^{(2)}$) of the highly-deformed bands of Pr, Pm, and Nd nuclei ($A=134-136$, see, e.g., Fig. 4 of Ref. [12]), without appreciable influence on the results. The side-feeding intensities were obtained from previously measured [8,12] in-band transition intensities (see Tables I and II), as the difference between the intensities of the deexciting and populating transitions for each individual level.

The slowing down of the Pr recoiling nuclei in the Pd target and the Au backing was described with electronic stopping powers using the shell-corrected Northcliffe-Schilling parametrization [24]. This parametrization is considered to describe the stopping of Ce, Pr, and Nd nuclei recoiling into Pd and Au at the recoil energy region of interest [3,25]. Since both bands were populated in the same reaction and have similar average excitation energies and the recoiling nuclei are slowing down in the same target and backing, systematic errors due to the parametrization of the energy loss mechanism are largely eliminated, thus justifying a direct comparison of the deduced quadrupole moments of the two bands.

Figure 1 shows examples of the resulting line-shape fits at forward and backward angles for transitions in the positive-parity band of ^{134}Pr. The best estimates of the in-band Q_t values and the corresponding lifetimes for the individual levels are shown in Fig. 2 and Table I. A linear fit to the individual quadrupole moments is also shown in Fig. 2, leading to an average in-band Q_t value of $3.9\pm0.3\,e$b. The corre-

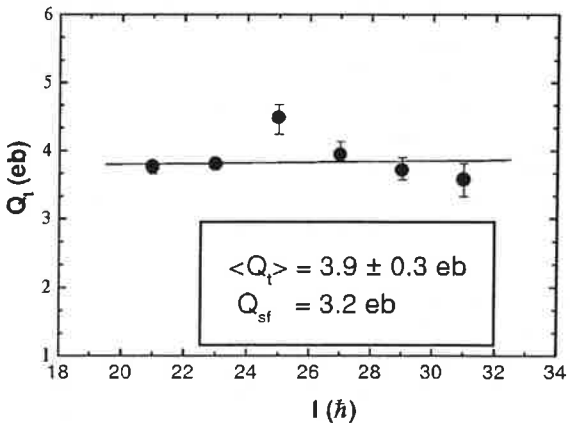

FIG. 2. Transition quadrupole moments as a function of spin for the positive-parity doubly-decoupled band of ^{134}Pr. The horizontal straight line is the average of the six Q_t values ($\langle Q_t\rangle=3.9\,e$b).

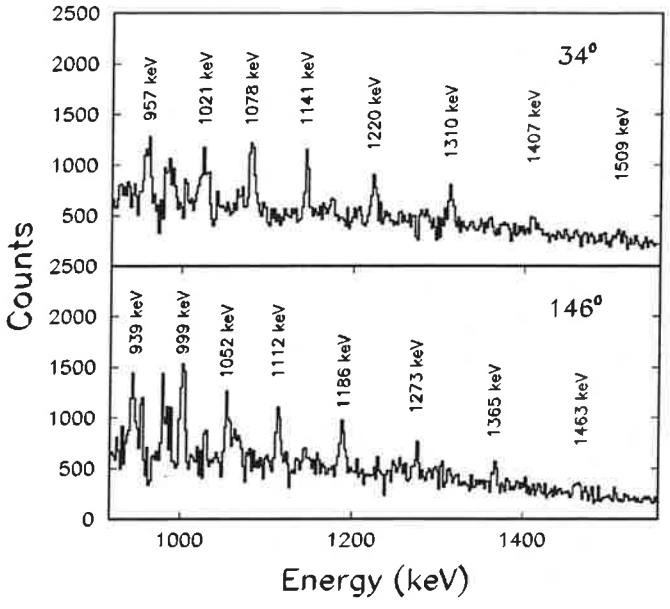

FIG. 3. Doppler-shifted spectra of the negative-parity doubly-decoupled band in ^{134}Pr, at forward and backward angles.

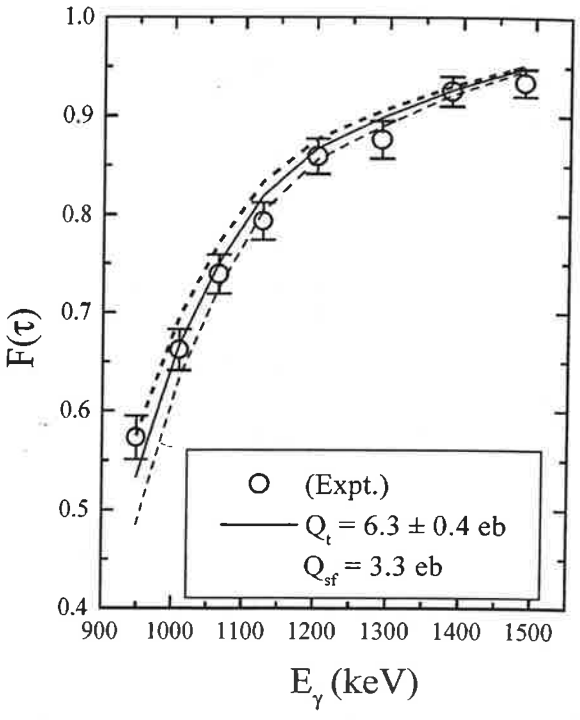

FIG. 4. Fractional Doppler shifts vs transition energy for the negative-parity double-decoupled band in ^{134}Pr. The dashed lines correspond to the upper and lower limits of Q_t obtained for a reduced chi-squared value of $\chi^2_{\min}+1$.

sponding side-feeding quadrupole moment obtained is $Q_{sf}=3.2\pm0.3\ e$b. A centroid-shift analysis of the top four transitions of this band, which had short enough lifetimes, yielded a value of $Q_t\approx Q_{sf}\approx3.2\pm0.4\ e$b. However, since the line-shape analysis is more reliable than the centroid-shift method for several of the lifetimes involved in this band, we adopt the results from the line-shape analysis shown in Fig. 2 and Table I.

Figure 3 presents the Doppler-shifted spectra of the negative-parity doubly-decoupled band at forward and backward angles. The measured values of the fractional Doppler shifts are compared in Fig. 4 with the $F(\tau)$ versus E_γ curve calculated with the computer code FTAU. The best fit to the data, obtained with a χ^2 minimization assuming a constant quadrupole moment for the whole band, yields a value of $Q_t=6.3\pm0.4\ e$b for the in-band transition quadrupole moment with $Q_{sf}=3.3\pm0.5e$b. The relatively small quadrupole moment of the side-feeding ($\sim 1/2Q_t$) is similar to the slow side-feeding deduced for the isotone ^{135}Nd [3,26].

Total Routhian surface calculations including quadrupole and monopole pairing correlations have been performed for both bands of interest. In these calculations the pairing field is calculated self-consistently and the Routhian is minimized with respect to the deformation parameters β_2, β_4, and γ at each step in frequency [27]. The expectation value of the quadrupole operators Q_{20} and Q_{22} are calculated using the intrinsic wave functions at the minimum of the TRS calculations.

The configuration assigned to the positive-parity band above the crossing at $\hbar\omega\approx0.4$ MeV is $\pi(h_{11/2})^3\otimes\nu(f_{7/2},h_{9/2})$ [8,12]. In the present TRS calculations the minimum of the positive-parity configuration involving the $f_{7/2}/h_{9/2}$ orbit is at $(\beta_2,\gamma)=(0.22,+11°)$. The quadrupole moment calculated using the intrinsic wave functions is $Q_t\approx3.5\ e$b, about 10% lower than the average experimental value of $\langle Q_t^{\exp}\rangle=3.9\ e$b.

The quadrupole deformation and the triaxiality parameter for the $\pi(h_{11/2})^3\otimes\nu i_{13/2}$ configuration assigned to the negative-parity doubly-decoupled band [12] are calculated to vary smoothly from $(\beta_2,\gamma)=(0.30,+3°)$ at low rotational frequency to $(\beta_2,\gamma)=(0.28,+12°)$ at the highest observed frequency. The calculated quadrupole moment decreases from $Q_t=5.7\ e$b at $\hbar\omega=0.45$ MeV to $Q_t=4.3\ e$b at $\hbar\omega=0.85$ MeV. Such a decrease of the quadrupole moment at high spin has been recently discussed for the highly deformed bands of Nd and Ce nuclei [3], where the calculations were in very good agreement with experiment. In the present case, however, the best fit to the data were obtained with a constant in-band quadrupole moment of $6.3\pm0.4\ e$b. The average calculated Q_t for this band is about 20% lower than this measured value.

In summary, the lifetime of levels in two doubly-decoupled bands of the odd-odd nucleus ^{134}Pr have been measured using the line shape and centroid shift methods. The band involving the $\nu i_{13/2}$ orbit has a much larger deformation than the one with a neutron in the $(f_{7/2}/h_{9/2})$ orbit, confirming the predicted polarizing effect of the $N=6$ intruder orbit on the nuclear shape.

We wish to express our gratitude to R. Wyss for providing the TRS calculations and to M. Ionescu Bujor for enlightening discussions. The valuable technical assistance of A. Buscemi, R. Isocrate, and R. Zanon is greatly appreciated. We also thank the staff of the XTU-Tandem of LNL for the smooth operation of the accelerator. This work was partially supported by the Fundação de Amparo à Pesquisa do Estado de São Paulo (FAPESP) and the Conselho Nacional de Desenvolvimento Científico e Tecnológico (CNPq), Brazil.

[1] R. Wyss, J. Nyberg, A. Johnson, R. Bengtsson, and W. Nazarewicz, Phys. Lett. B **215**, 211 (1988).
[2] R. M. Clark *et al.*, Phys. Rev. Lett. **76**, 3510 (1996).
[3] C. M. Petrache *et al.*, Phys. Rev. C **57**, R10 (1998).
[4] A. Galindo-Uribarri, D. Ward, V. P. Janzen, D. C. Radford, S. M. Mullins, and S. Filibotte, Atomic Energy of Canada Ltd., Report AECL-11132, PR-TASCC-09, 1994, p. 3.1.15.
[5] A. Galindo-Uribarri *et al.*, Phys. Rev. C **50**, R2655 (1994).
[6] A. Galindo-Uribarri, D. Ward, H. R. Andrews, G. C. Ball, D. C. Radford, V. P. Janzen, S. M. Mullins, J. C. Waddington, A. V. Afanasjev, and I. Ragnarsson, Phys. Rev. C **54**, 1057 (1996).
[7] A. V. Afanasjev and I. Ragnarsson, Nucl. Phys. **A608**, 176 (1996).
[8] C. M. Petrache, D. Bazzacco, S. Lunardi, C. Rossi Alvarez, G. de Angelis, M. De Poli, D. Bucurescu, C. A. Ur, P. B. Semmes, and R. Wyss, Nucl. Phys. **A597**, 106 (1996) and references therein.
[9] C. M. Petrache *et al.*, Nucl. Phys. **A603**, 50 (1996).
[10] M. J. Godfrey, Y. He, I. Jenkins, A. J. Kirwan, P. J. Nolan, R. Wadsworth, and S. M. Mullins, J. Phys. G **15**, L163 (1989).
[11] S. Shi, C. W. Beausang, D. B. Fossan, R. Ma, E. S. Paul, and N. Xu, Phys. Rev. C **37**, 1478 (1988).
[12] K. Hauschild *et al.*, Phys. Rev. C **50**, 707 (1994).
[13] D. J. Hartley *et al.*, Phys. Rev. C **55**, R985 (1997).
[14] R. Wadsworth, S. M. Mullins, P. J. Bishop, A. Kirwan, M. J. Godfrey, P. J. Nolan, and P. H. Regan, Nucl. Phys. **A526**, 188 (1991).
[15] M. A. Riley *et al.*, Phys. Rev. C **47**, R441 (1993).
[16] D. Bazzacco, in Proceedings of the International Conference on Nuclear Structure at High Angular Momentum, Ottawa, 1992 (Report No. AECL 10613), Vol. 2, p. 376.
[17] E. Farnea *et al.*, Nucl. Instrum. Methods **A400**, 87 (1998).
[18] J. C. Wells and N. R. Johnson, ORNL Report (unpublished).
[19] H. Savajols, private communication.
[20] J. Gascon *et al.*, Nucl. Phys. **A513**, 344 (1990).
[21] J. C. Bacelar, R. M. Diamond, E. M. Beck, M. A. Delaplanque, J. Draper, and F. S. Stephens, Phys. Rev. C **35**, 1170 (1987).
[22] W. M. Currie, Nucl. Instrum. Methods **73**, 173 (1969).
[23] F. James and M. Roos, Comput. Phys. Commun. **10**, 343 (1975).
[24] L. C. Northcliffe and R. F. Schilling, Nucl. Data, Sect. A **7**, 233 (1970).
[25] J. Gableske, private communication.
[26] R. M. Diamond, C. W. Beausang, A. O. Macchiavelli, J. C. Bacelar, J. Burde, M. A. Delaplanque, J. E. Draper, C. Duyar, R. J. McDonald, and F. S. Stephens, Phys. Rev. C **41**, R1327 (1990).
[27] W. Satula and R. Wyss, Phys. Scr. **T56**, 159 (1995).

High-spin state spectroscopy of ^{143}Dy

J. R. B. Oliveira, E. W. Cybulska, N. H. Medina, M. N. Rao, R. V. Ribas, and W. A. Seale
Instituto de Física, Universidade de São Paulo, São Paulo, SP, Brazil

F. R. Espinoza-Quiñones
Departamento de Engenharia Química, Universidade Estadual do Oeste do Paraná (UNIOESTE), Toledo, PR, Brazil

M. A. Rizzutto
Departamento de Ciências Exatas e Tecnológicas, Faculdades Integradas de Guarulhos, Guarulhos, SP, Brazil

D. Bazzacco, F. Brandolini, S. Lunardi, C. M. Petrache, Zs. Podolyák, C. Rossi-Alvarez, and C. A. Ur
Dipartimento di Fisica dell'Università, and INFN, Sezione di Padova, Padova, Italy

G. de Angelis, D. R. Napoli, P. Spolaore, A. Gadea, D. De Acuña, M. De Poli, E. Farnea, D. Foltescu, M. Ionescu-Bujor,* and A. Iordachescu*
INFN, Laboratori Nazionali di Legnaro, Legnaro, Italy

(Received 31 May 2000; published 25 October 2000)

The ^{143}Dy nucleus has been studied with the ^{92}Mo (^{54}Fe, $2pn\gamma$) reaction at 240 MeV incident energy. A rich variety of structures was observed at high spin. The nearly spherical $\nu h_{11/2}$ $I=11/2$ isomer is the basis of a negative parity irregular yrast structure which is observed up to $I=51/2$. A positive parity band presenting a large dynamic moment of inertia was observed, similar to the deformation enhanced $\nu i_{13/2}$ bands known to exist in this mass region. However, we propose an alternative assignment for this band, namely the triaxial collective minimum with $\beta=0.2$ predicted by total Routhian surface calculations for a $N_{osc}=4$ quasineutron excitation coupled to pairs of aligned quasiparticles. Another negative parity structure, with strong $M1$ and weak $E2$ crossover transitions, was observed.

PACS number(s): 21.10.Re, 23.20.En, 23.20.Lv, 27.60.+j

I. INTRODUCTION

Neutron-deficient nuclei in the $A\approx140$ mass region display a rich variety of band structures. Axially symmetric prolate shapes ($\gamma=0°$) are favored for the $h_{11/2}$ quasiproton excitations from the lower midshell in these nuclei with γ-soft cores. The quasineutrons, on the other hand, from the upper part of this shell exert a driving force towards collectively rotating oblate nuclear shapes ($\gamma=-60°$, according to the Lund convention [1]), resulting in shape changes in these nuclei. The systematics of the strongly deformation driving intruder orbital $\nu i_{13/2}\,[660]1/2^+$ have been extensively investigated in recent years in several odd-N ($N=73,77$) nuclei in the mass 130–140 region (Refs. [2–10]). In ^{133}Nd a g-factor measurement [11] for a positive parity band has confirmed the $\nu i_{13/2}$ configuration assignment. The experimental data obtained up to now in several of these nuclei, including in particular, the measured quadrupole moments, are consistent with the prediction [12] of a quadrupole deformation of $\beta\approx0.35$ for the $\nu i_{13/2}$ configuration, a value close to a prolate nuclear shape with a 3:2 axis ratio. The decoupled $\nu i_{13/2}$ bandhead energies and deformations of odd-N nuclei of this region ($Z=56$–64) and ($N=69$–77) have also been systematically investigated using the Nilsson-Strutinsky method [13].

With a view to extend the systematics of the $i_{13/2}$ band, we recently performed an experiment to produce and investigate extremely neutron deficient Dy nuclei in the $A\approx140$ region, by means of the ^{54}Fe+^{92}Mo reaction at 240-MeV incident energy. Of the various nuclei (with $Z=63$ to 66; $N=75$ to 78) produced in this experiment, the $3p$ channel leading to ^{143}Tb was the strongest one populated at the incident energy used, and the results on the high-spin structures populated in ^{143}Tb were described in [14]. We report here the results on the $2pn$ channel leading to the odd nucleus ^{143}Dy which was among the six most intense channels populated in the experiment. No data on excited states of ^{143}Dy have been published previous to this work.

II. EXPERIMENTAL PROCEDURES

The high spin states in the odd-N nucleus ^{143}Dy have been populated by the ^{92}Mo (^{54}Fe,$2pn\gamma$)^{143}Dy reaction at 240-MeV incident beam energy. The target used was an approximately 1.0 mg/cm^2 thick enriched (>97%) ^{92}Mo foil. The beam was provided by the tandem XTU accelerator of Legnaro National Laboratories. Gamma rays have been detected using the GASP array [15] composed of 40 Compton-suppressed high-efficiency HPGe and the 80-element BGO inner ball. The multi-telescope light-charged-particle detector array (ISIS) [16], consisting of 40 Si surface-barrier $\Delta E-E$ telescopes, enabled the selection of the multiplicities of the evaporated charged particles in coincidence with the observed γ rays. In order to permit the identification of the

*Permanent address: Institute of Physics and Nuclear Engineering, Bucharest, Romania.

various masses produced in the reaction, the recoil mass spectrometer (RMS) [17] was coupled to GASP. The coupled GASP-RMS system has an intrinsic mass resolution better than 1/300 and the average transmission efficiency in this experiment was about 1% (efficiencies of this order of magnitude are usual for charged particle emission reactions and with relatively thick targets [18]). Events have been collected on tape when at least two Compton-suppressed HPGe detectors and two BGO detectors fired in coincidence. A total of 1.3×10^9 Compton-suppressed events was collected. The data have been sorted into charged particle-γ-γ, mass-γ-γ and γ-γ-γ cubes.

According to CASCADE code [19] calculations the following cross sections were expected for the evaporation reaction channels: about 100 mb for ^{143}Tb, 40 to 60 mb for each of ^{142}Gd, ^{143}Dy, ^{140}Gd, ^{142}Tb, 20 to 30 mb for each of ^{141}Tb and ^{144}Dy, about 10 mb for each of ^{137,139}Eu, ^{140}Tb and 2 mb or less for ^{141}Dy and others. These predictions are roughly consistent with our experimentally observed yields.

Due to the fact that the efficiency of the charged particle detection system is not 100%, the observed γ-ray spectra gated by charged particle type and fold contain transitions from higher particle multiplicity channels. We have used linear combinations of particle-gated γ-γ matrices to generate clean spectra consisting of transitions from each individual charged particle multiplicity channel of the reaction. As neutrons were not detected, this procedure does not allow the separation of the contribution of different neutron multiplicity channels. The comparison with the mass-143 gated spectra then permitted unambiguous assignment of several γ-transitions to the ^{143}Dy nucleus (Fig. 1). Background-subtracted spectra generated from those matrices were used to construct the level scheme of ^{143}Dy. The data were analyzed using the VAXPAK [20] and RADWARE [21] spectrum analysis codes. The fully symmetrized γ-γ-γ cube was used to construct γ-γ matrices in coincidence with several transitions in each observed cascade. This procedure is particularly important for the weaker transitions (relative intensity below about 3%), which can be confirmed only in the double-gated spectra.

The assignment of the spins and parities to the ^{143}Dy levels was based on the DCO (directional correlation from oriented states) ratios. A γ-γ matrix was constructed by sorting the data from the eight detectors positioned at the 72° and 108° rings in the GASP array against the 12 detectors in the 34° and the 146° rings. Gates were set on both axes on several strong quadrupole transitions and the intensity of other transitions observed in the two spectra has been extracted. If $I_\gamma(72°+108°)$ and $I_\gamma(34°+146°)$ represent the intensity of a transition when gating on the (72°+108°) rings and (34°+146°) rings, respectively, the theoretical DCO ratios

$$R_{\mathrm{DCO}}=\frac{I_\gamma(72°+108°)}{I_\gamma(34°+146°)},$$

which one obtains, for the present geometry, are R_{DCO} $=1.00$ for quadrupole transitions and $R_{\mathrm{DCO}}=0.55$ for pure dipole transitions. Furthermore, $\Delta I=0$ dipole transitions yield $R_{\mathrm{DCO}}=1.07$.

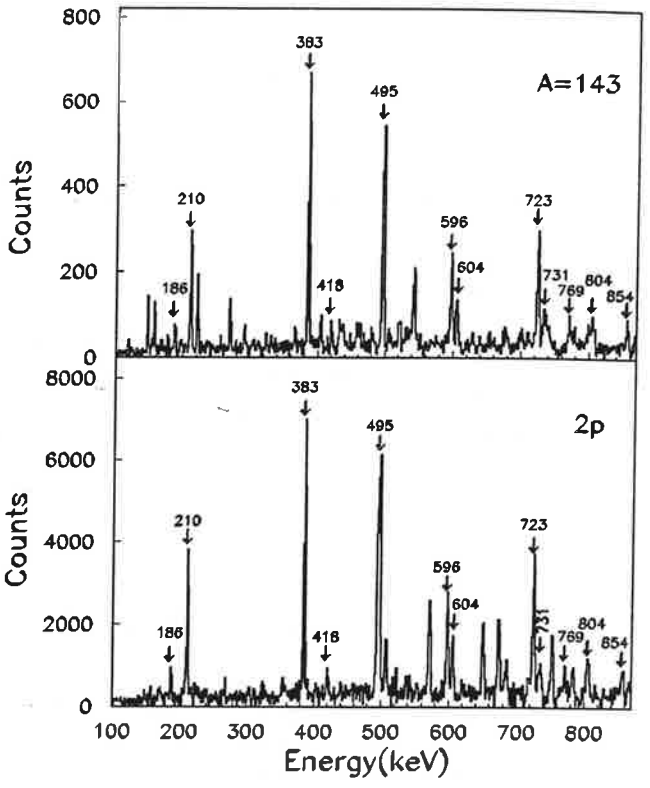

FIG. 1. Gamma-ray spectrum (not efficiency corrected) in coincidence with the 530 keV line (^{143}Dy). (a) Gated with mass 143; (b) gated with particle fold $2p$. The peaks present in both spectra can be assigned to ^{143}Dy. Their energy is shown in keV. The other peaks are contaminants from ^{143}Tb in spectrum (a) and ^{144}Dy in spectrum (b).

III. RESULTS

The level scheme of ^{143}Dy deduced from the present work is shown in Fig. 2. It is consistent with the coincidence relationships, intensity and energy balances from the $2p$-gated matrix and double-gates of the γ-γ-γ cube (except for the cases explicitly mentioned below). The γ-ray energies and relative intensities of all the transitions assigned to ^{143}Dy are given in Table I, which also shows the DCO ratios and the resulting spin and parity assignments. These assignments are, however, all based on the assumption that the spin (parity) of the level populated by the 495 keV transition is $\frac{11}{2}^-$, which is inferred from systematics of the mass region and from the close similarity to the level scheme of the isotone ^{141}Gd [10]. The assignments without parentheses are, therefore, to be regarded as certain, from the DCO results, relative to the spin of that state.

Due to the fact that the $\Delta I=0$ dipole transitions yield an R_{DCO} ratio close to that of a stretched quadrupole, there is an ambiguity of interpretation for the weak transitions (with larger uncertainties). This is the case of the 514 keV transi-

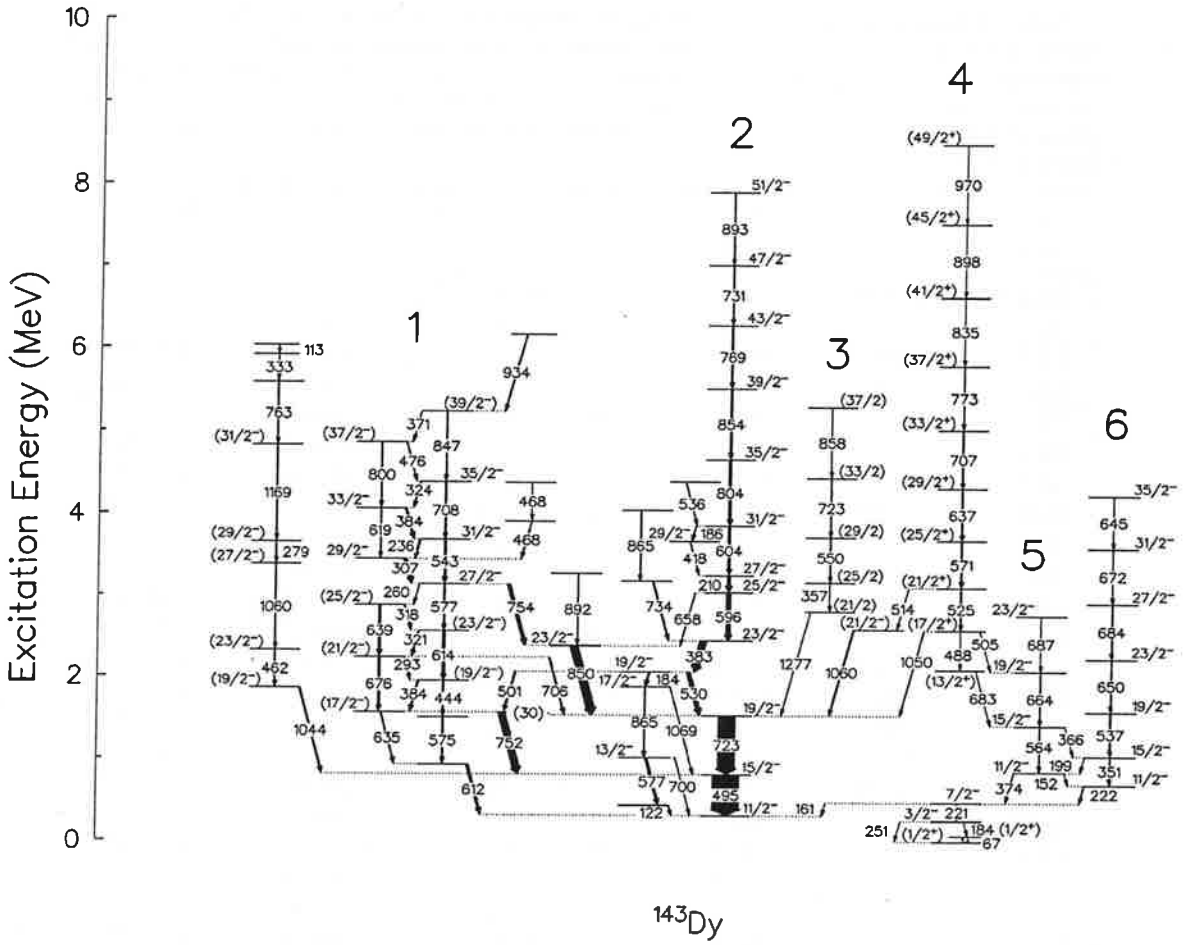

FIG. 2. The level scheme of ^{143}Dy. The energies of the γ-ray transitions are given in keV. The width of the arrows is proportional to the γ -ray relative intensity.

tion linking (together with the 1060 keV line) band 4 to the $\frac{19}{2}^-$ state. For this reason, another possible assignment would be two units larger for all the states of band 4. This ambiguity has no important consequence with regards to the interpretation of this band, discussed below.

There are some alternatives with respect to the ordering of the transitions in the weakly populated cascade presented to the left of structure 1 in Fig. 2. They are presented in order of decreasing relative intensity but other possibilities are consistent within the experimental errors.

Figure 3 shows a sum of clean double gates of the positive parity band of ^{143}Dy (band 4). The coincidence relationships can be verified to be consistent with the observed spectrum. It is apparent from the figure that the sum of the relative intensities of the 184 and 251 keV transitions which decay from the $(\frac{3}{2}^-)$ is significantly below that of the feeding transition 221 keV, indicating that the $(\frac{3}{2}^-)$ state is isomeric and/or its decay is fragmented in additional unobserved lines. A similar situation happens with the lower states of bands 5 and 6. The intensity balance of the $\frac{11}{2}^-$ states shows a loss of observed intensity in the decays. The order of the transitions is fixed, however, by the interband transitions which are well established from the analysis of the double-gated spectra.

IV. DISCUSSION

A. The negative parity bands

The nearly spherical $\nu h_{11/2}$ $I=11/2$ state is the basis of a negative parity irregular yrast structure which is observed in ^{143}Dy (band 2) up to $I=51/2$. The irregularity and the presence of dipole transitions within the cascade indicate a weakly deformed structure. The transitions of structure 2 and the linking transitions between structures 2 and 1 in ^{143}Dy have an almost one-to-one correspondence in ^{141}Gd [10], indicating a strong similarity between the negative parity states. Similar states have been successfully described within the IBFM+ broken pairs model [22] in ^{137}Nd [8] and ^{139}Sm [9]. A stretched $E2$ cascade, band 6 appears to be yrast between spin $I=23/2$ and $I=35/2$. However, it is much less intense than the main sequence (band 2), indicating that it is not fed from higher spin yrast states. There is no clear correspondence between band 6 and the negative parity structures in the neighboring isotones.

Another negative parity band (structure 1, above $I=\frac{27}{2}$), with strong $M1$ and rather weak $E2$ crossover transitions is a possible magnetic rotation band [23,24], based on the $[h_{11/2}]^2$ proton particle pair and $[h_{11/2}]^{-1}$ neutron hole configuration. This type of band appears as a solution of the

TABLE I. Gamma-ray energy, initial and final excitation energy, spin assignments, relative intensity and DCO ratio for the transitions in ^{143}Dy. E_i and E_f are the energies of the initial and final states corresponding to each transition. The γ-ray energies are accurate to ± 0.2 keV rising to ± 0.5 keV for the weak transitions and above 1 MeV. The relative intensities were obtained from the analysis of the $2p$-gated background subtracted (clean) matrix. The uncertainties given may be underestimated for the very weak transitions (below about 3).

E_γ [keV]	E_i [keV]	E_f [keV]	$I_i^\pi \rightarrow I_f^\pi$	I_γ	DCO ratio
(29.9)[a]	1558.0	1529.1	$(17/2^-) \rightarrow 19/2^-$	0.19(3)	
66.7	66.7	0.0	$(1/2^+) \rightarrow (1/2^+)$	2(1)	
112.7	6029.0	5916.2		0.32(3)	0.44(15)
122.1	432.7	310.6	$\rightarrow 11/2^-$	1.0(3)[b]	0.57(15)
151.5	845.3	693.5	$11/2^- \rightarrow 11/2^-$	0.02(3)	
161.2	471.8	310.6	$7/2^- \rightarrow 11/2^-$	0.36(8)	1.08(23)
183.8	2058.7	1874.9	$19/2^- \rightarrow 17/2^-$	4.97(28)	0.52(7)
184.2	250.9	66.7	$3/2^- \rightarrow (1/2^+)$	0.4(5)	1.18(15)
185.7	3851.9	3666.3	$31/2^- \rightarrow 29/2^-$	1.85(11)	
198.7	1044.2	845.3	$15/2^- \rightarrow 11/2^-$	0.07(6)	
209.8	3248.2	3038.4	$27/2^- \rightarrow 25/2^-$	11.11(43)	0.55(6)
220.9	471.8	250.9	$7/2^- \rightarrow 3/2^-$	1.09(21)	1.3(2)
221.8	693.5	471.8	$11/2^- \rightarrow 7/2^-$	1.84(17)	0.94(20)
236.0	3676.2	3440.3	$31/2^- \rightarrow 29/2^-$	5.41(22)	0.61(5)
250.9	250.9	0.0	$3/2^- \rightarrow (1/2^+)$	0.4(4)	1.08(15)
260.0	3133.3	2873.4	$27/2^- \rightarrow (25/2^-)$	2.01(13)	0.60(13)
279.0	3651.0	3372.0	$(29/2^-) \rightarrow (27/2^-)$	2.01(16)	0.59(10)
293.3	2234.7	1941.6	$(21/2^-) \rightarrow (19/2^-)$	2.39(19)	
307.0	3440.3	3133.3	$29/2^- \rightarrow 27/2^-$	12.3(5)	0.57(3)
318.0	2873.4	2555.7	$(25/2^-) \rightarrow (23/2^-)$	3.42(24)	
321.2	2555.7	2234.7	$(23/2^-) \rightarrow (21/2^-)$	5.29(36)	0.58(21)
324.2	4384.2	4060.0	$35/2^- \rightarrow 33/2^-$	3.67(19)	0.45(18)
327.7[c]	3201.1	2873.4	$\rightarrow 25/2^-$	2.4(24)	
333.2	5916.2	5583.1		1.02(10)	0.44(15)
350.7	1044.2	693.5	$15/2^- \rightarrow 11/2^-$	3.65(20)	
356.7	3162.7	2806.0	$(25/2^-) \rightarrow (21/2^-)$	2.1(6)	0.84(7)
366.2	1409.4	1044.2	$15/2^- \rightarrow 15/2^-$	0.14(8)	
370.9	5230.9	4859.9	$(39/2^-) \rightarrow (37/2^-)$	1.52(16)	
373.6	845.3	471.8	$11/2^- \rightarrow 7/2^-$	2.08(23)	0.94(16)
383.5	2442.2	2058.7	$23/2^- \rightarrow 19/2^-$	26.8(12)	0.97(12)
383.8	1941.6	1558.0	$(19/2^-) \rightarrow (17/2^-)$	5.7(6)	
383.9	4060.0	3676.2	$33/2^- \rightarrow 31/2^-$	7.1(5)	
418.4	3666.3	3248.2	$29/2^- \rightarrow 27/2^-$	3.05(25)	0.66(9)
444.4	1941.6	1497.3	$19/2^- \rightarrow$	3.73(29)	
462.3	2312.0	1849.7	$(23/2^-) \rightarrow (19/2^-)$	3.3(5)	1.19(13)
467.6	4376.0	3908.4		0.74(26)	
468.2	3908.4	3440.3	$\rightarrow 29/2^-$	3.9(4)	
475.6	4859.9	4384.2	$(37/2^-) \rightarrow 35/2^-$	2.51(21)	
487.5	2579.1	2091.6	$(17/2^+) \rightarrow (13/2^+)$	1.08(18)	
495.0	805.6	310.6	$15/2^- \rightarrow 11/2^-$	100.0(10)[d]	1.00(6)
501.1	2058.7	1558.0	$19/2^- \rightarrow (17/2^-)$	5.6(5)	
504.5	2579.1	2073.3	$(17/2^-) \rightarrow 19/2^-$	0.21(14)	
513.6	3104.0	2590.0	$(21/2^+) \rightarrow (21/2^-)$	0.88(21)	1.18(33)
524.9	3104.0	2579.1	$(21/2^+) \rightarrow (17/2^+)$	4.2(5)	1.06(17)
529.5	2058.7	1529.1	$19/2^- \rightarrow 19/2^-$	15.8(9)	1.17(7)
535.9	4387.8	3851.9	$\rightarrow 31/2^-$	2.19(29)	
537.3	1581.5	1044.2	$19/2^- \rightarrow 15/2^-$	4.09(27)	1.12(11)

TABLE I. (*Continued*).

E_γ [keV]	E_i [keV]	E_f [keV]	$I_i^\pi \rightarrow I_f^\pi$	I_γ	DCO ratio
542.8	3676.2	3133.3	$31/2^- \rightarrow 27/2^-$	7.7(4)	1.19(15)
550.5	3713.2	3162.7	$(29/2) \rightarrow (25/2)$	2.0(4)	
557.2[c]	4465.6[c]	3908.4		1.49(15)	
564.1	1409.4	845.3	$15/2^- \rightarrow 11/2^-$	3.20(28)	1.04(12)
571.3	3675.2	3104.0	$(25/2^+) \rightarrow (21/2^+)$	6.4(6)	1.25(20)
574.5	1497.3	922.8		5.3(7)	
577.2	1009.9	432.7	$13/2^- \rightarrow$	9.8(14)	0.57(11)
577.4	3133.3	2555.7	$27/2^- \rightarrow (23/2^-)$	5.57(39)	
596.3	3038.4	2442.2	$25/2^- \rightarrow 23/2^-$	17.1(7)	0.46(6)
603.7	3851.9	3248.2	$31/2^- \rightarrow 27/2^-$	10.1(4)	0.92(10)
612.4	922.8	310.6		9.55(10)	
613.9	2555.7	1941.6	$(23/2^-) \rightarrow (19/2^-)$	8.5(6)	
619.2	4060.0	3440.3	$33/2^- \rightarrow 29/2^-$	2.26(23)	
628.2[c]	3666.3	3038.4	$29/2^- \rightarrow 25/2^-$	1.61(29)	
635.3	1558.0	922.8	$(17/2^-) \rightarrow$	4.4(5)	
637.2	4312.4	3675.2	$(29/2^+) \rightarrow (25/2^+)$	5.4(5)	
638.7	2873.4	2234.7	$(25/2^-) \rightarrow (21/2^-)$	8.4(6)	
644.6	4232.1	3587.5	$35/2^- \rightarrow 31/2^-$	0.68(18)	1.1(4)
645.4[c]	3201.1[c]	2555.7	$(27/2^-) \rightarrow (23/2^-)$	5.6(5)	
650.1	2231.6	1581.5	$23/2^- \rightarrow 19/2^-$	4.01(34)	1.25(12)
658.0	3038.4	2379.3	$25/2^- \rightarrow 23/2^-$	1.90(22)	
663.9	2073.3	1409.4	$19/2^- \rightarrow 15/2^-$	2.60(34)	0.95(13)
671.9	3587.5	2915.6	$31/2^- \rightarrow 27/2^-$	1.9(4)	1.33(16)
676.4	2234.7	1558.0	$(21/2^-) \rightarrow (17/2^-)$	6.4(7)	
682.8	2091.6	1409.4	$(13/2^+) \rightarrow 15/2^-$	0.9(4)	
684.0	2915.6	2231.6	$27/2^- \rightarrow 23/2^-$	2.89(24)	1.2(2)
686.9	2760.2	2073.3	$23/2^- \rightarrow 19/2^-$	1.24(25)	
700.2	1009.9	310.6	$13/2^- \rightarrow 11/2^-$	1.9(6)	
706.2	2234.7	1529.1	$(21/2^-) \rightarrow 19/2^-$	5.4(6)	
707.3	5019.7	4312.4	$33/2^- \rightarrow 29/2^-$	5.0(4)	
707.9	4384.2	3676.2	$35/2^- \rightarrow 31/2^-$	5.4(4)	1.15(13)
722.7	4435.9	3713.2	$(33/2) \rightarrow (29/2)$	1.3(4)	
723.4	1529.1	805.6	$19/2^- \rightarrow 15/2^-$	68.4(29)	1.08(4)
731.4	7010.3	6279.0	$47/2^- \rightarrow 43/2^-$	4.54(25)	1.1(2)
733.6	3175.7	2442.2	$\rightarrow 23/2^-$	5.1(6)	
752.5	1558.0	805.6	$(17/2^-) \rightarrow 15/2^-$	25.8(22)	
753.8	3133.3	2379.3	$27/2^- \rightarrow 23/2^-$	12.2(8)	1.05(7)
762.6	5583.1	4820.4	$\rightarrow (31/2^-)$	1.92(29)	
769.4	6279.0	5509.5	$43/2^- \rightarrow 39/2^-$	6.06(31)	1.01(18)
773.5	5793.2	5019.7	$(37/2^+) \rightarrow (33/2^+)$	3.14(37)	
799.8	4859.9	4060.0	$(37/2^-) \rightarrow 33/2^-$	2.39(34)	
803.6	4655.6	3851.9	$35/2^- \rightarrow 31/2^-$	10.6(5)	1.12(13)
821.7[c]	3201.1[c]	2379.3	$\rightarrow 23/2^-$	3.9(6)	
835.4	6628.6	5793.2	$(41/2^+) \rightarrow (37/2^+)$	2.09(28)	
847.1	5230.9	4384.2	$(39/2^-) \rightarrow 35/2^-$	3.41(35)	
850.0	2379.3	1529.1	$23/2^- \rightarrow 19/2^-$	30.5(16)	1.08(3)
854.0	5509.5	4655.6	$39/2^- \rightarrow 35/2^-$	7.35(38)	1.12(17)
858.4	5294.3	4435.9	$(37/2) \rightarrow (33/2)$	1.00(21)	
864.6	4040.3	3175.7		2.6(4)	
865.0	1874.9	1009.9	$17/2^- \rightarrow 13/2^-$	4.1(7)	1.26(7)[e]
892.4	3271.6	2379.3	$\rightarrow 23/2^-$	3.7(6)	
893.1	7903.5	7010.3	$51/2^- \rightarrow 47/2^-$	1.84(18)	1.16(28)

TABLE I. (*Continued*).

E_γ [keV]	E_i [keV]	E_f [keV]	$I_i^\pi \rightarrow I_f^\pi$	I_γ	DCO ratio
898.5	7527.1	6628.6	$(45/2^+) \rightarrow (41/2^+)$	0.81(25)	
934.2	6165.1	5230.9	$\rightarrow 39/2^-$	3.48(30)	
970.4	8497.4	7527.1	$(49/2^+) \rightarrow (45/2^+)$	0.24(22)	
1044.1	1849.7	805.6	$(19/2^-) \rightarrow 15/2^-$	5.4(19)	1.09(16)
1049.9	2579.1	1529.1	$(17/2^+) \rightarrow 19/2^-$	2.3(5)	0.68(24)
1060.1	3372.0	2312.0	$(27/2^-) \rightarrow (23/2^-)$	2.9(5)	0.61(9)
1060.1	2590.0	1529.1	$(21/2^-) \rightarrow 19/2^-$	4.8(12)	0.35(16)
1069.4	1874.9	805.6	$17/2^- \rightarrow 15/2^-$	1.66(36)	
1169.5	4820.4	3651.0	$(31/2^-) \rightarrow (29/2^-)$	1.86(23)	0.55(16)
1276.9	2806.0	1529.1	$(21/2) \rightarrow 19/2^-$	1.5(6)	0.57(10)

[a]Gamma-ray below experimental energy threshold. Inferred indirectly from coincidence relations.
[b]Observed intensity. Probable decay from isomeric state leading to underestimated value.
[c]Tentative gamma ray or level. Not shown in level scheme for simplicity.
[d]Sum of the intensities of the transitions feeding the $15/2^-$ level: 1044, 752, 1069, and 723 keV, normalized to 100.
[e]Contaminated.

tilted axis cranking model applied to nearly spherical nuclei. The particle and hole excitations tend to couple their angular momenta perpendicularly. In order to generate higher spins the angular momentum vectors of particles and holes gradually align, resembling the closing of a pair of blades. For this reason this type of band is also known as a "shears band." In ^{143}Dy, the $M1$ band appears as a rather irregular band, which is an exception among the neighboring isotones, and may not be the expected band based on the shears mechanism.

The $B(M1)/B(E2)$ ratios obtained for the levels of structure 1 are shown in Fig. 4. The levels below $I=\frac{29}{2}$ present lower values for this ratio than the ones above, suggesting a change in configuration. The $E_\gamma=754$ keV $E2$ interband transition was not considered in the calculation of the ratio for the $I=\frac{27}{2}$ state. In ^{141}Gd [10] there are no $M1$ transitions, observed below spin $\frac{25}{2}$, which connect the $M1$ structure to the $(\frac{17}{2}^-)$ state, as in band 1. The $B(M1)/B(E2)$ ratios for band 1 are relatively small (by a factor of 2–3) as compared to those for the magnetic rotation bands of ^{137}Nd [8] and ^{139}Sm [24].

B. The positive parity band

A very regular structure consisting of stretched $E2$ transitions, presenting a large dynamic moment of inertia, was observed in ^{143}Dy (band 4). It is very tempting to assign to this structure the $\nu i_{13/2}$ configuration, which is known to generate enhanced deformation bands in this region, in particular, in the $N=77$ isotones: ^{137}Nd [8], ^{139}Sm [9], and ^{141}Gd [10]. However the TRS calculations which will be presented in the next subsection indicate another possible interpretation for ^{143}Dy which cannot be ruled out with the presently available experimental data. Figure 5 shows the dynamic moments of inertia for the positive parity bands of the $N=77$ isotones. Both ^{143}Dy and ^{137}Nd show very stable moments of inertia around $60\hbar^2$/MeV. The ^{137}Nd nucleus is the heaviest Nd isotope for which the transition quadrupole moment

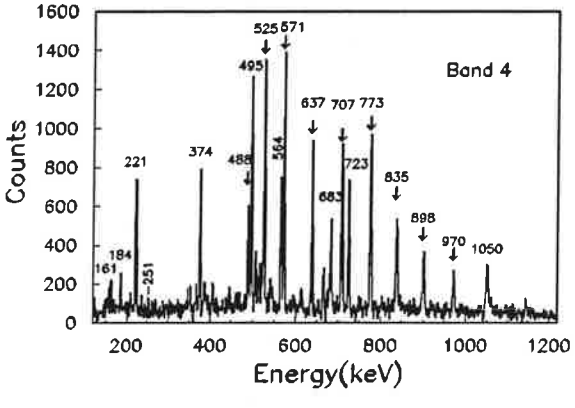

FIG. 3. Sum of clean double gates for the positive parity band of ^{143}Dy (band 4). The in-band transitions are indicated with arrows. The linking transitions, as well as the low lying transitions fed by the band can also be seen.

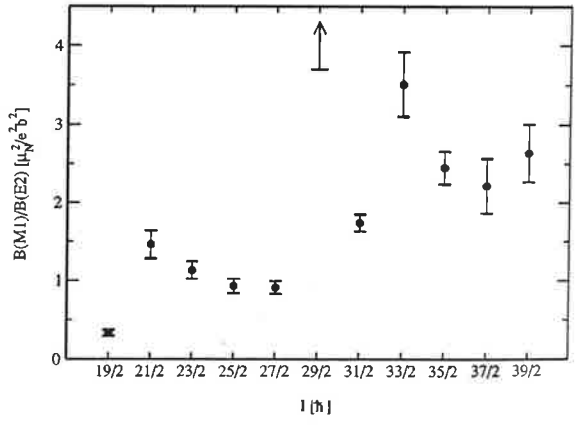

FIG. 4. Ratio of reduced transition probabilities $B(M1)/B(E2)$ as a function of spin for structure 1 in ^{143}Dy.

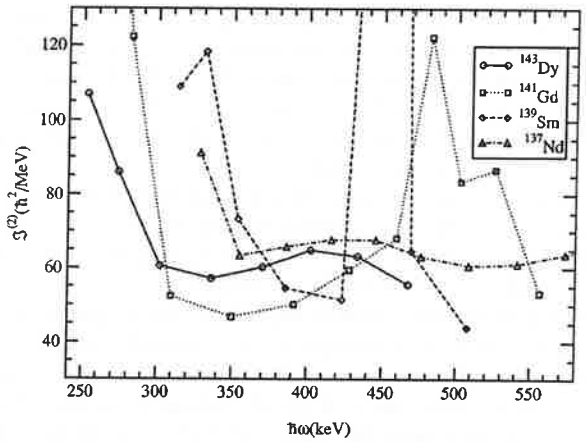

FIG. 5. Dynamic moments of inertia for positive parity bands in $N=77$ isotones (circles ^{143}Dy, squares ^{141}Gd, diamonds ^{139}Sm, and triangles ^{137}Nd).

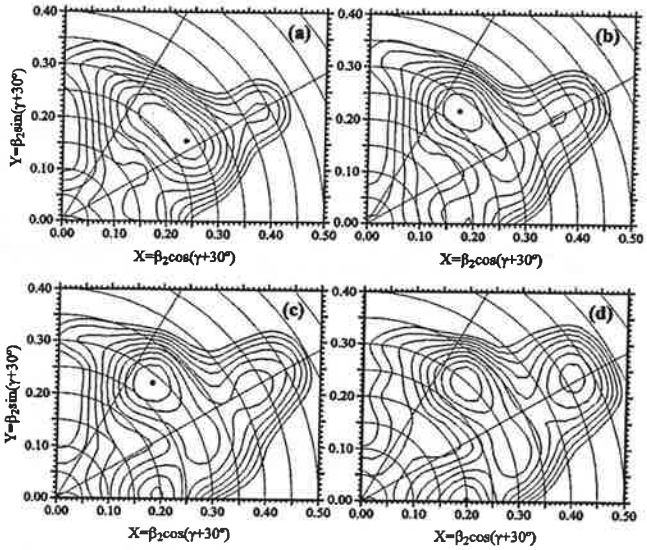

FIG. 6. Total Routhian surface calculations for positive parity configurations at $\hbar\omega\approx0.5$ MeV in $N=77$ odd nuclei from $Z=60$ to $Z=66$: (a) ^{137}Nd, (b) ^{139}Sm, (c) ^{141}Gd, and (d) ^{143}Dy.

of the $\nu i_{13/2}$ band has been measured. It has the least deformed $i_{13/2}$ band of the Nd isotopes since the number of neutrons is departing from the $N=72$ gap, whose role in stabilizing enhanced deformations has been discussed in an article by Kondev *et al.* [25].

C. Theoretical calculations

Standard total Routhian surface (TRS) calculations [12] were obtained for the yrast positive parity configurations in the $N=77$ isotones. The results, presented in Fig. 6, show an interesting trend as one increases the number of protons from $Z=60$ to $Z=66$. Besides the $\beta\approx0.3$ minimum, with positive γ, which has been assigned to the Nd $i_{13/2}$ band, an additional minimum appears around $\beta\approx0.2$, $\gamma\approx-30°$, which becomes favored in ^{143}Dy. The configuration of this minimum is based on positive parity neutron states of the $N_{\mathrm{osc}}=4$ oscillator shell (from mixed $\nu d_{3/2}, s_{1/2}, g_{7/2}$ states on a spherical basis, or $[400]\frac{1}{2}^+$, $[402]\frac{3}{2}^+$, $[404]\frac{5}{2}^+$, $[402]\frac{5}{2}^+$ and others on the deformed basis) coupled to a broken pair of intruder $N_{\mathrm{osc}}=5$ ($h_{11/2}$) aligned protons. Also, the least excited $N_{\mathrm{osc}}=5$ (from mixed $g_{9/2}, f_{7/2}$ states) neutron pair gradually aligns in the frequency range of the band. This minimum constitutes another possible interpretation for the positive parity band of ^{143}Dy. It should be noted that due to a compensation between the degree of collectivity and deformation, the two minima should present rather similar moments of inertia.

The quasiparticle Routhians for a deformed Woods-Saxon potential calculated for ^{143}Dy are shown in Fig. 7. The deformation and the pairing gap parameters used were obtained from the TRS results (above) at a rotational frequency of

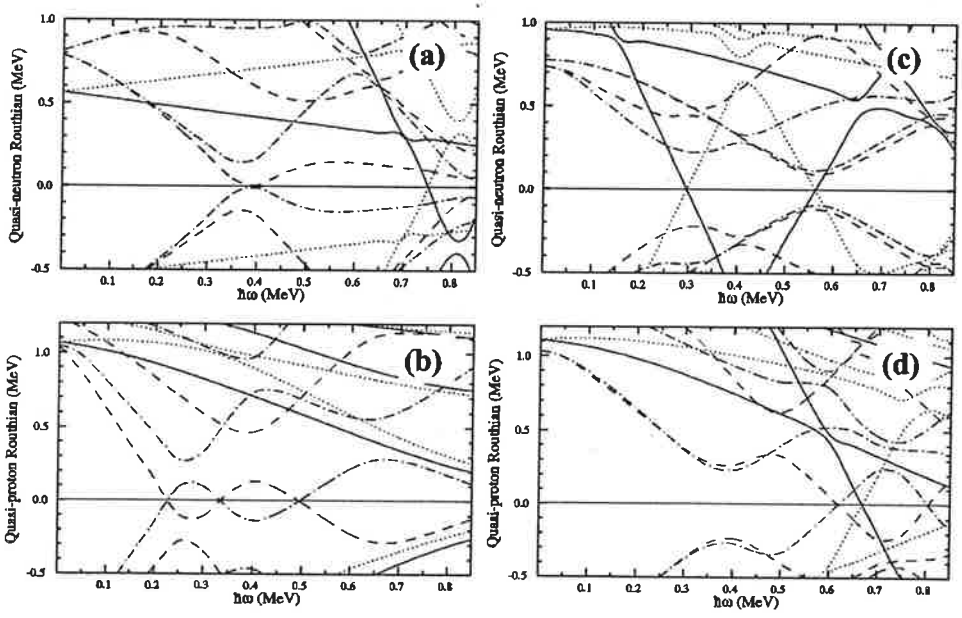

FIG. 7. Quasiparticle Routhians for ^{143}Dy (a) quasineutrons and (b) quasiprotons with deformation parameters corresponding to the absolute minimum of Fig. 3(d): $\beta=0.2$, $\gamma=-30°$; (c) quasineutrons and (d) quasiprotons with deformation parameters corresponding to the $\nu i_{13/2}$ local minimum: $\beta=0.29$, $\gamma=19°$. The line type indicates the parity and signature (π,α): solid $(+,1/2)$, dotted $(+,-1/2)$, dashed $(-,-1/2)$, and dot-dashed $(-,1/2)$.

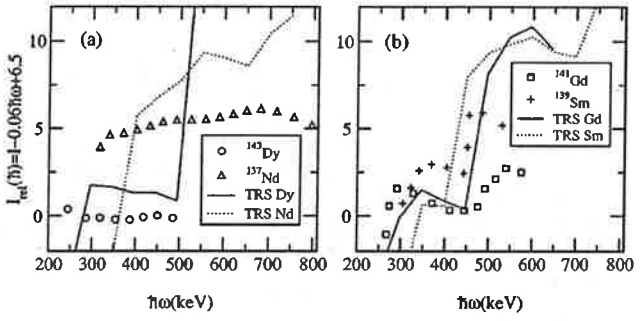

FIG. 8. Relative alignments for the positive parity bands of $N=77$ isotones. A reference of $I_{ref}=0.06\hbar\omega-6.5$ was subtracted. The circles, triangles, squares, and plus signs are the experimental data for Dy, Nd, Gd, and Sm, respectively. The solid and dotted lines are the TRS calculations for Dy and Nd respectively in (a), and for Gd and Sm in (b).

$\hbar\omega\approx0.5$ MeV (for each of the two minima), but were kept fixed at all frequencies. The $\nu i_{13/2}$ quasineutron state is out of scale at low frequency in Fig. 7(a) and crosses with the lowest $N=4$ positive parity state at $\hbar\omega\approx0.7$ MeV, while in Fig. 7(c) it is the lowest positive parity configuration above $\hbar\omega\approx0.15$ MeV. It should be noted that the calculations corresponding to the $\nu i_{13/2}$ minimum for ^{143}Dy and ^{137}Nd quasineutrons are very similar, since they are isotones, and the equilibrium deformations are nearly the same.

Figure 8 presents relative spin plots with respect to a linear reference ($I_{ref}=0.06\hbar\omega-6.5$) which is a rough description of the ^{143}Dy data [Fig. 8(a)]. The relative spin for ^{137}Nd is about 5 units larger, with a little larger dynamic moment of inertia (the slight upward slope observed). The TRS calculations are also shown in the figure and are in very good qualitative agreement with the experimental results for both nuclei. The moment of inertia for Nd is larger than for Dy, although this effect is overestimated in the calculation. The spin for these two shapes at the same frequency is both calculated and observed to be smaller in the heaviest isotone. In addition, the Dy band is observed down to $I=13/2$, while in Nd, $I=19/2$ was the lowest spin populated. The calculations predict that the shape is stable (at the referred minimum) in Dy in the frequency range from 300 keV to 500 keV, coinciding very well with the range of the band observed experimentally. In Nd the shape is calculated to be stable above 400 keV, roughly coinciding with the beginning of the observed band at about 330 keV. The steep jumps in the theoretical plots correspond to sudden changes in the yrast equilibrium deformation. For the other two intermediate isotones (^{139}Sm, ^{141}Gd) there is reasonably good agreement [Fig. 8(b)], and there appears to be a strong suggestion of a transition between the two deformation minima as predicted by TRS calculations. However, the amount of the alignment increase in the transition is overestimated. In summary, there is a good overall interpretation for the positive parity bands of the $N=77$ isotones assuming competition between the two positive parity minima with the two distinct configurations. The general trends are predicted by the TRS calculations.

In the alternative assignment of the $i_{13/2}$ basic configuration (and shape) for all of these bands, the behavior of the relative spins (as in Fig. 8) could perhaps be explained by the possibility that a pair of $h_{11/2}$ quasiprotons align generating the observed upward slopes in Sm and Gd. The crossing frequency would be increasing from $Z=60$ to $Z=66$, as expected, since the proton chemical potential is being raised. In this case the Dy band would be completely below the crossing while that of Nd would be completely above. The 5 units of spin difference would come from the alignment of the quasiproton pair. Although this is a satisfactory interpretation, the predicted crossing frequencies of the $h_{11/2}$ proton pair (from calculations of the same type as in Fig. 6) have only a modest increase from 0.28 MeV to 0.38 MeV from Nd to Dy. In Gd the quasiproton alignment has been considered "perturbed." It appears to be delayed and to have an unusually large interaction strength. The situation is, therefore, also not very clear.

In ^{137}Nd the measured transition quadrupole moment is consistent with the predicted $\beta\approx0.3$ deformation, when the positive γ deformation (towards the noncollective shape) is taken into account [26]. For ^{143}Dy, a similar transition quadrupole moment is expected, since the negative γ (in the collective sector) compensates for the decrease in β deformation.

V. CONCLUSIONS

The high spin states of the very neutron deficient nucleus of ^{143}Dy have been measured for the first time. Among the structures observed, there is a $M1$ band, somewhat irregular, and a very regular positive parity band presenting large dynamic moment of inertia. Two possible assignments have been considered for the configuration of this band, with different deformations: one based on the $i_{13/2}$ coupled to $N_{osc}=5$ quasineutron states, and the other on low-j $N_{osc}=4$ positive parity states coupled to high-j $N_{osc}=5$ protons and neutrons. We suggest that this second configuration could also be involved in the perturbed positive parity bands of the Gd and Sm isotones. It would be interesting to measure lifetimes of the individual states of these bands. In order to distinguish between the two possible assignments, a g-factor measurement would be adequate, since they differ, among other things, by a broken pair of protons. This is a very difficult measurement, however, due to the weak relative intensity of the gamma cascade and the short lifetimes expected.

ACKNOWLEDGMENTS

We thank G. Manente for the preparation of the targets, and the staff of the XTU-Tandem of LNL for the smooth operation of the accelerator. This work was partially supported by the Fundação de Amparo à Pesquisa do Estado de São Paulo (FAPESP) and the Conselho Nacional de Desenvolvimento Científico e Tecnológico (CNPq), Brazil.

[1] G. Andersson, S. E. Larsson, G. Leander, P. Möller, S. G. Nilsson, I. Ragnarsson, S. Åberg, R. Bengtsson, J. Dudek, B. Nerlo-Pomorska, K. Pomorski, and Z. Szymański, Nucl. Phys. **A268**, 205 (1976).
[2] E. S. Paul *et al.*, Phys. Rev. Lett. **61**, 42 (1990) and references therein.
[3] R. Ma *et al.*, J. Phys. G **16**, 1233 (1990).
[4] E. S. Paul *et al.*, J. Phys. G **18**, 121 (1992).
[5] P. H. Regan *et al.*, J. Phys. G **18**, 847 (1992).
[6] P. Willsau *et al.*, Phys. Rev. C **48**, R494 (1993).
[7] D. Bazzacco *et al.*, Phys. Lett. B **309**, 235 (1993); Phys. Rev. C **49**, R2281 (1994).
[8] C. M. Petrache *et al.*, Nucl. Phys. **A617**, 228 (1997).
[9] C. Rossi Alvarez *et al.*, Phys. Rev. C **54**, 57 (1996).
[10] S. M. Mullins *et al.*, Phys. Rev. C **47**, R2447 (1993).
[11] N. H. Medina, F. Brandolini, D. Bazzacco, P. Pavan, C. Rossi-Alvarez, R. Burch, S. Lunardi, R. Menegazzo, M. De Poli, G. Maron, R.V. Ribas, and M. Ionescu-Bujor, Nucl. Phys. **A589**, 106 (1995).
[12] R. Wyss, J. Nyberg, A. Johnson, R. Bengtsson, and W. Nazarewicz, Phys. Lett. B **215**, 211 (1988).
[13] Jing-ye Zhang and N. Xu, Phys. Rev. C **43**, 2449 (1999).
[14] F. R. Espinoza-Quiñones *et al.*, Phys. Rev. C **60**, 054304 (1999).
[15] D. Bazzacco, in Proceedings of the International Conference on Nuclear Structure at High Angular Momentum, Ottawa, 1992, Report No. AECL 10613, Vol. 2, p. 376.
[16] E. Farnea *et al.*, Nucl. Instrum. Methods Phys. Res. A **400**, 87 (1998).
[17] P. Spolaore, J. D. Larson, C. Signorini, S. Beghini, Z. Xi-Kai, and S. Hou-Zhi, Nucl. Instrum. Methods Phys. Res. A **238**, 381 (1985).
[18] P. Spolaore *et al.*, Nucl. Instrum. Methods Phys. Res. A **359**, 500 (1995).
[19] F. Pühlhofer, Nucl. Phys. **A280**, 267 (1977).
[20] W. T. Milner, Holifield Heavy Ion Research Facility Computer Handbook, Oak Ridge National Laboratory, Oak Ridge, Tennessee, 1987.
[21] D. Radford, Nucl. Instrum. Methods Phys. Res. A **361**, 297 (1995).
[22] F. Iachello and D. Vretenar, Phys. Rev. C **43**, 945 (1991).
[23] S. Frauendorf, Z. Phys. A **358**, 163 (1997).
[24] F. Brandolini *et al.*, Phys. Lett. B **388**, 468 (1996).
[25] F. G. Kondev *et al.*, Phys. Rev. C **60**, 011303 (1999).
[26] C. M. Petrache *et al.*, Phys. Lett. B **383**, 145 (1996).

PHYSICAL REVIEW C, VOLUME 60, 054304

High-spin state spectroscopy in ^{143}Tb

F. R. Espinoza-Quiñones*
Departamento de Física—CCE, Universidade Estadual de Londrina, Londrina, PR, Brazil

M. A. Rizzutto
Departamento de Ciências Exatas e Tecnológicas, Faculdades Integradas de Guarulhos Guarulhos, SP, Brazil

E. W. Cybulska, W. A. Seale, J. R. B. Oliveira, N. H. Medina, R. V. Ribas, and M. N. Rao
Instituto de Física, Universidade de São Paulo, São Paulo, SP, Brazil

D. Bazzacco, F. Brandolini, S. Lunardi, C. M. Petrache, Zs. Podolyák, C. Rossi-Alvarez, F. Soramel, and C. A. Ur
Dipartimento di Fisica dell'Università, and INFN, Sezione di Padova, Padova, Italy

M. A. Cardona,† G. de Angelis, D. R. Napoli, P. Spolaore, A. Gadea, D. De Acuña, M. De Poli, E. Farnea, D. Foltescu, M. Ionescu-Bujor,‡ A. Iordachescu,‡ V. Roca,§ and F. Terrasi‖
INFN, Laboratori Nazionali di Legnaro, Legnaro, Italy

A. Chatterjee and A. Saxena
Bhabha Atomic Research Center, Bombay, India

L. Sajo Bohus
Instituto de Fisica, Universidad Simon Bolivar, Caracas, Venezuela

(Received 21 December 1998; revised manuscript received 18 May 1999; published 27 September 1999)

The ^{143}Tb nucleus has been studied with the ^{92}Mo (^{54}Fe, $3p\gamma$) reaction at 240-MeV incident energy, extending the systematics of odd-A, $N=78$ isotones to higher Z. For the yrast band, excited states up to a spin of $59/2^-$ have been observed. The first allowed backbend occurs at a rotational frequency of $\hbar\omega = 0.38$ MeV. Three- and five-quasiparticle structures were identified, similar to those seen in lower mass $N = 78$ isotones. Two of these structures have characteristics typical of mixed proton-neutron oblate configurations with one pair of aligned $h_{11/2}$ neutrons. In addition, two bands consisting of stretched $E2$ transitions have been observed with no known analogous structures in neighboring nuclei. The results are discussed in terms of the cranking model. [S0556-2813(99)03310-5]

PACS number(s): 21.10.Re, 23.20.En, 23.20.Lv, 27.60.+j

I. INTRODUCTION

Neutron-deficient nuclei in the $A \approx 130$–140 mass region display a rich variety of rotational band structures. Axially symmmetric prolate shapes ($\gamma = 0°$) are favored for these nuclei with γ-soft cores, for the $h_{11/2}$ quasiproton excitations from the lower midshell. The quasineutrons, on the other hand, from the upper part of this shell exert a driving force towards collectively rotating oblate nuclear shapes ($\gamma = -60°$, according to the Lund convention [1]), resulting in shape changes in these nuclei.

In odd-Z nuclei cranked shell model (CSM) calculations predict that, as the nuclear shape changes from prolate to oblate, the first allowed $h_{11/2}$ proton crossing frequency rises while that of the $h_{11/2}$ neutron crossing falls. The alignments of a pair of allowed protons and neutrons can occur at similar rotational frequencies, giving rise to shape coexistence effects.

Systematics for several $N=78$ odd-proton nuclei, ^{137}Pr [2], ^{139}Pm [3], and ^{141}Eu [4], including both prolate and oblate nuclear shapes are available in the literature. The prolate nuclear shapes involve one $h_{11/2}$ proton at low spin, and at higher spins, the $[\pi h_{11/2}]^3$ configuration due to the alignment of the second and third $h_{11/2}$ protons. Three quasiparticle configurations $\pi h_{11/2} \otimes [\nu h_{11/2}]^2$ with collective oblate shapes induced by quasineutron alignments have also been observed in these nuclei. In addition to the bands of negative parity, bands believed to be built on positive parity three quasiparticle configurations, viz., $[\pi d_{5/2}, \pi g_{7/2}] \otimes [\pi h_{11/2}]^2$ have been seen. Moreover, CSM calculations predict configurations involving protons and $h_{11/2}$ neutrons with collective oblate shapes, with five quasiparticles. Possible

*Present address: Departamento de Engenharia Química, Universidade Estadual do Oeste do Paraná (UNIOESTE), Toledo, PR, Brazil.

†Permanent address: Unidad de Actividad Fisica, Comisíon Nacional de Energia Atomica, Buenos Aires, Argentina.

‡Permanent address: Institute of Physics and Nuclear Engineering, Bucharest, Romania.

§Permanent address: Dipartimento di Scienze Fisiche, Universitá Federico II, Napoli and INFN, Sezione di Napoli, Napoli, Italy.

‖Permanent address: Dipartimento di Scienze Ambientali, Seconda Universitá di Napoli, via Arena 22, 81100 Caserta and INFN, Sezione di Napoli, Napoli, Italy.

configurations, such as $\pi h_{11/2}\otimes[\nu h_{11/2}]^2\otimes[\pi g_{7/2}]^2$, $\pi h_{11/2}\otimes[\nu h_{11/2}]^4$, and $\pi h_{11/2}\otimes[\nu h_{11/2}]^3\otimes\nu g_{7/2}$ have been tentatively identified in these works.

The present work is an extension of the systematics of $N=78$ isotones to the ^{143}Tb nucleus with $Z=65$. The lowest three transitions (520.8, 674.0, and 771.9 keV) in the yrast band were known previously [5]. A preliminary level scheme extending to $\approx$4.3 MeV had been obtained earlier by the Milan-Padova group [6]. In the present work, information on high spin states in this nucleus has been obtained up to an excitation energy of 10.1 MeV. Several rotational bands have been identified which resemble previously observed structures in other isotones with $Z=59$, 61, and 63.

II. EXPERIMENTAL PROCEDURES

High spin states in the odd-Z nucleus ^{143}Tb have been populated by the ^{92}Mo(^{54}Fe, $3p\gamma$)^{143}Tb reaction, at 240-MeV incident beam energy. The $3p$ channel was the strongest channel populated in this experiment, which had as an objective the search for the first excited states of the β-delayed proton emitter ^{141}Dy [7]. The target used was an approximately 1.0 mg/cm^2 thick enriched ^{92}Mo foil. The beam was provided by the tandem XTU accelerator of Legnaro National Laboratories. γ rays have been detected using the GASP array [8] composed of 40 Compton-suppressed high-efficiency HPGe and the 80-element BGO inner ball. The multitelescope light-charged-particle detector array (ISIS) [9], consisting of 40 Si surface-barrier ΔE-E telescopes, enabled the selection of the multiplicities of the evaporated charged particles in coincidence with the observed γ rays. In order to increase the detection sensitivity and permit the identification of the various masses produced in the reaction, the recoil mass spectrometer (RMS) [10] was coupled to GASP. The coupled GASP-RMS system has an intrinsic mass resolution better than 1/300 and the transmission efficiency in this experiment was about 1%. Events have been collected on tape when at least two Compton-suppressed HPGe detectors and two BGO detectors fired in coincidence. A total of 1.3×10^9 Compton-suppressed events was collected.

III. RESULTS

The data have been sorted into charged particle-γ-γ, mass-γ-γ, and also charged particle-mass-γ cubes. Matrices were then obtained with appropriate conditions on the particle type and multiplicity to select the events associated with the $3p$ channel and mass 143. This procedure permitted unambiguous assignment of several newly observed γ transitions to the ^{143}Tb nucleus. In order to enhance the different band structures seen in ^{143}Tb, fully symmetrized γ-γ-γ cubes were used to construct γ-γ matrices in coincidence with the strongest transitions in each observed regular sequence. Background-subtracted double gated spectra generated from these matrices were used to construct the level scheme of ^{143}Tb. These matrices were analyzed using the VAXPAK [11] and RADWARE [12] spectrum analysis codes. Examples of some gated spectra are displayed in Fig. 1.

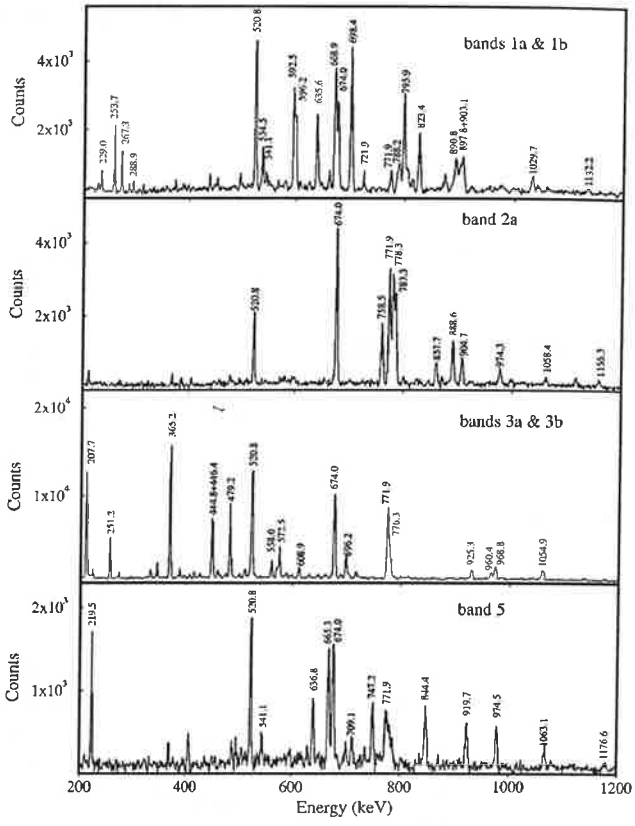

FIG. 1. Double-gated coincidence spectra for bands 1, 2, 3, and 5 in ^{143}Tb with gates set on several transitions in each structure. Bands 3a and 3b, spectrum gated on the 867.5-keV transition; band 5, the multiple peak at $\approx$772 keV appears due to contamination of γ rays of similar energies in the gate.

γ-ray cascades were assigned to ^{143}Tb on the basis of coincidence relationships, relative intensities and the systematics of odd-Z $N=78$ isotones. The intensities of the transitions were determined from the total projection of the matrix produced by gating the charged particle-γ-γ cube on the $3p$ channel. The sum of the relative intensities of all the transitions feeding the 520.8-keV, $15/2^-$ level was normalized to 1000.

The assignment of the spins and parities to the ^{143}Tb levels was based on the DCO (directional correlation from oriented states) ratios. A γ-γ matrix was constructed by sorting the data from the 8 detectors positioned at the 72° and 108° rings in the GASP array against the 12 detectors in the 34° and the 146° rings. Gates were set on both axes on several strong quadrupole transitions and the intensity of other transitions observed in the two spectra have been extracted. If $I_\gamma(72°+108°)$ and $I_\gamma(34°+146°)$ represent the intensity of a transition when gating on $(72°+108°)$ and $(34°+146°)$ axes, respectively, the theoretical DCO ratios

$$R_{\mathrm{DCO}}=\frac{I_\gamma(72°+108°)}{I_\gamma(34°+146°)},$$

which one obtains, for the present geometry, are R_{DCO}

$=1.00$ for quadrupole transitions and $R_{DCO}=0.55$ for pure dipole transitions. Furthermore, $\Delta I=0$ dipole transitions yield $R_{DCO}=1.07$.

The γ-ray energies and relative intensities of all the transitions assigned to ^{143}Tb are given in Table I, which also shows the DCO ratios and the resulting spin and parity assignments. The level scheme of ^{143}Tb deduced from the present study is shown in Fig. 2.

The lower part of the band labeled 2a is the favored signature of the yrast band, while band 2b (extreme right-hand side of the Fig. 2) formed by the cascade of 875.6- [$(\frac{25}{2}^-) \rightarrow \frac{21}{2}^-$], 807.4- ($\frac{21}{2}^- \rightarrow \frac{17}{2}^-$), and 677.2-keV ($\frac{17}{2}^- \rightarrow \frac{13}{2}^-$) transitions, is the unfavored component of the $\pi h_{11/2}$ decoupled yrast band, which depopulates through the 541.1-keV transition to the $11/2^-$ level.

DCO ratios determined the $E2$ character for the transitions deexciting the levels shown with definite spins and parities in the cascades 1a, 1b, and 2a. The assignment of the spin and parity of $\frac{17}{2}^-$ to the 1423.8-keV level populated by the 668.9-keV transition in band 1b could be independently confirmed based on the following arguments.

(i) The 229.0-keV dipole transition, linking this level to the $\frac{19}{2}^-$ level of band 2a sets a minimum possible spin of $\frac{17}{2}$, while the 882.7-keV $E2$ transition, linking this level to the 541.1-keV $\frac{13}{2}^-$ level of band 2b sets a maximum spin of $\frac{17}{2}$ and negative parity.

(ii) This assignment is corroborated by the $E2$ character of the in-band (1b) transitions together with the dipole character of the 903.1-keV linking transition between cascade 1b and the ground state band (2b). The DCO ratios for the other linking transitions between these two bands which could be obtained from the present data (897.8 and 536.1 keV) are also consistent with the spin assignments shown. The spin of the lowest level of the cascade of quadrupole transitions 1b has been assigned to be $\frac{13}{2}^-$ consistent with the DCO ratio (0.92 ± 0.08) of the 635.6-keV transition feeding this level. This level deexcites to the $\frac{11}{2}^-$ ground state through the 253.7- and 534.5-keV transitions. It is not possible to confirm the ordering of the 253.7- and the 534.5-keV transitions on the level scheme. Above the $\frac{33}{2}^-$ state at 3979.7 keV, a weakly populated, $\Delta I=2$ cascade (1a) is seen, consisting of 658.0, 783.3, 802.3, 871.0, and 1040.3-keV transitions.

A discontinuity in the main yrast sequence (band 2) is observed around 2.8 MeV, where two bands (labeled 2a and 3) are built on two distinct $\frac{27}{2}^-$ states, which depopulate into the $\pi h_{11/2}$ ground state band through the strong 778.3- and 867.5-keV $E2$ transitions, respectively. These two bands show very different rotational characteristics. The negative parity band 2a built on the lower $\frac{27}{2}^-$ level, is a $\Delta I=2$ band. On the other hand, the structure labeled 3a and 3b, above the higher $\frac{27}{2}^-$ level, has strong $M1$ and weaker $E2$ transitions and decays into the ground state band also through the 89.4- ($\frac{27}{2}^- \rightarrow \frac{27}{2}^-$), 455.1- ($\frac{29}{2}^- \rightarrow \frac{27}{2}^-$), and 661.7-keV ($\frac{31}{2}^- \rightarrow \frac{27}{2}^-$) transitions. Band 3 was observed up to spin $\frac{55}{2}^-$, at the energy of 8750.9 keV and shows a pronounced backbend around spin $\frac{41}{2}^-$.

The structure labeled 4 consisting of the four sequences of transitions 4a, 4b, 4c, and 4d, decays to levels of both signature partners of the g.s. band through several high-energy (1288.9, 1116.0, 1014.8, 951.7, 733.0, and 709.1 keV) transitions with about 5–10 % relative intensities. Similar strutures have been observed in the neighbouring odd-proton nuclei, ^{137}Pr, ^{139}Pm, and ^{141}Eu, which are based on positive-parity configurations linked to the negative-parity ground state band through $E1$ linking transitions [4]. In analogy, we assign positive parity to the levels of structure 4. The $E1$ multipolarities assigned to the two linking transitions, 1116.0 and 951.7 keV, both ($\frac{21}{2}^+ \rightarrow \frac{19}{2}^-$) are consistent with their DCO ratios. The structures 4c and 4d probably consist of $\Delta I=2$ sequences and the rather irregular sequences 4a and 4b are composed, at their lower part, of fairly strong $E2$ transitions and above spin $\frac{37}{2}^+$, of strong $M1$ transitions. The 118.1-, 219.5-, and 155.7-keV transitions deexciting the structures 4a, 4b, and 4d into the lowest excited states, have relative intensities of 1.75, 17.4, and 10.1 %, respectively, and their placements and ordering in band 4 have been unambiguously established on intensity arguments and the linking transitions to the yrast band. The 219.5-keV transition has $DCO=0.56\pm0.02$, consistent with its assigned $E1$ multipolarity.

A weak stretched $E2$ band, labeled 5, was observed up to 9.3 MeV excitation energy. This band decays to the level at 2302.5 keV in band 4 with the spin assignment of $\frac{23}{2}^+$, by means of the 636.8-keV transition, which has a DCO of 0.92 ± 0.14 and thus has a quadrupole multipolarity. The spin of the 2302.5-keV level is based on the DCO ratios of the strong deexciting transitions to the unfavored component of the yrast band.

IV. DISCUSSION

The experimental Routhians and alignments (i_x) shown in Figs. 3 and 4 as a function of rotational frequency ($\hbar\omega$), were calculated according to the standard procedure described in Ref. [13], with the Harris parametrization [14] of the moment of inertia $\mathcal{J}_0=12\,\mathrm{MeV}^{-1}\hbar^2$ and $\mathcal{J}_1=25\,\mathrm{MeV}^{-3}\hbar^4$, used in the case of the neighboring nucleus ^{141}Eu [4]. The quasiparticle Routhians for a deformed Woods-Saxon potential calculated for $Z=65$ and $N=78$ are shown in Fig. 5. The deformation parameters used ($\beta_2=0.18$, $\beta_4=0.0$, $\gamma=-30°$) were chosen in accordance with the total Routhian surface (TRS) calculations [15] for the $\pi h_{11/2}$ configuration. The pairing gap parameter was calculated self consistently for $\omega=0$ and was kept fixed for other frequencies. The lowest quasiproton energy levels of negative parity are labeled A, B, C, and D; and those of positive parity ($\pi g_{7/2}$, $\pi d_{5/2}$), E, F, G, and H. Similarly, the lowest quasineutron energy levels of negative parity are labeled a, b, c, and d.

A. The yrast band

Bands 2a and 2b are yrast at low spin and can be associated with the $\pi h_{11/2}$ favored and unfavored signature partners A and B, respectively. TRS calculations predict a triaxial shape ($\gamma\approx-27°$) for this configuration, which reflects

TABLE I. Energies, spin assignments, relative intensities, and DCO ratios for the γ-ray transitions in ^{143}Tb. The γ-ray energies are accurate to ± 0.3 keV rising to ± 0.5 keV for the weak transitions. E_i and E_f are the energies of the initial and final states corresponding to each transition.

E_γ [keV]	E_i [keV]	E_f [keV]	$I_i^\pi \rightarrow I_f^\pi$	I_γ	DCO ratio
89.4	2834.5	2745.2	$27/2^- \rightarrow 27/2^-$	4.8(2)	0.73(19)
118.1	1927.4	1809.4	$19/2^- \rightarrow 17/2^-$	17.5(6)	0.57(10)
122.1	5191.2	5069.2	$37/2^+ \rightarrow (35/2^+)$	3.0(1)	
145.8	5337.0	5191.2	$39/2^+ \rightarrow 37/2^+$	29(1)	0.61(5)
146.0	2834.5	2688.7	$27/2^- \rightarrow 25/2^-$	1.1(1)	
152.7	3231.1	3078.6	$(27/2^+) \rightarrow 27/2^+$	6.1(2)	
155.7	2302.5	2146.7	$23/2^+ \rightarrow 21/2^+$	101(3)	0.56(2)
167.5	5108.7	4941.2	$39/2^- \rightarrow 37/2^-$	40(1)	0.57(4)
175.7	5337.0	5161.2	$39/2^+ \rightarrow 37/2^+$	16.6(5)	0.53(3)
207.7	3407.0	3199.6	$31/2^- \rightarrow 29/2^-$	99(3)	0.61(1)
211.2	3996.5	3785.3		3.0(2)	
215.6	4212.0	3996.5		2.4(1)	
219.5	2146.7	1927.4	$21/2^+ \rightarrow 19/2^-$	174(5)	0.56(2)
229.0	1423.8	1194.8	$17/2^- \rightarrow 19/2^-$	6.6(3)	0.63(10)
251.2	5804.8	5553.6	$43/2^- \rightarrow 41/2^-$	38(1)	0.55(3)
253.7	788.0	534.5	$13/2^- \rightarrow$	22(1)	0.51(5)
267.3	788.0	520.8	$13/2^- \rightarrow 15/2^-$	13.3(6)	0.72(8)
268.4	5989.6	5721.2	$43/2^+ \rightarrow 41/2^+$	47(1)	0.57(2)
271.6	2582.4	2310.8	$23/2^+ \rightarrow 21/2^+$	8.2(4)	0.77(13)
280.0	2582.4	2302.5	$23/2^+ \rightarrow 23/2^+$	5.7(2)	0.72(15)
288.9	2688.7	2399.7	$25/2^- \rightarrow 23/2^-$	6.9(3)	
290.8	4664.0	4373.5	$35/2^+ \rightarrow 33/2^+$	13.2(4)	0.52(8)
307.7	4287.3	3979.7	$35/2^- \rightarrow 33/2^-$	3.7(2)	
321.6	6445.5	6124.0	$45/2^+ \rightarrow 43/2^+$	8.7(3)	0.52(11)
341.0	4941.2	4600.3	$37/2^- \rightarrow 35/2^-$	18.9(6)	0.71(6)
365.2	3199.6	2834.5	$29/2^- \rightarrow 27/2^-$	171(5)	0.57(2)
369.4	5145.0	4775.6	$39/2^- \rightarrow 37/2^-$	4.0(2)	
380.9	8790.0	8409.2		3.6(2)	
384.3	5721.2	5337.0	$41/2^+ \rightarrow 39/2^+$	78(2)	0.54(3)
389.6	3468.2	3078.6	$29/2^+ \rightarrow 27/2^+$	15.8(6)	0.36(9)
392.0	1927.4	1535.4	$19/2^- \rightarrow 17/2^-$	10.1(4)	
392.5	7734.4	7342.2	$51/2^- \rightarrow 49/2^-$	3.0(2)	
402.8	6124.0	5721.2	$43/2^+ \rightarrow 41/2^+$	34(1)	
403.0	2705.5	2302.5	$25/2^+ \rightarrow 23/2^+$	58(2)	0.53(4)
411.3	6773.8	6362.6	$47/2^- \rightarrow 45/2^-$	9.1(3)	0.59(21)
423.2	8409.2	7986.0	$\rightarrow 53/2^-$	7.6(3)	
430.8	7336.9	6906.1	$\rightarrow 47/2^+$	17.3(6)	
434.6	6033.7	5599.1	$43/2^- \rightarrow 41/2^-$	6.8(3)	
434.8	2834.5	2399.7	$27/2^- \rightarrow 23/2^-$	9.7(4)	
444.8	5553.6	5108.7	$41/2^- \rightarrow 39/2^-$	60(2)	0.49(3)
446.4	4332.4	3886.2	$35/2^- \rightarrow 33/2^-$	75(2)	0.50(3)
448.5	6938.3	6489.8	$47/2^- \rightarrow 45/2^-$	2.8(2)	
450.1	6895.6	6445.5	$\rightarrow 45/2^+$	9.3(3)	
455.1	3199.6	2745.2	$29/2^- \rightarrow 27/2^-$	15.2(6)	
455.9	6445.5	5989.6	$45/2^+ \rightarrow 43/2^+$	44(1)	0.50(5)
460.7	6906.1	6445.5	$47/2^+ \rightarrow 45/2^+$	26(1)	0.48(7)
475.9	3979.7	3503.8	$33/2^- \rightarrow 31/2^-$	11.3(5)	
479.2	3886.2	3407.0	$33/2^- \rightarrow 31/2^-$	167(5)	0.57(3)
484.2	2786.8	2302.5	$25/2^+ \rightarrow 23/2^+$	32(1)	0.60(9)
485.3	2796.1	2310.8	$(25/2^+) \rightarrow 21/2^+$	13(1)	

TABLE I. (*Continued*).

E_γ [keV]	E_i [keV]	E_f [keV]	$I_i^\pi \rightarrow I_f^\pi$	I_γ	DCO ratio
497.3	5161.2	4664.0	$37/2^+ \rightarrow 35/2^+$	16.1(6)	0.48(7)
503.7	1927.4	1423.8	$19/2^- \rightarrow 17/2^-$	16.6(6)	0.82(10)
507.5	8916.6	8409.2		3.4(2)	
510.0	3588.5	3078.6	$29/2^+ \rightarrow 27/2^+$	19(1)	0.68(10)
514.0	9430.6	8916.6		4.1(3)	
518.1	8252.5	7734.4	$(53/2^-) \rightarrow 51/2^-$	14.3(6)	
520.8	520.8	0.0	$15/2^- \rightarrow 11/2^-$	(1000)[a]	0.92(2)
527.5	5191.2	4664.0	$37/2^+ \rightarrow 35/2^+$	18.4(6)	0.71(7)
530.8	1072.0	541.1	$15/2^- \rightarrow 13/2^-$	27(1)	0.67(12)
534.5	534.5	0.0	$\rightarrow 11/2^-$	22(1)	1.02(11)
536.1	3281.3	2745.2	$29/2^- \rightarrow 27/2^-$	35(1)	
541.1	541.1	0.0	$13/2^- \rightarrow 11/2^-$	171(4)	0.43(3)
543.2	7033.0	6489.8	$47/2^- \rightarrow 45/2^-$	1.6(3)	0.70(17)
558.0	6362.6	5804.8	$45/2^- \rightarrow 43/2^-$	37(1)	0.52(6)
566.8	3797.7	3231.1	$31/2^+ \rightarrow (27/2^+)$	21(1)	
568.1	7342.2	6773.8	$49/2^- \rightarrow 47/2^-$	18.9(6)	
572.5	3407.0	2834.5	$31/2^- \rightarrow 27/2^-$	72(2)	0.96(6)
575.8	4373.5	3797.7	$33/2^+ \rightarrow 31/2^+$	11.7(4)	0.71(12)
585.7	3785.3	3199.6	$\rightarrow 29/2^-$	17(1)	
588.2	2399.7	1811.6	$23/2^- \rightarrow (19/2^-)$	15(1)	
591.2	1809.4	1218.3	$17/2^- \rightarrow 17/2^-$	4.4(5)	1.02(7)
592.5	3281.3	2688.7	$29/2^- \rightarrow 25/2^-$	111(3)	1.02(4)
596.2	2688.7	2092.6	$25/2^- \rightarrow 21/2^-$	86(3)	0.89(6)
604.1	3186.5	2582.4	$(27/2^+) \rightarrow 23/2^+$	12.2(5)	0.72(15)
608.9	4941.2	4332.4	$37/2^- \rightarrow 35/2^-$	27(1)	0.69(9)
614.6	1809.4	1194.8	$17/2^- \rightarrow 19/2^-$	6.8(5)	
617.2	1811.6	1194.8	$(19/2^-) \rightarrow 19/2^-$	7.2(5)	
631.6	6230.7	5599.1	$43/2^- \rightarrow 41/2^-$	2.5(2)	
635.6	1423.8	788.0	$17/2^- \rightarrow 13/2^-$	60(2)	0.92(8)
636.8	2939.3	2302.5	$27/2^+ \rightarrow 23/2^+$	8.5(5)	0.92(14)
643.8	7986.0	7342.2	$53/2^- \rightarrow 49/2^-$	8.2(4)	1.04(17)
652.4	5989.6	5337.0	$43/2^+ \rightarrow 39/2^+$	19(1)	
658.0	5448.1	4790.2	$39/2^- \rightarrow 35/2^-$	12.6(5)	0.85(15)
661.7	3407.0	2745.2	$31/2^- \rightarrow 27/2^-$	57(2)	1.17(7)
665.3	3604.6	2939.3	$31/2^+ \rightarrow 27/2^+$	7.6(4)	1.05(23)
668.9	2092.6	1423.8	$21/2^- \rightarrow 17/2^-$	81(3)	1.03(5)
672.5	5448.1	4775.6	$39/2^- \rightarrow 37/2^-$	13(1)	
674.0	1194.8	520.8	$19/2^- \rightarrow 15/2^-$	808(25)	0.96(3)
677.2	1218.3	541.1	$17/2^- \rightarrow 13/2^-$	122(4)	[b]
686.6	3886.2	3199.6	$33/2^- \rightarrow 29/2^-$	11.0(5)	0.77(11)
696.2	5804.8	5108.7	$43/2^- \rightarrow 39/2^-$	69(2)	1.01(8)
697.7	1218.3	520.8	$17/2^- \rightarrow 15/2^-$	54(2)	
698.4	3979.7	3281.3	$33/2^- \rightarrow 29/2^-$	121(4)	0.97(3)
709.1	1927.4	1218.3	$19/2^- \rightarrow 17/2^-$	124(4)	0.77(4)
714.2	4600.3	3886.2	$35/2^- \rightarrow 33/2^-$	20(1)	
719.1	3797.7	3078.6	$31/2^+ \rightarrow 27/2^+$	27(1)	0.96(15)
721.9	2688.7	1966.9	$25/2^- \rightarrow 23/2^-$	27(1)	0.82(14)
732.9	3919.4	3186.5	$(31/2^+) \rightarrow (27/2^+)$	6.8(4)	1.43(43)
733.0	1927.4	1194.8	$19/2^- \rightarrow 19/2^-$	50(2)	1.15(13)
736.6	1809.4	1072.0	$17/2^- \rightarrow 15/2^-$	5.6(4)	
739.1	1811.6	1072.0	$(19/2^-) \rightarrow 15/2^-$	13(1)	
747.2	4351.8	3604.6	$35/2^+ \rightarrow 31/2^+$	10.5(5)	0.96(10)

TABLE I. (*Continued*).

E_γ [keV]	E_i [keV]	E_f [keV]	$I_i^\pi \rightarrow I_f^\pi$	I_γ	DCO ratio
758.5	3503.8	2745.2	$31/2^- \rightarrow 27/2^-$	112(4)	1.07(3)
771.7	3568.2	2796.1	$(29/2^+) \rightarrow (25/2^+)$	20(1)	0.94(11)
771.9	1966.9	1194.8	$23/2^- \rightarrow 19/2^-$	615(19)	1.01(2)
776.1	3078.6	2302.5	$27/2^+ \rightarrow 23/2^+$	82(3)	1.00(3)
776.3	5108.7	4332.4	$39/2^- \rightarrow 35/2^-$	65(2)	1.19(7)
778.3	2745.2	1966.9	$27/2^- \rightarrow 23/2^-$	305(9)	1.16(6)
782.6	6230.7	5448.1	$43/2^- \rightarrow 39/2^-$	13(1)	1.71(21)
783.3	4287.3	3503.8	$35/2^- \rightarrow 31/2^-$	75(3)	1.27(6)
784.8	4373.5	3588.5	$33/2^+ \rightarrow 29/2^+$	41(1)	0.96(24)
785.0	4353.2	3568.2	$(33/2^+) \rightarrow (29/2^+)$	11(1)	
787.3	5161.2	4373.5	$37/2^+ \rightarrow 33/2^+$	23(1)	1.31(51)
788.2	788.0	0.0	$13/2^- \rightarrow 11/2^-$	35(2)	
795.9	4775.6	3979.7	$37/2^- \rightarrow 33/2^-$	91(3)	0.96(5)
801.7	3588.5	2786.8	$29/2^+ \rightarrow 25/2^+$	3.2(2)	1.31(26)
802.3	7033.0	6230.7	$47/2^- \rightarrow 43/2^-$	22(1)	0.97(12)
807.4	2025.6	1218.3	$21/2^- \rightarrow 17/2^-$	22(1)	0.91(19)
810.5	4790.2	3979.7	$35/2^- \rightarrow 33/2^-$	13.2(6)	0.60(9)
817.4	5191.2	4373.5	$37/2^+ \rightarrow 33/2^+$	16.9(6)	
823.4	5599.1	4775.6	$41/2^- \rightarrow 37/2^-$	54(2)	1.15(7)
832.1	4751.5	3919.4	$(35/2^+) \rightarrow (31/2^+)$	13.4(6)	
837.7	5191.2	4353.2	$37/2^+ \rightarrow (33/2^+)$	10.1(4)	
844.4	5196.2	4351.8	$39/2^+ \rightarrow 35/2^+$	14.7(6)	0.84(15)
857.7	5145.0	4287.3	$39/2^- \rightarrow 35/2^-$	55(2)	0.95(5)
866.5	4664.0	3797.7	$35/2^+ \rightarrow 31/2^+$	27(1)	
867.5	2834.5	1966.9	$27/2^- \rightarrow 23/2^-$	232(1)	1.01(3)
871.0	7904.1	7033.0	$51/2^- \rightarrow 47/2^-$	14.9(6)	0.79(12)
875.6	2901.2	2025.6	$(25/2^-) \rightarrow 21/2^-$	11.0(6)	
880.3	4287.3	3407.0	$35/2^- \rightarrow 31/2^-$	6.7(4)	
882.7	1423.8	541.1	$17/2^- \rightarrow 13/2^-$	8.5(5)	1.29(18)
883.0	3588.5	2705.4	$29/2^+ \rightarrow 25/2^+$	15.5(6)	1.36(41)
888.6	6033.7	5145.0	$43/2^- \rightarrow 39/2^-$	44(1)	0.90(4)
890.8	6489.8	5599.1	$45/2^- \rightarrow 41/2^-$	35(1)	1.12(10)
897.8	2092.6	1194.8	$21/2^- \rightarrow 19/2^-$	30(1)	0.77(8)
903.1	1423.8	520.8	$17/2^- \rightarrow 15/2^-$	37(1)	0.60(5)
904.7	6938.3	6033.7	$47/2^- \rightarrow 43/2^-$	27(1)	0.90(4)
905.3	4373.5	3468.2	$33/2^+ \rightarrow 29/2^+$	20(1)	0.90(11)
919.7	6115.9	5196.2	$43/2^+ \rightarrow 39/2^+$	9.8(4)	0.89(15)
925.3	4332.4	3407.0	$35/2^- \rightarrow 31/2^-$	58(2)	1.02(9)
928.6	3231.1	2302.5	$(27/2^+) \rightarrow 23/2^+$	15.7(6)	
951.7	2146.7	1194.8	$21/2^+ \rightarrow 19/2^-$	33(1)	0.54(10)
960.4	7734.4	6773.8	$51/2^- \rightarrow 47/2^-$	30(1)	1.05(7)
968.8	6773.8	5804.8	$47/2^- \rightarrow 43/2^-$	60(2)	1.02(4)
974.3	7912.7	6938.3	$51/2^- \rightarrow 47/2^-$	17(1)	1.00(13)
974.5	7090.3	6115.9	$(47/2^+) \rightarrow 43/2^+$	6.6(4)	0.72(18)
979.6	7342.2	6362.6	$49/2^- \rightarrow 45/2^-$	9.7(4)	0.99(21)
994.6	1535.4	541.1	$17/2^- \rightarrow 13/2^-$	14(1)	
1014.8	1535.4	520.8	$17/2^- \rightarrow 15/2^-$	12(1)	0.71(17)
1016.6	8750.9	7734.4	$55/2^- \rightarrow 51/2^-$	6.6(3)	1.06(20)
1029.7	7519.5	6489.8	$49/2^- \rightarrow 45/2^-$	17.1(6)	1.02(12)
1040.3	8944.3	7904.1	$55/2^- \rightarrow 51/2^-$	11.7(5)	1.42(30)
1054.9	4941.2	3886.2	$37/2^- \rightarrow 33/2^-$	60(2)	1.07(11)

TABLE I. (*Continued*).

E_γ [keV]	E_i [keV]	E_f [keV]	$I_i^\pi \rightarrow I_f^\pi$	I_γ	DCO ratio
1058.4	8971.1	7912.7	$55/2^- \rightarrow 51/2^-$	10.0(5)	1.28(20)
1058.4	8971.1	7912.7	$55/2^- \rightarrow 51/2^-$	10.0(5)	1.28(20)
1063.1	8153.5	7090.3	$(51/2^+) \rightarrow (47/2^+)$	3.1(3)	
1116.0	2310.8	1194.8	$21/2^+ \rightarrow 19/2^-$	48(2)	0.50(4)
1132.2	8651.7	7519.5	$53/2^- \rightarrow 49/2^-$	6.2(4)	1.17(17)
1155.3	10126.4	8971.1	$(59/2^-) \rightarrow 55/2^-$	7.5(4)	
1176.6	9330.1	8153.5	$(55/2^+) \rightarrow (51/2^+)$	1.9(2)	
1183.4	5069.2	3886.2	$(35/2^+) \rightarrow 33/2^-$	7.4(5)	
1193.5	4600.3	3407.0	$35/2^- \rightarrow 31/2^-$	16(1)	
1288.9	1809.4	520.8	$17/2^- \rightarrow 15/2^-$	76(3)	0.73(12)

[a]Sum of the relative intensities of γ rays feeding the 520.8-keV level.

[b]The quadrupole nature of the γ ray was obtained from angular distribution data.

the tendency to more triaxial shapes as the number of protons rises in the $h_{11/2}$ subshell. The ^{139}Pm isotone, for example, is quoted to have $\gamma \approx -15°$ [3]. This is a possible explanation for the fact that the signature splitting is rather constant in the $Z=59$ to 65 isotone systematics. For a constant deformation the signature splitting would be expected to decrease as the less aligned $h_{11/2}$ orbits are populated.

The experimental ratio of the reduced transition probabilities $B(M1)/B(E2)$ for the 1218.3-keV, $\frac{17}{2}^-$ level in band 2b, obtained from the relative intensities of the 697.7- and the 677.2-keV transitions, assuming negligible mixing for the $M1$ γ ray, was ≈ 0.13 (see Fig. 6). Somewhat larger values, but within an order of magnitude, have been published for the lower levels in the unfavored partner of the $h_{11/2}$ yrast bands in ^{137}Pr and ^{141}Eu [2,4].

The first allowed proton bandcrossing BC can probably be associated with the gain in alignment of about 6 $\hbar$ (which is a reasonable value for the alignment of the B and C qua-

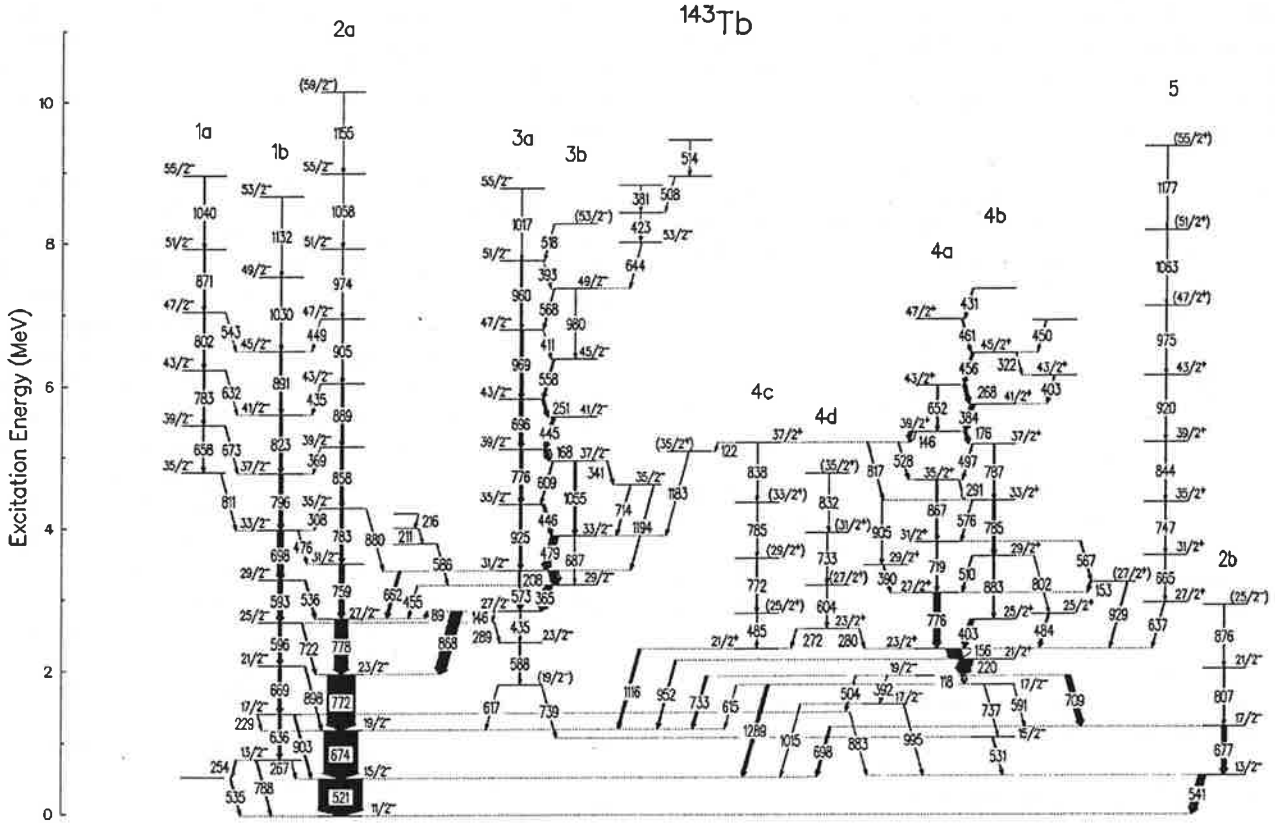

FIG. 2. The level scheme of ^{143}Tb obtained from the ^{92}Mo(^{54}Fe,$3p\gamma$) reaction at 240 MeV.

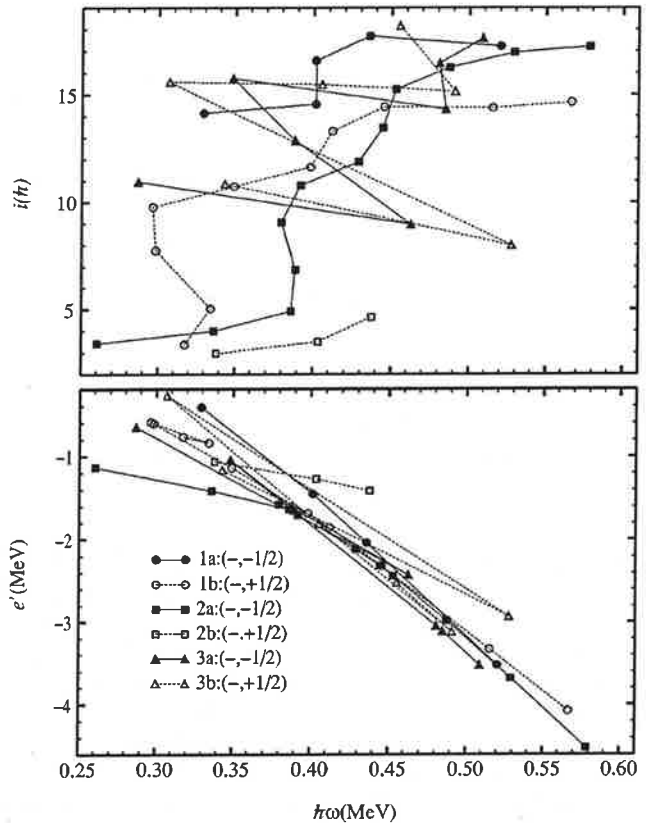

FIG. 3. Experimental quasiparticle (a) alignments and (b) Routhians for the negative parity rotational bands in ^{143}Tb. The following symbols are used: Filled circles, band 1a; open circles, band 1b; filled squares, band 2a; open squares, band 2b; filled triangles, band 3a; and open triangles, band 3b.

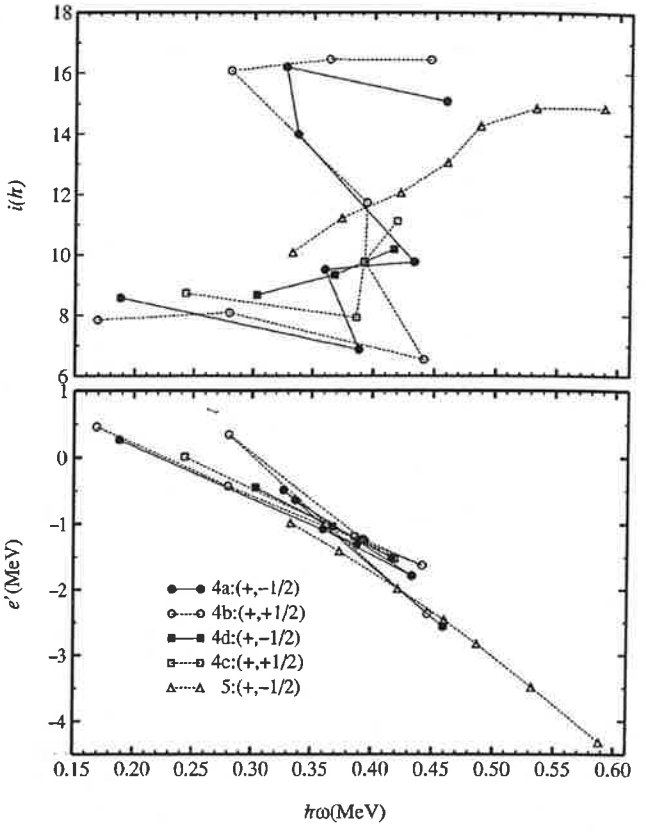

FIG. 4. Experimental quasiparticle (a) alignments and (b) Routhians for the positive parity rotational bands in ^{143}Tb. The following symbols are used: Filled circles, band 4a; open circles, band 4b; open squares, band 4c; filled squares, band 4d; and triangles, band 5.

siprotons), observed to occur in band 2a around $\hbar\omega = 0.38$ MeV. However, an additional upbend of ≈ 4 units is observed at a slightly higher frequency ($\hbar\omega = 0.44$ MeV). A double backbend, due to the simultaneous alignment of a pair of $h_{11/2}$ protons and a pair of $h_{11/2}$ neutrons has been observed at $\hbar\omega = 0.43$ MeV in the yrast band of ^{139}Pm, with a total increase of $\approx 14\hbar$, and with a triaxiality parameter stabilized around $\gamma = -15°$ [3]. In ^{141}Eu, on the other hand, only the BC crossing is observed as a sharp backbend at a frequency of 0.37 MeV [4]. Thus the situation in ^{143}Tb does not resemble that in either of these two isotones. We tend to believe that the additional upbend in band 2a may not correspond to the ab quasineutron alignment, since a higher alignment would be expected for quasineutrons at $\gamma = -27°$. In addition, a change in deformation towards the oblate shape is expected to be induced by the ab quasineutrons modifying the band characteristics. We note that an upbend of a few units of $\hbar$ in the 0.4–0.5 MeV frequency range is observed also in bands 1a, 1b, and 5, in addition to band 2a.

B. Three- and five-quasiparticle oblate configurations

We assign the tentative configuration Aab and Bab with an oblate deformation for the signature partners 3a and 3b, respectively. Both the reduced signature splitting and the strong $M1$ transitions are evidences for this assignment. As discussed also in Ref. [4], the polarization forces of the ab quasineutrons drive the γ-soft shape towards $\gamma \approx -60°$, where the splitting between the AB quasiprotons is small, and the approximately perpendicular coupling of protons and neutrons results in a coherent addition of the components of the magnetic moment responsible for $M1$ radiation, thus enhancing the $M1$ transition probabilities. The large initial alignment of the band is consistent with the presence of the ab aligned quasineutrons. Bands with these characteristics have been seen in several neighboring odd-proton, $N = 74$, 76, and 78 nuclei. (see, for example, ^{131,133}La [16,17], ^{133,137}Pr [18,2], ^{139}Pm [3], and ^{141}Eu [4]). The experimental $B(M1)/B(E2)$ ratios for the signature partners 3a and 3b are shown in Fig. 6 along with those obtained for the other observed configurations in ^{143}Tb in the present work. These ratios have been deduced assuming negligible mixing in the $M1$ transitions. As can be seen from this figure, the present $B(M1)/B(E2)$ values scatter between ≈ 1 to 25 $(\mu_N/e\ \mathrm{b})^2$. Predictions based on the semiclassical model of Dönau and Frauendorf [19], for K values of $\frac{11}{2}, \frac{13}{2}$, below and above the crossing, respectively, are also shown in this figure, as solid lines. These ratios have been published for the $(\pi h_{11/2}) \otimes (\nu h_{11/2})^2$ configuration in ^{137}Pr [2] and ^{141}Eu [4] and vary between approximately 10 and 100 $(\mu_N/e\ \mathrm{b})^2$.

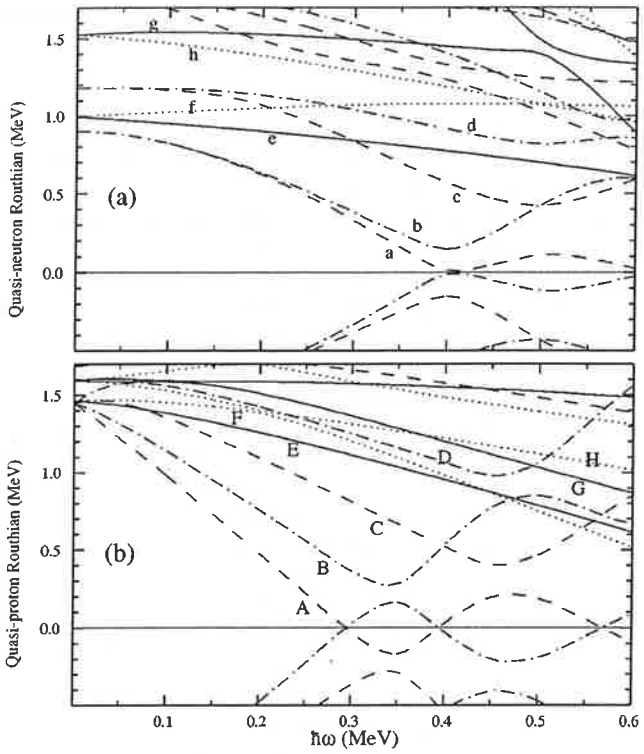

FIG. 5. Quasiparticle Routhians as a function of rotational frequency in ^{143}Tb for (a) neutrons and (b) protons ($\beta_2=0.18$, $\beta_4=0$, $\gamma=-30°$). The following convention is used for the levels: solid line ($\pi=+$, $\alpha=+\frac{1}{2}$), dotted line ($\pi=+$, $\alpha=-\frac{1}{2}$), dashed-dotted line ($\pi=-$, $\alpha=+\frac{1}{2}$), dashed line ($\pi=-$, $\alpha=-\frac{1}{2}$).

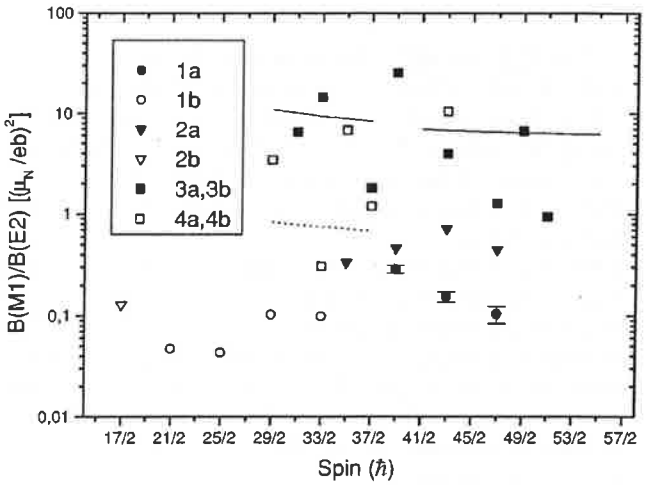

FIG. 6. Experimental $B(M1;I\rightarrow I-1)/B(E2;I\rightarrow I-2)$ ratios of reduced transition probabilities for the various configurations in ^{143}Tb. The following symbols have been used: Filled circles, band 1a; open circles, band 1b; filled triangles, band 2a; open triangles, band 2b; filled squares, band 3a, 3b; open squares, band 4a, 4b. The solid lines are predictions based on the semiclassical model of Dönau and Frauendorf [19] for $K=\frac{11}{2}$ for band 3a, 3b. The dashed line is for band 4a, for $K=\frac{5}{2}$.

Band 3 has a crossing around $\hbar\omega=0.4$ MeV with an alignment gain of 5 $\hbar$. This can be attributed to the BC (for $\alpha=-1/2$) and AD (for $\alpha=+1/2$) crossings. The crossing frequency is, however, lower than expected for $\gamma\approx-60°$ ($\hbar\omega=0.5$ MeV). Adopting this assignment one should infer that the polarizing effect of the pair of aligned quasineutrons ab dominate over the three quasiprotons ABC. Other possible assignments for the high-spin part of the negative parity bands 3a and 3b are, (as also proposed for the bands populating the Aab and Bab configurations in ^{141}Eu), $AEFab$, $Aabcd$ (and respective signature partners), which are however, expected to cross at even higher frequencies and have less parentage to the lower spin part of the band, in contradiction to the decay pattern observed.

C. The negative parity bands 1a and 1b

No structures similar to 1b and 1a are known in nearby odd-Z nuclei. Band 1a behaves as a signature partner to band 1b at high spin. Band 1b appears to be a signature partner of band 2a at moderate and high spins. However, band 2b has the more appropriate characteristics and fits better the systematics of the unfavored signature partner ($\alpha=1/2$) of band 2a at low spin. There is no observed transition linking bands 1b and 2b. These two bands cannot be considered the continuation of one another. Band 1b presents a strong upbend at $\hbar\omega=0.32$ MeV. This is in the frequency region of the AB proton crossing. This might be taken to indicate the absence of the negative parity quasiparticles A and B, which, if present, would block the AB crossing. The next $\pi=-$, $\alpha=+1/2$ quasiparticle is D and is rather high lying according to the calculations. Thus the lower lying $\alpha=-1/2$ signature partner C would be expected to be more easily populated, which is not the case. In addition, after the first crossing the configuration of band 1b would be ABD, which should be the natural continuation of band 2b. In spite of these problems the D configuration crossing with ABD seems to be the most probable interpretation. Another possibility considered is the coupling of the γ vibration, which is observed at rather low excitation in nearby even-even nuclei [20], to the unpaired quasiproton (B). In this case there would be no explanation for the early upbend and for the absence of the favored signature $\alpha=-1/2$ band at low spin, which would result from the coupling of the A quasiparticle to the γ-vibration quadrupole phonon.

The $B(M1)/B(E2)$ ratios obtained for the levels in bands 1a and 1b are shown in Fig. 6 and are much smaller than those obtained for the three quasiparticle bands 3a and 3b, being about 0.05 to 0.3 $(\mu_N/e\ \mathrm{b})^2$. Also shown in Fig. 6 are the $B(M1)/B(E2)$ ratios for the transitions involving bands 2a [≈0.6 $(\mu_N/e\ \mathrm{b})^2$], and 1b [≈0.05–0.10 $(\mu_N/e\ \mathrm{b})^2$].

In conclusion, bands 1b and 1a present an unexpected puzzle which could not be understood from the present analysis. One could question the assignment of negative parity to this band, which seems to be well established from the experimental data, but even for a positive parity assignment there will be great difficulty in explaining the experimental results, particularly the presence of several dipole transitions linking bands 1b and 1a, which is a strong indication of similarity of structures.

D. The positive parity bands

The high spin part of bands 4a and 4b can be assigned the $ABEab$ and $ABFab$ 5—quasiparticle configurations with oblate shape, which is consistent with the observation of strong $M1$ transitions and reduced signature splitting, as already discussed for bands 3a and 3b. For the lower spin part (below the crossing which occurs around $\hbar\omega = 0.37$ MeV) two possibilities can be considered for $\alpha = +1/2$ $(-1/2)$: ABE (ABF) with triaxial shape and abE (abF) with oblate shape. The latter is preferable for two main reasons: there would be no shape change from high to low spin, and according to cranking calculations, the F quasiproton is favored for oblate shapes (in agreement with the data) while for triaxial shapes E is favored. In both cases a significant splitting is expected, as observed. For $\gamma = 0$, the splitting should be rather small.

The more excited positive parity orbits G and H in place of E and F are the candidates for participating in the configurations of bands 4c and 4d, together with either AB or ab. Since the experimental signature splitting is small and the structure was only observed at low spin we have insufficient evidence in this case for making a choice between aligned protons or neutrons.

The experimental ratios of transition probabilities $B(M1)/B(E2)$ obtained for the levels of the positive parity band structures 4a and 4b are shown in Fig. 6. These values scatter around 0.3 and 10 $(\mu_N/e\ \mathrm{b})^2$. The dashed line in Fig. 6 is the Dönau and Frauendorf model prediction [19] for a K value of $\frac{5}{2}$. No information is known in the literature for these ratios in neighboring nuclei for positive parity configurations.

Finally, the weak positive parity band 5, has been assigned the ABF configuration which is consistent with the absence of any sharp crossing up to the highest frequencies. The signature partner E was not observed. According to Fig. 5(b), the F Routhian becomes favored (for triaxial deformation) at ≈ 0.45 MeV.

V. SUMMARY

The ^{143}Tb nucleus has been studied to high spin, and several rotational structures have been observed. The yrast band based on a decoupled $h_{11/2}$ proton was found to have a crossing at a rotational frequency of 0.38 MeV. As in several neighboring odd-Z nuclei, bands with high $M1$ transition rates and reduced signature splitting indicative of the break up and alignment of a pair of $h_{11/2}$ neutrons, resulting in oblate configurations, have also been observed in this nucleus. Above the crossing which occurs at about 0.4 MeV it is believed that these five-quasiparticle bands have an $h_{11/2}$ proton with a pair each of aligned protons and neutrons (3a and 3b). A set of structures (4a and 4b) assigned positive parity have probably a five-quasiparticle configuration of oblate shape, consistent with the strong $M1$ transitions and small signature splitting observed. The lower spin part below the crossing at 0.37 MeV, possibly contains the $g_{7/2}/d_{5/2}$ proton with a pair of aligned $h_{11/2}$ protons or neutrons. An assignment of $[\pi h_{11/2}]^2 \otimes \pi g_{7/2}$ to band 5 is consistent with the absence of any sharp crossing up to the highest frequencies. Finally, bands 1a and 1b have no analogs in neighboring odd-A nuclei and their structure is not understood.

ACKNOWLEDGMENTS

We thank G. Manente for the preparation of the targets, and the staff of the XTU-Tandem of LNL for the smooth operation of the accelerator. This work was partially supported by the Fundação de Amparo à Pesquisa do Estado de São Paulo (FAPESP) and the Conselho Nacional de Desenvolvimento Científico e Tecnológico (CNPq), Brazil.

[1] G. Andersson, S. E. Larsson, G. Leander, P. Möller, S. G. Nilsson, I. Ragnarsson, S. Åberg, R. Bengtsson, J. Dudek, B. Nerlo-Pomorska, K. Pomorski, and Z. Szymański, Nucl. Phys. **A268**, 205 (1976).

[2] N. Xu, C. W. Beausang, R. Ma, E. S. Paul, W. F. Piel, Jr., and D. B. Fossan, Phys. Rev. C **39**, 1799 (1989).

[3] N. Xu, C. W. Beausang, E. S. Paul, W. F. Piel, Jr., P. K. Weng, D. B. Fossan, E. Gulmez, and G. A. Leander, Phys. Rev. C **36**, 1649 (1987).

[4] N. Xu, C. W. Beausang, J. R. Hughes, Y. Liang, R. Ma, E. S. Paul, W. F. Piel, Jr., S. Shi, and D. B. Fossan, Phys. Rev. C **43**, 2189 (1991), and references therein.

[5] L. Göttig, W. Gelletly, C. J. Lister, R. Moscrop, and J. Varley, Nucl. Phys. **A475**, 569 (1987).

[6] D. Bazzacco, S. Lunardi, F. Soramel, M. A. Cardona, G. de Angelis, M. De Poli, V. Roca, and F. Terrasi (unpublished).

[7] J. M. Nitschke, P. A. Wilmarth, P. K. Lemmertz, W.-D. Zeitz, and J. A. Honkannen, Z. Phys. A **316**, 249 (1984).

[8] D. Bazzacco, in Proceedings of the International Conference on Nuclear Structure at High Angular Momentum, Ottawa, 1992, Report No. AECL 10613, Vol. 2, p. 376.

[9] E. Farnea *et al.*, Nucl. Instrum. Methods Phys. Res. A **400**, 87 (1998).

[10] P. Spolaore, J. D. Larson, C. Signorini, S. Beghini, Z. Xi-Kai, and S. Hou-Zhi, Nucl. Instrum. Methods Phys. Res. A **238**, 381 (1985).

[11] W. T. Milner, *Holifield Heavy Ion Research Facility Computer Handbook* (Oak Ridge National Laboratory, Oak Ridge, Tennessee, 1987).

[12] D. Radford, Nucl. Instrum. Methods Phys. Res. A **361**, 297 (1995).

[13] R. Bengtsson and S. Frauendorf, Nucl. Phys. **A327**, 139 (1979).

[14] S. M. Harris, Phys. Rev. **138**, B509 (1965).

[15] R. Wyss, J. Nyberg, A. Johnson, R. Bengtsson, and W. Nazarewicz, Phys. Lett. B **215**, 211 (1988).

[16] E. S. Paul, C. W. Beausang, D. B. Fossan, R. Ma, W. F. Piel, Jr., N. Xu, and G. Leander, Phys. Rev. Lett. **58**, 984 (1987).

[17] L. Hildingsson, W. Klamra, Th. Lindblad, C. G. Lindén, G. Sletten, and G. Székely, Z. Phys. A **338**, 125 (1991).
[18] L. Hildingsson, C. W. Beausang, D. B. Fossan, and W. F. Piel, Jr., Phys. Rev. C **37**, 985 (1988).
[19] F. Dönau and S. Frauendorf, in *Proceedings of the Conference on High Angular Momentum Properties of Nuclei*, Oak Ridge, 1982, edited by N. R. Johnson (Harwood Academic, New York, 1983), p. 143; F. Dönau, Nucl. Phys. **A471**, 469 (1987).
[20] E. S. Paul, K. Ahn, D. B. Fossan, Y. Liang, R. Ma, and N. Xu, Phys. Rev. C **39**, 153 (1989), and references therein.

High-K bands in the ^{166}Yb region

J.R.B. Oliveira,* S. Frauendorf,† M.A. Deleplanque, B. Cederwall, R.M. Diamond, A.O. Macchiavelli, F.S. Stephens, and J. Burde‡
Nuclear Science Division, Lawrence Berkeley Laboratory, 1 Cyclotron Rd., Berkeley, California 94720

J.E. Draper, C. Duyar, and E. Rubel
University of California, Davis, California 95616

J.A. Becker, E.A. Henry, M.J. Brinkman, A. Kuhnert, M.A. Stoyer, and T.F. Wang
Lawrence Livermore National Laboratory, Livermore, California 94550
(Received 3 February 1994)

High-K bands have been observed in the ^{166,167,168}Yb isotopes following the ^{124}Sn(^{48}Ca,$xn\gamma$) reaction. The $\nu h_{11/2}$ band in ^{167}Yb has been extended to higher spins. The high-K bands in the even-even isotopes were observed for the first time and show very high $B(M1)/B(E2)$ ratios. Configuration assignments for the new bands are proposed. The results are interpreted within the tilted cranking model.

PACS number(s): 21.60.Cs, 21.10.Re, 27.70.+q

I. INTRODUCTION

The recent development of the "tilted axis cranking" (TAC) model [1,2] has revived the interest in the signature-degenerate $\Delta I = 1$ rotational bands. In that semiclassical model, the axis of rotation is no longer considered to coincide with one of the principal axes of the nuclear quadrupole deformation, but to be parallel to the total angular momentum vector. As a consequence, the intrinsic signature is undefined. In this case no energy staggering should be expected between odd and even spin states. The Yb region around mass 166 presents some of the best normal-deformed axially symmetric rotors known, and is therefore suitable for the observation of "tilted bands," as they are now called, without the complications of β- or γ-soft nuclear systems. On the other hand, tilted bands are rare in that nuclide region. The only high-Ω orbitals available are the $\nu[505]11/2^-$ from the $h_{11/2}$ neutron subshell, the $\pi[404]7/2^+$ ($g_{7/2}$), and the $\pi[523]7/2^-$ from the $h_{11/2}$ proton subshell. The last two orbitals are known to couple to a $I^\pi = 7^-$ bandhead state in some Er and Yb isotopes. High-Ω orbitals are necessary to boost high components of angular momentum along the symmetry axis (called K in this paper for simplicity). Another characteristic feature of most high-K bands is the appearance of strong $M1$ transitions. The present work reports the observation of bands with those characteristics in ^{167}Yb, ^{166}Yb, and ^{168}Yb. Part of the band in ^{167}Yb had been previously observed, and had been assigned the $\nu h_{11/2}$ configuration ($[505]11/2^-$). The other two bands were observed for the first time. For them we propose the $\pi([404]7/2 \otimes [523]7/2)$ proton configuration coupled to two distinct neutron configurations, $\nu[AB]$ and $\nu[AE]$ for ^{166}Yb and ^{168}Yb, respectively, where A and B are the first and second positive parity quasiparticle excitations (from the $i_{13/2}$ subshell), and E is the first negative parity quasiparticle excitation (from [523]5/2 and [521]1/2 parentage). These assignments give slightly better agreement with experimental data than the more simple $\nu[h_{11/2} \otimes i_{13/2}]$ configuration. However, the present data do not distinguish unambiguously between the two.

II. EXPERIMENTAL MEASUREMENTS AND RESULTS

The high-spin states of $^{165-168}$Yb were studied with the High Energy Resolution Array (HERA) at the 88-Inch Cyclotron of the Lawrence Berkeley Laboratory. HERA consisted of 20 Compton-suppressed germanium detectors and an inner ball of 40 BGO (bismuth germanate) detectors. The high-spin states were populated in the reaction ^{124}Sn(^{48}Ca,xn) at 210, 220, and 225 MeV. A stack of three self-supporting ^{124}Sn (97%) targets with ≈ 0.5 mg/cm^2 each separated by 0.5 mm gaps was used. About 420, 570, and 166×10^6 coincidence events [$\approx 80\%$ high fold ($k > 11$) doubles and $\approx 20\%$ triples] were recorded at each beam energy respectively. From the 210 MeV data, 650×10^6 counts were accumulated into a symmetrized $E\gamma \times E\gamma$ matrix with fold $k > 17$ and sum $H > 13$ MeV in the inner ball detectors. From the 220 and 225 MeV data two matrices were sorted at each beam energy, one with requirements of total fold (Ge + BGO) $15 < k < 25$, and total sum $13 < H(\text{MeV}) < 26$ (with 770 and 570×10^6 counts, respectively) and another

*Present address: Universidade de São Paulo, São Paulo, SP, 01498, C.P. 20516, Brazil.
†Present address: Institut für Kern und Hadronen Physik, FZ-Rossendorf, PF.19 0-8051 Dresden, Germany.
‡Present address: The Racah Institute for Physics, The Hebrew University, Jerusalem, Israel.

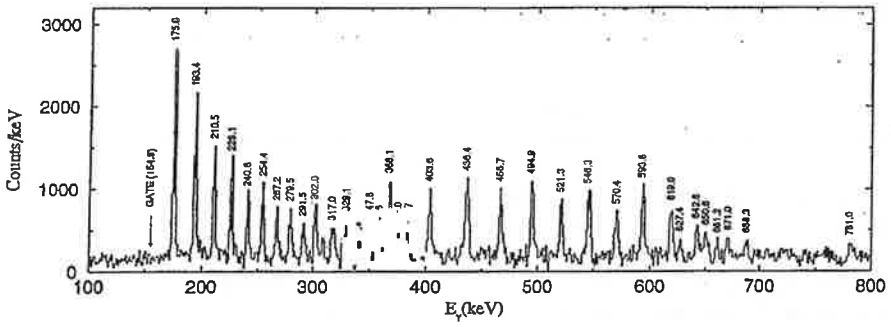

FIG. 1. Added spectra in coincidence with the 155 keV γ ray (^{167}Yb) from all the five matrices referred to in the text.

with $k > 24$, $H > 7$ MeV (with 227 and 154×10^6 counts, respectively).

Figures 1, 2, and 3 show coincidence spectra of energy gates on members of bands observed from those matrices. These bands show the characteristic pattern of high-K rotational bands, i.e., a sequence of regularly spaced lower energy transitions with no staggering, and higher energy crossover transitions. The crossover transitions are very weak in the cases of Figs. 2 and 3. Some of the indicated crossovers can only be confirmed in summed coincidence spectra of several energy gates, and in sums of double-gated spectra from three- and higher-fold Ge coincidences (Fig. 4). It was not possible to determine the decay paths connecting those bands with other lower lying states in the respective nuclei. This is due to the long half-life of the $11/2^-$ bandhead of the $\nu h_{11/2}$ band in ^{167}Yb (about 180 ns [3]), and probably to the same reason (long "bandhead" lifetimes) for the other bands, assigned here to ^{166}Yb and ^{168}Yb. In addition, such bands represent roughly 1% and 0.5% of the respective channel yields; i.e., they are very weakly populated structures. The $\nu h_{11/2}$ band in ^{167}Yb is populated with about 7% of the channel yield. We believe that the main reason why it is possible to observe such weakly populated structures, which supposedly lie at high excitation energy, is their high angular momentum component K along the symmetry axis. A high-K structure is not likely to deexcite to the other lower lying low-K structures due to K forbiddeness. Another reason is that most of the intensity of these bands goes through the dipole transitions, which are in an energy range of low density of $E2$ transitions from the stronger structures in the spectrum. Although some members of the respective ground state bands seem to be present in the spectra of Figs. 2 and 3, this cannot be considered as very good evidence for the channel assignments since those transitions are among the most intense in the corresponding sets of data, and their intensity is therefore very sensitive to changes in background subtraction.

The assignment of each band to the corresponding evaporation channel is based on the fold and sum-energy distributions associated with the in-band γ rays. Table I shows the ratio between in-beam γ-ray coincidence intensities from the two different sets of k and H requirements at a beam energy of 225 MeV, i.e.,

$$R = \frac{I_\gamma(i, f, 15 < k < 25, 13 < H < 26)}{I_\gamma(i, f, k > 24, H > 7)},$$

where $I_\gamma(i, f, k, H)$ is the coincidence intensity between γ rays from states i and f for a given condition on fold (k) and sum energy (H). As can be seen from that table, the ratio obtained for known coincident transitions is very sensitive to the number of neutrons of the respective evaporation residue. This ratio shows also very little sensitivity, if any, to the spin of the highest state of the decay path defined by the coincident transitions. We rely on this table to assign the band of Fig. 2 to the ^{166}Yb nucleus. The assignment of the band of Fig. 3 to ^{168}Yb is based on the fact that it is only observed on the 210 MeV data set, where the ^{168}Yb is by far the strongest channel. The ^{167}Yb transitions are observed with about the same intensity in both the 210 MeV matrix and in the $15 < k < 25$, $13 < H$(MeV)< 26 matrix at 225 MeV.

Figure 5 presents the level schemes for the high-K bands observed in the present work. They are generally consistent with the coincidence intensity between the transitions and sum-energy relationships between paral-

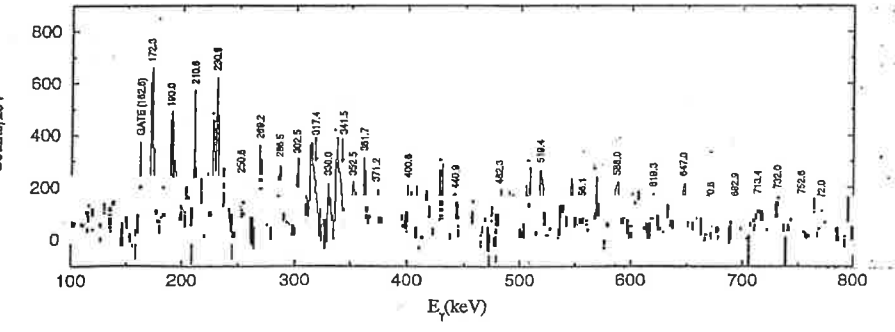

FIG. 2. Added spectra in coincidence with the 162 keV γ ray (^{166}Yb) from the $15 < k < 25$, $13 < H$(MeV)< 26 at 225 and 220 MeV matrices. Transitions marked with an asterisk belong to the ground state band of ^{166}Yb.

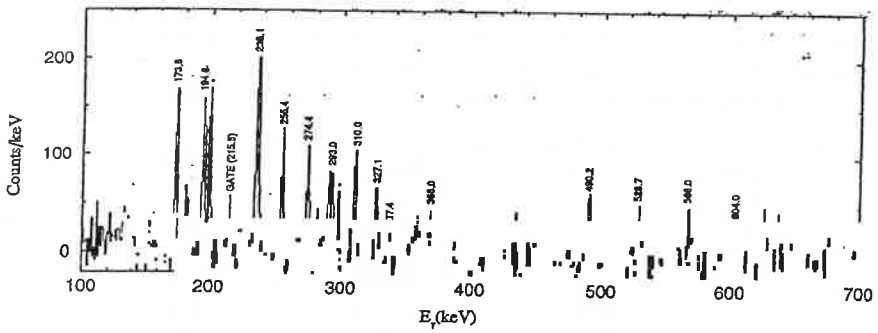

FIG. 3. Spectrum in coincidence with the 215 keV γ ray (^{168}Yb) from the $k > 17$, $H > 13$ MeV at 210 MeV matrix. Transitions marked with an asterisk belong to the ground state band of ^{168}Yb.

lel gamma-ray paths. The intensity of the 251 keV line (^{166}Yb) seems to be significantly below the average trend of the $\Delta I = 1$ transitions both in Figs. 2 and 4. This is not an effect of background subtraction since there is not a strong line with that energy in the background spectrum. Nevertheless, the scheme of Fig. 5(b) is the one that provided the best overall consistency with the data. The spins (I) of the "bandheads" in ^{166,168}Yb were not determined. The $\nu h_{11/2}$ band in ^{167}Yb was previously known from $(\alpha, 3n)$ [4] studies up to spin $(21/2^-)$ (the bandhead state $11/2^-$, with an excitation energy of 571 keV and lifetime of $\approx$ 180 ns was known from ^{167}Lu decay studies [3,5]). We added several higher lying transitions, and we disagree as to the existence of the 228.6 keV and the 454.0 gamma rays, which were tentatively assigned to the $(23/2) \rightarrow (21/2)$ and $(23/2) \rightarrow (19/2)$ transitions in Ref. [4]. The other bands were observed for the first time in the present work. The intensity pattern indicates that there is very little, if any, decay out of the band other than from the lowest lying state observed in each band. For that reason one could refer to those states as bandheads, although they may not be really so. Linking transitions to other states were not observed; therefore the relative excitation from the "bandhead" states to the ground state is not known. We expect it to be high (above 2 MeV) since the structures are very weakly populated.

From the branching ratio $I_\gamma(M1)/I_\gamma(E2)$ on each level it is possible to extract the reduced transition probability ratio $B(M1)/B(E2)$ from the formula (γ-ray energies in MeV)

$$\frac{B(M1)}{B(E2)}[(\mu_N)^2/(e^2b^2)] = 0.693 \times \frac{E_\gamma^5(E2)}{E_\gamma^3(M1)} \frac{I_\gamma(M1)}{I_\gamma(E2)}.$$

The results are presented in Figs. 6, 7, and 8. For the even-even nuclei, since the spins are not known, the plot is done as a function of the rotational frequency rather than as a function of spin. The large uncertainties, particularly for the even-even isotopes, are due to the low statistics of the weak $E2$ transitions. The experimental points are calculated assuming a multipolarity mixing ratio $I_\gamma(E2)/I_\gamma(M1) = \delta^2 = 0$ for the $\Delta I = 1$ transitions. Our directional correlation (DCO) measurements for the $\nu h_{11/2}$ band in ^{167}Yb (Fig. 9) are consistent with a small mixing ratio ($\leq 10\%$). Due to the low statistics of this kind of measurement no attempt was made to measure the DCO ratios for the other weaker bands in the even-even nuclei. The assumption of $\Delta I = 1$, $M1$ $(+E2)$ transitions and $\Delta I = 2$, $E2$ crossovers is based on the close resemblance between the three level schemes (Fig. 5).

Figure 10 shows the dynamic moment of inertia of the high-K bands of the present investigation as a function of rotational frequency. The two $i_{13/2}$ quasineutron band (AB) in ^{166}Yb is also shown for comparison. The dynamic moment of inertia ($\mathcal{J}^{(2)}$) is calculated from each adjacent pair of in-band γ-ray transitions from

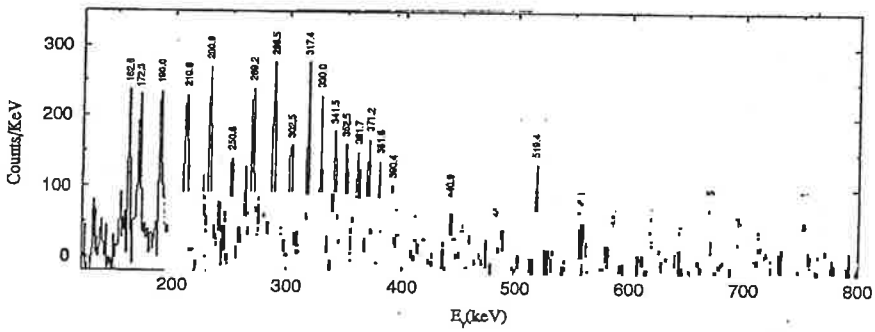

FIG. 4. Sum of doubled-gated spectra on all dipole members of the ^{166}Yb band [$15 < k < 25$, $13 < H(\text{MeV}) < 26$ at 225 MeV]. The background spectrum was chosen to be the total projection of the cube, normalized to give zero total counts in the subtracted spectrum. The 588 keV line does not appear because there is a very large peak in the total projection with that energy.

TABLE I. Ratio between coincidence intensities from two k and H conditions, as defined in the text. $E\gamma(i)$ and $E\gamma(f)$ are the coincident γ rays from the initial and final states with spin $I(i)$ and $I(f)$, respectively. The corresponding evaporation residue (channel) is indicated, where known. New assignments are in parentheses.

$E\gamma(i)$ (keV)	$E\gamma(f)$ (keV)	$I(i)(\hbar)$	$I(f)(\hbar)$	Ratio	Channel
298	199	6	4	0.13(1)	^{168}Yb
552	298	14	6	0.127(5)	^{168}Yb
174	155	15/2	13/2	0.85(7)	^{167}Yb
193	155	17/2	13/2	0.88(9)	^{167}Yb
210	155	19/2	13/2	0.8(1)	^{167}Yb
313	222	21/2	17/2	0.87(1)	^{167}Yb
743	222	49/2	17/2	0.86(2)	^{167}Yb
172	162	$(I+2)$	$(I+1)$	2.6(6)	(^{166}Yb)
269	162	$(I+7)$	$(I+1)$	1.8(8)	(^{166}Yb)
337	228	6	4	2.50(4)	^{166}Yb
666	228	22	4	2.54(5)	^{166}Yb
322	206	21/2	17/2	7.2(5)	^{165}Yb
429	322	25/2	21/2	7.77(15)	^{165}Yb
524	322	29/2	21/2	7.52(16)	^{165}Yb

$$\mathcal{J}^{(2)} = (\Delta I)^2\hbar^2/\Delta E_\gamma(\Delta I),$$

where $\Delta I = 1$ for the high-K bands and $\Delta I = 2$ for the AB band, and E_γ are the energies of the transitions. We assume that the frequency is $\hbar\omega = E_\gamma/\Delta I$ where the energy of the lower transition of the pair is used. No signature splitting is observed in any of the three bands (except possibly at the highest frequencies) of the present investigation which is characteristic of high K.

III. DISCUSSION

As mentioned in the Introduction, high-K bands are not commonly observed in this mass region. Most of the neutron orbits near the Fermi surface have $\Omega = 5/2$ or less and do not yield high angular momentum projections onto the symmetry axis. The only exception is the [505]11/2 holelike state from the top of the $h_{11/2}$ subshell, which is, however, not very near to the Fermi surface except for larger β deformation. Bands built on this state are known in a number of Er, Dy, Gd, and Sm odd-N isotopes, and in ^{149}Nd and ^{167}Yb. The proton states are usually not active due to the $Z = 70$ gap. A $I^\pi = K^\pi = 7^-$ state can be formed by combining the [523]7/2 with the [404]7/2 proton states. Bands built on this state are known in a few Er isotopes and in ^{170}Yb.

The high-K band in ^{167}Yb has been assigned the ν[505]11/2 configuration [3,4]. Our measurement of the $B(M1)/B(E2)$ ratios for this band are in reasonable agreement with what can be expected from such a configuration. Also, the part of the band extended to higher-

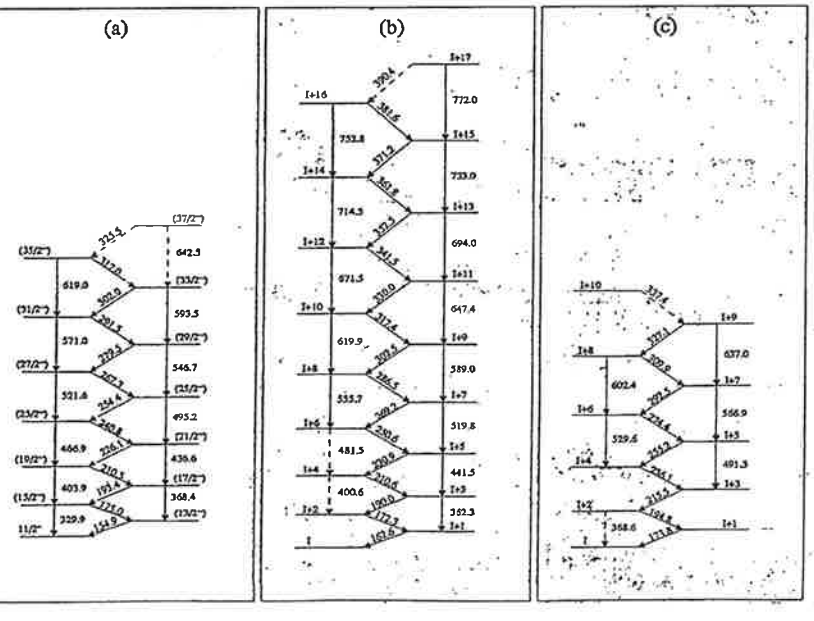

FIG. 5. Level schemes for the $\Delta I = 1$ bands in (a) ^{167}Yb, (b) ^{166}Yb, and (c) ^{168}Yb.

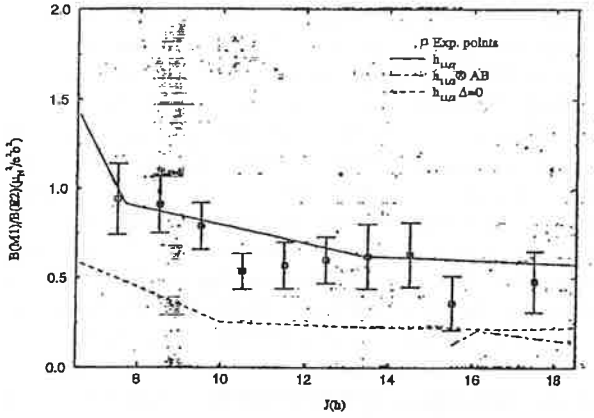

FIG. 6. Experimental and calculated $B(M1)/B(E2)$ ratios as a function of the total spin (J) for the ^{167}Yb band. The solid and dot-dashed lines are for the $\nu h_{11/2}$ and $\nu h_{11/2}AB$ configurations, respectively, as calculated from the TAC model. The dashed line is for $\nu h_{11/2}$ with $\Delta_\nu = 0$.

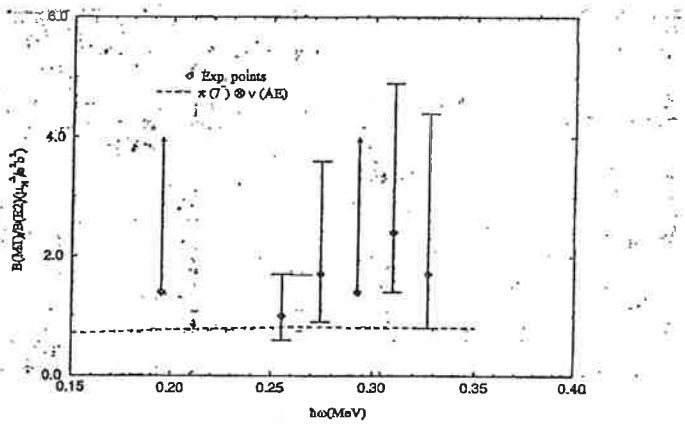

FIG. 8. Experimental and calculated $B(M1)/B(E2)$ ratios as a function of rotational frequency for the ^{168}Yb band ($\delta = 0$ assumed). The solid curve is calculated from the tilted model for the $\pi[7^-] \otimes \nu[AE]$ configuration.

spin states is consistent with an increase in alignment from a very smooth AB crossing Ref. [6]. The AB crossing is not blocked for any negative parity single quasiparticle configuration in contrast to the positive parity ones. We therefore agree with the aforementioned assignment.

For the bands in the even-even isotopes $^{166-168}$ Yb we considered various possible assignments. The coupling of the $h_{11/2}$ quasineutron with the first $i_{13/2}$ quasineutron A would yield the least excited two quasiparticle band with a relatively high K. The AB crossing would be blocked for such a configuration. No backbend is observed around the AB crossing frequency (0.25 MeV) in the ^{166}Yb band [7] and no upbend in the ^{168}Yb band [8]. The $\nu[h_{11/2} \otimes i_{13/2}]$ (or simply $\nu[h_{11/2}A]$) assignment seemed therefore attractive for both bands. However, calculations of the $B(M1)/B(E2)$ ratio for that configuration underestimate by at least a factor of 2 the experimental results obtained (Fig. 7). This is due to a partial cancellation of the magnetic moment perpendicular to the spin axis from the "deformation-aligned" (DAL) $h_{11/2}$ quasineutron and the more "rotation-aligned" (RAL) quasineutron $i_{13/2}$. In addition, there is evidence for an upbend in the dynamic moment of inertia at low fre-

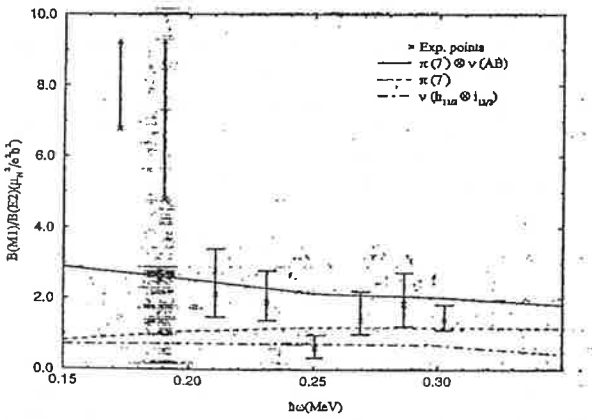

FIG. 7. Experimental and calculated $B(M1)/B(E2)$ ratios as a function of rotational frequency for the ^{166}Yb band ($\delta = 0$ assumed). The solid, dashed, and dot-dashed lines are for the $\pi[7^-] \otimes \nu[AB]$, $\pi[7^-]$, and $\nu[h_{11/2} \otimes A]$ configurations, respectively, as calculated from the TAC model.

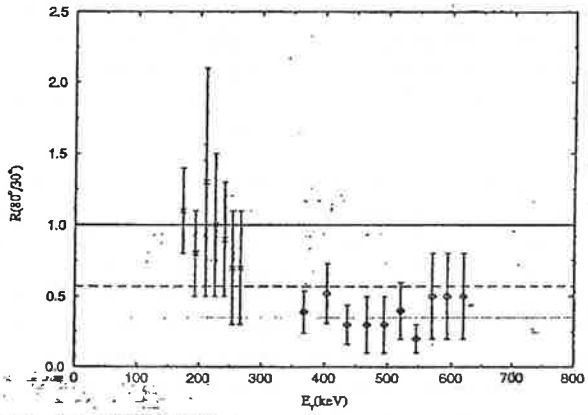

FIG. 9. Directional correlation measurements (DCO) for the γ-ray transitions of the $\nu h_{11/2}$ band in ^{167}Yb. The ratio of coincidence intensities indicated, $R(80°/30°)$, is given by the intensity of the γ rays (of energy E_γ) detected at $\approx 80°$ or (180–80)° in coincidence with the 155 keV γ ray detected at $\approx 30°$ or (180–30)° divided by the intensity of the γ rays (of energy E_γ) detected at $\approx 30°$ or (180–30)° in coincidence with the 155 keV γ ray detected at $\approx 80°$ or (180–80)° (the angles are measured to the beam direction). The solid line is the expected value for transitions of the same multipolarity as that of the 155 keV transition. The 155 keV transition is presumably of $M1+\delta^2 E2$ multipolarity. With this hypothesis, the dashed and dotted lines would be the expected values for pure $E2$ transitions in coincidence with the 155 keV transition for $\delta^2 = 0$ and $\delta^2 = 0.1$, respectively. The expected values were calculated specifically for the HERA system. The data points marked with crosses and diamonds were tentatively assigned to $M1 + \delta^2 E2$ and $E2$ multipolarities, respectively, [see Fig. 5(a)].

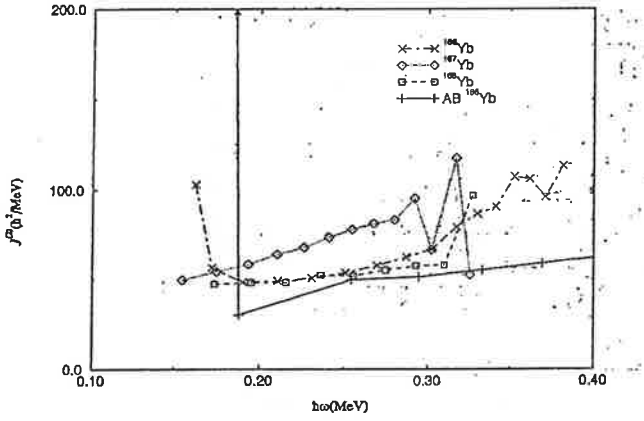

FIG. 10. Experimental dynamic moments of inertia as a function of rotational frequency for the $^{166-168}$Yb high-K bands. Diamonds ^{167}Yb, ×'s ^{166}Yb, squares ^{168}Yb (the error bars are about equal to or smaller than the symbol sizes). The AB (or s) band of ^{166}Yb (K=0) is also shown for comparison (+). The first data point (indicated by an arrow) is off scale at $\hbar\omega = 0.182$ MeV, $\mathcal{J}^{(2)} = 387\hbar^2$/MeV. The lines are traced to guide the eye only.

quency for the ^{166}Yb band (Fig. 10). Such an upbend could not be explained with the $\nu[h_{11/2}A]$ assignment.

This situation led us to search for alternative assignments for those bands. One possibility is the quasiproton configuration $\pi([523]7/2 \otimes [404]7/2)$ which is known to form the $I^\pi = 7^-$ in some Er and Yb isotopes. For simplicity we will refer to this configuration as $\pi[7^-]$. The calculated $B(M1)/B(E2)$ branching ratio for this high-K proton configuration is close to 1 for a wide frequency range, and therefore closer to the experimental values. A disadvantage of this assignment is that the first neutron crossing (AB) is not blocked and should be present. A rather weak interaction would be expected for this crossing in ^{166}Yb [7] and a strong interaction in ^{168}Yb [8] as happens in the crossing of the ground state band with the s band ($\nu[AB]$) of the respective nuclei. No crossings with these characteristics are present in the bands of this work. We therefore propose that the band seen experimentally is the $\pi[7^-]$ coupled to the first "aligned" pair of $i_{13/2}$ quasineutrons ($\nu[AB]$). For this configuration the moment of inertia should be smooth down to the spin where it crosses with the $\pi[7^-]$. This is an analog case to the crossing of the s with the g band of ^{166}Yb seen in Fig. 10. The upper branch of the crossing occurs at $\omega \approx 0.18$ MeV in the s band whereas it is seen at $\omega \approx 0.16$ MeV in the high-K band. We believe this difference is not incompatible with the proposed assignment since $\mathcal{J}^{(2)}$ is a quantity very sensitive to small disturbances. For this configuration strong magnetic transitions are expected since the aligned neutrons contribute to the already large magnetic moment perpendicular to the spin axis from the high-K proton configuration. This is consistent with the very large $M1/E2$ branching ratios observed down to the lowest frequencies (Fig. 7).

In ^{168}Yb, however, no upbend is seen in the dynamic moment of inertia plot down to the lowest observed transitions. For this band we considered the same proton configuration coupled to the first negative parity neutron configuration (AE) which has the AB crossing blocked. The $M1/E2$ branching ratios are not as large as in the $\pi[7^-]\otimes\nu[AB]$ configuration, but are still rather large. We would like to point out that the AB crossing should have a large interaction in ^{168}Yb, which would result in a rise of the dynamic moment of inertia over a wide frequency range in contradiction with experiment (Fig. 10).

If these assignments are correct, though, we should explain why the pure proton configuration is not seen in either of the two isotopes. Both bands, particularly $\pi[7^-] \otimes \nu[AB]$, should decay to the $\pi[7^-]$ configuration. A possible explanation is that, because of the sharp backbend, the connection of the bands with the $\pi[7^-]$ configuration is lost. The $\Delta I = 1$ gamma-ray energies should jump from around 160 keV to 320 keV, and fall in a range of difficult observation, due to the presence of stronger discrete gamma rays from other bands. It is possible also that there is some delay in the connecting transitions, during which the recoiling nuclei might fly away from the center of the target chamber, therefore decreasing detection efficiency. The lower-spin states should be seen, though, from direct population, provided that the $\pi[7^-]$ band does not decay out easily, which we expect from K forbiddeness. Perhaps there is not enough direct population at these relatively low spins to make the band observable.

The values of the $M1/E2$ branching ratio as a function of frequency, calculated from the TAC model, are given in Figs. 6, 7, and 8. There is a reasonable agreement with the experimental data for the configurations proposed. However, from this agreement alone we cannot rule out the $\nu[h_{11/2}A]$ configuration for the bands in the even-even nuclei. Nevertheless, we believe this together with the moment of inertia behavior makes the proposed configurations more likely.

IV. TILTED AXIS CRANKING CALCULATIONS

The configuration assignments can be substantiated by tilted axis cranking (TAC) calculations, which study the interplay between rotational- and deformation-aligned angular momenta in a quantitative way providing both energies and in-band transition probabilities. The method is described in Refs. [1,2]. It has been recently applied to high-K bands in ^{163}Er [9], which seems to have some structural resemblance to ^{167}Yb. Details about the TAC calculations can be found in these references. Here we mention only some important features needed to understand the results. The rotational bands are associated with quasiparticle configurations in a potential that uniformly rotates about an axis tilted with respect to the principal axes of the deformed potential. The orientation is determined by minimizing the routhian (energy in the rotating frame) with respect to the tilting angle. For this equilibrium orientation the expectation value of the angular momentum $\vec{J}$ has the same direction as the cranking axis ($\vec{J} \parallel \vec{\omega}$). For the bands studied in this paper we assume axial symmetry which is a good approximation in this region (cf. [2]). The orientation is

TABLE II. Results of the tilted axis cranking model. The calculated tilting angle θ is given, together with the spin J, and its projection onto the symmetry axis J_3. The routhian e' is taken relative to the ground state band (g.s.) of ^{166}Yb. The reduced transition probabilities $B(M1)$ and $B(E2)$ are also given. The calculations were performed at a rotational frequency of $\omega = 0.25$ MeV.

Configuration	θ	$J(\hbar)$	$J_3(\hbar)$	e' (MeV)	$B(M1)$ (μ_N^2)	$B(E2)(e^2\,b^2)$
g.s.	90°	9.0	0.0	0.0	0.0	1.75
$\nu h_{11/2}$	44°	7.7	5.5	1.271	0.408	0.447
$\nu[h_{11/2}A]$	51°	12.9	8.2	1.13	0.474	0.657
$\pi[7^-]$	45°	10.5	7.4	0.876	0.564	0.470
$\pi[7^-] \otimes \nu[AB]$	64°	19.0	8.5	1.191	2.58	1.21
$\pi[7^-] \otimes \nu[AE]$	45°	18.2	12.8	1.171	0.553	0.626

fixed by the angle θ between the rotational axis and the symmetry axis (denoted by 3). In the calculations we use the deformation parameters $\epsilon_2 = 0.25$ and $\epsilon_4 = 0.01$. The pairing field is constant. The gap parameters are $\Delta_\pi = 0.91$ MeV and $\Delta_\nu = 0.86$ MeV. The proton and neutron chemical potentials are kept fixed and are chosen such that the expectation values are $Z \approx 70$ and $N \approx 97$ respectively at $\omega = 0$.

In the analysis of the experimental spectra it is useful to introduce the experimental angular velocity ω. In contrast to the standard cranked shell model (CSM) we operate with the total angular velocity instead of its projection onto the one-axis. The experimental frequency is simply equal to the γ-ray energy of the transition $I \to I - 1$ to which the angular momentum $J = I$ is assigned. The intraband transition probabilities are calculated from the TAC wave functions by means of the semiclassical expressions given in Refs. [1,2,11,9]. The results for $\omega = 0.25$ MeV are given in Table II.

Figure 11 shows the quasiparticle spectra in the TAC model. The lowest excitations are of quasineutron type. Since the collective rotation is about the one-axis ($\theta =$

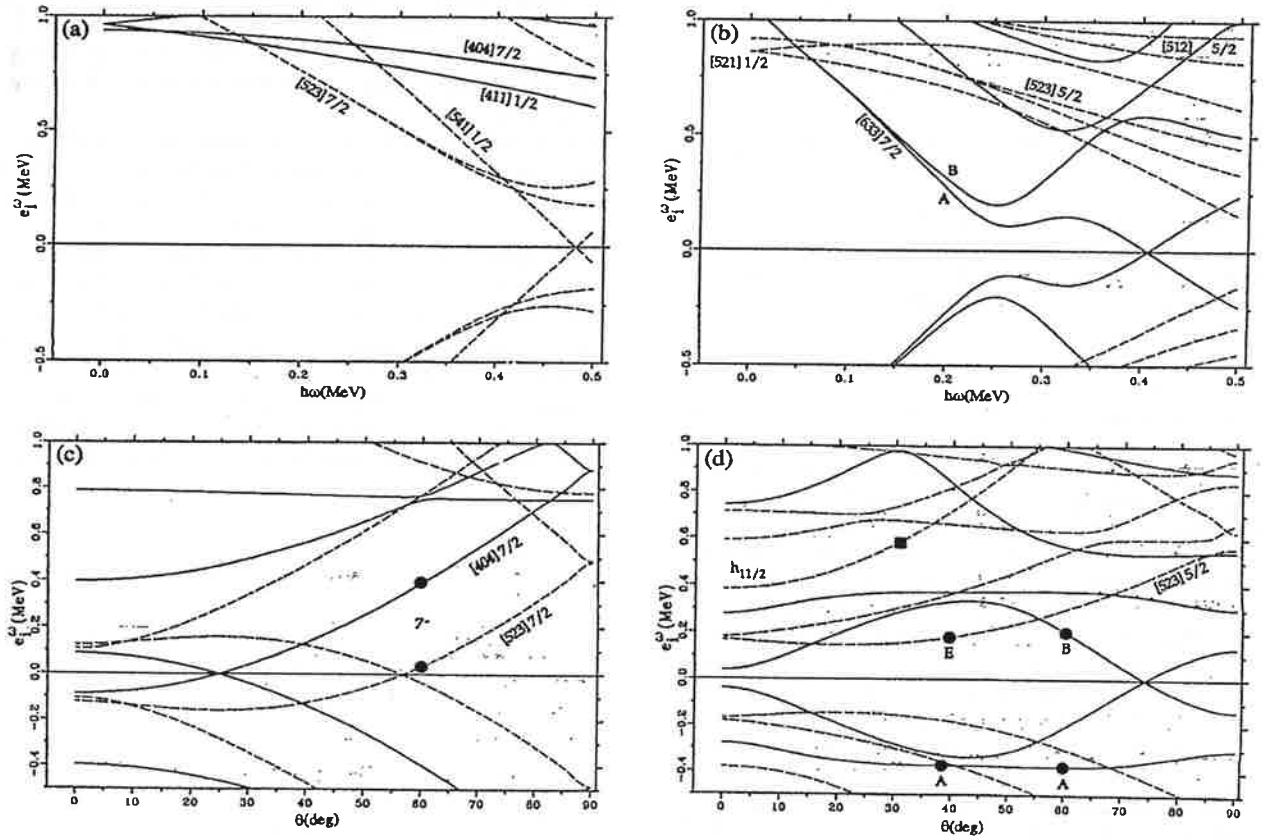

FIG. 11. Quasiparticle spectra for ^{166}Yb calculated from the TAC model. (a) Quasiproton routhians as a function of rotational frequency for $\theta = 90°$. (b) Quasineutron routhians as a function of rotational frequency for $\theta = 90°$. (c) Quasiproton routhians as a function of the tilting angle (θ) at $\hbar\omega = 0.3$ MeV. The circles indicate the occupation for the $\pi[7^-]$ configuration. (d) Quasineutron routhians as a function of the tilting angle (θ) at $\hbar\omega = 0.3$ MeV. The square indicates the occupation for the $\nu h_{11/2}$ configuration. The circles around $\theta = 60°$ and around $\theta = 38°$ indicate the occupations for the AB and AE configurations, respectively.

90°), the lowest quasineutron excitations are PAC (principal axis cranking) solutions with $\theta = 90°$. They form the lowest bands in ^{166,167,168}Yb, which can be classified as traditional CSM configurations with good signature quantum number [8,11]. An exception is the $h_{11/2}$ quasineutron orbit, which strongly slopes down towards $\theta = 0°$. It is a good example of strong coupling to the deformed potential, i.e., a DAL state in terms of the classification introduced in Ref. [12]. Figure 12(a) shows that at finite rotation the $h_{11/2}$ quasineutron has $i_3 \approx 5.5\hbar$ and a very small i_1 component. This is reflected by the routhian in Fig. 11(d), which is $e' \approx e'_0 - 5.5\hbar\omega\cos\theta$. The $h_{11/2}$ band observed in ^{167}Yb is assigned to this one quasineutron configuration. It is a TAC solution that represents what one is used to calling a high-K band. The component $J_3 = K$, the band starts at $I = K$, and all the angular momentum increase comes from the collective angular momentum R [cf. Fig. 12(a)] The tilting angle is to a good approximation given by the strong coupling expression

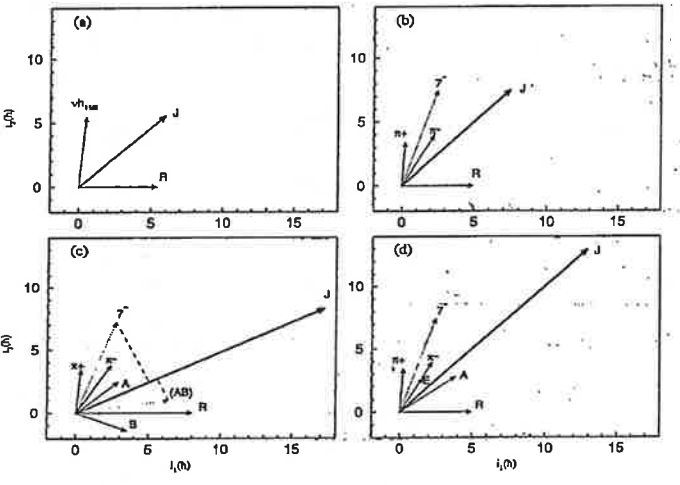

FIG. 12. Vector diagrams at $\hbar\omega = 0.25$ MeV. The thin solid line vectors represent the angular momentum of each quasiparticle, and the rotational angular momentum (R), which is parallel to the one-axis. The total spin (J) which is the vector addition of the quasiparticle and rotational angular momenta is indicated by a thick solid line vector. The angular momentum projections onto the one-axis is denoted by i_1 and onto the three-axis (the symmetry axis of the ellipsoid) by i_3. (a) Diagram for the $\nu h_{11/2}$ band. (b) Diagram for the $\pi[7^-]$ band. The dashed line vector is the vector addition of the two quasiprotons angular momenta. The positive parity quasiproton ($\pi[404]7/2^+$) is marked as π^+, and the negative parity one ($\pi[523]7/2^-$) as π^-. (c) Diagram for the $\pi[7^-] \otimes \nu[AB]$ band. The quasiproton angular momenta is indicated as in (b). The dashed line vector marked as (AB) is the vector addition of the two quasineutrons (A and B) angular momenta. The long-dashed lines represent the projection of the quasiproton and quasineutron angular momenta perpendicular to the total spin. Since the g factors of protons and neutrons have opposite signs, the magnetic moments add, yielding high $M1$ transition probabilities. (d) Diagram for the $\pi[7^-]\otimes\nu[AE]$ band. In this case the perpendicular component of the quasineutron angular momenta (A and E) is small.

$$\cos\theta = K/I, \quad I = \mathcal{J}\omega.$$

Figure 13 shows this behavior, which has the typical Hopf bifurcation [12] at the bandhead, which corresponds to the frequency $\omega_h = K/\mathcal{J}$ in the case of strong coupling. The calculated value $\hbar\omega_h = 0.198$ MeV is the lowest possible frequency for the $h_{11/2}$ band ($\theta = 0°$). As seen in Fig. 14, the calculations predict a back bend at $J = 15\hbar$ corresponding to the AB crossing in the $i_{13/2}$ quasineutron system. The presence of the $h_{11/2}$ quasineutron delays the AB crossing by $2\hbar$ as compared to the yrast line (shown in Fig. 14 as well). The experimental function $\mathcal{I}(\omega)$ [Fig. 15(b)] does not show any irregularity up to I=33/2. Figure 10 seems to indicate a very smooth gain of moment of inertia that could be due to a very much smoothed out AB crossing. The systematic absence of the AB crossing in the $h_{11/2}$ quasineutron bands [9] is not fully understood at present. We performed also a $\Delta_\nu = 0$ calculation for this configuration. The corresponding $B(M1)/B(E2)$ is shown in Fig. 6. The experimental values lie more or less in between the $\Delta_\nu = 0$ and the full pairing calculation at the upper part of the band. Figure 15(a) shows also a $\Delta_\nu = 0$ calculation for the $\nu h_{11/2}$ band. Its spins are larger than for the full pairing calculation at the same frequency (the kinematic moment of inertia is larger), in agreement with the experimental trend. This indicates that pairing might be reduced for this configuration already at relatively low spins. This might explain the absence of the AB crossing in this band.

In the even-even isotopes both the neutron and proton excitations must be considered. The lowest two quasineutron excitations are the $(i_{13/2})^2$ configuration AB and the negative parity configuration AE, which are PAC solutions with $\theta = 90°$. They are the lowest bands. In Fig. 14 we show the g band and AB for reference. The combination of the $h_{11/2}$ quasineutron with the $i_{13/2}$ quasineutron A results in a TAC solution. Its tilting angle is shown in Fig. 13, its energy in Fig. 14, and spin in Fig. 15(a). It is one candidate for the observed $\Delta I = 1$ bands. As can be seen in Fig. 6, it has relatively small $B(M1)/B(E2)$ values, since the transversal magnetic moments of the two

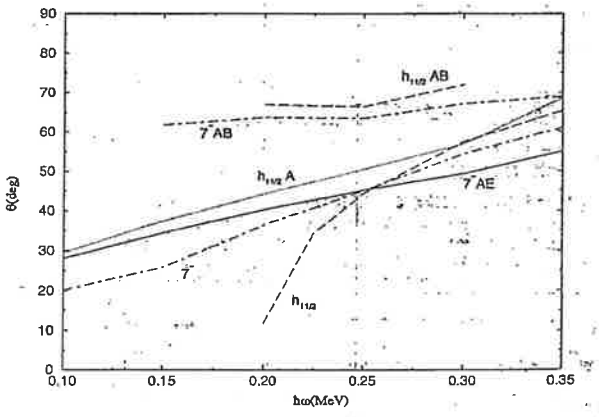

FIG. 13. Tilting angle as a function of rotational frequency. The configuration corresponding to each line is indicated in simplified notation (see text).

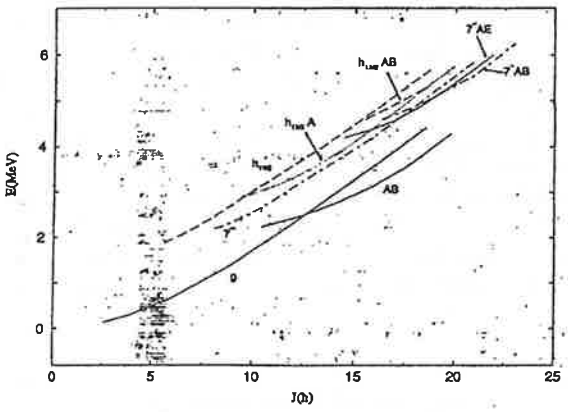

FIG. 14. Total energy (E) as a function of spin (J). The configurations are indicated as in Fig. 13.

quasineutrons cancel to a large extent.

Figure 11(c) shows that most of the quasiproton orbitals drive towards $\theta = 0°$, since they are relatively strongly coupled to the deformed field. For $\theta < 45°$ the orbitals coming from the Nilsson states [523]7/2 ($h_{11/2}$) and [404]7/2 are lowest. They combine into a two quasiproton configuration with $J_3 \approx 7$. For short notation we call it the 7^- configuration although its structure is more complicated than that of a simple K=7-band. As seen in Fig. 12(b), the $h_{11/2}$ quasiproton (π^-) is appreciably tilted away from the three-axis. Its energy minimum in Fig. 11(c) lies near $\theta = 30°$ indicating a character intermediate between DAL and FAL (Fermi-aligned) according to the classification scheme of Ref. [12]. The tilting takes place at the beginning of the band causing the relatively flat behavior of $\theta(\omega)$ at low ω in Fig. 13. The 7^- band has not been seen in the present experiment, but it is known in ^{164}Er [14].

For higher spin the 7^- two quasiproton configuration combines with quasineutron excitations. The lowest two quasineutron excitations are the configurations AB and AE coming from the corresponding PAC configurations at $\theta = 90°$ (cf. discussion above). However, the resulting four quasiparticle configuration is not just a simple combination of the 7^- with the AB and AE PAC bands. As can be seen from Fig. 11(d), the quasineutron orbits change noticeably with the orientation.

The orbital A has a minimum at $\theta = 45°$ qualifying it as a FAL quasineutron. Its energy does not depend very much on θ. It can follow the orientation of the rotational axis much better than other orbitals, since due to the reduction of its quadrupole moment by pairing it is only weakly coupled to the deformed field. The orbital B is RAL according to the classification in Ref. [12], since it has its minimum at $\theta = 90°$. It is responsible for the larger θ values in the configuration 7^-AB as compared with 7^- (cf. Fig. 13). This increase of θ and the contribution of B (negative g factor) to the transversal magnetic moment, which adds to the proton part, significantly enhance the $B(M1)$ values (cf. Fig. 7). This is illustrated in Fig. 12(c), which also demonstrates that A contributes only very little to the transversal magnetic moment. This is an example of the improvement brought

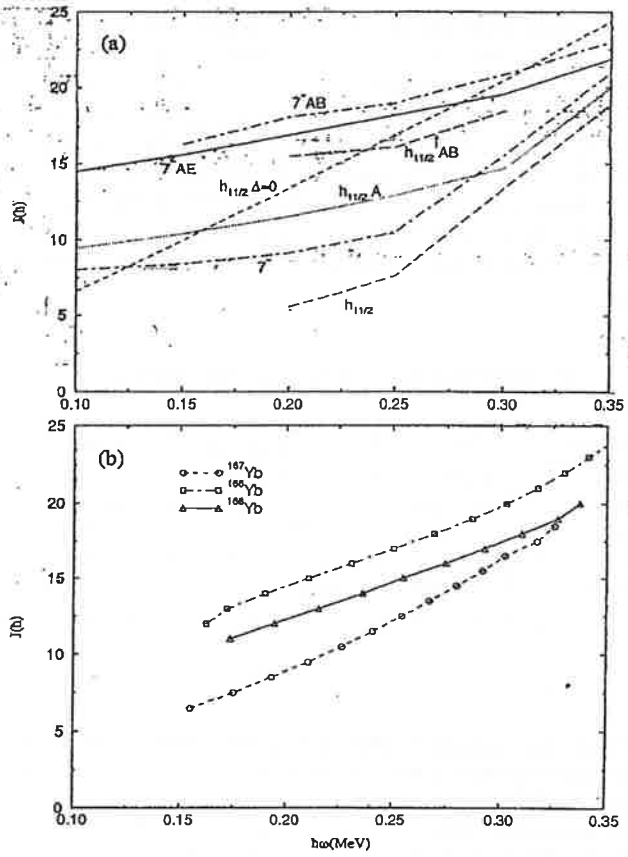

FIG. 15. Total angular momentum (J) as a function of rotational frequency. (a) TAC results. The configurations are indicated as in Fig. 13. (b) Experimental results. Circles ^{167}Yb ($\nu h_{11/2}$), squares ^{166}Yb (7^-AB, $I = 11$ assumed for the lowest-spin state), triangles ^{166}Yb (7^-AE, $I = 10$ assumed for the lowest-spin state). The experimental rotational frequency ($\hbar\omega$) of each state of spin J is the energy of the dipole γ-ray transition depopulating that state (see Fig. 5).

by the TAC calculation, when the simple estimates of the magnetic moments suggested in Ref. [10] are inaccurate (the three-component of A would not be included making its contribution much larger).

The E orbital changes its character with θ. At 90° it consists mainly of [521]1/2 having a routhian that is almost θ independent (as is characteristic of a $\tilde{\Lambda} = 0$ pseudospin state). Since they slope down with decreasing θ, orbits coming from Nilsson levels with larger K take over at lower θ. As a consequence, the quasineutron E contributes about $2.6\hbar$ to J_3 in the configuration 7^-AE, whereas lowest negative parity bands in ^{166,168}Yb (AE and AF) show a large signature splitting, characteristic for $J_3 \approx 0$ [7,8,11]. The $B(M1)$ values of 7^-AE are close to the ones of 7^-, since both A and E have small angles with the axis of rotation $\vec{J}$ [cf. Fig. 12(d)]. The large i_1 components of the quasineutrons A, B, and E make the tilting angle $\theta(\omega)$ much less spin dependent than would be expected from the strong coupling estimate (1). This is clearly seen in Fig. 13 when comparing the $h_{11/2}$ band with the other configurations.

The configurations 7^-AB, 7^-AE, and $\nu h_{11/2}A$ are

three candidates for the $\Delta I = 1$ sequences observed in ^{166,168}Yb. As seen in Fig. 14, we expect them to be close in energy. Our assignment to the 7^- quasiproton excitations is based on the slightly lower energy and the larger $B(M1)/B(E2)$ values compared to $\nu h_{11/2}A$. The assignment of 7^-AB to ^{166}Yb and of 7^-AE to ^{168}Yb relies on the evidence for an AB crossing in ^{166}Yb discussed in Sec. III. In view of the restricted information our data contain, these assignments must be considered as tentative.

V. SUMMARY AND CONCLUSIONS

Weakly populated high-K bands have been observed in the ^{166}Yb region. The properties of the bands observed for the first time in ^{166}Yb and ^{168}Yb have led to rather unusual tentative configuration assignments, i.e., $\pi[7^-]\otimes\nu[AB]$ and $\pi[7^-]\otimes\nu[AE]$, respectively. The tilted cranking model predicts lower excitation energies for such bands than would be expected from traditional models, and is able to reproduce the large $B(M1)/B(E2)$ ratios observed. Another possible configuration would be the $\nu[h_{11/2}\otimes i_{13/2}]$ for both bands in the even-even nuclei, which should present, however, lower $B(M1)/B(E2)$ ratios. The $\nu h_{11/2}$ band in ^{167}Yb has been extended to higher spins. A smooth increase in the dynamic moment of inertia as a function of spin is observed for this band up to $I = 33/2$. The presence or absence of the AB crossing in this band is not clear from the experimental data. The possibility of weaker pairing for this band is raised.

ACKNOWLEDGMENTS

This work was supported by the Director, Office of Energy Research, Division of Nuclear Physics of the Office of High Energy and Nuclear Physics of the U.S. Department of Energy under Contract No. DE-AC03-76SF00098 (LBL), and the U.S. Department of Energy under Contract No. W-7405-Eng. 48 (LLNL).

[1] S. Frauendorf, in *Proceedings of the International Symposium on Future Directions in Nuclear Physics with 4π Gamma Detection Systems of the New Generation*, Strasbourg, 1991, edited by J. Dudek and B. Haas, AIP Conf. Proc. No. 259 (AIP, New York, 1992), p. 223.
[2] S. Frauendorf, Nucl. Phys. **A557**, 259c (1993).
[3] K. Ya. Gromov *et al.*, Z. Phys. A **277**, 395 (1976).
[4] Th. Lindblad, Nucl. Phys. **A238**, 287 (1975).
[5] B. J. Meijer, F. W. N. De Boer, and P. F. A. Goudsmit, Nucl. Phys. **A259**, 213 (1976).
[6] R. Bengtsson and S. Frauendorf, Nucl. Phys. **A314**, 27 (1979).
[7] E. M. Beck, J. C. Bacelar, M. A. Deleplanque, R. M. Diamond, F. S. Stephens, J. E. Draper, B. Herskind, A. Holm, and P. O. Tjøm, Nucl. Phys. **A464**, 472 (1987).
[8] J. C. Bacelar, M. Diebel, C. Ellegaard, J. D. Garrett, G. B. Hagemann, B. Herskind, A. Holm, C.-X. Yang, J.-Y. Zhang, P. O. Tjøm, and J. C. Lisle, Nucl. Phys. **A442**, 509 (1985).
[9] A. Brokstedt, J. Lyttkens-Lindén, M. Bergström, L. P. Ekström, H. Ryde, J. C. Bacelar, J. D. Garrett, G. B. Hagemann, B. Herskind, F. R. May, P. O. Tjøm, and S. Frauendorf, Nucl. Phys. **A557**, 469c (1993); Nucl. Phys. **A571**, 337 (1994).
[10] F. Dönau and S. Frauendorf, in *Proceedings of the Conference on High Angular Momentum Properties of Nuclei*, Oak Ridge, Tennessee, 1982, edited by N. R. Johnson, Nucl. Sci. Res. Conf. Series No. 4 (Harwood, New York, 1983), p. 143.
[11] J. R. B. Oliveira, S. Frauendorf, M. A. Deleplanque, R. M. Diamond, F. S. Stephens, C. W. Beausang, J. E. Draper, C. Duyar, E. Rubel, J. A. Becker, E. A. Henry, and N. Roy, Phys. Rev. C **47**, R926 (1993).
[12] S. Frauendorf, Phys. Scr. **24**, 349 (1981).
[13] G. Jeschke, *Mathematik der Selbstorganisation* (Deutscher Verlag der Wissenschaften, Berlin, 1989), Chap. 6, p. 155.
[14] F. W. N. de Boer, P. F. A. Goudsmit, P. Koldewijn, and B. J. Mejer, Nucl. Phys. **A169**, 577 (1971).

RAPID COMMUNICATIONS

PHYSICAL REVIEW C VOLUME 47, NUMBER 3 MARCH 1993

Rotation-induced transition from superfluid to normal phase in mesoscopic systems: ^{168}Yb and adjacent nuclei

J. R. B. Oliveira,* S. Frauendorf,† M. A. Deleplanque, R. M. Diamond, F. S. Stephens, and C. W. Beausang‡
Nuclear Science Division, Lawrence Berkeley Laboratory, 1 Cyclotron Road, Berkeley, California 94720

J. E. Draper, C. Duyar, and E. Rubel
University of California, Davis, California 95616

J. A. Becker, E. A. Henry, and N. Roy
Lawrence Livermore National Laboratory, Livermore, California 94550
(Received 8 September 1992)

The transition from strong static pairing to weak static pairing and its consequences to the excitation spectrum of a mesoscopic (medium number of particles) system are investigated. New levels have been measured in ^{168}Yb. A reasonable description of the $A \approx 168$ isotopes spectra is obtained. The adequacy of the phase transition concept is discussed.

PACS number(s): 23.20.Lv, 21.10.Re, 21.60.Ev, 27.70.+q

Shortly after the discovery of pair correlations of the BCS type in nuclei, Mottelson and Valatin [1] predicted that pairing should collapse in rapidly rotating nuclei much like superconductivity in a strong magnetic field. How this transition actually takes place has been a subject of study in high-spin nuclear physics ever since. In nuclei only a small number of particles (typically 10) participate in the pairing correlations, and the fluctuations of the pairing field create a substantial part of the total correlation energy. The adequacy of the phase transition concept is therefore questionable [2]. The transition from the "superfluid" to the "normal nuclear phase" is analogous to the transition from deformed to spherical nuclei, with vibrations around the equilibrium shapes. Following Refs. [3, 4] we call dynamic pairing the oscillations of the pairing field around its static value, which vanishes at high spin. The dynamic pairing correlations decrease the moment of inertia of all low-lying configurations by about the same amount [2, 3], while affecting very little the relative excitation spectrum. As pointed out in Refs. [4–6] the disappearance of static pairing corresponds then to a major change of the excitation spectrum, from the quasiparticle (qp) to the particle-hole (ph) spectrum. The former is characterized by strong alignment of the single qp angular momentum with the rotational axis, and related band crossings that strongly depend on parity and weakly on the particle number N. The latter shows small alignment in general, and a characteristic individuality with respect to N. Examples of the appearance of the ph spectra at high spin have been discussed in Refs. [4–7]. The purpose of the present work is to understand the excitation spectra over a wide frequency range. We studied experimentally the ^{168}Yb nucleus and propose a calculation scheme, based on a schematic frequency dependence of the pairing gap, which describes the transition from the qp to the ph picture.

The high-spin states of ^{168}Yb have been measured by means of in-beam gamma-ray spectroscopy with the High Energy Resolution Array (HERA) at the 88-Inch Cyclotron of the Lawrence Berkeley Laboratory. HERA consists of 20 Compton-suppressed germanium detectors and an inner ball of 40 BGO detectors. The ^{168}Yb nucleus was produced in the reaction ^{124}Sn(^{48}Ca,4n) at 210 MeV. A gamma-gamma coincidence matrix containing 315×10^6 counts was generated, with requirements of fold > 17 and sum energy > 13 MeV in the inner-ball detectors. The level scheme based on the present work is presented in Fig. 1. Five bands previously reported by Bacelar *et al.* [5] were confirmed (1 to 5 in Fig. 1) and extended by one or two higher-lying transitions. In addition, four new bands (6–9, Fig. 1), two extending up to $I \approx 40\hbar$, were observed. Part of band 6 had been independently observed by Khazaie *et al.* [8] but we disagree as to how this band decays to the ground-state band. In Fig. 1 the dashed transitions indicate the intensity flow from band 6 to the ground-state band, according to our coincidence data. The actual linking transitions, however, were not observed. Spin values of bands 5 to 9 are tentative and are based on the coincidence relations of the transitions (and γ-γ directional correlations in the case of band 7) and the relative intensities of the bands at high spin, which correlate rather strongly with the

*On leave from the Universidade de São Paulo, S. Paulo, SP, Brazil.

†On leave from the Institut für Kern und Hadronen Physik, FZ-Rossendorf, PF.19 0-8051 Dresden, Germany.

‡Present address: University of Liverpool, Liverpool L69 3BX, United Kingdom.

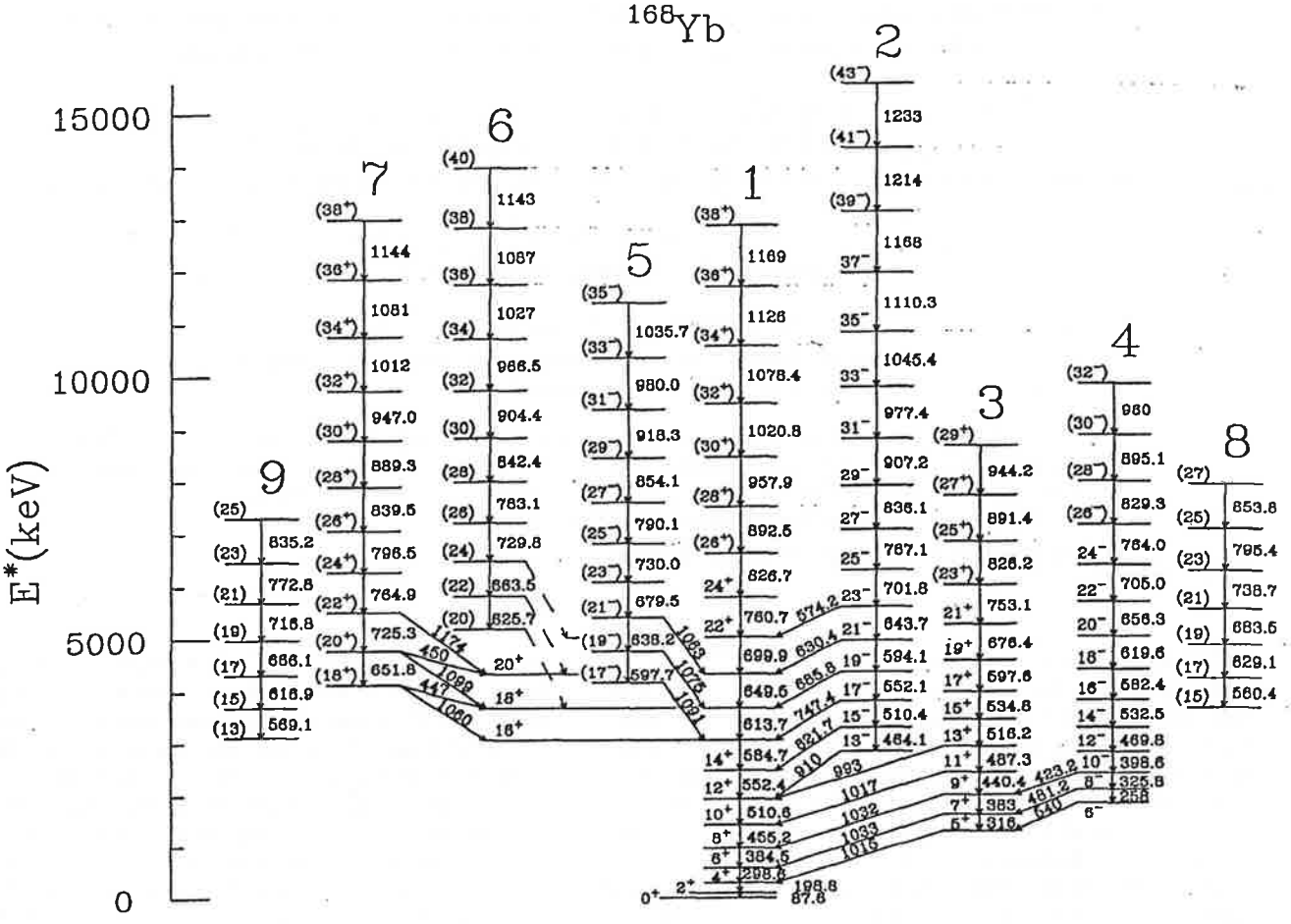

FIG. 1. The level scheme of ^{168}Yb. The different bands are numbered for further reference.

proximity to the yrast line. The lower members of bands 8 and 9 are also seen to feed low-lying states of the other bands but again the linking transitions were not found. Figure 2(c) shows the experimental Routhians e' (excitation energies in the rotating frame [9]) relative to band 2 as a function of the rotational frequency ω.

The expected change of the neutron spectrum is calculated from the quasiparticle energies in a deformed rotating potential (cranked shell model [9, 10], with deformation parameters from Ref. [10]), in which the static pairing-gap parameter Δ decreases linearly from the full value (0.8 MeV) at $\omega = 0.25$ MeV (where the AB crossing occurs) to zero at $\omega = 0.5$ MeV. In this frequency interval a crossing occurs in each band, leading to a substantial decrease in Δ according to microscopic calculations [3]. The chemical potential is adjusted to give the right particle number for the yrast configuration. The spectrum generated by exciting pairs of qp is depicted in Fig. 2(a). At the top of the figure we provide the scale for Δ. Since the qp formalism does not distinguish between particles and holes, for small Δ (large ω) the spectrum contains besides the ph excitations in the $N = 98$ system a number of spurious particle-particle and hole-hole states [since the single-particle (sp) occupation numbers are close to 0 or 1] belonging to $N = 96$ and 100 [11]. They can be eliminated by comparing with ph states calculated from the sp energies without pairing. All the remaining physical (ph) states are shown in Fig. 2(b) at $\omega > 0.5$ MeV (only the bands that exist at high spin were traced down to low ω for simplicity). On the other hand, all low-lying qp configurations are physical for large Δ (since each qp has comparable particle and hole components). The qp states do not always connect continuously with ph states, usually because of avoided crossings between spurious and physical ones where they interchange character. We reconnect (diabatically) the physical branches by interpolation, as demonstrated in Fig. 2(a) (around $\omega = 0.5$ MeV). Although rough and not free from ambiguities, this procedure provides a reasonable description of the transition region between the large Δ and zero Δ spectra, as seen from the comparison between Figs. 2(b) and (c). There is only one low-lying configuration which is not observed experimentally; the lowest negative-parity ($\pi = -$), zero-signature ($\alpha = 0$) configuration. An assignment of this configuration to band 6 is not excluded; however, our spin and energy estimates re-

sult in high alignment and this is more consistent with a proton configuration, which still has strong pairing. For this reason band 6 was left out of Fig. 2(c). Figures 3, 4, and 5 demonstrate that the same approach describes well the excitation spectra in the adjacent Yb isotopes. The same conclusion is valid for the corresponding isotones (e.g., Hf), which show very similar neutron excitation spectra.

The nuclei of the ^{168}Yb region show a transition from a qp to a ph spectrum in the frequency range from 0.3 to 0.4 MeV. It reflects the disappearance of static pairing at high spin. That transition is described quite well by our method. In mesoscopic systems such as nuclei, the presence of fluctuations and configuration dependence make

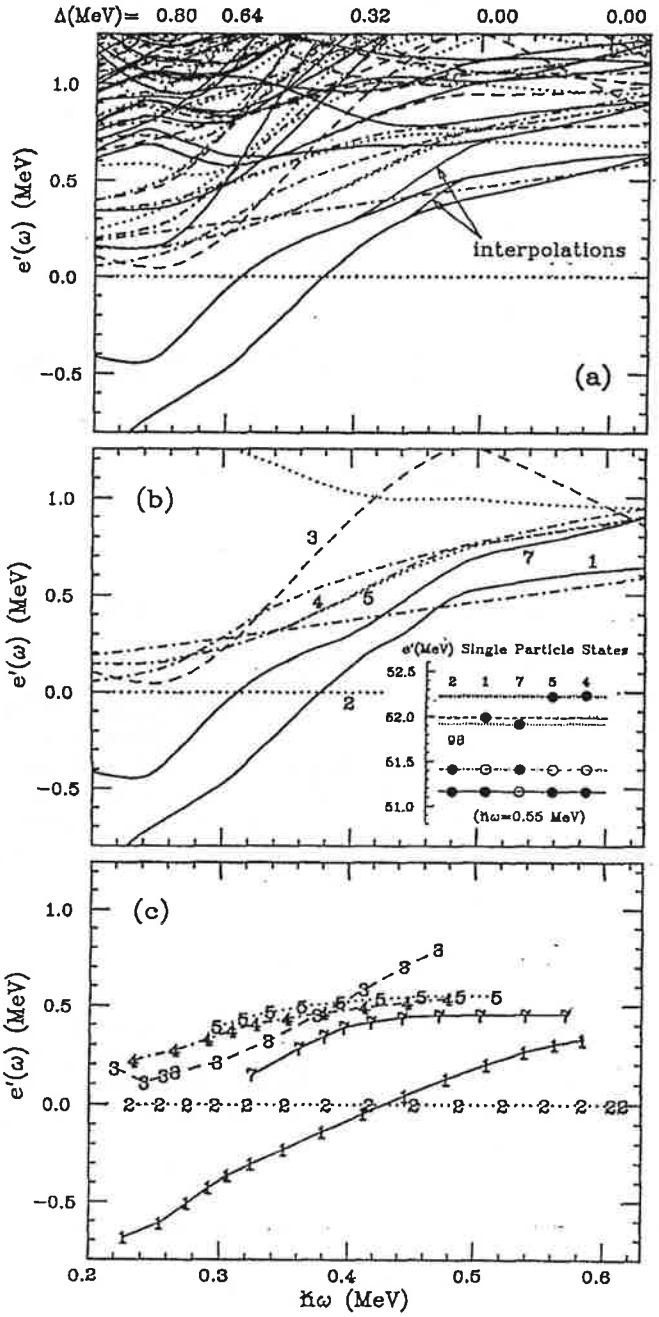

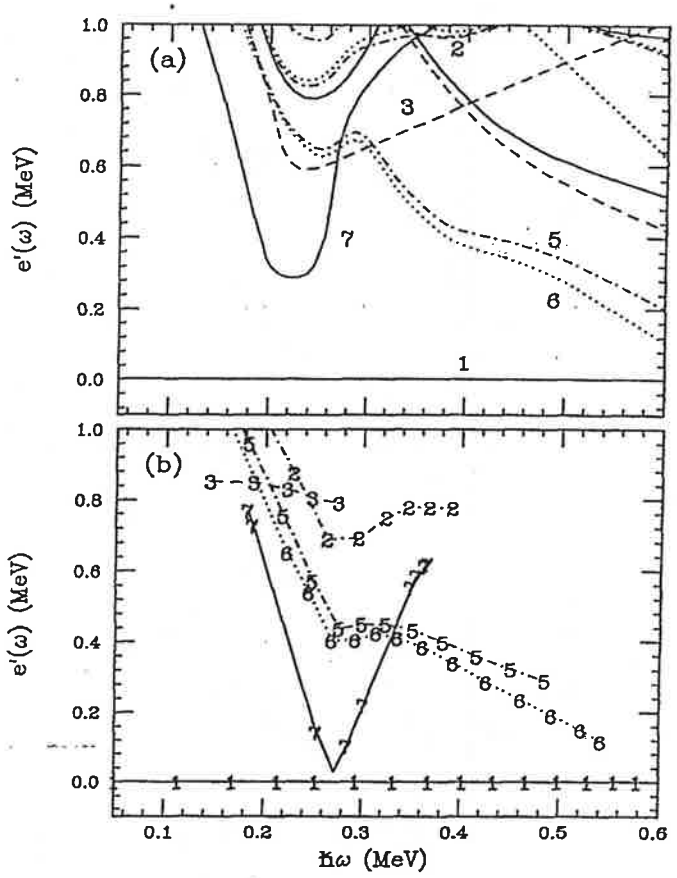

FIG. 3. Band structure of ^{168}Yb. (a) Calculation with decreasing Δ. (b) Experimental results [12]. The line conventions are the same as in Fig. 2.

FIG. 2. Band structure of ^{168}Yb. Comparison between (a) the quasiparticle states; (b) the calculated physical states; and (c) the experimental results. The Routhians (energies in the rotating frame) are plotted relative to the lowest $(\pi,\alpha) = (-,1)$ configuration (band 2). The solid, dashed, dot-dashed, and dotted lines correspond to $(\pi,\alpha) = (+,0)$, $(+,1)$, $(-,0)$, and $(-,1)$, respectively. All 0, 2, and 4 quasiparticle states calculated with decreasing pairing gap Δ (see text) are shown in (a). Diabatic interpolations are shown as thin lines for the two lowest $\pi = +$ states only. In (b) the relevant physical states selected from (a) by exclusion of states with wrong particle number are shown. On the inset at the bottom right of (b), the particle-hole excitations of the $(-,1)$ core (band 2) are shown [in this case the solid, dashed, dot-dashed, and dotted lines correspond to $(\pi,\alpha) = (+,1/2)$, $(+,-1/2)$, $(-,1/2)$, and $(-,-1/2)$, respectively]; they are strictly valid only above $\omega = 0.5$ MeV where $\Delta = 0$. The corresponding Nilsson labels are, from top to bottom, $([512]5/2^-)^2$, $[642]5/2^+$, $[521]1/2^-$, $[521]1/2^-$, and $[642]5/2^+$. In (c) the experimental points are indicated by the numbers and correspond to the in-band quadrupole transitions in Fig. 1.

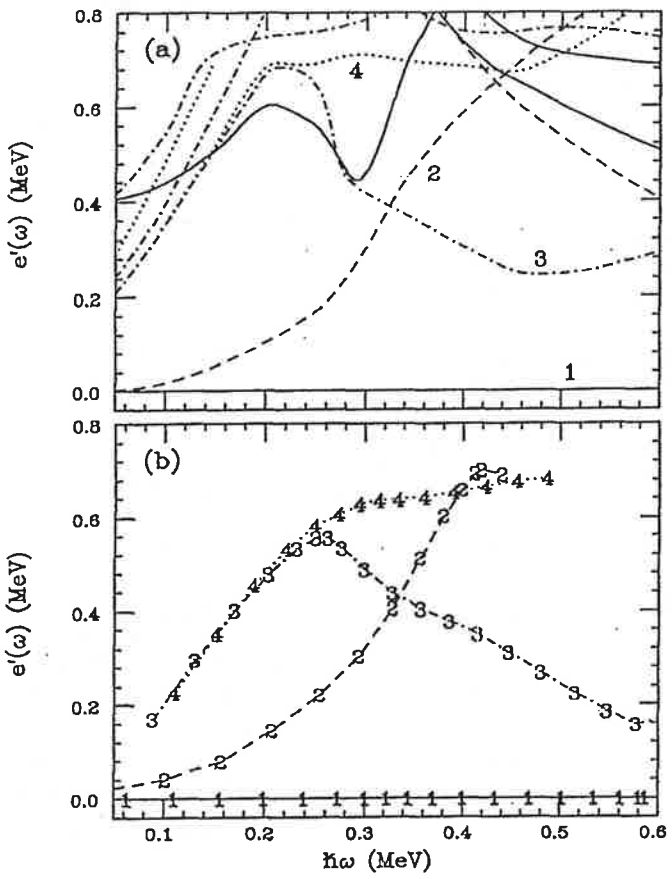

FIG. 4. Band structure of ^{167}Yb. (a) Calculation with decreasing Δ. (b) Experimental results [5, 8]. The line conventions are the same as in the inset of Fig. 2(b).

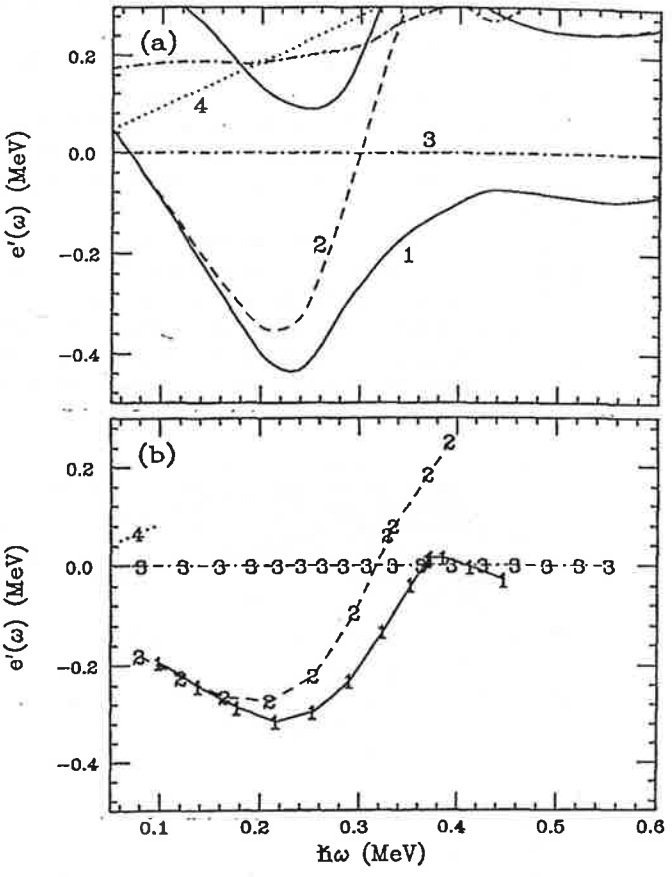

FIG. 5. Band structure of ^{169}Yb. (a) and (b), same as in Fig. 4.

the transition from superfluid to normal very diffuse. In a macroscopic system the very large number of particles allows for relatively small fluctuations and yields a sharp phase transition. In superconductors, for example, the relation between magnetization and magnetic field has a singularity at the critical field where the phase transition occurs. In nuclei the analogous relation between the canonical variables I and ω shows a steep rise in the transition region but its shape varies considerably from band to band. Although some aspects of the destruction of static pairing by rotation resemble a phase transition, there are also significant differences to it.

We would like to thank J. Garrett for comments. One of us (J.R.B.O.) acknowledges partial support from the Fundação de Amparo à Pesquisa do Estado de São Paulo. This work was supported by the Office of Energy Research, Division of Nuclear Physics of the Office of High Energy and Nuclear Physics of the U.S. Department of Energy under Contract No. DE-AC03-76SF00098 (LBL), and the U.S. Department of Energy under Contract No.W-7405-Eng. 48 (LLNL).

[1] B. R. Mottelson and J. G. Valatin, Phys. Rev. Lett. **5**, 511 (1960).
[2] Y. R. Shimizu, Nucl. Phys. **A520**, 477c (1990).
[3] Y. R. Shimizu *et al.*, Rev. Mod. Phys. **61**, 131 (1989), and references therein.
[4] S. Frauendorf, Nucl. Phys. **A409**, 243c (1983).
[5] J. C. Bacelar *et al.*, Nucl. Phys. **A442**, 509 (1985).
[6] J. D. Garrett, in *The Response of Nuclei under Extreme Conditions*, edited by R. A. Broglia and G. F. Bertsch (Plenum, New York, 1988), p. 1.
[7] M. A. Ryley *et al.*, Nucl. Phys. **A520**, 279c (1990).
[8] F. Khazaie *et al.*, Schuster Lab., Univ. of Manchester, Nucl. Phys. Annual Report 1987 (unpublished), p. 47.
[9] T. Bengtsson and I. Ragnarsson, Nucl. Phys. **A436**, 14 (1985).
[10] R. Bengtsson, S. Frauendorf, and F. R. May, At. Data Nucl. Data Tables **35**, 15 (1986).
[11] R. Bengtsson and H.-B. Håkansson, Nucl. Phys. **A357**, 61 (1981).
[12] E. M. Beck *et al.*, Nucl. Phys. **A464**, 472 (1987).

Shears bands in ^{193}Pb

G. Baldsiefen,[1] M. A. Stoyer,[2] J. A. Cizewski,[1] D. P. McNabb,[1] W. Younes,[1] J. A. Becker,[2] L. A. Bernstein,[2] M. J. Brinkman,[2] L. P. Farris,[2] E. A. Henry,[2] J. R. Hughes,[2] A. Kuhnert,[2] T. F. Wang,[2] B. Cederwall,[3] R. M. Clark,[3] M. A. Deleplanque,[3] R. M. Diamond,[3] P. Fallon,[3] I. Y. Lee,[3] A. O. Macchiavelli,[3] J. Oliveira,[3] F. S. Stephens,[3] J. Burde,[3] D. T. Vo,[4] and S. Frauendorf[5]

[1]*Rutgers University, New Brunswick, New Jersey 08903*

[2]*Lawrence Livermore National Laboratory, Livermore, California 94550*

[3]*Lawrence Berkeley Laboratory, Berkeley, California 94720*

[4]*Iowa State University, Ames, Iowa 50011*

[5]*Forschungszentrum Rossendorf, D-01314 Dresden, Germany*

(Received 25 April 1996)

Four bands of enhanced dipole transitions, with weak crossovers, have been observed in ^{193}Pb. Three of these bands are connected to the spherical levels. In addition, the spherical level scheme has been extended. The nuclear spectroscopy was done with the early implementation of GAMMASPHERE and HERA arrays of Ge detectors. The nucleus ^{193}Pb was populated in the ^{174}Yb(^{24}Mg,5n) reaction at beam energies of 129, 131, and 134 MeV. The experimental results are compared to tilted-axis cranking calculations. The systematical behavior of the dipole bands in the heavier odd-A Pb isotopes, ^{195,197,199,201}Pb, is also discussed. [S0556-2813(96)06409-6]

PACS number(s): 21.10.Hw, 21.60.−n, 23.20.−g, 27.80.+w

I. INTRODUCTION

Sequences of enhanced magnetic dipole bands have recently been discovered in more than 20 isotopes in the lead region [1–16]. All of these sequences show similar properties. They consist of strong magnetic dipole transitions with weak $E2$ crossover transitions. Despite the small nuclear deformations deduced from lifetime measurements [17–21], the bands have fairly regular energy spacings and show no or only small signature splitting up to the highest rotational frequencies.

The bands are understood as being built on configurations involving the high-K proton $h_{9/2}$ and $i_{13/2}$ orbitals and holes in the low-K orbitals of the $i_{13/2}$ neutron shell. Therefore, near the bandhead the angular momentum of the protons is aligned along the symmetry axis, while the angular momentum of the neutrons is aligned perpendicular to the symmetry axis. Hence, the direction of the total angular momentum is tilted by an angle of about 45° with respect to the symmetry axis.

A striking feature of these $M1$ bands is that the ratio of the dynamic moment-of-inertia to the $B(E2)$ value is about ten times larger than in well deformed nuclei. This indicates that part of the moment-of-inertia stems from sources other than collective rotation. Recently, the characteristics of these bands with enhanced $M1$ transitions have been successfully interpreted in terms of the tilted axis cranking model [22,23]. In this model the increase in the angular momentum within the bands is created by the increase in the alignment of the proton and the neutron spins in the direction of the total spin. Since the change in the neutron and proton spin vectors is similar to the closing of the blades of a pair of shears, the term "shears bands" was suggested for these $M1$ bands.

II. EXPERIMENTS

The experiment was performed at the 88-Inch Cyclotron Facility at Lawrence Berkeley National Laboratory. Data were collected using initially the High Energy Resolution Array (HERA) and, subsequently, early implementation of Gammasphere. The reaction was ^{174}Yb(^{24}Mg,5n) at beam energies of 131 MeV (Gammasphere) and 129 and 134 MeV (HERA). The targets consisted of a stack of three self-supporting foils each with a thickness of $\sim$0.5 mg/cm^2. The HERA experiments involved 20 Compton-suppressed Ge detectors ($\sim$25% efficient with respect to a 7.5 cm × 7.5 cm NaI detector at 25 cm) and a 40-element bismuth-germanate (BGO) inner ball. The numbers (angles with respect to the beam direction) of the Ge detectors were: 4(37°), 2(51°), 4(79°), 2(103°), 4(123°), 2(152°), and 2(154°). Each detector was 15.5 cm from the target. The Gammasphere experiment involved 36 Compton-suppressed Ge detectors with $\sim$80% efficiency. Six detectors were placed at 90°, and five each at 17°, 32°, 37°, 143°, 148°, and 163° with respect to the beam direction. All of these detectors were located 25 cm from the target. The HERA data set consisted of 160×10^6 and 310×10^6 γ-γ coincidences at 129 and 134 MeV, respectively. The Gammasphere data set consisted of 5×10^8 three- and higher-fold events, yielding 9×10^8 unfolded γ-γ-γ coincidences.

The HERA data were sorted into symmetrized γ-γ matrices and forward/backward vs 90° matrices for a directional correlation analysis (DCO). A preliminary level scheme [24], including levels up to $E_{ex}\approx5$ MeV and $I\approx45/2\hbar$, was obtained using coincidence relationships, relative γ-ray intensities and ΔI spin measurements from DCO ratios.

The Gammasphere data were sorted [25] into a symmetrized three-dimensional cube and the level scheme was extended to $E_{ex}=7.0$ MeV and $I=55/2\hbar$. A DCO matrix was generated with the 90° detectors on one axis and the forward plus backward detectors on the other axis. DCO ratios were determined by setting gates on clean strong transitions on both axes. The DCO ratios were normalized to known $E2$

TABLE II. Gamma-ray intensities and DCO ratios for normal transitions in ^{193}Pb.

E_γ (keV)	I_γ [a]	R_{DCO} [b]	$E_i \rightarrow E_f$
Group 1			
72.7			2212 → 2140
158.4	28.0 ± 4.0	0.67 ± 0.20	2584 → 2426
213.0	23.0 ± 3.4	0.60 ± 0.17	2426 → 2212
219.1	4.2 ± 1.0	1.04 ± 0.26	2212 → 1993
431.9	1.7 ± 0.7	0.59 ± 0.14	2426 → 1993
519.6	81.8 ± 9.6	0.96 ± 0.11	1401 → 881
527.3	10.2 ± 1.9	1.05 ± 0.15	1549 → 1022
590.6	30.0 ± 5.7	0.97 ± 0.15	2140 → 1549
592.5	35.4 ± 8.8	1.08 ± 0.14	1993 → 1401
668.0	9.0 ± 1.7	0.58 ± 0.07	1549 → 881
739.0	18.8 ± 4.0	0.58 ± 0.07	2140 → 1401
811.7	9.8 ± 1.9	0.91 ± 0.12	2212 → 1401
881.3	100.0 ± 11.3	0.96 ± 0.11	881 → 0
1022.1	12.2 ± 2.1	0.77 ± 0.14	1022 → 0
Group 2			
97.7	2.2 ± 0.8		2523 → 2426
146.4	4.8 ± 1.8	0.48 ± 0.21	4148 → 4001
148.7	4.5 ± 2.3	0.53 ± 0.18	4297 → 4148
164.3	7.5 ± 2.1	0.51 ± 0.16	4001 → 3837
224.3	1.7 ± 0.8		5168 → 4943
279.1	3.4 ± 1.3		4576 → 4297
296.3	4.9 ± 1.5	0.53 ± 0.11	3375 → 3078
310.8	9.9 ± 1.9	0.63 ± 0.13	2523 → 2212
367.8	2.5 ± 1.0		4943 → 4576
395.4	5.5 ± 1.7		3770 → 3375
438.3	2.1 ± 0.8		4208 → 3770
462.6	13.0 ± 3.3	0.49 ± 0.07	3837 → 3375
555.0	6.6 ± 2.3	0.52 ± 0.07	3078 → 2523
758.9	2.3 ± 0.9	1.16 ± 0.31	3837 → 3078
851.3	16.0 ± 5.4	0.96 ± 0.14	3375 → 2523
Group 3			
85.5			2610 → 2525
447.6	0.9 ± 0.3		3860 → 3412
531.5	3.8 ± 1.1	0.93 ± 0.17	2525 → 1993
539.5	1.8 ± 1.2		3904 → 3365
581.4	0.8 ± 0.3		4441 → 3860
632.2	1.3 ± 0.9		4239 → 3607
644.0	0.6 ± 0.3		4757 → 4113
677.0	9.9 ± 1.9	0.93 ± 0.11	2670 → 1993
701.2	1.6 ± 0.5		4113 → 3412
741.9	4.5 ± 1.2	0.97 ± 0.17	3412 → 2670
754.4	5.6 ± 3.0		3365 → 2610
996.5	3.0 ± 1.8		3607 → 2610
Group 4			
180.2	12.1 ± 2.9	0.61 ± 0.16	2321 → 2141
184.3	19.5 ± 3.0	1.07 ± 0.28	1585 → 1401
301.6	1.8 ± 0.6		2705 → 2404
331.3	0.5 ± 0.3		2652 → 2321
340.7	1.9 ± 0.6		2993 → 2652
384.4	1.5 ± 0.7		2705 → 2321
421.2	4.4 ± 1.3	0.89 ± 0.17	3127 → 2705
472.1	4.8 ± 1.4	0.46 ± 0.13	2057 → 1585
542.2	2.8 ± 1.0		3247 → 2705
546.3	6.4 ± 1.7	1.11 ± 0.17	3539 → 2993
555.5	29.5 ± 9.4	0.77 ± 0.09	2141 → 1585
564.6	7.2 ± 1.9	0.89 ± 0.15	2705 → 2141
594.3	2.6 ± 1.3		2652 → 2057
612.6	8.3 ± 2.2	0.96 ± 0.13	3739 → 3127
638.3	3.2 ± 1.0	1.13 ± 0.19	4177 → 3539
647.5	1.3 ± 0.5		4634 → 3987
655.7	1.9 ± 0.8		4395 → 3739
672.0	6.9 ± 1.8	1.09 ± 0.15	2993 → 2321
692.8	3.2 ± 1.0	0.89 ± 0.15	4432 → 3739
711.5	0.7 ± 0.4		4889 → 4177
729.3	1.5 ± 0.6	0.97 ± 0.30	5162 → 4432
739.5	1.8 ± 0.6		3987 → 3247
766.5	0.8 ± 0.4		5162 → 4395
805.9	8.8 ± 2.2	0.91 ± 0.11	3127 → 2321
819.0	3.3 ± 1.0		2404 → 1585
Group 5			
302.8	1.0 ± 0.4	0.45 ± 0.12	4469 → 4166
319.5	2.4 ± 0.8	0.53 ± 0.10	3639 → 3320
415.3	1.9 ± 1.0		4055 → 3639
423.3	1.3 ± 0.5	0.44 ± 0.09	4589 → 4166
441.7	1.0 ± 0.4		5031 → 4589
444.4	3.4 ± 1.1	0.46 ± 0.08	4166 → 3721
454.6	0.7 ± 0.4		4589 → 4135
482.5	1.9 ± 0.9	0.45 ± 0.08	4537 → 4055
834.0	2.8 ± 1.3		3418 → 2584
845.8	1.1 ± 0.5		4166 → 3320
867.8	1.2 ± 0.5		4589 → 3721

[a]Gamma-ray intensities are normalized to the 881-keV transition.
[b]DCO ratios are normalized to $E2$ quadrupole transitions.

character in Fig. 1. The parity of the levels in group 2 cannot be determined because the electric vs magnetic character of the 97 and 310-keV lines which depopulate the 2523-keV level cannot be uniquely determined. The ordering of the 146.4, 148.7, and 164.3-keV lines above the 3837-keV level could not be firmly established. However, this uncertainty has no influence on the excitation energy and spin of band 2. The DCO ratios of all three lines are consistent with $\Delta I = 1$ dipole transitions, therefore, suggesting a spin of 39/2 for the 4297-keV bandhead. However, again mixed $\Delta I = 0$ transitions cannot be completely excluded. Intensity arguments lead to the conclusion that none of the lines at 146.4, 148.7 and 164.3 keV can be magnetic dipoles, because $M1$ transitions are mainly converted at these low energies. The intensity and also the DCO ratio of the 148.7-keV line could only be roughly determined, as it is coincident with an additional line with a transition energy of ≈149 keV which is not placed in the level scheme. There are additional weak lines in the upper part of group 2 which could not be placed. Therefore, only tentative spin assignments have been made for levels above 3837 keV. Although the levels of group 2 are irregularly spaced, it is not clear that this group belongs to the spherical part of the level scheme. As is the case for the $M1$ bands, this group consists of dipole transitions with

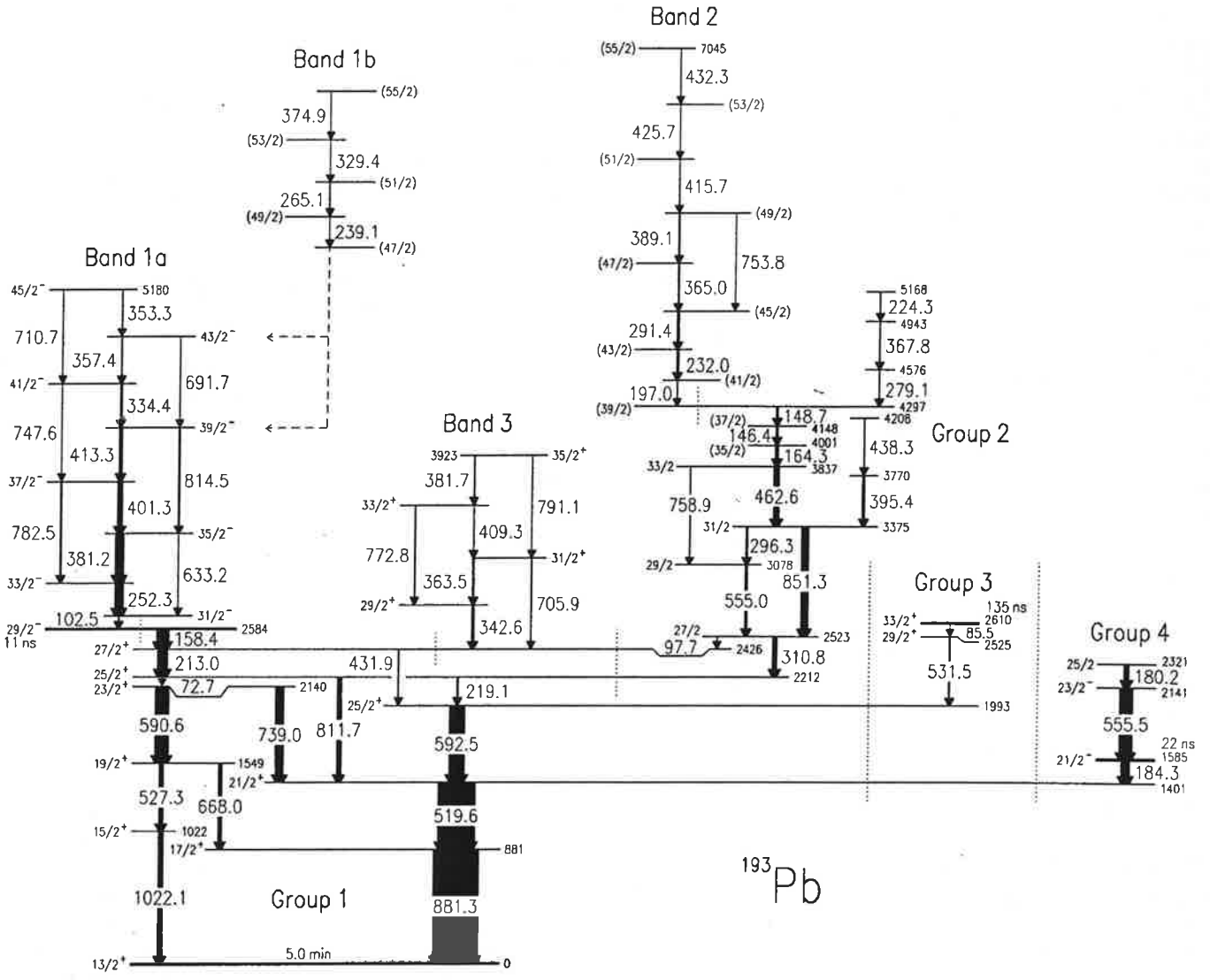

FIG. 1. Partial level scheme of ^{193}Pb. Lifetimes of the $21/2^-$, $29/2^-$, and $33/2^+$ isomers are taken from [26]. The lifetime of the $13/2^+$ isomer is taken from [27]. The widths of the arrows are proportional to the γ-ray intensities. The strongest lines of groups 1, 3, and 4 are included in both parts of the level scheme (Figs. 1 and 2). To aid the reader, the groups and bands shown in Figs. 1, 2, and 3 are separated by dotted lines.

$E2$ crossover transitions. Similar structures have been found, e.g. in ^{194}Pb (groups a, b, and d of Ref. [15]), ^{197}Pb (group 2 of Ref. [16]), ^{198}Pb (group b of Ref. [12]), and ^{200}Pb (group 1 of Ref. [23]).

The transitions of groups 3 and 4 in Fig. 2 extend the spherical level scheme. While none of these transitions are in coincidence with any of the dipole bands, this part of the level scheme might be of interest in the search for transitions which could link the superdeformed bands found in ^{193}Pb [28] to normal excitations. The lifetimes, spins and parities of the levels of groups 3 and 4 displayed in Fig. 1 are taken from [26]. Our DCO ratios confirm the spin assignments given in [26] with the exception of the 2321 level in group 4. Our analysis gives a DCO ratio of 0.61 ± 0.16 for the 180-keV transition depopulating this level, which is not in agreement with the earlier proposed assignment of a stretched quadrupole transition. For most of the 32 new transitions in Fig. 2, DCO ratios could be determined. While many of the new transitions have DCO ratios consistent with stretched quadrupole character, $\Delta I = 0$ dipole or mixed multipolarities could not be excluded for all of these.

Figure 3 shows the transitions of group 5 which are feeding into band 1a. Most of these γ rays have transition energies near 400 keV (dipoles) and 800 keV ($E2$), as do the transitions in dipole band 1a. Also, the DCO ratios of the group 5 lines are comparable to those of the in-band $M1$ transitions. While the levels in this group have irregular spacings, their properties seem to be closer to those of the regular bands than to the spherical part of the level scheme.

B. Dipole bands

The strongest dipole band observed in the present study has been labeled band 1a in Fig. 1. The characteristics of this band, when combined with its proposed extension, band 1b, are similar to those observed for the strongest negative-parity dipole bands in the heavier odd-mass lead isotopes ^{195,197,199,201}Pb [16,23,29,30]. The second strongest band was

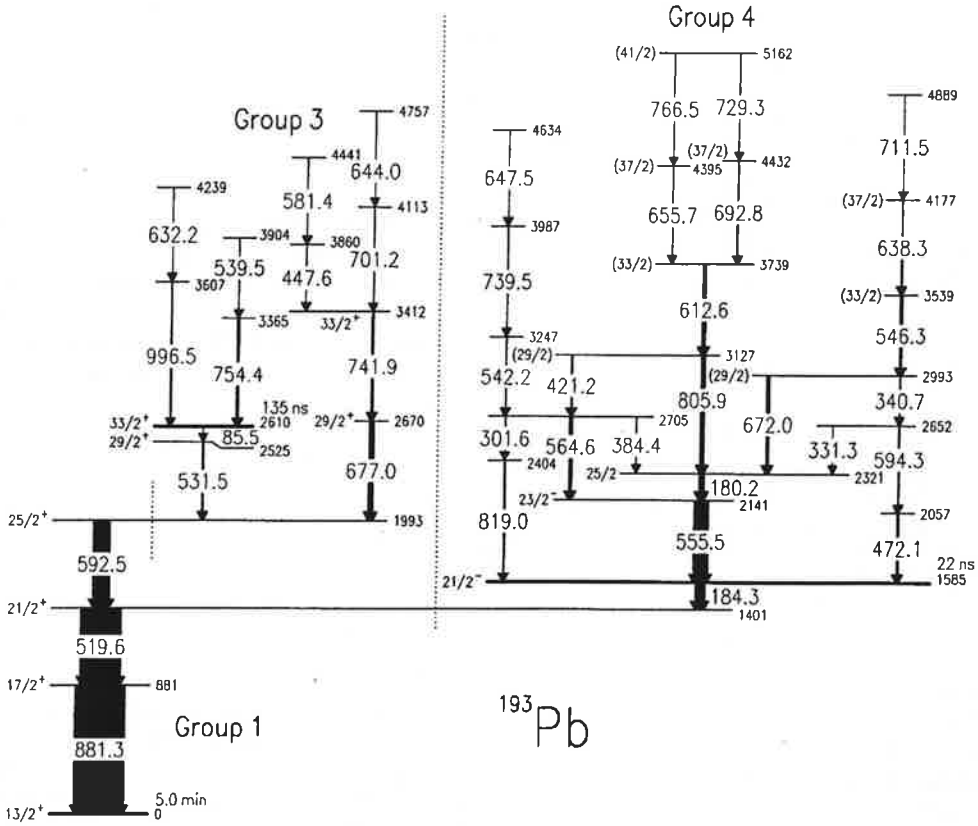

FIG. 2. Partial level scheme of ^{193}Pb showing the spherical part which is not connected to the dipole bands.

labeled band 2. This band is similar to the strongest positive-parity dipole bands in the heavier odd-A lead isotopes [16,23,29,30]. The bands 1a, 1b, 2, and 3 have been populated with 35 ± 6, 3 ± 2, 11 ± 3, and $10\pm2\%$ of the intensity of the 881.3-keV transition, respectively.

Figure 4(a) shows a sum of spectra double-gated on the dipole transitions of band 1a. These transitions are in coincidence with transitions in group 1 of the spherical levels. Six weak $E2$ crossover transitions have been found in band 1a. Since the connection to the ground state has been established, the spin and excitation energy of the bandhead are known quantities, which are essential for a comparison between theoretical and experimental values. The DCO ratios of all of the transitions in the cascade are consistent with stretched dipole character. Intensity arguments require an $M1$ assignment for the lowest energy lines. The crossover $E2$ transitions then require all of the levels in the band to have the same parity. The conversion corrected intensities of transitions depopulating the excitations of band 1 are listed in Table III, where the crossover transitions are included in

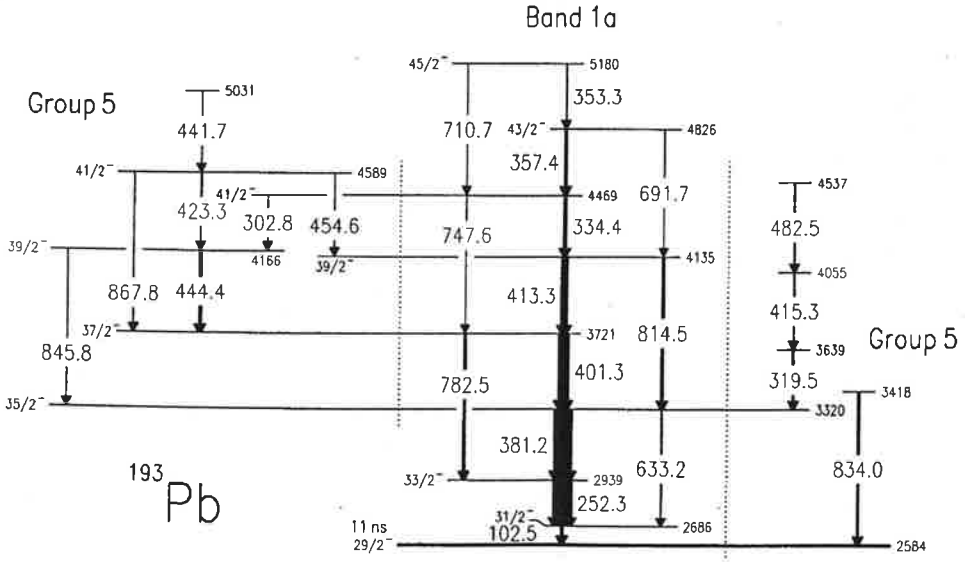

FIG. 3. Partial level scheme of ^{193}Pb showing band 1a and the transitions of group 5 which feed this band.

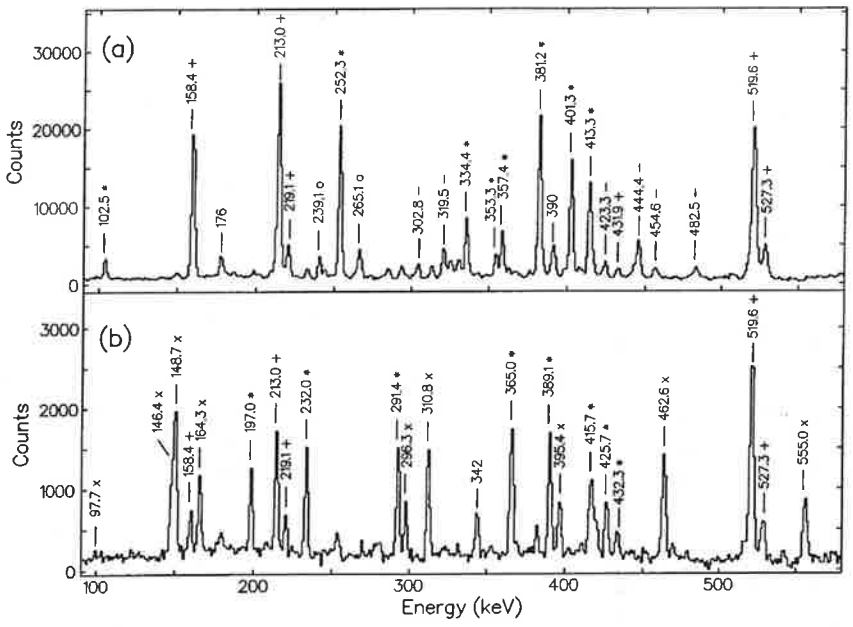

FIG. 4. Sum of double-gated coincidence spectra of bands 1 and 2 in ^{193}Pb. Transitions of bands 1a and 2 are labeled by an asterisk, transitions of band 1b with circles. The transitions within the groups in ^{193}Pb are labeled with "+," "×," and "−" signs for groups 1, 2 and 5, respectively.

the total intensity numbers. The $B(M1)/B(E2)$ ratios in Table III are smaller than in the heavier lead nuclei [19,23], but comparable to those in ^{195}Pb [29]. Intensity is feeding into band 1a over the entire spin range, but no depopulation is observed until below the bandhead.

Band 1b is only weakly populated. It decays via unobserved transitions into band 1a. Only four transitions have been assigned to this band. The bandhead spin is estimated to be $47/2 \pm 1\hbar$ from the decay pattern.

Figure 5(a) shows the experimental spins as a function of rotational frequency for band 1a and 1b in ^{193}Pb and for the corresponding bands in other odd-A Pb isotopes [16,23,29,30]. The structure in the lower part is very similar for all bands. The backbending starts at about $\hbar\omega \sim 0.4$ MeV, suggesting a crossing frequency of about 0.3 MeV for all odd-A lead isotopes. The two transitions at the top of band 1a in ^{193}Pb show a sharp upbend, which might be the onset of a second backbending or, perhaps, the band becomes irregular at higher spins. The curve of band 1b as displayed in Fig. 5(a) has approximately the same spin and slope as the upper part of band 1 in ^{197,199}Pb and band 1b in ^{195}Pb suggesting a similar structure.

Figure 4(b) shows a sum of spectra double-gated on the dipole transitions of band 2. These transitions are in coincidence with the transitions of group 2. The connection of this dipole band 2 to the spherical levels has been established, enabling a comparison of experimental and theoretical values. As discussed above, there remains an ambiguity in the spin assignment for band 2, and the parity could not be determined. Only one $E2$ crossover transition has been observed. The $B(M1)/B(E2)$ ratio given in Table III is small compared to the "shears" bands in the heavier lead isotopes [19,23]. The intensity pattern summarized in Table III is similar to that of most of the "shears" bands. There is sidefeeding over a wide spin range, but depopulation occurs only in parallel with the lowest transition. The transitions associated with the missing intensity depopulating the (41/2) level could not be observed. The spin versus rotational frequency, $\hbar\omega$, plot [Fig. 5(b)] shows that band 2 follows the systemat-

TABLE III. Spins, transition energies, total intensities, and $B(M1)/B(E2)$ values for dipole bands in ^{193}Pb.

I_{initial} ($\hbar$)	$E_\gamma(E2)$ (keV)	$E_\gamma(M1)$ (keV)	I_{tot} [a]	$B(M1)/B(E2)$ $(\mu/e\text{b})^2$
Band 1a				
$31/2^-$		102.5	100.0 ± 17.4	
$33/2^-$		252.3	99.3 ± 10.5	
$35/2^-$	633.2	381.2	77.9 ± 9.8	16.4 ± 5.2
$37/2^-$	782.5	401.3	54.9 ± 7.5	12.8 ± 2.6
$39/2^-$	814.5	413.3	33.8 ± 5.3	7.9 ± 2.0
$41/2^-$	747.6	334.4	15.8 ± 3.0	27.9 ± 11.4
$43/2^-$	691.7	357.4	12.6 ± 3.2	21.6 ± 8.0
$45/2^-$	710.7	353.3	6.2 ± 2.3	10.0 ± 3.8
Band 1b				
(49/2)		239.1	73.4 ± 19.8	
(51/2)		265.1	100.0 ± 22.0	
(53/2)		329.4	56.1 ± 18.2	
(55/2)		374.9	17.1 ± 7.4	
Band 2				
(41/2)		197.0	46.9 ± 15.0	
(43/2)		232.0	100.0 ± 15.6	
(45/2)		291.4	79.5 ± 12.7	
(47/2)		365.0	61.3 ± 9.8	
(49/2)	753.8	389.1	38.3 ± 7.3	8.2 ± 2.2
(51/2)		415.7	18.7 ± 4.7	
(53/2)		425.7	10.8 ± 3.2	
(55/2)		432.3	6.8 ± 2.5	
Band 3				
$29/2^+$		342.6	100.0 ± 12.4	
$31/2^+$	705.9	363.5	91.2 ± 14.6	7.0 ± 1.3
$33/2^+$	772.8	409.3	53.2 ± 10.6	4.1 ± 0.8
$35/2^+$	791.1	381.7	30.2 ± 8.4	4.9 ± 1.0

[a]Total intensity of dipole transitions plus intensity of the parallel $E2$ crossover transitions. The intensities are normalized to the strongest band transition.

ics of the strong, positive-parity bands found in the heavier odd-A Pb isotopes [16,23,29,30]. This similarity suggests positive parity for band 2 in ^{193}Pb. While bands 2 in ^{199}Pb and ^{201}Pb show a constant slope, the curve upbends in the lighter isotopes, probably indicating the alignment of additional $i_{13/2}$ neutrons.

Only four transitions have been observed in band 3. They have relatively large intensities and show a less regular energy pattern compared to the other bands in ^{193}Pb. Three crossover transitions have been assigned. Spin and parity could be assigned to this band as it decays directly to the known $27/2^+$ level at 2426 keV. It is possible that the transitions of this band are electric dipoles, but no $E1$ dipole bands have been previously observed in the neighboring lead isotopes. Intensity arguments can exclude $E1$ transitions for the other dipole bands, since these bands have low energy transitions near the bandhead which are strongly converted. For band 3 the $B(M1)/B(E2)$ ratios summarized in Table III are low compared to the other dipole bands in ^{193}Pb.

IV. DISCUSSION

A. Tilted-axis cranking calculations

Lifetime measurements [17–21] of magnetic dipole bands in the Pb isotopes indicate that these bands are built on weakly deformed structures; the oblate character is deduced from negative $E2/M1$ mixing ratios [1,2]. These results are supported by theoretical calculations, including those in the tilted-axis cranking (TAC) framework [23], which indicate that the quadrupole deformation parameter β is in the range $0.05 \leq \beta \leq 0.1$ and $\gamma \approx -70°$ for the bands found in the lead isotopes. For this deformation the highest occupied proton orbital is the $s_{1/2}$ level from which excitations are readily possible across the $Z=82$ gap into the high-K levels of the $h_{9/2}$ and $i_{13/2}$ subshells.

For the neutrons the $i_{13/2}$ subshell is partly filled and holes in the upper levels of this shell contribute to the neutron spin. These are the levels with small K values, and the angular momentum for the neutrons has only a small component in the direction of the nuclear symmetry axis. This means that near the bandhead proton and neutron spins are perpendicular to each other. The total spin is, therefore, tilted to the symmetry axis by an angle of about 45°. Tilted axis cranking (TAC) calculations show that this angle remains nearly constant within the bands. The generation of angular momentum within the bands can be explained by a continuous increase in the alignment of the proton and the neutron spins into the direction of the total spin [22]. At the top of the band both spins are expected to be parallel, resulting in the maximum total spin.

Theoretical calculations of the excitation energies of possible $M1$ band configurations have been performed by applying the semiclassical TAC formalism described in [22]. For simplicity the deformation parameters are kept constant at $\beta=0.1$ and $\gamma=-60°$ as the results of the calculations do not change strongly for slightly varying deformations. The pairing constants were $\Delta=0$ for the protons and $\Delta=0.75$ for the neutrons. The latter corresponds to 80% of the odd-even mass difference, which gives good agreement between theory and experiment in the lead region. The application of the calculations to the very similar isotope ^{199}Pb are described in more detail in [23]. To compare calculated and experimental values, the classical variable J is associated with the nuclear spin quantum number $I+1/2$ to account for the lowest order quantal corrections. For the transition $I \rightarrow I-1$ the transition energy is associated with $\hbar\omega$ and the classical transition spin $J=\frac{1}{2}[I+(I-1)]+\frac{1}{2}=I$.

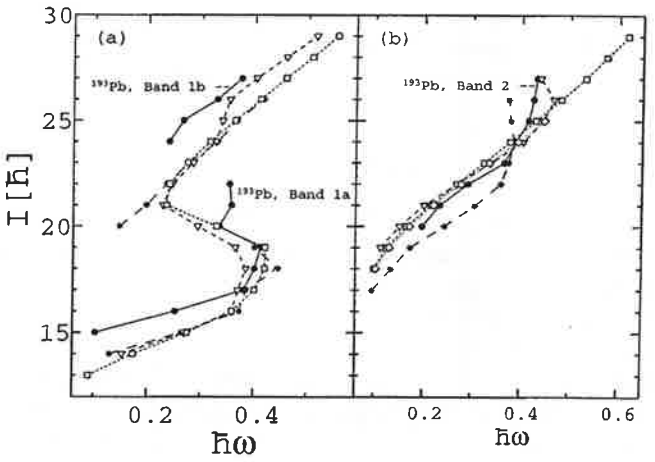

FIG. 5. Experimental spins as a function of rotational frequency for band 1 (a) and band 2 (b) in the odd-A Pb isotopes ^{193}Pb (●), ^{195}Pb (*), ^{197}Pb (▽), ^{199}Pb (□), and ^{201}Pb (◇). Values are taken from [16,23,29,30] and the present work.

B. Configuration assignment

The configurations which we propose to assign to the bands in ^{193}Pb are summarized in Table IV. In this table the nucleon configurations are labeled according to the standard cranked shell model convention. Neutron configurations with positive parity ($i_{13/2}$) are labeled with the letters A, B, C, and D in the order of rising level energy, while negative parity neutron orbitals ($p_{3/2}$ and $f_{5/2}$) are labeled E and F. The proton configurations are only labeled by the total proton spin, for example, 11 for one $h_{9/2}$ and one $i_{13/2}$ protons coupled to 11^-.

There are four points which support the assignments given in Table IV: (i) The systematics of the experimental spins in the odd-A lead isotopes, (ii) the systematics of the bandhead energies, (iii) comparison of TAC calculations with experimental spins and (iv) comparison of calculations with experimental excitation energies within the bands in

TABLE IV. Proposed configurations for dipole bands in ^{193}Pb.

Band	Configuration [a]	Neutrons	Protons
1a	A11	$(i_{13/2}^{-1})13/2^+$	$(s_{1/2}^{-2}h_{9/2}i_{13/2})11^-$
1b	ABC11	$(i_{13/2}^{-3})33/2^+$	$(s_{1/2}^{-2}h_{9/2}i_{13/2})11^-$
2	ABE11	$(i_{13/2}^{-2}p_{3/2}^{-1})27/2^-$	$(s_{1/2}^{-2}h_{9/2}i_{13/2})11^-$
	ABF11	$(i_{13/2}^{-2}f_{5/2}^{-1})29/2^-$	$(s_{1/2}^{-2}h_{9/2}i_{13/2})11^-$
3	A7	$(i_{13/2}^{-1})13/2^+$	$(s_{1/2}^{-1}i_{13/2})7^+$
	A8	$(i_{13/2}^{-1})13/2^+$	$(s_{1/2}^{-2}h_{9/2}^{2})8^+$

[a] Abbreviations are explained in the text.

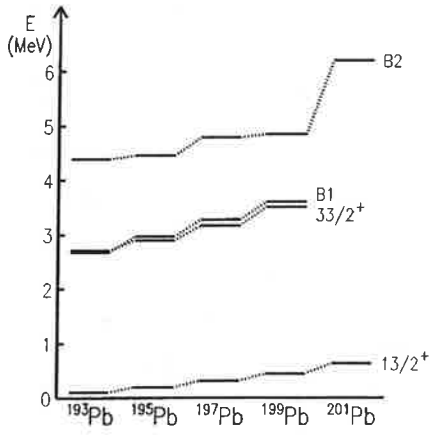

FIG. 6. Odd mass Pb systematics of the bandhead energies of band 1 ($B1$) and band 2 ($B2$) compared to the $13/2^+$ and $33/2^+$ spherical levels. Values are taken from [16,23,29,30] and the present work. The energy of the $13/2^+$ state in ^{193}Pb is estimated to be ≈ 100 keV from systematics. Unknown low energy transitions in ^{199}Pb (below band 2) and in ^{201}Pb ($29/2^- \rightarrow 25/2^-$) are assumed to have 70 keV. The single-particle configurations of the bandheads are given in Table IV; the configurations of the $13/2^+$ and $33/2^+$ levels are $\nu(i_{13/2}^{-1})$ and $\nu(i_{13/2}^{-3})$, respectively.

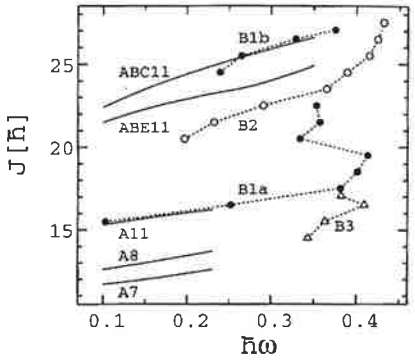

FIG. 7. Experimental and TAC-calculated spins as a function of the rotational frequency, $\hbar\omega$, for the dipole bands in ^{193}Pb. The experimental dipole bands [band 1 below ($B1a$) and above ($B1b$) the backbend, band 2 ($B2$) and band 3 ($B3$)] are indicated by symbols connected by dashed lines. The theoretical calculations (solid lines) are labeled by the configurations listed in Table IV. For band 1b and band 2 the experimental spins have an uncertainty of $\pm 1\hbar$.

^{193}Pb. The proton $(h_{9/2}i_{13/2})11^-$ configuration is also consistent with earlier lifetime measurements [18].

Figure 5 shows the experimental spins as a function of rotational frequency for band 1 and band 2 in the odd-A Pb isotopes. As already discussed above, the bands show similar properties in all isotopes, which suggests the assignment of the same nucleon configuration to all bands 1 and bands 2, respectively, in the odd-A Pb isotopes. In earlier work [16,23], band 1 has been assigned A11 below the backbend in the heavier isotopes. The configuration ABC11 has been assigned for band 1 above the backbend in ^{197,199}Pb [16,23] and for band 1b in ^{195}Pb [29]. These configurations correspond to one and three $i_{13/2}$ neutron holes (A and ABC in CSM notation), which couple to the 11^- proton configuration to form the "shears" bands. Band 2 has been proposed as ABE11 in ^{195,197,199,201}Pb [29,16,23,30] where the negative parity neutron "E" stems from the $f_{5/2}-p_{3/2}$ orbitals.

In Fig. 6 the bandhead energies of bands 1 and 2 in the odd-A lead isotopes are compared to the energies of the spherical $13/2^+$ and $33/2^+$ levels. The smooth increase of the bandhead excitation energies with increasing neutron number also suggests the assignment of the same nucleon configuration to all bands 1 and bands 2, respectively. The sharp increase of excitation energy for band 2 in ^{201}Pb can be explained by the filling of the $i_{13/2}$ neutron shell in this isotope and, therefore, more energy is necessary to excite neutrons across the shell gap.

Figure 7 shows the experimental spins of the dipole bands in ^{193}Pb versus $\hbar\omega$. The calculated values for all possible configurations are also included in Fig. 7. The experimental values for band 1a, 1b, and band 2 below the upbending are well-reproduced by the calculated values, thus suggesting the configurations A11, ABC11, and ABE11, respectively, which have also been assigned to the corresponding bands in the heavier lead nuclei. Band 2 could also have the configuration ABF11; since the calculated values for this configuration are similar to those for ABE11 they are not included in the figure. The configurations involving one neutron hole (A) could only be calculated up to 0.23 MeV because at this frequency there is a high level density for neutron orbitals in the Nilsson diagram. This high level density causes irregularities in the calculated energies which originate from competing quasi-neutron configurations. This is different from the calculations in the heavier isotopes, where one may follow the configuration up to much higher frequency [23]. This means that for neutron number around 110 the rearrangement of the neutrons into different quasiparticle configurations competes with the gradual closing of the blades of the shears, resulting in less regular dipole sequences. This aspect will be discussed further in the following section.

Band 3 has lower spin and excitation energy than the other bands. Therefore, the positive-parity configuration A7, in which only one high-j $i_{13/2}$ proton contributes, is a possible assignment for this band. The positive-parity configuration A8, in which two protons are excited in the $h_{9/2}$ orbital, could also explain the properties of band 3 and is, therefore, included in Fig. 7. Band 3 starts at $\hbar\omega=0.34$ while the calculations only provide reliable results up to $\hbar\omega=0.23$; extrapolating the calculated curves does not help to provide an unambiguous configuration assignment of band 3. This band, which lies high in frequency, is not very regular.

In Fig. 8 experimental and calculated excitation energies as a function of J are compared. The experimental values of bands 1a, 1b, and 2 have slopes similar to the calculated values for the proposed configurations. However, there remains an uncertainty in the configuration assignment for band 1b because the absolute excitation energy based on the decay pattern is only a rough estimate. Transitions which link this band to the rest of the level scheme have not been identified. Also in Fig. 8 the experimental values for band 3 are compared with the TAC calculations for the configurations A7 and A8. However, the calculations for both configurations predict a smaller slope than the experimental values.

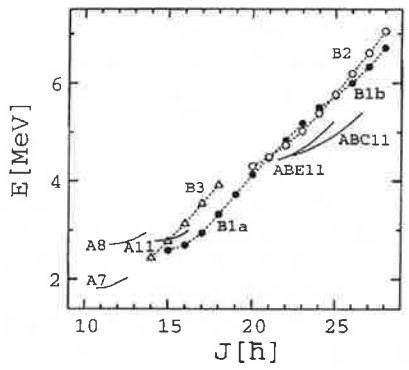

FIG. 8. Experimental and calculated excitation energies as a function of spin for the dipole bands in ^{193}Pb. For band 1b the absolute excitation energy is not known and only roughly estimated from the decay pattern. See also caption to Fig. 7.

C. Regularity of bands

Some of the ''shears'' bands in the heavier isotopes have been originally interpreted as irregular bands. Due to better statistics in recent experiments the order of the transitions has been reversed in ^{196}Pb [32], ^{197}Pb [16] and ^{198}Pb [33]. This leaves only regular bands in $^{195-202}$Pb, while there are slightly irregular bands in ^{192}Pb [34], ^{193}Pb and ^{194}Pb [35].

Generally, there is a tendency that the ''shears'' bands become shorter and less regular with decreasing neutron number. Such a behavior has been found in a shell model study of ''shears'' bands [31], where it has been attributed to a lack of particles in the $f_{5/2}-p_{3/2}$ orbitals, which serve as a kind of ''glue'' to fix the two blades of the shears.

The neutron number 112 marks the border between the regions where the neutron system prefers prolate instead of slight oblate deformation (cf., e.g., [36,37]). The lower $B(M1)/B(E2)$ values and the higher $\mathcal{J}^{(2)}$ value of the regular parts of bands 1a and 1b in ^{193}Pb, as compared to the heavier Pb isotopes, may be evidence for the tendency of the neutron system towards prolate deformation. The surprising fact that this leads to *less regular* bands can be understood. TAC calculations show that larger deformation suppresses the ''shears'' mechanism, because the restoring force that keeps the blades open increases. On the other hand, it becomes easier to generate collective angular momentum from the core nucleons, which do not participate in the shears. In the heavy Pb isotopes the ''shears'' mechanism is the dominating source of angular momentum [22], generating very regular sequences, whereas in the lighter ones the angular momentum contribution from the deformed core becomes more important. Since the deformation is still rather small, it does not lead to regular bands but rather to irregular quasirotational sequences. An additional element which could destabilize the ''shears'' mechanism is the change from small oblate to prolate deformation (cf. [36]), because the deformed field that ''glues'' the high j particles to the two blades of the ''shears'' is no longer optimal (cf. the overlap arguments given in Ref. [22]).

V. CONCLUSION

Excitations in ^{193}Pb up to $55/2\hbar$ and 7 MeV in energy were deduced from experiments with early implementation of GAMMASPHERE and HERA arrays of Compton-suppressed Ge detectors using the ^{174}Yb(^{24}Mg,5n) reaction at beam energies of 129, 131, and 134 MeV. The spherical part of the level scheme was considerably extended, which might be helpful in the search of the linking transitions for the superdeformed bands which have been found in this nucleus.

Four bands of enhanced dipole transitions have been observed in ^{193}Pb. Three of these bands have transitions which connect them to the spherical levels, thus enabling a comparison between experimental values and theoretical calculations. The bands are built on configurations involving the high-K proton $h_{9/2}$ and $i_{13/2}$ levels and holes in the low-K levels of the $i_{13/2}$ neutron shell. A comparison of the experimental results with tilted axis cranking (TAC) calculations shows a good agreement for the proposed configurations for bands 1 and 2, while the short, less regular band (band 3) cannot be assigned an unambiguous configuration. Probably band 3 is built on a configuration involving only one high-j proton particle and one high-j neutron hole.

As a result of the present work, the systematics of the $M1$ bands in the odd-A Pb isotopes have been extended. Bands 1 and 2 show a pattern similar to that of the corresponding bands in the heavier lead isotopes, ^{195,197,199,201}Pb, thus suggesting that all of these bands are built on the same configurations.

It appears that ^{193}Pb marks the lower borderline of the region of regular ''shears'' bands in the heavy lead isotopes. This change could be caused by a competition between the neutrons that begin to drive towards prolate deformation below $N=112$ and the closed shell of the proton system that does not allow for large deformation. This competition means that the change in $M1$ character materializes as the appearance of less regular bands instead of more regular ones.

ACKNOWLEDGMENTS

This work has been funded by the National Science Foundation (Rutgers) and by the Department of Energy, under Contract Nos. DE-AC03-76SF00098 (LBL) and W-7405-ENG-48 (LLNL). We want to thank the group in Orsay, France [29] for providing results on ^{195}Pb prior to publication.

[1] R.M. Clark, R. Wadsworth, E.S. Paul, C.W. Beausang, I. Ali, A. Astier, D.M. Cullen, P.J. Dagnall, P. Fallon, M.J. Joyce, M. Meyer, N. Redon, P.H. Regan, W. Nazarewicz, and R. Wyss, Phys. Lett. B **275**, 247 (1992).

[2] G. Baldsiefen, H. Hübel, D. Mehta, B.V. Thirumala Rao, U. Birkental, G. Fröhlingsdorf, M. Neffgen, N. Nenoff, S.C. Pancholi, N. Singh, W. Schmitz, K. Theine, P. Willsau, H. Grawe, J. Heese, H. Kluge, K.H. Maier, M. Schramm, R. Schubart,

and H.J. Maier, Phys. Lett. B **275**, 252 (1992); Prog. Part. Nucl. Phys. **28**, 427 (1992); in *Proceedings of the Xth International School on Nuclear Physics, Neutron Physics and Nuclear Energy,* Varna 1991, edited by W. Andreitscheff and D. Elenkov (Institute for Nuclear Research and Nuclear Energy, Sofia, 1991).

[3] A. Kuhnert, M.A. Stoyer, J.A. Becker, E.A. Henry, M.J. Brinkman, S.W. Yates, T.F. Wang, J.A. Cizewski, F.S. Stephens, M.A. Deleplanque, R.M. Diamond, A.O. Macchiavelli, J.E. Draper, F. Azaiez, W.H. Kelly, and W. Korten, Phys. Rev. C **46**, 133 (1992); Nucl. Phys. **A553**, 567c (1993).

[4] R.M. Clark, R. Wadsworth, E.S. Paul, C.W. Beausang, I. Ali, A. Astier, D.M. Cullen, P.J. Dagnall, P. Fallon, M.J. Joyce, M. Meyer, N. Redon, P.H. Regan, J.F. Sharpey-Schafer, W. Nazarewicz, and R. Wyss, Z. Phys. A **342**, 371 (1992).

[5] G. Baldsiefen, H. Hübel, F. Azaiez, C. Bourgeois, D. Hojman, A. Korichi, N. Perrin, and H. Sergolle, Z. Phys. A **343**, 245 (1992).

[6] N. Roy, J.A. Becker, E.A. Henry, M.J. Brinkman, M.A. Stoyer, J.A. Cizewski, R.M. Diamond, M.A. Deleplanque, F.S. Stephens, C.W. Beausang, and J.E. Draper, Phys. Rev. C **47**, R930 (1993).

[7] J.R. Hughes, Y. Liang, R.V.F. Janssens, A. Kuhnert, J.A. Becker, I. Ahmad, I.G. Bearden, M.J. Brinkman, J. Burde, M.P. Carpenter, J.A. Cizewski, P.J. Daly, M.A. Deleplanque, R.M. Diamond, J.E. Draper, C. Duyar, B. Fornal, U. Garg, Z.W. Grabowski, E.A. Henry, R.G. Henry, W. Hesselink, N. Kalantar-Nayestanaki, W.H. Kelly, T.L. Khoo, T. Lauritzen, R.H. Mayer, D. Nissius, J.R.B. Oliveira, A.J.M. Plompen, W. Reviol, E. Rubel, F. Soramel, F.S. Stephens, M.A. Stoyer, D. Vo, and T.F. Wang, Phys. Rev. C **47**, R1337 (1993).

[8] B. Cederwall, M.A. Deleplanque, F. Azaiez, R.M. Diamond, P. Fallon, W. Korten, I.Y. Lee, A.O. Macchiavelli, J.R.B. Oliveira, F.S. Stephens, W.H. Kelly, D.T. Vo, J.A. Becker, M.J. Brinkman, E.A. Henry, J.R. Hughes, A. Kuhnert, M.A. Stoyer, T.F. Wang, J.E. Draper, C. Duyar, E. Rubel, and J. de Boer, Phys. Rev. C **47**, R2443 (1993).

[9] G. Baldsiefen, U. Birkental, H. Hübel, N. Nenoff, B.V. Thirumala Rao, P. Willsau, J. Heese, H. Kluge, K.H. Maier, R. Schubart, and S. Frauendorf, Phys. Lett. B **298**, 54 (1993).

[10] R.M. Clark, R. Wadsworth, F. Azaiez, C.W. Beausang, A.M. Bruce, P.J. Dagnall, P. Fallon, P.M. Jones, M.J. Joyce, A. Korichi, E.S. Paul, and J.F. Scharpey-Schafer, J. Phys. G **19**, L57 (1993).

[11] P. Dagnall, C.W. Beausang, P. Fallon, P.D. Forsyth, E.S. Paul, J.F. Sharpey-Schafer, P.J. Twin, I. Ali, D.M. Cullen, M.J. Joyce, G. Smith, R. Wadsworth, R.M. Clark, P.H. Regan, A. Astier, M. Meyer, and N. Redon, J. Phys. G **19**, 465 (1993).

[12] R.M. Clark, R. Wadsworth, E.S. Paul, C.W. Beausang, I. Ali, A. Astier, D.M. Cullen, P.J. Dagnall, P. Fallon, M.J. Joyce, M. Meyer, N. Redon, P.H. Regan, J.F. Sharpey-Schafer, W. Nazarewicz, and R. Wyss, Nucl. Phys. **A562**, 121 (1993).

[13] Y. LeCoz, N. Redon, A. Astier, R. Berand, R. Duffait, M. Meyer, F. Hannachi, G. Bastin, I. Deloncle, B. Gall, M. Kaci, M.G. Porquet, C. Schück, F. Azaiez, C. Bourgeois, J. Duprat, A. Korichi, N. Perrin, N. Poffé, H. Sergolle, J.F. Sharpey-Schafer, C.W. Beausang, S.J. Gale, M.J. Joyce, E.S. Paul, R.M. Clark, K. Hauschild, R. Wadsworth, J. Simpson, M.A. Bentley, A.G. Smith, H. Hübel, P. Willsau, G. de France, S. Ahmad, M. Carpenter, R. Henry, R.V.F. Janssens, T.L. Khoo, and T. Lauritsen, Z. Phys. A **348**, 87 (1994).

[14] P.J. Dagnall, C.W. Beausang, R.M. Clark, R. Wadsworth, S. Bhattacharjee, P. Fallon, P.D. Forsyth, D.B. Fossan, G. de France, S.J. Gale, F. Hannachi, K. Hauschild, I.M. Hibbert, H. Hübel, P.M. Jones, M.J. Joyce, A. Korichi, W. Korten, D.R. LaFosse, E.S. Paul, H. Schnare, K. Starosta, J.F. Sharpey-Schafer, P.J. Twin, P. Vaska, M.P. Waring, and J.N. Wilson, J. Phys. G **20**, 1591 (1994).

[15] M.G. Porquet, F. Hannachi, G. Bastin, V. Brindejonc, I. Deloncle, B. Gall, C. Schück, A.G. Smith, F. Azaiez, C. Bourgeois, J. Duprat, A. Korichi, N. Perrin, N. Poffé, H. Sergolle, A. Astier Y. LeCoz, M. Meyer, N. Redon, J. Simpson, J.F. Sharpey-Schafer, M.J. Joyce, C.M. Beausang, R. Wadsworth, and R.M. Clark, J. Phys. G **20**, 765 (1994).

[16] G. Baldsiefen, S. Chmel, H. Hübel, W. Korten, M. Neffgen, W. Pohler, U.J. van Severen, J. Heese, H. Kluge, K.H. Maier, and K. Spohr, Nucl. Phys. **A587**, 562 (1995).

[17] T.F. Wang, E.A. Henry, J.A. Becker, A. Kuhnert, M.A. Stoyer, S.W. Yates, M.J. Brinkman, J.A. Cizewski, A.O. Macchiavelli, F.S. Stephens, M.A. Deleplanque, R.M. Diamond, J.E. Draper, F.A. Azaiez, W.H. Kelly, W. Korten, E. Rubel, and Y.A. Akovali, Phys. Rev. Lett. **69**, 1737 (1992).

[18] J.R. Hughes, J.A. Becker, M.J. Brinkman, E.A. Henry, R.W. Hoff, M.A. Stoyer, T.F. Wang, B. Cederwall, M.A. Deleplanque, R.M. Diamond, P. Fallon, I.Y. Lee, J.R.B. Oliveira, F.S. Stephens, J.A. Cizewski, L.A. Bernstein, J.A. Draper, C. Duyar, E. Rubel, W.H. Kelly, and D. Vo, Phys. Rev. C **48**, 2135 (1993).

[19] R.M. Clark, R. Wadsworth, H.R. Andrews, C.W. Beausang, M. Bergstrom, S. Clarke, E. Dragulescu, T. Drake, P.J. Dagnall, A. Galindo-Uribarri, G. Hackman, K. Hauschild, I.M. Hibbert, V.P. Janzen, P.M. Jones, R.W. MacLeod, S.M. Mullins, E.S. Paul, D.C. Radford, A. Semple, J.F. Sharpey-Schafer, J. Simpson, D. Ward, and G. Zwartz, Phys. Rev. C **50**, 84 (1994).

[20] E.F. Moore, M.P. Carpenter, Y. Liang, R.V.F. Janssens, I. Ahmad, I.G. Bearden, P.J. Daly, M.W. Drigert, B. Fornal, U. Garg, Z.W. Grabowski, H.L. Harrington, R.G. Henry, T.L. Khoo, T. Lauritsen, R.H. Mayer, D. Nisius, W. Reviol, and M. Sferrazza, Phys. Rev. C **51**, 115 (1995).

[21] M. Neffgen, G. Baldsiefen, S. Frauendorf, H. Grawe, J. Heese, H. Hübel, H. Kluge, A. Korichi, W. Korten, K.H. Maier, D. Mehta, J. Meng, N. Nenoff, M. Piiparinen, M. Schönhofer, R. Schubart, U.J. van Severen, N. Singh, G. Sletten, B.V. Thirumala Rao, and P. Willsau, Nucl. Phys. **A595**, 499 (1995).

[22] S. Frauendorf, Nucl. Phys. **A557**, 259c (1993).

[23] G. Baldsiefen, H. Hübel, W. Korten, D. Mehta, N. Nenoff, B.V. Thirumala Rao, P. Willsau, H. Grawe, J. Heese, H. Kluge, K.H. Maier, R. Schubart, S. Frauendorf, and H.J. Maier, Nucl. Phys. **A574**, 521 (1994).

[24] M.A. Stoyer *et al.*, *Proceedings of the 205th American Chemical Society*, Denver, Colorado, 1993, part II, abstract NUCL-56; M.A. Stoyer *et al.*, Bull. Am. Phys. Soc. **37**, 1321 (1992) and LLNL UCRL-JC-109941-ABS (1992); M.A. Stoyer *et al.*, Contribution to the International Conference on Nuclear Structure at High Angular Momentum, Ottawa, 1992 (unpublished), p. 72.

[25] H.-Q. Jin, Software package, Oak Ridge National Laboratory (1995).

[26] J.M. Lagrange, M. Pautrat, J.S. Dionisio, Ch. Vieu, and J. Vanhorenbeeck, Nucl. Phys. **A530**, 437 (1991).

[27] J.O. Newton, F.S. Stephens, and R.M. Diamond, Nucl. Phys. **A236**, 225 (1974).

[28] J.R. Hughes, J. A. Becker, L.A. Bernstein, M.J. Brinkman, L.P. Farris, E.A. Henry, R.W. Hoff, M.A. Stoyer, D.T. Vo, S. Asztalos, B. Cederwall, R.M. Clark, M.A. Deleplanque, R.M. Diamond, P. Fallon, I.Y. Lee, A.O. Macchiavelli, and F.S. Stephens, Phys. Rev. C **51**, R447 (1995).

[29] M. Kaci, M.G. Porquet, F. Hannachi, M. Aiche, G. Bastin, I. Deloncle, B.J.P. Gall, C. Schück, F. Azaiez, C.W. Beausang, C. Bourgeois, R.M. Clark, R. Duffait, J. Duprat, K. Hauschild, M.J. Joyce, A. Korichi, Y. Le Coz, M. Meyer, E.S. Paul, N. Perrin, N. Poffe, N. Redon, H. Sergolle, J.F. Sharpey-Schafer, J. Simpson, A.G. Smith, and R. Wadsworth, Z. Phys. A **354**, 267 (1996).

[30] G. Baldsiefen, P. Maagh, H. Hübel, W. Korten, S. Chmel, M. Neffgen, W. Pohler, H. Grawe, K.H. Maier, K. Spohr, R. Schubart, S. Frauendorf, and H.J. Maier, Nucl. Phys. **A592**, 365 (1995).

[31] S. Frauendorf, J. Reif, and G. Winter, Nucl. Phys. **A** (to be published).

[32] G. Baldsiefen, H. Hübel, W. Korten, U.J. van Severen, J.A. Cizewski, D. Bazzacco, N.H. Medina, C. Rossi Alvarez, G. Lo Bianco, and S. Signorelli, Z Phys. **A** (to be published).

[33] I.M. Hibbert and R. Wadsworth (private communication).

[34] A.J.M. Plompen, M.N. Harakeh, W.H.A. Hesselink, G. van't Hof, N. Kalantar-Nayestanaki, J.P.S. van Schagen, M.P. Carpenter, I. Ahmad, I.G. Bearden, R.V.F. Janssens, T.L. Khoo, T. Lauritsen, Y. Liang, U. Garg, W. Reviol, and D. Ye, Nucl. Phys. **A562**, 61 (1993).

[35] D. Mehta, W. Korten, H. Hübel, K. Theine, W. Schmitz, P. Willsau, C.X. Yang, F. Hannachi, D.B. Fossan, H. Grawe, H. Kluge, and K.H. Maier, Z. Phys. A **346**, 169 (1993).

[36] S. Frauendorf, F. R. May, and V. V. Pashkevich, in *Proceedings of the International Symposium on Future Directions in Studies of Nuclei far from Stability,* Nashville, Tennessee, 1979, edited by J. Hamilton, E.H. Spejewski, C.R. Bingham, and E.F. Zganjar (North-Holland, Amsterdam, 1980), p. 135.

[37] C. Roulet, G. Albouy, G. Auger, J.M. Lagrange, M. Pautrat, K.G. Rensfelt, H. Richel, H. Sergolle, and J. Vanhorenbeeck, Nucl. Phys. **A323**, 495 (1979).

Evidence for $M1$ Transitions between Superdeformed States in ^{193}Hg

P. Fallon, J. Burde, B. Cederwall, M. A. Deleplanque, R. M. Diamond, I. Y. Lee, J. R. B. Oliveira, and F. S. Stephens

Lawrence Berkeley Laboratory, 1 Cyclotron Road, Berkeley, California 94702

J. A. Becker, M. J. Brinkman, E. A. Henry, A. Kuhnert,[a] and M. A. Stoyer

Lawrence Livermore National Laboratory, Livermore, California 94550

J. E. Draper, C. Duyar, and E. Rubel

University of California, Davis, California 95616

(Received 19 November 1992)

Two-way decay has been observed between superdeformed bands in ^{193}Hg. It is proposed the decays have $M1$ multipolarity and connect signature partner bands. Candidates for the two-way gamma decays connecting superdeformed bands are observed for the first time.

PACS numbers: 21.10.Re, 23.20.Lv, 27.80.+w

Superdeformed states are associated with extremely large quadrupole deformations, typically $\beta_2 \approx 0.6$ in the mass 150 region [1,2] and $\beta_2 \approx 0.47$ in the mass 190 region [3,4]. The large quadrupole deformations enhance stretched $E2$ transition rates. Indeed both the mass 150 region and the mass 190 region have $B(E2)$ values [2–5] for superdeformed states which are 3 orders of magnitude larger than the corresponding single particle (Weisskopf) units. However, superdeformed bands around mass 190 extend to low frequencies ($\hbar\omega \sim 0.15$ MeV) and spins ($I_f \sim 8$) [6], much lower than for mass 150 nuclei. The large electron conversion coefficients associated with low energy $M1$ decays enhance the total $M1$ transition probability and the $E2$ transition probabilities decrease with decreasing transition energy [$T(E2) \propto E_\gamma^5$]. Thus it is more likely for $M1$ decays to compete with stretched $E2$ decays, resulting in cross talk between superdeformed states.

The first evidence for transitions between superdeformed bands was in ^{193}Hg [7]. Four superdeformed bands were observed and they were assigned as $[512]\frac{5}{2}$ $\alpha = -\frac{1}{2}$ (band 1), $[624]\frac{9}{2}$ $\alpha = \pm\frac{1}{2}$ (bands 2 and 3), and $j_{15/2}$ (band 4). Bands 1 and 3 ($\alpha = -\frac{1}{2}$) have identical transition energies at low spin. A fifth band was proposed (the "missing" $[512]\frac{5}{2}$ $\alpha = +\frac{1}{2}$ band) to have identical transition energies to band 2 ($\alpha = +\frac{1}{2}$) and this will be referred to as band 2′. Band 2′ would then be the signature partner to band 1. In order to clarify the ^{193}Hg superdeformed band assignments and to help prepare the way for the following discussion, a partial level scheme for bands 1, 2, 2′, and 3 is shown in Fig. 1. In Ref. [7] it was suggested that the decay proceeded from band 1 to band 3. The intensity of the cross talk was estimated to be of the order of 30% and it was proposed that the decays are $E1$.

In this paper we report on the first observation of two-way cross talk between superdeformed bands in ^{193}Hg. It is proposed that the cross talk is comprised of $M1$ transitions between superdeformed signature partner bands. In addition, candidates for the $M1$ γ decays are presented for the first time.

Excited states in ^{193}Hg were populated by the reaction ^{176}Yb(^{22}Ne,5n)^{193}Hg at a beam energy of 116 MeV. The gamma decay was detected using the high-energy-resolution array (HERA) Ge detector array at the Lawrence Berkeley Laboratory 88 in. cyclotron. The data were sorted into an E_γ-E_γ correlation matrix with

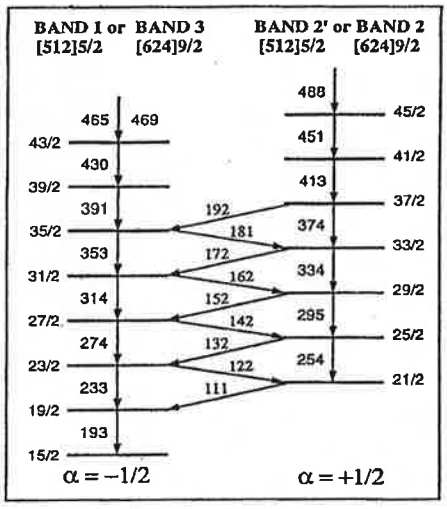

FIG. 1. Schematic partial level scheme for the proposed signature partner bands in ^{193}Hg. Following Ref. [7] we assume that there are two pairs of strongly coupled bands based on the two configurations $[512]\frac{5}{2}$ and $[624]\frac{9}{2}$. The two pairs of bands are "identical" up to the spins shown. Note that bands 2 and 2′ are not resolved and the single rotational sequence observed experimentally is assumed to be two bands. Also shown are $M1$ decays which may be expected to connect the signature partner bands. The $M1$ energies are *calculated* in the limit that the bands are strongly coupled. The spin assignments were derived from a fitting procedure and taken from Ref. [6].

the condition that at least two suppressed Ge detectors were in coincidence with a total γ-ray fold of 14 and higher. Approximately 680 million events were contained in this matrix of which $\sim$60% belonged to ^{193}Hg.

Figure 2(a) shows a γ-ray spectrum in coincidence with the 353 and 391 keV transitions in bands 1 and 3. [It is not possible to say whether the decay is from band 1, band 3, or both since the γ rays from these bands are identical (to within 0.5 keV) below 430 keV.] In addition to these bands, low lying transitions (254, 295, and 334 keV) in band 2 are seen to be in coincidence with the gating transitions. It is estimated that approximately 25% of the intensity from band 1 and/or band 3 goes over to band 2 (at spin $I \approx \frac{31}{2}$).

A spectrum of superdeformed γ rays in coincidence with the 451 keV γ ray in band 2 is shown in Fig. 2(b). Other members of band 2 can be clearly seen. However, this spectrum also contains transitions with energies of 233, 274, 314, and possibly 353 keV. These transition energies correspond to known γ rays in the superdeformed bands 1 and 3. The intensity of the cross talk is of the order of 30% relative to the inband decay (at spin $I \sim \frac{29}{2}$). Furthermore, a spectrum [Fig. 2(c)] gated by the 274 keV γ ray in bands 1 and 3 not only contains all transitions from bands 1 and 3 but also contains all transitions from band 2 starting from the 334 keV γ ray and is indicated in Fig. 2(c) by an asterisk. Note that the spectrum contains no evidence for a 254 or 294 keV superdeformed transition (band 2). This is consistent with bands 1 and 2′ and/or bands 3 and 2 being strongly coupled signature partner bands (Fig. 1). These observations [Figs. 2(a)–2(c)] suggest that not only is there evidence for decays from the $\alpha = -\frac{1}{2}$ to the $\alpha = +\frac{1}{2}$ structure (as observed by Cullen *et al.* [7]), but also from the $\alpha = +\frac{1}{2}$ to the $\alpha = -\frac{1}{2}$ structure. This is the first time that two-way cross talk has been reported between superdeformed bands.

Two-way cross talk, as observed in these data, implies little or no energy splitting between the connecting bands. Since it is proposed [7] that both positive and negative parity superdeformed bands exist, it is possible the decay may be either $E1$ or $M1$. Collective low energy $E1$ transitions between rotational bands of alternating parity may occur [8–10] in the presence of stable octupole deformations. However, ^{193}Hg is not expected [7] to exhibit stable octupole deformations. It is therefore suggested that in this case (^{193}Hg) two-way cross talk would most likely indicate the presence of $M1$ decays.

Calculations [11] specific to ^{193}Hg have shown that $M1$ cross talk of the order of 25% is not unreasonable for the proposed configurations (namely [512]$\frac{5}{2}$ and [624]$\frac{9}{2}$). The possibility that the one-way cross talk observed [7] in ^{193}Hg was more likely to be $M1$ than $E1$ was first mentioned in Ref. [12].

Assuming bands 1 and 2′ and/or bands 3 and 2 are strongly coupled [7], it is possible to predict the transition

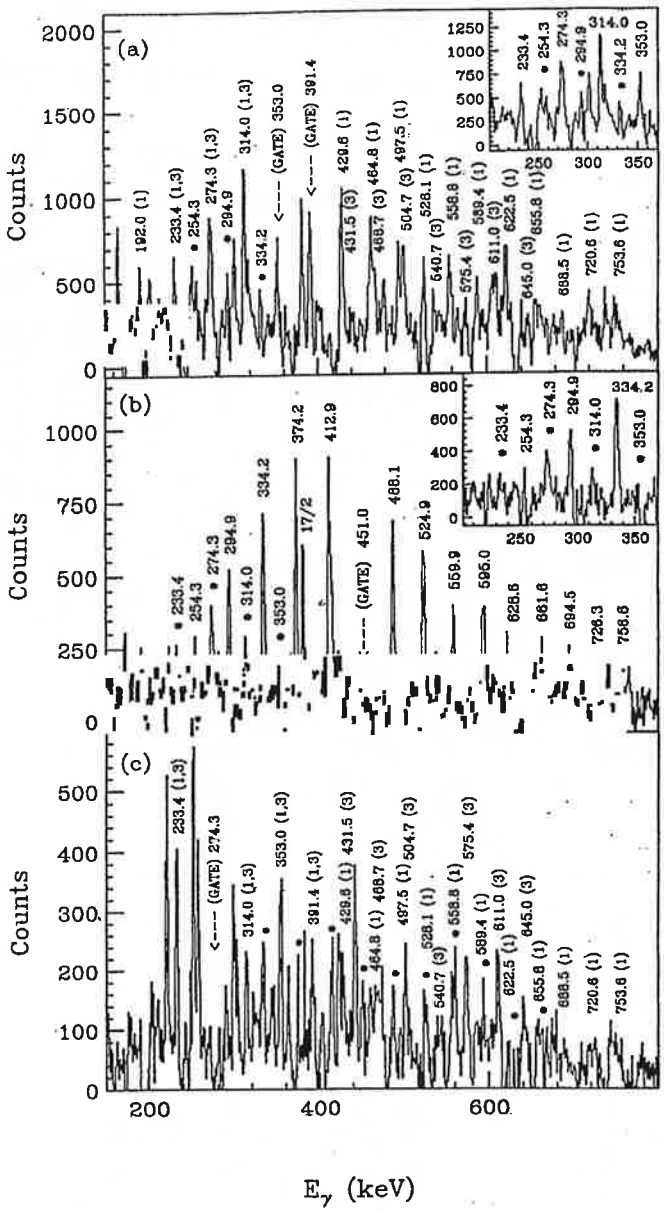

FIG. 2. (a) Spectrum of superdeformed transitions in coincidence with the 353 and 391 keV γ rays in bands 1 and 3. Transitions in bands 1 and 3 are labeled by energy and band assignment. Below 392 keV bands 1 and 3 are identical; at higher energies the bands diverge and are easily resolved. The γ rays marked with "*" correspond to known transitions in band 2. The inset is a section of the same spectrum expanded. (b) Spectrum of superdeformed transitions in coincidence with the 451 keV γ ray in band 2. Transitions in band 2 are labeled by energy. The γ rays marked with "*" correspond to known transitions in bands 1 and 3. The inset is a section of the same spectrum expanded. (c) Same as (a), except the gating transition is now the 274 keV γ ray in bands 1 and 3. Transitions in bands 1 and 3 are labeled by energy and band assignment. The γ rays marked with "*" correspond to transitions in band 2. The lowest γ ray in band 2 ("*") is at 334 keV and the highest is at 661 keV.

energies expected for $M1$ decays between the signature partner bands. For superdeformed states in the spin interval $\frac{21}{2} - \frac{37}{2}$ the $M1$ energies range from 111 to 192 keV and are separated by approximately 10 keV (Fig. 1). The lower portion of Fig. 3 shows a gate on the 391 keV transition in bands 1 and 3, while the upper portion is a section of the total projection spectrum, used to generate the background spectrum. The known superdeformed γ rays from bands 1 and/or 3 are indicated. In addition, at low frequencies there is evidence for a series of weak γ rays within 1 keV of the energies one calculates for $M1$ transitions. The dashed lines correspond to the energies where one may expect to observe $M1$ transitions. The peaks at 142 and 152 keV and to a lesser degree at 182 keV occur in a region where the background (total projection spectrum, upper part of Fig. 3) is relatively "flat" and as such these peaks are rather insensitive to the background subtraction. The gamma ray at 161 keV falls within a region of the spectrum which corresponds to a peak in the total projection and, as a result, is sensitive to background subtraction. For completeness we have also indicated, in brackets, the energies where one would expect to find other $M1$ gamma rays (see Fig. 1). The 132 and 172 keV transitions also correspond to regions in the total projection spectrum where large peaks occur and

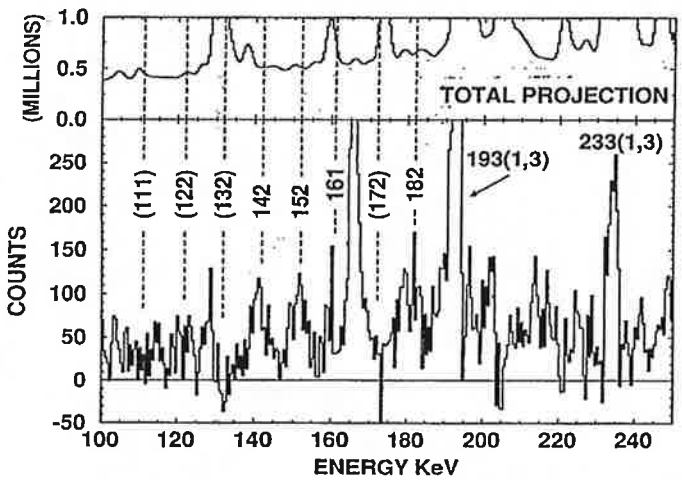

FIG. 3. Spectrum in coincidence with the 391 keV transition in bands 1 and 3. Superdeformed (SD) transitions in bands 1 and 3 are labeled by energy and band assignment. The 192 keV SD peak is a doublet with the $\frac{33}{2}^+ - \frac{29}{2}^+$ 193 keV transition. Other peaks labeled by energy (142, 152, 161, and 182 keV) correspond to where one would expect to see $M1$ γ rays decaying between the two pairs of strongly coupled superdeformed signature partner bands (assumed to be based on the $[512]\frac{5}{2}$ and $[624]\frac{9}{2}$ orbitals). For completeness we also show, in brackets, those energies where one may expect to observe the remaining $M1$ gamma-ray transitions (111, 122, 132, and 172 keV). The upper portion of the figure shows the total projection spectrum. The positions of the proposed $M1$ decays are indicated by a dashed line. See text for more information.

once more we may expect to observe large fluctuations in the final spectrum following background subtraction. For $M1$ transitions and energies as low as 111 and 122 keV, electron conversion is expected to dominate over gamma decay.

It is clear that the energies of the gamma rays shown in Fig. 3 are, within errors, exactly those one would expect for $M1$ decays (Fig. 1). However, the gamma rays are very weak and, as discussed above, several of the peaks are sensitive to the background subtraction. Other superdeformed transitions in bands 1 (and/or 3) and 2 (and/or 2′) are generally more contaminated than the 391 keV gate (Fig. 3); nevertheless, the low energy gamma rays seen in Fig. 3 show up consistently in these other gates. Moreover, a spectrum in coincidence with gamma rays at 142 and 152 keV includes peaks consistent with known inband superdeformed transitions in bands 1 (and/or 3) and 2. Since the gamma rays are weak it was not possible to obtain the multipolarity of the transitions from an angular correlation (directional correlation with oriented nuclei technique) measurement. Finally, one would expect the ratio of the measured γ-ray intensity to the total $M1$ decay intensity to be approximately $\frac{1}{3}$ (due to ce^- decay) whereas the ratio of γ rays to total $E1$ decay intensity would be closer to 1 (very little ce^- decay). The individual intensities for the 142 and 152 keV $M1$ gamma rays are 14(6)% and 15(6)% of the full superdeformed inband intensity respectively or $\sim\frac{1}{2}$ of the total cross talk intensity and hence are more consistent with $M1$ decay. We therefore suggest that the series of low energy transitions (Fig. 3) corresponds to the $M1$ decays between signature partner superdeformed bands (as indicated in Fig. 1).

If it is assumed that ^{193}Hg has the same quadrupole moment as ^{192}Hg (20 eb) [5], then from the measured branching ratios $[(\Delta I=1)/(\Delta I=2)]$ one estimates the $B(M1)$ strength to be of the order of $0.5\mu_N^2$ (for the $[512]\frac{5}{2}$ and the $[624]\frac{9}{2}$ levels, Ref. [11] calculates $B(M1)$ values of 0.5 and 1.0 μ_N^2, respectively). Furthermore, from the measured branching ratios it is also possible to calculate the expected $K\alpha$ x-ray yield due to ce^- decays. For $M1$ transitions in the energy range 111 to 181 keV, one obtains a $K\alpha$ x-ray yield of approximately 0.8 ± 0.2 per cascade (for $E1$ decays this value drops to 0.2 ± 0.06). In Ref. [13] a $K\alpha$ x-ray yield of 1.6 ± 0.4 was measured for band 1 in ^{193}Hg. It is clear that any significant difference between our calculated value (0.8), based on the measured branching ratios, and the measured value (1.6) could easily be due to $M1$ decays between superdeformed transitions which we do not observe.

Because of the very small intensity of the superdeformed bands (1%–2% of the ^{193}Hg channel [7]), it was not possible to decompose the cross talk into contributions from either pair of assumed signature partner bands ($[512]\frac{5}{2}$ or $[624]\frac{9}{2}$). Neither was it possible to rule out

the hypothesis that one-way $E1$ cross talk may also proceed from band 1 ($[512]\frac{5}{2}$ $\alpha=-\frac{1}{2}$) to band 2 ($[624]\frac{9}{2}$ $\alpha=+\frac{1}{2}$) as proposed by Cullen *et al.* [7].

In summary, the data presented here confirm the existence of cross talk between superdeformed bands. Unlike previous experiments the decay is observed both ways, indicating the presence of $M1$ transitions. Furthermore, a series of low energy γ-ray transitions has been identified and it is suggested that these correspond to the $M1$ decays between superdeformed bands.

The authors would like to thank M. A. Riley for useful discussions. This work was supported in part by the Office of Energy Research, Division of Nuclear Physics of the U.S. Department of Energy under Contract No. DE-AC03-76SF00098 (LBL) and in part by the U.S. Department of Energy under Contract No. W-7405-ENG-48 (LLNL).

[a]Present address: California Institute of Technology, Pasadena, CA 91125.

[1] P. J. Twin *et al.*, Phys. Rev. Lett. **57**, 811 (1986).
[2] M. A. Bentley *et al.*, Phys. Rev. Lett. **59**, 2141 (1987).
[3] E. F. Moore *et al.*, Phys. Rev. Lett. **63**, 360 (1989).
[4] M. P. Carpenter *et al.*, Phys. Lett. B **240**, 44 (1990).
[5] E. F. Moore *et al.*, Phys. Rev. Lett. **64**, 3127 (1990).
[6] J. Becker *et al.*, Nucl. Phys. **A520**, 187c (1990).
[7] D. M. Cullen *et al.*, Phys. Rev. Lett. **65**, 1547 (1990).
[8] D. Ward, Nucl. Phys. **A406**, 591 (1983).
[9] W. Nazarewicz *et al.*, Nucl. Phys. **A429**, 269 (1984).
[10] G. A. Leander *et al.*, Nucl. Phys. **A435**, 58 (1986).
[11] P. B. Semmes, I. Ragnarsson, and S. Aberg, Phys. Rev. Lett. **68**, 460 (1992).
[12] P. M. Walker, Phys. Rev. Lett. **67**, 1174 (1991).
[13] D. M. Cullen *et al.*, Phys. Rev. C **47**, 1298 (1993).

Superdeformation in ^{191}Au

D. T. Vo, W. H. Kelly, F. K. Wohn, and J. C. Hill
Iowa State University, Ames, Iowa 50011

M. A. Deleplanque, R. M. Diamond, F. S. Stephens, J. R. B. Oliveira,* J. Burde,† A. O. Macchiavelli,‡ J. deBoer,§ B. Cederwall, I. Y. Lee, and P. Fallon
Nuclear Science Division, Lawrence Berkeley Laboratory, Berkeley, California 94720

J. A. Becker, E. A. Henry, M. J. Brinkman, A. Kuhnert,‖ M. A. Stoyer, and J. R. Hughes
Lawrence Livermore National Laboratory, Livermore, California 94550

J. E. Draper, C. Duyar, and E. Rubel
University of California, Davis, California 95616
(Received 28 December 1992)

A superdeformed band has been observed for the first time in an Au isotope. The reaction used was ^{11}B + ^{186}W, demonstrating that very light ions can be used to populate superdeformed (SD) bands at high angular momentum. The band is assigned to ^{191}Au. The γ-ray energies are at the quarter-point energies of the ^{192}Hg SD band, indicating that it is "identical" to that of ^{192}Hg.

PACS numbers: 23.20.Lv, 21.10.Re, 27.80.+w

The search for new superdeformed (SD) bands is important in many respects. Perhaps most obviously, SD bands are a critical test of our ability to predict nuclear properties. Multiple bands in a given nucleus give us information about the orbitals involved at large deformations, which may be quite different from those in normally deformed nuclei. Superdeformed bands are often identical to others in neighboring nuclei and new examples often provide clues that will help us understand this puzzling phenomenon. "Identical" SD bands, usually in different nuclei, refer to rotational bands that have not only the same moment of inertia, but also identical or "equivalent" transition energies. The "equivalent" transition energies correspond to half-points or quarter-points between two consecutive transition energies in the identical band. Since each transition carries two units of angular momentum, this means that any additional single particle contribution to the angular momentum must be half-integer or integer. This is not expected in the "traditional" models and may lead to the development of new concepts and reveal new symmetries.

In the mass 190 region, superdeformed nuclei are known only for the Hg, Tl, and Pb isotopes [1], although they are predicted [2,3] for both higher and lower atomic numbers. In the SD candidate nuclei with $Z > 82$, it is very difficult to find new superdeformed bands because of higher fission competition. Prior to this work, no SD bands had been found in this region for $Z < 80$. These relatively neutron-rich nuclei can only be populated at high angular momentum with very light neutron-rich projectiles. We report here the first superdeformed band found in a gold ($Z = 79$) nucleus, ^{191}Au. This SD band is the first experimental evidence that this region of superdeformation extends below $Z = 80$. In this odd-Z nucleus, we find that the superdeformed band is "identical" to quarter-point energies of the SD band in the "doubly magic" ^{192}Hg and to an excited band in ^{191}Hg, an odd-neutron nucleus. This is different from the behavior of the Tl nuclei, the other odd-Z SD nuclei in this region, where the extra odd proton does not produce a SD band identical to that in ^{192}Hg.

The experiments were carried out at the Lawrence Berkeley Laboratory 88-Inch Cyclotron using the High Energy-Resolution Array (HERA) facility. HERA consisted of twenty Compton-suppressed Ge detectors and a central 40-element bismuth germanate (BGO) ball. States in ^{190,191,192}Au were populated in the reaction ^{186}W(^{11}B, xn) at three different beam energies: 78, 84, and 86 MeV. The targets consisted of one to three stacked self-supporting 0.5 mg/cm^2 ^{186}W. All threefold and higher γ-ray coincidences were recorded. The twofold coincidence events were recorded only if they were in coincidence with at least six inner ball detectors. All events were recorded together with the γ-ray sum energy and the multiplicity of the inner ball. Also, in the 86-MeV reaction, the time differences between the γ rays detected in the BGO ball and the first-coincident Ge detector were recorded to enable the rejection of delayed γ rays and neutron-induced events. A total of 2.0×10^8, 1.9×10^8, and 3.7×10^8 double events and 3.5×10^7, 4.3×10^7, and 5.0×10^7 triple and higher coincidence events were recorded for the three runs at 78, 84, and 86 MeV, respectively. In each case Doppler-shift corrections were made on the energies of the γ rays emitted from the recoiling nuclei. In a separate set of experiments, the ^{176}Yb(^{19}F,xn) reaction was used at 100- and 105-MeV bombarding energies with a target consisting of three stacked ^{176}Yb metallic foils of 0.5 mg/cm^2 thick-

0031-9007/93/71(3)/340(4)$06.00

ness. Summed over both energies, a total of 3.4×10^8 double and 1.2×10^8 triple and higher coincidence events were recorded.

Correlation matrices of E_γ-E_γ coincidences were constructed with various γ-ray sum-energy (H) and multiplicity (k) requirements. A channel-by-channel search of the matrices revealed a band of at least 13 transitions from $E_\gamma = 229$ to 678 keV in the 86-MeV and 84-MeV data sets for the ^{186}W(^{11}B,xn) reaction (Fig. 1). There is also some weak indication of this band in the 78-MeV data set. The transition indicated by * in Fig. 1 is found in coincidence with SD band members. It has the same energy (371 keV) as the known low-spin $13/2^-$-$9/2^-$ transition in ^{191}Au [4]. However, this transition feeds the 10-ns isomer in ^{191}Au. Because the recoiling nuclei move out of view of the Ge detectors, the 274-keV ($9/2^-$-$11/2^-$) and subsequent transitions in the decay of the isomer are not seen. The relative intensity pattern of the band is shown in the inset. The uncertainties are relatively large due to the very weak intensities. The transition intensities, internal conversion included, increase as the transition energies decrease, become relatively constant for energies from 500 keV down to 300 keV, and decrease after that. This intensity pattern is similar to those of the bands in ^{191}Hg [5]. The energy spacings of the transitions in this band are similar to others in this region, with the differences between adjacent transitions being $\approx$ 41 keV for the lowest energy transitions and $\approx$ 34 keV for the highest energy transitions.

The assignment of the new band to ^{191}Au is supported by the excitation function and cross bombardment results. The SD band is much weaker in the 78-MeV reaction data where ^{192}Au is much more intense (compared with either the 84- or 86-MeV reaction) so that one may rule out the possibility of the SD band belonging to ^{192}Au. Known states with similar spins were populated in the other experiment, ^{176}Yb(^{19}F,xn). The residual nucleus has about the same energy of excitation and maximum angular momentum as those in the ^{186}W(^{11}B,6n) reaction. The statistics of ^{190}Au in this reaction are much better while the ^{191}Au populations are much smaller than those in the ^{186}W(^{11}B,xn) reaction at 84 and 86 MeV. Careful searches for this SD band were performed in these data and it was not found. This suggests that this SD band most likely belongs to ^{191}Au and not to ^{190,192}Au. With a multiplicity $k \geq 18$ and sum energy $H \geq 14$ MeV, the band intensity is only 0.15% of the total ^{191}Au intensity. It is one of the most weakly populated SD bands found to date. There are not sufficient statistics for making a directional correlation analysis to establish multipolarities, and it may be possible that this is a dipole band. However, a plot of the dynamic moments of inertia against frequency ($\hbar\omega$) for this new band compared with similar plots of dipole bands (e.g., in ^{197}Pb and in ^{199}Pb) [6,7] and other SD bands in this region shows a behavior of the dynamic moments of inertia more regular than those of dipole bands and more similar to that of the SD bands. In fact, the band is identical to some other SD bands. Therefore, we made a reasonable assumption that these cascade γ rays of the SD band have multipolarity $L = 2$. Because of the weakness of this SD band one might be tempted to assign it to a Pt nucleus produced by a competing (^{11}B,pxn) reaction. However, our data show that the amount of the Pt produced by the competing pxn channel is a factor of about 30 less than the Au. Typically SD bands in this region are populated at $\approx$ 1% or less. For the observed SD band to be in Pt, therefore, it would have to be populated at the unusually high 5% level to give the intensity observed. We regard this alternative as unlikely.

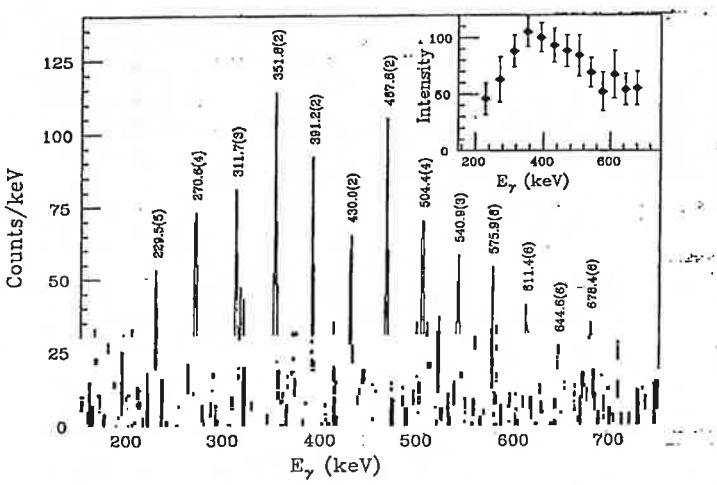

FIG. 1. The γ-ray spectrum of the SD band produced in the ^{186}W(^{11}B,6n)^{191}Au reaction. The data represent the sum of the 84-MeV and 86-MeV data sets. This spectrum is obtained by double gating threefold and higher events. For the 84-MeV data set, the gates are nine transitions from 228 keV to 540 keV. The gates for the 86-MeV data set are all 13 band members. The transition indicated by * is 371 keV (see text). The inset shows the transition intensities, deduced from the double-gated spectrum.

In order to compare this SD band to other bands in this mass region, its dynamic moment of inertia is displayed in Fig. 2 together with those of ^{192}Hg [8,9] and ^{191}Hg* (band 3 in Ref. [5]). It is seen that the moment of inertia for ^{191}Au is very similar to those of the SD bands of ^{192}Hg and ^{191}Hg*. The energy differences between the transitions of ^{191}Au, ^{192}Hg, and ^{191}Hg* SD bands are also shown. Except for the lowest and highest energy transitions, all the comparable transitions in the band are within 2 keV of quarter-point energies of the ^{192}Hg band and those of the ^{191}Hg* SD band.

The fact that the transition energies of the SD band are identical to the quarter-point energies of the ^{192}Hg band implies that the odd proton hole (relative to the ^{192}Hg core) occurs in an orbital which has a zero or an integer alignment. In addition, the absence of a signature partner band to the ^{191}Au SD band suggests some

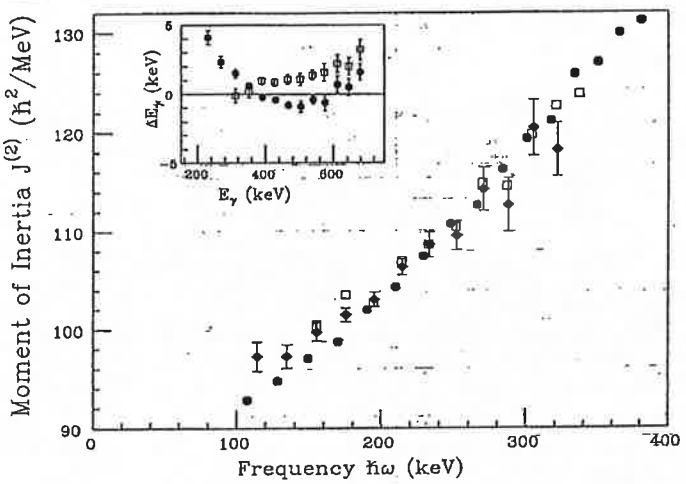

FIG. 2. The dynamic moment of inertia of the ^{191}Au SD band (diamonds) compared to those in ^{192}Hg (circles) and ^{191}Hg* (squares). The inset shows the energy differences between the bands (circles, ^{191}Au - ^{192}Hg quarter-point energies; squares, ^{191}Au - ^{191}Hg*).

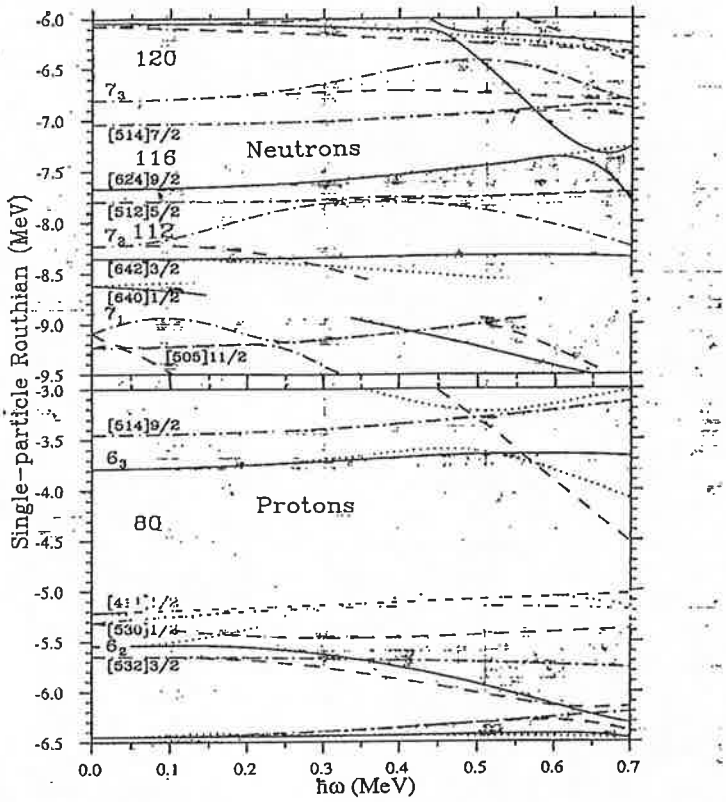

FIG. 3. Single-particle Routhians for ^{191}Au with deformation parameters $\beta_2 = 0.457$, $\beta_4 = 0.048$, and $\gamma = 0.0$. The parameters are taken from the lowest SD minimum in the TRS calculations. (π,α) : solid = (+,+1/2), dotted = (+,−1/2), dash-dotted = (−,+1/2), and dashed = (−,−1/2).

signature splitting. It therefore appears that this band is not based on a strongly coupled orbital.

In order to help assign this odd-Z band to a specific orbital we refer to the single-particle Routhians (Fig. 3). The deformation parameters used to produce this plot were obtained from total Routhian surface (TRS) calculations, based on a deformed Woods-Saxon potential and the Strutinsky shell correction formalism with a monopole pairing interaction [10,11]. Figure 3 shows that at these deformations there are several orbitals near the Fermi surface, including the [411]1/2 and [530]1/2. Other possibilities are the 6_2 and the [532]3/2 orbitals. However, these seem less likely because the 6_2 orbital has a changing alignment and the [532]3/2 appears farther away from the Fermi level in these calculations. Both the [411]1/2 and the [530]1/2 orbitals are fairly flat in the observed frequency range. Since a proton hole in a flat orbital will produce no alignment relative to ^{192}Hg, these assignments are not inconsistent with the observed γ energies. This requires that the decoupling parameter for this orbit be different at these deformations. Indeed particle-rotor model calculations suggest that this may be the case.

The spins of the states are suggested using the methods of Draper *et al.* [12] and Becker *et al.* [13]. Using the two methods to fit the energies of the transitions gives an average of 11.2(1) for the spin parameter of the upper level of the 229-keV transition. Since the nucleus is odd-A, the most likely spin consistent with the above least-squares analysis for the upper level is 23/2.

The alignment plots [14] for ^{191}Au and ^{191}Hg* relative to ^{192}Hg are displayed in Fig. 4. As with many other examples of superdeformed bands in this region, ^{191}Au shows an alignment of $i = 1$ relative to ^{192}Hg. This general phenomenon is not well understood. However, it has been discussed [14] in terms of the aligned intrinsic pseudospins of a pair of valence nucleons. The weak coupling of the pseudo-orbital to the pseudointrinsic spin is a property of the observed approximate pseudospin symmetry

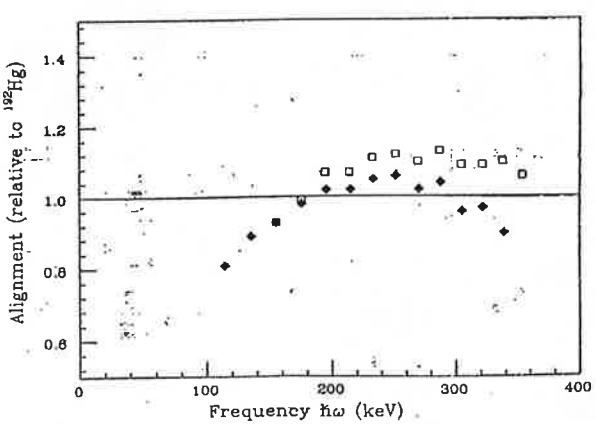

FIG. 4. Alignment of the ^{191}Au SD band (diamonds) and the ^{191}Hg* SD band (squares) relative to the ^{192}Hg SD band.

in nuclear systems [15].

In addition to the SD band in ^{191}Au described above, we have observed another somewhat weaker band with energies nearly identical to the yrast SD band in ^{191}Hg [16]. The transition energies are nearly the same as those in the newly found SD band for low E_γ and they diverge at high E_γ. The energies of the higher energy transitions in this band are 506, 543, 580, 616, 651, and 686 keV. Weak evidence for several of these peaks can be seen in Fig. 1. The peaks are more prominent under different gating conditions. This second band was seen only in the 86-MeV data set and the data are insufficient to allow us to assign it to a nucleus. Because of its apparent relationships to the SD bands of ^{191}Hg and ^{191}Au, it would be very interesting to characterize this band further.

In conclusion, we note that the SD band in ^{191}Au represents the first experimental evidence concerning the nature of the proton orbitals below $Z = 80$ in superdeformed nuclei. The band may be characterized by either the [411]1/2 or the [530]1/2 proton orbital. This is the first observation of an SD band in this region based on these orbitals. This band has an unexpected and interesting property: it shows an identical band relationship to the yrast (quarter-point energies) band in ^{192}Hg. However, there is no evidence as yet of a signature partner band. This band is very weak and it represents a limit of what can be done with the current generation of Compton-suppressed Ge arrays. A great deal remains to be learned concerning the properties of this SD region and the relationships between the SD bands. It is important that we continue extending this region of superdeformation with the next generation of detector arrays.

This work is supported in part by the Research Corporation Grant No. R-152 and an IPA Independent Research Agreement with the Division of Undergraduate Education of the National Science Foundation (Kelly), the U.S. Department of Energy under Special Research Grant No. DE-FG02-92ER40692 (ISU), under Contracts No. DE-AC03-76SF00098 (LBL) and No. W-7405-ENG-48 (LLNL), and Grant No. DFG Bo1109 (deBoer).

---

* Permanent address: Universidade de São Paulo, São Paulo, SP, Brazil.
† Permanent address: The Racah Institute for Physics, The Hebrew University, Jerusalem, Israel.
‡ Permanent address: Comisión Nacional de Energia Atómica 1429 - Buenos Aires, Argentina.
§ Permanent address: Universität München, Am Coulombwall 1, D - 8046 Garching, Germany.
‖ Permanent address: California Institute of Technology, Pasadena, CA 91125.

[1] R.V.F. Janssens and T.L. Khoo, Annu. Rev. Nucl. Part. Sci. **41**, 321 (1991), and references therein.
[2] R.R. Chasman, Phys. Lett. B **219**, 227 (1989).
[3] S. J. Krieger *et al.*, Nucl. Phys. **A542**, 43 (1992).
[4] Y. Gono *et al.*, Nucl. Phys. **A327**, 269 (1979).
[5] M.P. Carpenter *et al.*, Phys. Lett. B **240**, 44 (1990).
[6] A. Kuhnert *et al.*, Phys. Rev. C **46**, 133 (1992).
[7] G. Baldsiefen *et al.* (to be published).
[8] J.A. Becker *et al.*, Phys. Rev. C **41**, R9 (1990).
[9] D. Ye *et al.*, Phys. Rev. C **41**, 13 (1990).
[10] R. Wyss *et al.*, Phys. Lett. B **215**, 255 (1988).
[11] W. Nazarewicz *et al.*, Nucl. Phys. **A435**, 397 (1985).
[12] J.E. Draper *et al.*, Phys. Rev. C **42**, R1791 (1990).
[13] J.A. Becker *et al.*, Phys. Rev. C **46**, 889 (1992).
[14] F. Stephens *et al.*, Phys. Rev. Lett. **65**, 301 (1990).
[15] A. Bohr, I. Hamamoto, and Ben R. Mottelson, Phys. Scr. **26**, 267 (1982).
[16] E.F. Moore *et al.*, Phys. Rev. Lett. **63**, 360 (1989).

"Investigação da estrutura nuclear de altos spins por meio de espectroscopia gama e reações com íons pesados" - J.R.B. Oliveira

ERRATA

Sumário

Pgs. 5 e 6 - Todas as páginas listadas no Sumário encontram-se defasadas de uma unidade para menos.

Capítulo 1

Pg. 7 - Introdução - Parágrafo 1 - Linha 7: "... outros são..." ao invés de: "... outrossão...".

Capítulo 2

Pg. 9 - Subseção 2.1.1 - Parágrafo 1 - Linha 2: "... àquela..." ao invés de: " ... à aquela..."; Subseção 2.1.2 Modelo rotacional - Parágrafo 1 - Linha 1: "... características..." ao invés de: "... característica..."; Subseção 2.1.2: Substituir as 3 fórmulas (pgs. 9 e 10) por: $E(I) = \frac{I(I+1)\hbar^2}{2\mathcal{J}}$; $\mathcal{J}^{(1)} = \frac{2I-1}{E_\gamma}\hbar^2$; e $\mathcal{J}^{(2)} = \frac{4\hbar^2}{\Delta E_\gamma}$.

Pg. 12 - Subseção 2.3.1 - Emparelhamento - Parágrafo 1 - Linha 4: "... supercondutor, ..." ao invés de: "... superfluido, ...".

Pg. 17 - Seção 2.4 *Tilted Axis Cranking (TAC)* - Último parágrafo - Linha 2: "... semelhantes às do modelo..." ao invés de: "... semelhantes ao modelo..." .

Pg. 19 - Subseção 2.4.3 - Linha 1: "... do modelo de TAC é a..." ao invés de: "... do modelo de TAC, a...".

Capítulo 4

Pg. 33 - Penúltima linha do penúltimo parágrafo da Subseção 4.2.1: "... ^{11}B/Pb) para ..." ao invés de "... ^{11}B/Pb para ...".

Pg. 34 - Subseção 4.2.2 - Último parágrafo antes de "Bandas quirais" - Ante-penúltima linha: " ... dá-se em..." ao invés de: "... se dá em..."; Segundo parágrafo de "Bandas quirais" - Linha 6: "... reforçar a triaxialidade..." ao invés de: "... reforçar a tendência para a triaxialidade...".

Pg. 35 - Penúltimo parágrafo da Subseção 4.2.3 - Linha 3: "... prevêem..." ao invés de: "... preveem...".